Technische Universität München
TUM School of Engineering and Design

Linearized Modeling of Thermoacoustic Systems utilizing a Discontinuous Galerkin Finite Element Method

Maximilian Johannes Meindl

Vollständiger Abdruck der von der TUM School of Engineering and Design der Technischen Universität München zur Erlangung des akademischen Grades eines

DOKTORS DER INGENIEURWISSENSCHAFTEN

genehmigten Dissertation.

Vorsitzender:
Prof. Dr. Steffen Marburg
Prüfer der Dissertation:
Prof. Wolfgang Polifke, Ph.D.
Prof. Dr. Kilian Oberleithner

Die Dissertation wurde am 23.03.2021 bei der Technischen Universität München eingereicht und durch die TUM School of Engineering and Design am 14.09.2021 angenommen.

Abstract

This thesis is aimed at expanding the linear thermoacoustic modeling spectrum, especially by models that account not only for acoustic, but also convective waves, as well as interactions between the mean flow and the perturbations. The most advanced models derived in this work even account for locally linearized reaction mechanisms, thus yielding more accurate predictions of combustion instabilities than previous state-of-the-art approaches.

In addition to new conceptual approaches, the Discontinuous Galerkin Finite Element Method is applied for the first time in linear thermoacoustic modeling. This numerical ansatz unites several desirable features, which include robust and flexible flux discretization, physically motivated stabilization by means of upwinding and straight forward adaptability to higher order basis functions.

The spatially discretized models emerging from this special Finite Element Method can be cast in state-space form, which is a generalized representation for linear, time-invariant first order differential equations. The state-space framework allows the interconnection of multiple (thermo-)acoustic models stemming from different sources and employing different assumptions. Thus, it is possible to couple one dimensional network models, which account only for acoustic waves, to geometrically complex three dimensional models, which include beyond acoustics also vortical as well as entropic perturbations. This *divide et impera* approach facilitates highly accurate modeling strategies where necessary (e.g. in the vicinity of the flame) and reduced order modeling where possible (e.g. in regions where the flow is predominantly axial).

The methodology suggested in this thesis is shown to predict thermoacoustic eigenmodes with increased accuracy compared to modeling strategies that employ stronger simplifications, albeit the computational cost is very low compared to high fidelity methods such as reacting Large Eddy Simulation. For laminar flames, the flame response to acoustic forcing is derived with high accuracy in a fraction of the time that would be required for state-of-the-art approaches employing broadband forcing of non-linear reacting flow simulations coupled to system identification. This is extremely appealing, as the determination of the flame dynamics is by far the most costly aspect of numerical thermoacoustic stability analysis. The presented methodology thus supports fast and predictive assessment of operational stability in the design phase of gas turbines.

Kurzfassung

Die vorliegende Arbeit zielt darauf ab, das Spektrum der Modellierungsansätze in der Thermoakustik zu erweitern, insbesondere um Modelle, die nicht nur akustische, sondern auch konvektive Wellenarten, sowie deren Interaktion mit dem mittleren Strömungsfeld berücksichtigen. Die am weitesten entwickelten Modelle in dieser Arbeit betrachten hierzu sogar örtlich aufgelöste linearisierte Reaktionschemie, was genauere Vorhersagen von Verbrennungsinstabilitäten erlaubt als Ansätze gemäß dem vorherigen Stand der Technik.

Zusätzlich zu den neuen Modellierungsansätzen wird erstmals die Discontinuous Galerkin Finite Elemente Methode in linearen thermoakustischen Modellen verwendet. Dieser numerische Ansatz vereint einige wünschenswerte Eigenschaften, wie zum Beispiel die robuste und flexible Diskretisierung numerischer Flüsse, eine durch die Physik des Problems motiviert Stabilisierung des Verfahrens durch richtungsabhängige Schemata, sowie die einfache Erweiterbarkeit hin zu Ansatzfunktionen höherer Ordnung.

Die örtlich diskretisierten Modelle, die durch diese spezielle Finite Elemente Methode entstehen, können im Zustandsraum formuliert werden, was eine generalisierte Darstellungsweise für lineare, zeitinvariante Differentialgleichungen erster Ordnung ist. Die Zustandsraumdarstellung ermöglicht die Verbindung mehrerer (thermo-)akustischer Modelle verschiedenen Ursprungs, die auf unterschiedlichen Vereinfachungen basieren. So ist es möglich, eindimensionale Netzwerkmodelle, die nur akustische Wellen berücksichtigen, mit dreidimensionalen Modellen komplizierter Geometrien zu koppeln, die darüber hinaus auch Störungen in der Wirbelstärke und der Entropie auflösen. Diese *divide et impera* Herangehensweise ermöglicht den Einsatz präziser Modellierungsansätze, wo nötig (beispielsweise in Flammennähe), und von Modellen mit reduzierter Ordnung, wo möglich (beispielsweise in Regionen, in denen die Strömung hauptsächlich axial ist).

Die Methodiken, die in der vorliegenden Arbeit vorgestellt werden, können thermoakustische Eigenmoden genauer vorhersagen als Modellierungsansätze die stärkere Vereinfachungen nutzen, obwohl der Rechenaufwand im Vergleich zu hochaufgelösten Methoden wie der Large Eddy Simulation reagierender Strömungen sehr gering ist. Für laminare Flammen kann die Flammenantwort auf akustische Anregung mit hoher Präzision bestimmt werden, wobei die Laufzeit nur einen Bruchteil der Zeit beträgt, die der gängige Ansatz mit einer Kombination aus breitbandiger Anregung einer nichtlinearen Verbrennungssimulation und anschließender Systemidentifikation braucht. Das ist vor allem deshalb sehr attraktiv, da die Bestimmung der Flammendynamik der kostspieligste Aspekt der numerischen thermoakustischen Stabilitätsanalyse ist. Die in dieser Arbeit vorgestellte Methodik ist deshalb gut für die schnelle und prädiktive Evaluierung der Betriebsstabilität von Gasturbinen im Entwicklungsstadium geeignet.

Vorwort

Die vorliegende Arbeit entstand während meiner Zeit als Lehrassistent an der Professur für Thermofluiddynamik der Technischen Universität München. Ich möchte mich ganz herzlich bei meinem Doktorvater Wolfgang Polifke bedanken, der mir einerseits immer mit Rat und Tat zur Seite stand, mir andererseits aber auch sämtliche Freiheiten gab, meine Forschung selbst zu gestalten. Nur durch das Vertrauen, das er mir entgegengebracht hat, konnte sich die Arbeit thematisch in diese Richtung entwickeln. Sein Mentorat wirkt jedoch deutlich über den fachlichen Bereich hinaus. Besonders mein Vortragsstil und die Art und Weise, Studierende zu betreuen, sind stark durch sein Vorbild geprägt. Ihm ist es auch zu verdanken, dass am Institut eine lockere und dennoch produktive Stimmung herrscht.

Die meisten der Ideen, die im Rahmen dieser Arbeit entstanden sind, wurden in enger Zusammenarbeit mit Wolfgang Polifke und meinen Kollegen am Institut entwickelt. Obwohl es mir schwer fällt, einige meiner Mit-Doktoranden aus dieser wirklich großartigen Gruppe hervorzuheben, möchte ich dennoch ein paar von ihnen persönlich erwähnen. Tobias Holzinger, Ralf Blumenthal und Thomas Steinbacher waren als Student meine ersten Kontakte zum Lehrstuhl im Praktikum Grundlagen numerischer Thermofluiddynamik. Stefan Jaensch brachte mir die Grundzüge der Thermoakustik während meiner Semesterarbeit bei. Thomas Emmert betreute nicht nur in geduldigster Weise meine Masterarbeit, sondern ermöglichte mir auch einen idealen Einstieg in die Gepflogenheiten als Doktorand. Darüber hinaus weiß ich nicht, wie oft ich die Frage „Wo kann man das denn nachlesen?“ eines Kollegen mit „Das hat mir Thomas damals am Whiteboard erklärt.“ beantwortet habe. Alexander Avdonin hatte die Idee des Linearized Reactive Flows, der die vorliegende Arbeit stark geprägt hat. Ohne seine motivierenden Worte hätte ich wohl nach Monaten vergeblicher Implementierungsversuche aufgegeben und mich der damals gängigen Meinung unter den Kollegen angeschlossen, dass linearisierte Verbrennungschemie einfach nicht funktioniert. Mit Christian Lang durfte ich leider nur ein Jahr im Büro verbringen, an das ich mich aber immer gerne zurück erinnere. Unsere Diskussionen über die Navier-Stokes Gleichungen haben einen bleibenden Eindruck auf mein Verständnis der Fluidmechanik hinterlassen. Guillaume Fournier, mit dem ich in den letzten zwei Jahren das Büro teilte, war mir immer ein Vorbild an Gewissenhaftigkeit und Durchhaltevermögen. Unsere Gespräche werden mir sehr fehlen. Moritz Merk, der nicht nur mein Forschungsthema, sondern auch meine Lehrtätigkeit als Assistent für die Wärmetransportphänomene weiterführt, hat mir vieles an Arbeit abgenommen und mich in der Entwicklung neuer Ideen unterstützt. Last but not least möchte ich mich noch bei Felix Schily und Simon van Buren bedanken, die während meiner Zeit am Institut nicht nur zu vertrauten Kollegen, sondern zu Freunden wurden. Ihre Hilfe in schwierigen Zeiten als Doktorand war unbezahlbar.

Das wichtigste jedoch, was mich täglich antreibt, ist meine Familie. Ein herzliches Dankeschön

an meine Eltern und Großeltern, die mich während Studium und Promotion immer unterstützt haben, sich mit mir über Erfolge gefreut haben und mir in schweren Zeiten die Kraft gegeben haben, weiter zu machen. Die größte Unterstützung fand ich in meiner Frau Sabrina, sowie in meinen Söhnen Noah, Jakob und Linus. Ohne euch wäre diese Arbeit niemals entstanden, und euch im speziellen möchte ich sie widmen.

Contents

1 Introduction

The ecological challenge of the 21st century is to meet the drastically growing need for electrical power, while reducing the generated emissions of the production [1]. The long term solution, generation of electrical power from renewable resources such as wind and solar energy, comes with one significant drawback: the unsteadiness in supply. To counterbalance the fluctuating availability of electrical energy from renewable sources, gas turbines are commonly used as one of the more ecologically friendly conventional power sources. Beyond the importance during the transitional phase towards renewable energy sources, "power-to-gas" technologies that store excess energy in chemical form rather than by means of batteries, can utilize gas turbines in the conversion process to electrical energy [2]. Quick start-up times as well as a wide operational range are required to guarantee the flexibility needed for the on-demand operation. Additionally, combustion is kept in the lean premixed regime to reduce pollutant emissions, which however makes the engines susceptible to thermoacoustic combustion instabilities [3–5]. Meeting the requirements for stable, flexible and robust operation under aggravated conditions leads to a significant increase in complexity during the design phase of gas turbines.

The most challenging kind of combustion instabilities found in lean premixed gas turbines are thermoacoustic instabilities [6]. These are based on a feedback loop between acoustic waves impinging on the flame and unsteady combustion, which in turn generates acoustics, leading to oscillations possibly throughout the whole engine. When positive interference between the unsteady combustion and the acoustic waves at the flame occurs, the amplitudes of these oscillations can grow in time and be detrimental to safe and efficient operation of the machine [7]. High pressure amplitudes can damage finer structures of the engine and lead to increased noise emission. Additionally, the unsteady combustion has a negative influence on material wear as well as pollutants in the exhaust gas. In extreme cases, thermoacoustic instabilities lead to blow out, flash back or even the destruction of the engine.

Therefore, tools are required to predict combustion dynamics with high accuracy, but at affordable cost, as early as possible in the design phase of a gas turbine. Lord Rayleigh was already aware of the interaction between acoustic waves and combustion in the 19th century [7]. The interest for technical applications grew in the 1950s when rocket engines failed in spectacular manner due to thermoacoustic instabilities. The first quantitative descriptions of the reaction of the perturbed combustion due to acoustic waves [8] as well as the relation between the perturbed heat release rate and the generated acoustics were formulated [9]. Today, a plethora of analytical as well as numerical models for the prediction of thermoacoustic instabilities are available, from inexpensive reduced order descriptions that rely heavily on simplifying assumptions to highly complex compressible reactive flow solvers that require a super computer to run, but therefore include the interaction between acoustics, turbulence, species mixing and combustion kinetics, to name only a few.

The focus of the work summarized in this publication-based thesis is the extension of the lin-

ear thermoacoustic model spectrum in terms of introducing more detailed governing equations. Thus, the gap between linearized reduced order models, which often employ strong simplifications to the physics, and non-linear thermoacoustic modeling approaches based on more sophisticated governing equations, can be closed (compare e.g. Fig. 1 in [10]). The motivation to account for the intricate interplay between flow perturbations, acoustic waves and the unsteady combustion by making as few a priori assumptions as possible about the perturbed flow is to increase the predictive quality of linear thermoacoustic methods. This is achieved by introducing the Linearized Reactive Flow (LRF), a modeling approach that takes into account not only perturbations of the flow, but also in the species transport and the local combustion reaction rates.

The main difference between the LRF and current state-of-the-art reduced order models is that it is not hybrid in nature, i.e. the reacting flow is modeled as one monolithic system instead of the common *divide et impera* approach to represent the thermoacoustic system by connection of dedicated submodels for the flow perturbations and the flow-flame interaction. Furthermore, the disadvantages of the hybrid modeling approach are investigated and it is shown that spurious entropy perturbations are produced if the coupling of the submodels does not account for flame movement, which is a crucial property of every flame.

Beyond the linearized thermoacoustic modeling equations, their numerical treatment with a Discontinuous Galerkin Finite Element Method is introduced. It provides a robust ansatz with straight forward extensibility to higher order schemes to discretize the governing equations and thus the overall approach allows predictive thermoacoustic modeling. Beyond the scope of LRF, the presented numerical methodology is applied to hybrid models based on Linearized Navier-Stokes and Linearized Euler Equations.

The purpose of this publication-based thesis is to give an overview of the fundamentals of thermoacoustic modeling with the Discontinuous Galerkin Finite Element Method and provide the context around and connections between the papers of this thesis.

2 Governing Equations

Experimental investigation of gas turbines and rocket engines, including the required measurements to diagnose the occurring thermoacoustic instabilities, are prohibitively expensive and only possible after the initial design phase. The restricted access to quantities of interest via diagnostics additionally complicates the investigation of those instabilities by means of an experimental setup. Therefore, numerical simulations are often employed to complement or even replace those setups. This chapter introduces the governing equations employed for those kinds of studies.

2.1 Reactive Flow

The basis for the numerical tools in thermoacoustics are the governing equations for a reactive flow, consisting of the Navier-Stokes Equations alongside the species transport equations. For combustion, the formulation of the energy equation in terms of total enthalpy is oftentimes favorable [5]. Note that in the frame of this thesis work, viscous heating is neglected, because the Mach number in combustion chambers is typically small enough such that this effect has no major contribution to the energy balance. The term for the heat flux caused by diffusion of species with different enthalpies is also ignored.

$$\frac{\partial \rho}{\partial t} + \frac{\partial}{\partial x_j}\left(\rho u_j\right) = 0 \tag{2.1}$$

$$\frac{\partial}{\partial t}\left(\rho u_i\right) + \frac{\partial}{\partial x_j}\left(\rho u_i u_j\right) = -\delta_{ij}\frac{\partial p}{\partial x_j} + \frac{\partial \tau_{ij}}{\partial x_j} \tag{2.2}$$

$$\frac{\partial}{\partial t}\left(\rho h_t - p\right) + \frac{\partial}{\partial x_j}\left(\rho h_t u_j\right) = \frac{\partial}{\partial x_j}\left(\lambda \frac{\partial T}{\partial x_j}\right) + \dot{q}_V \tag{2.3}$$

$$\frac{\partial}{\partial t}\left(\rho Y_k\right) + \frac{\partial}{\partial x_j}\left(\rho Y_k u_j\right) = \frac{\partial}{\partial x_j}\left(D_k \frac{\partial Y_k}{\partial x_j}\right) + \dot{\omega}_k \tag{2.4}$$

Here, thermal and species diffusion is modeled by Fourier's and Fick's law, respectively. Assuming Stokes' hypothesis and a Newtonian fluid, the viscous stress tensor is given by

$$\tau_{ij} = \mu\left(\frac{\partial u_i}{\partial x_j} + \frac{\partial u_j}{\partial x_i} - \delta_{ij}\frac{2}{3}\frac{\partial u_k}{\partial x_k}\right), \tag{2.5}$$

and the relation between pressure, density and temperature can be modeled via the ideal gas law for the cases presented in this thesis.

$$p = \rho R T \tag{2.6}$$

The reaction rates that govern the volumetric heat release rate $\dot{q}_V$ and the production rate of species k, $\dot{\omega}_k$, are typically expressed as non-linear functions of the thermodynamic state variables T, p, ρ as well as the species mass fractions Y_k.

2.2 Linearized Reactive Flow

Equations (2.1) - (2.4) can be solved numerically for laminar cases, together with a suitable chemical reaction model. For turbulent cases, it is common to employ filtering techniques to avoid the resolution of small-scale turbulent structures. Two popular approaches employ temporal filtering via Reynolds averaging (Reynolds Averaged Navier Stokes, RANS) or spatial filtering (Large Eddy Simulation, LES) to these equations and subsequently solve them with similar approaches to a laminar flow. Due to the non-linear nature of the governing equations, phenomena such as mode coupling, transfer of perturbation energy between different frequencies as well as the excitation of higher harmonic oscillations can be represented. Although these are effects that can appear in real thermoacoustic systems, and thus their nature needs to be studied, they complicate the identification of the fundamental instability mechanisms. For example, the non-linear dynamics can obscure the presence of a second unstable thermoacoustic eigenmode, which is suppressed by a primary instability.

Beyond the challenges in interpretation of results, non-linearity of the reactive flow equations also restricts the solution algorithms predominantly to simulations in the time-domain. Compared to computations in the frequency domain as well as an eigenvalue analysis (both are methods that can be employed in a straight-forward manner for linear systems), time-domain simulations require significant computational effort, provided the phenomenon under investigation is inherently connected to (a superposition of) harmonic oscillations. Therefore, it is desirable to broaden the variety of investigation methods by linearization of the governing equations, simultaneously eliminating non-linear thermoacoustic effects. This linearization, consequently, results in methods that can only predict the linear onset of combustion instabilities, and lack any information about their non-linear temporal evolution, e.g. the amplitude of limit-cycle oscillations.

2.2.1 Governing Equations

A commonly made perturbation ansatz employed as a first step towards linearization of the governing equations is the Reynolds decomposition, which splits the unknown variables $\Phi = (\rho, u_i, p)$ in a steady-state mean flow $\bar{\Phi}(\boldsymbol{x})$ and perturbations $\Phi'(\boldsymbol{x}, t)$,

$$\Phi(\boldsymbol{x}, t) = \bar{\Phi}(\boldsymbol{x}) + \Phi'(\boldsymbol{x}, t). \tag{2.7}$$

Inserting this ansatz into Eqs. (2.1)-(2.6) and neglecting non-linear terms, the Linearized Reactive Flow (LRF) equations can be obtained.

$$\frac{\partial \rho'}{\partial t} + \frac{\partial}{\partial x_j}\left(\rho' \bar{u}_j + \bar{\rho} u'_j\right) = 0 \tag{2.8}$$

$$\frac{\partial}{\partial t}\left(\rho' \bar{u}_i + \bar{\rho} u'_i\right) + \frac{\partial}{\partial x_j}\left(\rho' \bar{u}_j \bar{u}_i + \bar{\rho} u'_j \bar{u}_i + \bar{\rho} \bar{u}_j u'_i\right) + \delta_{ij}\frac{\partial p'}{\partial x_j} = \frac{\partial \tau'_{ij}}{\partial x_j} \tag{2.9}$$

$$\frac{\partial}{\partial t}\left(\rho' \bar{h} + \bar{\rho} h' - p'\right) + \frac{\partial}{\partial x_j}\left(\rho' \bar{h} \bar{u}_j + \bar{\rho} h' \bar{u}_j + \bar{\rho} \bar{h} u'_j\right) = \frac{\partial}{\partial x_j}\left(\lambda' \frac{\partial \bar{T}}{\partial x_j} + \bar{\lambda}\frac{\partial T'}{\partial x_j}\right) + \dot{q}'_V \tag{2.10}$$

$$\frac{\partial}{\partial t}\left(\rho' \bar{Y}_k + \bar{\rho} Y'_k\right) + \frac{\partial}{\partial x_j}\left(\rho' \bar{Y}_k \bar{u}_j + \bar{\rho} Y'_k \bar{u}_j + \bar{\rho} \bar{Y}_k u'_j\right) = \frac{\partial}{\partial x_j}\left(D'_k \frac{\partial \bar{Y}_k}{\partial x_j} + \bar{D}_k \frac{\partial Y'_k}{\partial x_j}\right) + \dot{\omega}'_k \tag{2.11}$$

$$\tau'_{ij} = \bar{\mu}\left(\frac{\partial u'_i}{\partial x_j} + \frac{\partial u'_j}{\partial x_i} - \delta_{ij}\frac{2}{3}\frac{\partial u'_k}{\partial x_k}\right) + \mu'\left(\frac{\partial \bar{u}_i}{\partial x_j} + \frac{\partial \bar{u}_j}{\partial x_i} - \delta_{ij}\frac{2}{3}\frac{\partial \bar{u}_k}{\partial x_k}\right) \tag{2.12}$$

$$\frac{T'}{\bar{T}} = \frac{p'}{\bar{p}} - \frac{\rho'}{\bar{\rho}} \tag{2.13}$$

Expressions for the perturbations in material properties dynamic viscosity μ', thermal conductivity λ' and species diffusivity D' have to be provided additionally. The source terms $\dot{q}'_V$ and $\dot{\omega}'_k$ of the monolithic LRF approach depend on the unknown variables via a linearized combustion mechanism. Examples are the linearized one-step Westbrook and Dryer mechanism [11, 12] or the linearized two-step 2S-CM2 mechanism [13, 14] (both for methane-air combustion).

As can be seen from Eq. (2.7), a steady-state mean flow is required for the LRF. This steady state is usually computed from non-linear Computational Fluid Dynamics (CFD). It should be noted that the computation of this steady-state takes only a fraction of the effort it would take to determine the thermoacoustic stability of a system purely via CFD. Thus, the LRF approach with comparatively small computational cost to solve for the linearized governing equations, has significant cost advantages even after factoring in the effort to compute the mean flow. For cases that are inherently unsteady, e.g. turbulent flow, usage of a time-averaged, instead of a steady-state flow field was demonstrated to be viable [15–19]. This is important especially for reacting cases, as RANS, which produces steady-state solutions, as well as unsteady RANS, were shown to be incapable of reproducing accurately the flame shape and dynamics [20]. Solutions from LES, on the other hand, although capable of representing the flame dynamics in good agreement to experimental observations, are inherently unsteady due to turbulent fluctuations.

2.2.2 Transformation to the Laplace Domain

The linearized governing equations given in this chapter are presented in the time-domain. In thermoacoustics, it is often advantageous to perform a space-time separation of the perturbed variables and to assume harmonic time dependence.

$$\Phi'(\boldsymbol{x}, t) = \hat{\Phi}(\boldsymbol{x}) e^{st} \tag{2.14}$$

Here, $s = \sigma + i\omega$ is the Laplace variable, used to represent a temporal oscillation with frequency ω and growth rate σ. $\hat{\Phi}(\boldsymbol{x})$ is the complex valued spatial distribution of the perturbation variable. Inserting this ansatz into one of the governing equations allows to determine the system's response to external forcing in the linear regime for a given s. Alternatively, the computation of the eigenfrequencies and -modes of the system in the homogeneous case is possible. It is often preferred to investigate thermoacoustic systems in the Laplace instead of the time-domain because of the reduced computational effort and the clear separation between oscillation frequencies.

3 Hybrid Thermoacoustic Modeling Approaches

This chapter introduces and motivates the concept of hybrid as opposed to monolithic linearized thermoacoustic models like the LRF. Both of these approaches, however, rely on non-linear computations to provide a steady-state mean-flow as the basis for linearization, and are thus not a stand-alone approach for thermoacoustic stability analysis.

3.1 Scale Disparity in Thermoacoustic Models

The physical mechanisms involved in thermoacoustic combustion instabilities happen on largely different scales: acoustic waves feature large spatial extent and propagate comparatively fast, with the speed of sound augmented by the mean flow velocity. This fast propagation limits the time step size in numerical simulations, as typically the Courant-Friedrichs-Lewy number should stay below unity [21]. The chemical reactions in the combustion zone are strongly impacted by the species and heat transport, which are diffusive processes that require high spatial resolution to be correctly represented. Additionally, the strong non-linear nature of the reaction mechanisms leads to a stiff system of equations, requiring iterative solution procedures. Convective waves are usually of intermediate spatial extent and propagate slower than acoustic waves.

This disparity in scales, which is present in monolithic thermoacoustic models, leads to strong restrictions on the time step as well as the mesh size. As a result, the computational effort to deduce the flame response to acoustic forcing from laminar CFD or LES in the time domain is very significant. A strong gain in efficiency can be achieved by employing the LRF. Due to the linear nature, iterative solution procedures can be avoided and a transformation to the Laplace domain is possible. This allows to directly deduce the response of the system at a given complex frequency by solving only one system of linear equations. Note however, that the restrictions on mesh size are not alleviated by the LRF approach. The combustion zone as well as parts of the geometry that produce significant hydrodynamic perturbations have to be highly resolved to correctly capture thermoacoustic instabilities.

3.2 Hybrid Models

Due to the high computational demand of monolithic models, a common approach in thermoacoustics is the use of *hybrid models*, in which the small and large scales of the problem are

treated separately.

First, a non-linear CFD simulation is employed to determine the response of the flame to acoustic forcing. Because most often, the combustion zone is compact with regard to the acoustic wavelength, the correct propagation velocity of the acoustics is insignificant for the flame response. Therefore, the assumption of a weakly compressible flow is justified, which expresses density as a function of temperature, but not pressure. This alleviates the computational demand because the time-step size can be increased compared to a fully compressible approach. The flow-flame interaction model is determined via post-processing methods of the forced combustion simulation. Two commonly used approaches are Fourier transformation of a harmonically forced case, leading to a model that is only known at the discrete frequencies of forcing, and system identification of a broadband forced case. The latter method is a form of regression analysis, usually between the time series of the spatially integrated heat-release perturbation (output) and the velocity fluctuations at a reference position (input), both induced by the forcing. This methodology requires only one simulation, as opposed to the necessity for an individual simulation for each forcing frequency in the Fourier transformation procedure. However, the quality of the model determined via system identification is dependent on the parameters as well as the signal-to-noise ratio and the frequency content in the time series.

In a second step, the flow-flame model is connected to a linear reduced order model for the propagation of acoustic and possibly also flow perturbations, see Fig. 3.1. The solution of this connected hybrid model is orders of magnitudes cheaper than solving for a monolithic nonlinear model, although the cost for determination of the flow-flame interaction model has to be factored in.

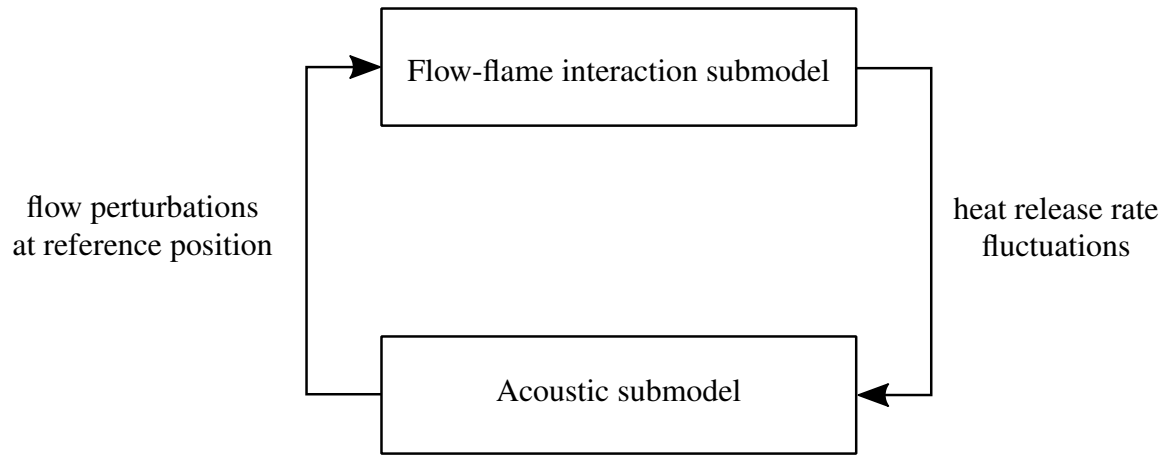

Figure 3.1: Connection of submodels in thermoacoustic hybrid approaches.

3.2.1 Acoustic Models

The submodel governing the flow perturbations in hybrid modeling can be derived by introducing various simplifications to the LRF governing equations. Omitting the linearized species transport, Eq. (2.11), as well as the linearized reaction mechanism for the source terms from the LRF equations, the Linearized Navier-Stokes Equations (LNSE) are obtained.

Further simplifying the LNSE by omission of the thermo-viscous terms, i.e. $\tau' = \lambda' = \bar{\lambda} = 0$, yields the Linearized Euler Equations (LEE), which have seen frequent use in aero- but also thermoacoustics. The underlying reasoning is that viscous terms have little impact on large-scale acoustic waves. However, the damping due to unsteady boundary layers as well as the viscous dissipation of vortices in shear layers of the mean flow can significantly contribute to the perturbation field, as shown by Meindl et al. [22] for the acoustic scattering behavior of swirl generators. Beyond this, the LEE can lead to inconsistencies with the mean flow: the steady-state flow fields are most often a solution of the Navier-Stokes Equations from laminar CFD, RANS or LES, which feature thermo-viscous effects. These inconsistencies are especially critical for the velocity boundary conditions on no-slip walls of the mean flow ($\bar{\boldsymbol{u}} = \boldsymbol{0}$), as the LEE only allow for slip boundary conditions ($\boldsymbol{u}' \cdot \boldsymbol{n} = 0$, where $\boldsymbol{n}$ is the boundary normal vector) due to the lack of viscous terms. Consequently, unphysical vortical perturbation structures can ensue in the boundary layers of the mean flow, which pollute the solution and might even grow unstable [22, 23].

When zero mean velocities are assumed for the LEE, the wave equation can be obtained. The homogeneous wave equation can be derived from linearized mass and momentum equation. For inclusion of the source term due to heat release rate perturbations, as required in thermoacoustics, the linearized energy instead of the mass conservation equation has to be used in the derivation. For this to work, we have to assume no mean heat release rate and constant specific heat capacities in the mean flow [24].

$$\frac{\partial^2 p'}{\partial t^2} - \bar{p}\gamma \frac{\partial}{\partial x_j}\left(\frac{1}{\bar{\rho}}\frac{\partial p'}{\partial x_j}\right) = \left(\gamma - 1\right)\frac{\partial \dot{q}'_V}{\partial t} \tag{3.1}$$

Due to the zero mean velocity assumption, $\bar{p} = \text{const}$ follows directly from the mean flow momentum conservation equation, as no viscous pressure losses occur. Thus, with $c^2 = \gamma \bar{p}/\bar{\rho}$, the wave equation becomes (without any further assumptions):

$$\frac{\partial^2 p'}{\partial t^2} - \frac{\partial}{\partial x_j}\left(c^2 \frac{\partial p'}{\partial x_j}\right) = \left(\gamma - 1\right)\frac{\partial \dot{q}'_V}{\partial t} \tag{3.2}$$

Under the assumption of isentropic perturbations, i.e. $p' = c^2 \rho'$, the wave equation with the c^2 term outside the spatial gradient can be derived.

$$\frac{\partial^2 p'}{\partial t^2} - c^2 \frac{\partial^2 p'}{\partial x_j^2} = \left(\gamma - 1\right)\frac{\partial \dot{q}'_V}{\partial t} \tag{3.3}$$

The homogeneous part of the wave equation is self-adjoint, as opposed to the LRF/LNSE/LEE. This is advantageous for the numerical treatment, as no stabilization terms for the discretization of the spatial gradients are required. Together with the reduced degrees of freedom following from only one scalar unknown, this makes the wave equation attractive for reduced order modeling in thermoacoustics. However, it should be noted that the assumption of zero heat release rate and constant heat capacities in the mean flow, necessary to derive Eqs. (3.1) and (3.2), both strongly contradict the nature of reactive flows. The simplification towards Eq. (3.3) introduces an additional unjustified assumption, as perturbations only behave isentropically if there are no velocities and entropy gradients in the mean flow, both of which are ubiquitous in combustion chambers. Thus, the use of the wave equation as shown in Eq. (3.3), but also Eq. (3.2), in thermoacoustics comes with strong restrictions and one has to be aware of the modeling mistakes made when interpreting the results.

3.2.2 Flow-flame Interaction Models

To account for the flow-flame coupling in hybrid models, the source term $\dot{q}'_V(\boldsymbol{x}, t)$ for the perturbed heat release rate is governed by an external model, like a Flame Transfer Function (FTF) determined from CFD/LES and appropriate post-processing. The FTF $\mathcal{F}$ is a linear model connecting $\dot{q}'_V(\boldsymbol{x}, t)$ to the time lagged axial velocity perturbations $u'_{\mathrm{ref}}(t-\tau)$ normal to a plane located at a reference position x_{ref}. In the most general case, a local FTF $\mathcal{F}_L$ is employed, which depends on both space $\boldsymbol{x}$ and complex frequency s. This relation is conveniently formulated in the Laplace domain as

$$\frac{\hat{\dot{q}}_V(\boldsymbol{x})}{\bar{\dot{Q}}} = \mathcal{F}_L(\boldsymbol{x}, s)\frac{\hat{u}_{\mathrm{ref}}}{\bar{u}_{\mathrm{ref}}}. \tag{3.4}$$

Here, the volume integral of the mean heat release rate, $\bar{\dot{Q}} = \int_\Omega \bar{\dot{q}}_V \,\mathrm{d}\boldsymbol{x}$, as well as the mean velocity at the reference position, $\bar{u}_{\mathrm{ref}}$, are used for normalization.

For acoustically compact flames, and in connection to governing equations that do not support entropy waves, the spatial distribution of the perturbed heat release rate can be neglected and a global FTF $\mathcal{F}_G$, which only depends on complex frequency s, can be employed.

$$\frac{\hat{\dot{Q}}}{\bar{\dot{Q}}} = \mathcal{F}_G(s)\frac{\hat{u}_{\mathrm{ref}}}{\bar{u}_{\mathrm{ref}}} \tag{3.5}$$

Note that $\hat{\dot{Q}} = \int_\Omega \hat{\dot{q}}_V \,\mathrm{d}\boldsymbol{x}$. A comparison of the ensuing heat release rate perturbations for $\mathcal{F}_L$ and $\mathcal{F}_G$ connected to LNSE is shown in Fig. 3.2 for a duct flame, which was investigated in [13].

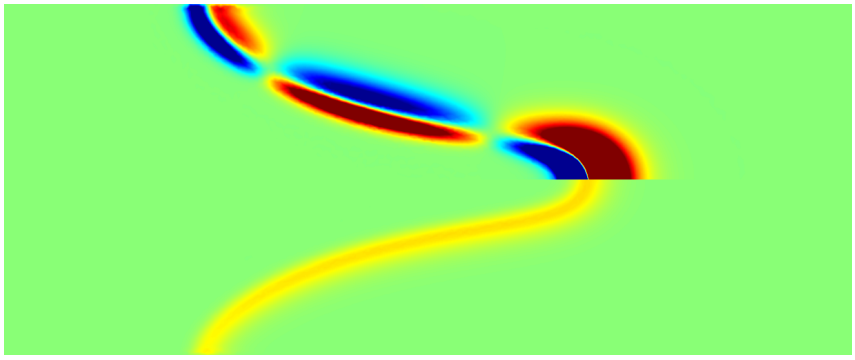

Figure 3.2: Instantaneous heat release rate perturbations of a 2D duct flame as governed by a fully local FTF (top) and a global FTF (bottom). Forced response at 400 Hz. The spatial distribution for the global FTF has been chosen proportional to the mean heat release rate and is in-phase along the length of the flame due to the lack of knowledge about the spatial phase information.

The identification of $\mathcal{F}_G$, rather than $\mathcal{F}_L$, requires less sophisticated techniques and computational effort. Thus, it is very common in thermoacoustics to employ a global FTF, if the system to be modeled permits this simplification. For cases where the acoustic submodel does not support entropy waves, but the flame is not compact with regards to the acoustic waves traveling in axial direction, segmented FTFs $\mathcal{F}_S$ were applied in several studies to correctly account for the correct phase and gain between the acoustics and the perturbed heat release rate [25–33]. A

segmented FTF is only resolved in the axial direction (here assumed to be x_1). The perturbed heat release rate is either continuously axially distributed, or in a discrete manner by averaging over a sequence of contiguous sub-domains, which are small enough to assume acoustic compactness for each.

$$\frac{\hat{\dot{q}}_V(x_1)}{\bar{\dot{Q}}} = \mathcal{F}_S(x_1, s)\frac{\hat{u}_{\text{ref}}}{\bar{u}_{\text{ref}}} \tag{3.6}$$

Beyond the scope of linear flow-flame models, non-linear models such as the Flame Describing Function (FDF) are employed to determine limit cycle amplitudes of thermoacoustic instabilities with hybrid models. Those, however, are out of the scope of this thesis.

3.2.3 Common Hybrid Modeling Approaches

The various linear thermoacoustic models can be sorted by complexity. Higher complexity comes with a more detailed description of the system (usually by applying less simplifications to the governing equations), but at a higher computational cost. Therefore, a trade-off between accurate predictions and effort is the unavoidable result.

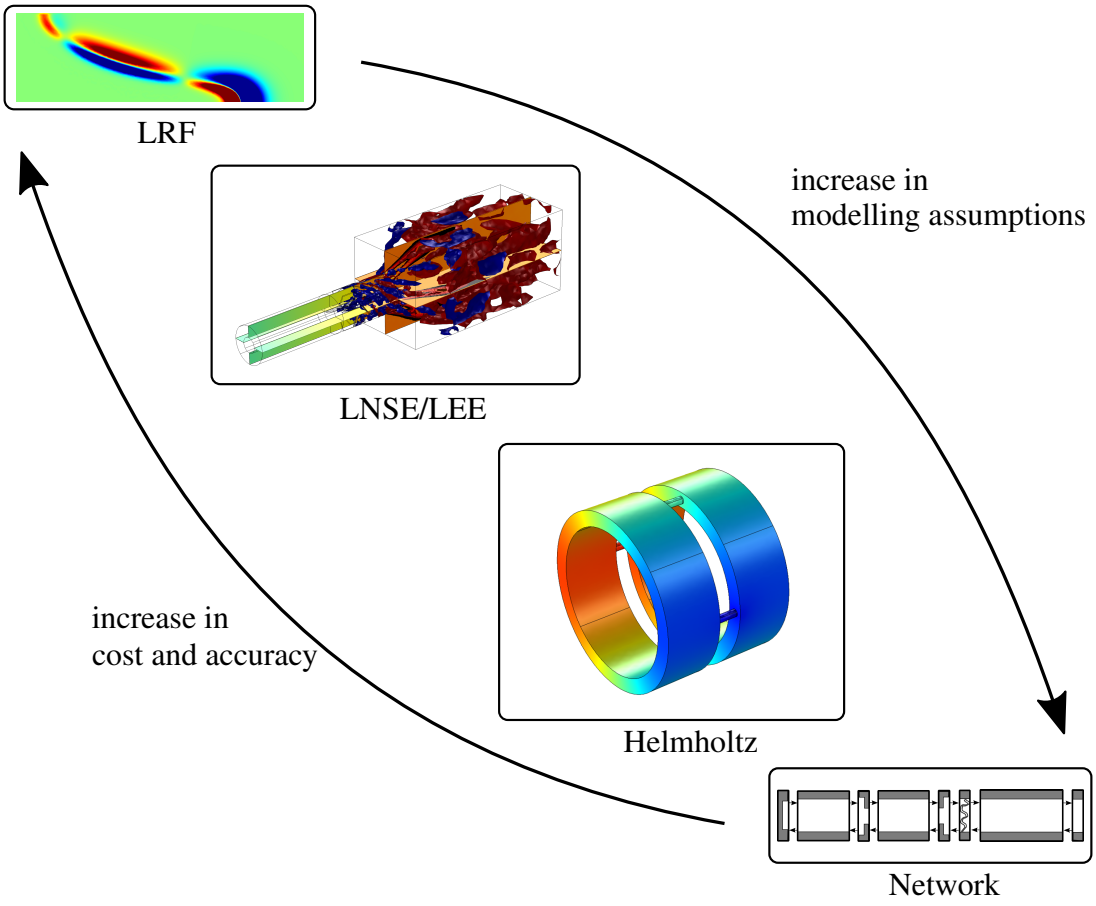

Figure 3.3: Hierarchical representation of the most common linear thermoacoustic modeling approaches.

The following bullet points list some of the most common thermoacoustic hybrid models in

order of ascending accuracy and cost, without any claim to be comprehensive. Compare also Fig. 3.3.

- **Network models** are most often based on the assumption that the acoustics mainly travel along one dimension (usually the axial or azimuthal direction). The gas turbine is then represented by the connection of multiple fundamental elements, such as ducts of constant cross-section, area jumps or (non-)reflecting terminations. The flame is assumed to be compact with respect to acoustic waves in most models, i.e. the acoustic wave lengths are much larger than the spatial extent of the flame, such that it can be approximated by a discontinuity in the network. The propagation of acoustic waves through the fundamental elements as well as the influence of perturbed heat release rate on the acoustics is known analytically. It is thus possible to connect these elements to form a compound model. To account for the flow-flame interaction that can not be described sufficiently in a 1D manner, a global FTF relating the perturbed heat release rate to time delayed upstream velocity fluctuations is often employed. The connected network model can be used to analyze the thermoacoustic stability of the system.
- Thermoacoustic models based on the **2D/3D Helmholtz equation** describe the acoustic wave propagation purely with the speed of sound, neglecting the influence of the mean flow velocities. The system under consideration is often modeled as a continuous computational domain, which can feature geometrically complex shapes, as are common in gas turbines. The flow-flame interaction is accounted for in a similar way to the network model approach, although the heat release zone has a finite extent. The influence of perturbed heat release rate on the acoustic field is inherently represented by the source term in the Helmholtz equation, as opposed to the explicitly formulated relation used in network models.
- The **Linearized Navier-Stokes** and **Linearized Euler** Equations are used to model the acoustic, hydrodynamic and entropic perturbations of a flow which account for or neglect, respectively, thermo-viscous effects. The augmentation of the acoustic propagation velocity by the mean flow is inherently accounted for. These features lead to an increased accuracy in thermoacoustic stability predictions, but come at significant additional cost and numerical challenges compared to the Helmholtz equation. As for the previous models, the flow-flame interaction is taken into account by an external submodel such as an FTF.

3.2.4 Disadvantages

The ramifications of introducing simplifying assumptions to the governing equations can be severe. As shown in the course of this thesis research, the seemingly appropriate assumption that an acoustically compact flame can be modeled with a single input / single output global FTF, generates significant amounts of spurious entropy in a thermoacoustic hybrid model that relies on the LNSE to represent the propagation of acoustics and flow perturbations. Contrarily, the more general LRF, as well as LNSE coupled to a local FTF, show good agreement with reference solutions from CFD. Thus, care has to be taken when simplifying assumptions are made, and it is often preferable to solve for the computationally more expensive LRF equations.

In addition to the advantage of not requiring an external flow-flame interaction model, the results from LRF allow investigation of the involved species transport, which can be advantageous especially for technically premixed flames. For these, acoustic forcing induces fluctuations in mixture ratio at the injector, which are then dispersed while being convected towards the flame. Representing this mechanism in a hybrid model requires an additional input for an FTF, while it is inherently captured by the LRF.

4 The Discontinuous Galerkin Finite Element Method in Thermoacoustics

The Finite Element Method (FEM) is one of the most generic approaches to solve partial differential equations numerically. Due to its flexibility regarding the formulation, easy extensibility to higher order schemes as well as the applicability to curved meshes, FEM is widely used in nearly every field of science and engineering. The following section will shed light on the difficulties for employing a standard FEM in problems of fluid mechanics, as well as an adaption, the Discontinuous Galerkin Finite Element Method (DG-FEM), to circumvent these.

4.1 Fundamentals of the Discontinuous Galerkin Finite Element Method

For ease of demonstration, this section is only concerned with scalar-valued governing equations. The Finite Element Method can also be expanded to systems of equations without essential difficulty.

The idea behind the Finite Element Method is to project a differential equation for the unknown quantity $u(\boldsymbol{x}, t)$,

$$\mathcal{L}(u(\boldsymbol{x}, t)) \;=\; 0, \tag{4.1}$$

onto a function $w(\boldsymbol{x})$ based in a space V of finite dimensionality and then postulate that the residual integrated over the domain of interest Ω, instead of the residual of the differential equation at every point, has to vanish for all $w(\boldsymbol{x})$. As this alleviates the conditions that the solution has to adhere to, this form is called the *weak form*.

$$\int_\Omega w(\boldsymbol{x}) \mathcal{L}(u(\boldsymbol{x}, t)) \, \mathrm{d}\boldsymbol{x} = 0 \tag{4.2}$$

If the solution $u(\boldsymbol{x}, t)$ is sought from the same space V, onto which the differential equation is projected, a *Galerkin method* results. One major difference to other numerical methods for solving differential equations is that the FEM solves the approximate problem exactly (within computational accuracy), rather than finding an approximate solution to the exact problem (Finite Difference Method, Finite Volume Method). This is due to the projection of the differential equation with an infinite dimensional solution space onto a finite dimensional space, in which the exact solution can be found.

Various formulations of the FEM can be derived by choosing the spaces for the projection of the differential equation and the basis for the solution. In the context of the FEM, the computational

domain is approximated by a partition $\mathcal{P}_h$, which is the union of K non-overlapping elements Ω_e,

$$\Omega \approx \bigcup_{\Omega_e \in \mathcal{P}_h}^{K(\mathcal{P}_h)} \Omega_e^k. \tag{4.3}$$

The functions $w(\boldsymbol{x}), u(\boldsymbol{x}, t)$ are then approximated as the sum of local functions $w_h^k(\boldsymbol{x}), u_h^k(\boldsymbol{x}, t)$, which are non-zero only within one respective element Ω_e^k,

$$w(\boldsymbol{x}) \approx w_h(\boldsymbol{x}) = \bigoplus_{k=1}^{K} w_h^k(\boldsymbol{x}), \tag{4.4}$$

$$u(\boldsymbol{x}, t) \approx u_h(\boldsymbol{x}, t) = \bigoplus_{k=1}^{K} u_h^k(\boldsymbol{x}, t). \tag{4.5}$$

The element wise defined functions $w_h^k(\boldsymbol{x})$ and $u_h^k(\boldsymbol{x}, t)$ are chosen as a weighted sum of test and trial functions, respectively. Two common choices for the test/trial functions are the modal and the nodal form. The former employs locally defined polynomials $\psi_n(\boldsymbol{x})$ of order $n = 0, \ldots, N_p - 1$ as basis with $\hat{w}_n^k$ and $\hat{u}_n^k(t)$ as the weights for the test and trial functions. The basis for the nodal form can be defined by a set of interpolating Lagrange polynomials $l_i^k(\boldsymbol{x})$ on N_p local stencils with position $\boldsymbol{x}_i^k$, alongside their weights w_i^k and u_i^k [34].

$$w_h^k(\boldsymbol{x}) = \sum_{n=1}^{N_p} \hat{w}_n^k \psi_n(\boldsymbol{x}) = \sum_{i=1}^{N_p} w_i^k l_i^k(\boldsymbol{x}) \tag{4.6}$$

$$u_h^k(\boldsymbol{x}) = \sum_{n=1}^{N_p} \hat{u}_n^k(t) \psi_n(\boldsymbol{x}) = \sum_{i=1}^{N_p} u_i^k(t) l_i^k(\boldsymbol{x}) \tag{4.7}$$

Note that in this context, the index i of the expression $\boldsymbol{x}_i^k$ does not refer to the spatial coordinate, but is instead the summation index representing the i-th stencil position that is connected to the weighting factor u_i^k of element k. The nodal basis functions $l_i^k(\boldsymbol{x})$ are unity at $\boldsymbol{x}_i^k$ and zero at $\boldsymbol{x}_j^k, j \neq i$.

The properties of the resulting method are determined by the space from which $\psi_n(\boldsymbol{x})$ or $l_i^k(\boldsymbol{x})$ are taken. For the Discontinuous Galerkin method used in this thesis, discontinuous nodal basis functions with Gauß-Lobatto node positions are employed and the test and trial functions are taken from the same space $V(\mathcal{P}_h)$. Figures 4.1 and 4.2 show continuous and discontinuous nodal basis functions of first order in one dimension, represented by Lagrange polynomials. While the continuous basis has only one node at the element interfaces, which is a shared anchor point for the basis in both adjacent elements, the discontinuous basis has a duplicate node at the element interfaces. Thus, the basis for adjacent elements in the DG-FEM has no inherent connection.

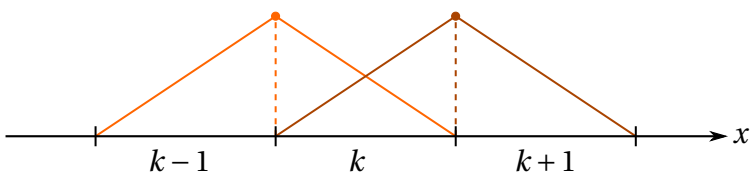

Figure 4.1: Continuous linear nodal basis functions in one dimension.

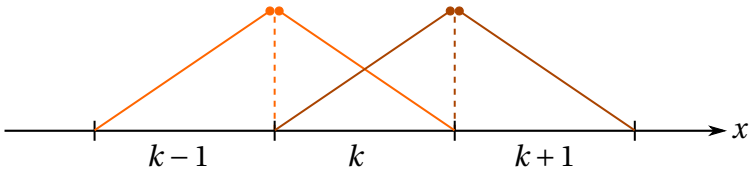

Figure 4.2: Discontinuous linear nodal basis functions in one dimension.

Due to the discontinuous nature of the basis functions, the integration of the governing equation as defined in Eq. (4.2) can not be performed on the computational domain Ω as a whole, but on the individual elements Ω_e^k instead. In contrast to the standard FEM, the solutions of the elements are thus not inherently coupled. To reintroduce this connection, the Gauß theorem is applied to the divergence terms of the governing equation, leading to a term describing the flux over the boundaries of every cell. This manipulation is a necessity in deriving the discrete form of the governing equations in the Finite Volume Method, thus the similarity between both methods. On a very general level, the DG-FEM can be seen as a Finite Volume Method between cells, where the flux conveys information, and a Finite Element Method in the element interiors, where the solution is approximated on a given basis. Thus, the best of both worlds can be combined: a stable and robust flux can be chosen to guarantee a conservative and stable numerical scheme, and higher order basis functions may be employed, tailored to the physics of the problem, which provide superior convergence and accuracy.

The main field of application for DG-FEM is the numerical solution of pure or mixed hyperbolic differential equations, such as the Euler, Navier-Stokes, or Maxwell's equations. An otherwise unstabilized FEM discretization leads to a numerically unstable scheme for these equations [35]. In the framework of the DG-FEM, the inter-cell flux can be chosen based on the solutions of the two neighboring cells, analogously to the Finite Volume formulation. Due to the decades of experience in hyperbolic problem solving with the Finite Volume Method, there is a plethora of flux formulations available, which generate stable, non-oscillatory solutions for differential equations governing directional physical processes. There is no essential difficulty in applying these formulations to the DG-FEM, facilitating the rapid development of consistent and stable methods.

4.2 Comparison to other Numerical Methods

The Finite Difference Method (FDM) and the Finite Volume Method (FVM) are, next to FEM in general, two of the most popular methods for numerically solving partial differential equations in science and engineering. Some important aspects to evaluate when choosing one of these methods in comparison to (DG-)FEM are as follows (loosely based on [34]):

- **Mesh compatibility:** Due to the higher order basis functions usable in the FEM, curved meshes consisting of non-straight elements can be employed. This is especially important if round shapes, such as a circular duct, have to be represented. While it is possible to treat curvilinear meshes with the FVM [36], it requires much more effort to achieve highly accurate schemes than with the FEM. For the FDM, curved boundaries are not

commonly used. Beyond the treatment of curved meshes, the FVM suffers from convergence and accuracy falloff if the connection line between two neighboring cell centers is not orthogonal to their inter-cell boundary. This is because the values of the unknown variables have to be known on the interface to compute the flux, but are typically stored in the cell centers. For flux reconstruction, interpolation schemes are employed, which are not representative for the whole interface if the cells are strongly non-orthogonal or skew. The DG-FEM method excels in this regard, because the solution by means of the weighted trial functions is known throughout the whole cell, and therefore the variables to compute the flux can be evaluated directly at the inter-cell boundary.

- **Extensibility to higher order schemes:** The extension of both the order of the discretization as well as the representation of the solution is straight forward with the (DG-)FEM, as the formulations for higher order basis functions are readily available. For the FDM, considering additional neighboring nodes allows to derive higher order schemes with rather low effort. For the FVM, this issue is more complex because the flux reconstruction on the element boundaries is required. Thus, the industry standard for FVM solvers are second order schemes. Note that while the (DG-)FEM approach to increasing the order is a local one, i.e. the basis function stays within the element even if the order is increased, both FDM and FVM require extended stencils ranging to (multiple) neighboring nodes. Inclusion of neighboring cells in the flux discretization has three main disadvantages; firstly, the bandwidth of the discretized system matrix increases, which is detrimental for parallelization; secondly, at the boundaries, where no neighboring cells exist in one direction, either lower order or one-sided schemes have to be used, both of which negatively impact the accuracy of the method; and thirdly, on unstructured meshes it is not a trivial task to define what the neighboring cells are.

- **Efficient explicit time-stepping:** The mass matrix resulting from the standard continuous FEM is, opposed to all other methods including DG-FEM, not block-diagonal. This leads to a comparatively costly matrix inversion if explicit time-stepping is employed. In contrast, a block-diagonal matrix can be inverted by individual inversion of the blocks, which are usually much smaller than the mass matrix as a whole.

- **Degrees of freedom:** The major drawback of the DG-FEM is that a multiple degrees of freedom for each variable are stored at each node, cf. Fig. 4.2. For linear basis functions, this increases the degrees of freedom by a factor of 2^D compared to the standard FEM, where D is the spatial dimension. However, because increasing the order of the method does not add additional nodes to the mesh, but only stencils for the basis functions inside the cells, this factor between the Discontinuous Galerkin and continuous FEM approaches unity for very high orders. From a cost oriented perspective, it is thus desirable to employ a coarser mesh with higher order basis functions in the DG-FEM approach, i.e. to strive for an optimal combination of p and h convergence.

Beyond DG-FEM, there are also various other stabilized Finite Element Methods that can be applied to solve aero- and thermoacoustic governing equations. Two well known representatives are the Streamline-Upwind Petrov-Galerkin (SUPG) [37] and the Galerkin Least Squares (GLS) [38] approach. In both of these methods, artificial terms weighed by a stabilization parameter are added to the governing equations in order to suppress spurious solutions. These

methods are very sensitive to the amount of the introduced stabilization, as shown by Hofmeister et al. [39] for the investigation of vortex shedding at a combustor inlet, employing LEE with an SUPG scheme: while too little may not be sufficient to produce a stable scheme, too much stabilization leads to artificial dissipation of the physical perturbations in the solution. Choosing the amount of stabilization for a predictive method, i.e. without any available validation data to match numerical results, is challenging. However, strategies are being developed to elicit the physical damping of stabilized FEM solutions by comparison to results produced with governing equations that do not require stabilization [40].

4.3 Application to Thermoacoustics

The DG-FEM has been widely employed in aeroacoustics (see e.g. [41–44]), but has not seen, to this date, any application in thermoacoustics except for the studies connected to this thesis. The connection of these two topics is straightforward however, because the governing equations of aero- and thermoacoustics share commonalities to a great extent, with the exception of the source terms. Starting with LEE, which are commonly used governing equations in aeroacoustics, one can arrive at the various governing equations used in thermoacoustics by adding additional terms. The addition of thermo-viscous terms to the LEE yields the LNSE. Further expanding the set of equations by adding linearized species transport equations alongside a linearized reaction mechanism leads to the LRF.

In the DG-FEM framework, these additional terms and equations are treated independently from each other, thus allowing the numerical formulation to mirror the hierarchy of the governing equations. For example, when the LEE are expanded to the LNSE by addition of the thermo-viscous terms, the original discretization of the LEE stays untouched. The convective terms are discretized employing either an approximate (local Lax-Friedrichs flux) or exact upwinding flux (e.g. obtained by flux difference splitting) in order to construct a stable scheme. For the diffusive terms, a penalty formulation first introduced by Babuška et. al [45] for pure diffusion problems, and later expanded to convection-diffusion problems [46] and the Navier-Stokes Equations [47] by Baumann et al., is used. Source terms require no special numerical treatment.

Boundary conditions can be given either in the strong or the weak form. While the former method directly eliminates the respective unknown variable and replaces it with the given value, the latter approach is based on providing the flux (e.g. the perturbed energy flow), such that the desired constraint (e.g. $T' = 0$) will automatically be fulfilled by the governing equations. Providing the boundary conditions in the weak form is the naturally emerging alternative to the strong form, and lends itself very well to the DG-FEM formulation, in which the communication between cells and across the boundary of the computational domain is purely realized via the flux. Beyond this, it is straight forward to incorporate coupled boundary conditions, such as an anechoic outlet ($p' = \bar{\rho} c \boldsymbol{u}' \cdot \boldsymbol{n}$ for zero mean flow), in the weak form. In practice, it proved useful to combine the use of boundary conditions in both strong form and weak forms. Velocity perturbations at no-slip walls can easily be eliminated via strong boundary conditions, whereas giving isothermal boundary conditions ($T' = 0$) is not possible in the strong form, because T' is not one of the independent variables. Instead, the coupled boundary condition $p'/\bar{p} = \rho'/\bar{\rho}$ is given in the weak form.

4.4 Diagonalization of the Non-Viscous Flux

The LRF, Eqs. (2.8)-(2.11), as well as all derived equations thereof, can be written in matrix vector representation.

$$\boldsymbol{M}\frac{\partial \Phi'}{\partial t} + \frac{\partial \boldsymbol{F}_j}{\partial x_j} = \frac{\partial \boldsymbol{F}_j^v}{\partial x_j} + \boldsymbol{s} \tag{4.8}$$

$\boldsymbol{F}_j$ and $\boldsymbol{F}_j^v$ are the non-viscous and viscous flux, respectively, while $\boldsymbol{M}$ is the mass matrix and $\boldsymbol{s}$ is a vector containing the sources. Both $\boldsymbol{F}_j$ and $\boldsymbol{F}_j^v$ can be expressed as product of operators containing only the mean fields (and spatial derivatives thereof) and the unknown perturbation quantities Φ'.

$$\boldsymbol{F}_j = \boldsymbol{K}_j \Phi', \quad \boldsymbol{F}_j^v = \boldsymbol{K}_j^v \Phi' \tag{4.9}$$

The formulation of $\boldsymbol{F}_j$ is of special interest here, as the eigenvalues of the matrices $\boldsymbol{K}_j$ are the flux characteristics of the non-viscous part of the flow. The diagonalization of the non-viscous flux prefactor matrix $\boldsymbol{K}_j$ normal to a surface with unit normal vector components n_j reveals the eigenvalues and -vectors [47]:

$$\boldsymbol{F}_n = \boldsymbol{K}_j n_j \Phi' = \boldsymbol{V}\boldsymbol{\Lambda}\boldsymbol{V}^{-1}\Phi'. \tag{4.10}$$

$\boldsymbol{V}$ is a matrix containing the eigenvectors of $\boldsymbol{K}_j$ as rows, while $\boldsymbol{\Lambda}$ is a diagonal matrix with the eigenvalues $\lambda_1 \dots \lambda_{N_D+N_K+2}$ of the non-viscous flux of LRF equations on the diagonal, where N_D is the spatial dimension and N_K is the number of species transport equations. Subsequently to the diagonalization, the flux can be split into contributions leaving and entering the domain through the boundary. This is done by accounting for only the positive or negative entries of $\boldsymbol{\Lambda}$. Based on this procedure, the numerical boundary conditions can be given in terms of the characteristics entering the computational domain, and accurate directional discretization schemes such as the flux difference splitting approach can be employed.

The resulting eigenvalues exhibit either acoustic $\lambda_{\text{ac}} = \bar{u}_j n_j \pm c$ or convective $\lambda_{\text{con}} = \bar{u}_j n_j$ propagation speed. The convective waves comprise vortices (if $N_D > 1$), entropy waves and the characteristics for species transport. Note that due to the diagonal form of $\boldsymbol{\Lambda}$, these characteristics propagate independently of each other, as long as the mean flow is homogeneous, viscous effects are absent and no coupling at boundaries exists. In a homogeneous mixture without viscous effects and spatial gradients in the mean flow, i.e. a flow governed by the LEE, the vortical characteristics only influence velocity perturbations, the entropy waves only act on density perturbations, while the acoustic waves perturb all fields, including the pressure [6]. As soon as viscous effects are accounted for in the governing equations, such as the LNSE, the system is no longer hyperbolic in nature, and thus strictly speaking, no characteristics exist. This is caused by the impact of the diffusion-type terms, which act on the whole domain with infinite propagation velocity due to the continuum assumption on the fluid. In applications, however, it is found that when viscous terms are not dominant, i.e. at sufficiently large Peclet numbers, the LNSE and LRF can be treated as a superposition of the hyperbolic system with its characteristics and the diffusion-type terms, thus allowing for flux-difference splitting and boundary conditions based on the characteristic waves.

Figure 4.3 illustrates the propagation of the vortical and acoustic characteristics in a perturbed nozzle flow governed by the LNSE. Even though viscous effects are present, the separation

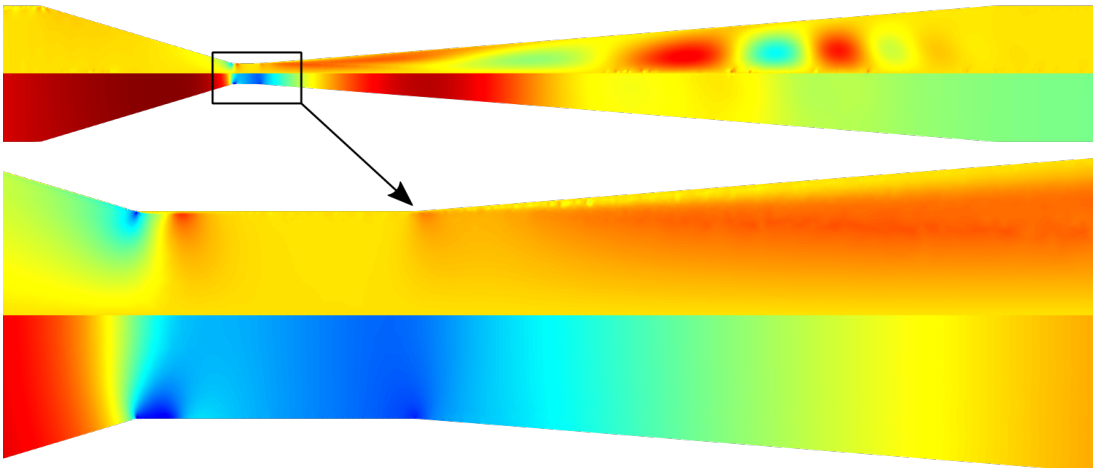

Figure 4.3: Radial velocity perturbations (top half of each depiction) and pressure perturbations (bottom half) of a nozzle forced acoustically at the inlet, computed with LNSE. The mean flow is slightly subsonic, forcing frequency is 800 Hz.

between the characteristics is still obvious. Vortices form in the shear layers induced after the throat of the nozzle and are convected downstream. Their wavelength reduces with increasing nozzle diameter as a result of reduced axial mean flow velocity. The acoustic perturbations can clearly be seen in the pressure perturbations. They feature larger wavelengths than the vortices. The coupling between both characteristics is strong only in the throat, where flow separation at the transition from the convergent section induces pressure fluctuations at the no-slip boundaries.

4.5 Implementation: felicitaX

felicitaX is a **F**inite **E**lement **Li**nearized **C**ombust**i**on **T**hermo-/**A**eroacoustics solver using the above described DG-FEM discretization method. It is based on the open-source computing platform FEniCS [48], version 2019.1.0. FEniCS provides the framework for the automated derivation of discretized systems based on the weak form of the governing equations, as well as pre- and post-processing routines such as mesh interfacing, file in-/output and evaluation of symbolic expressions. The software is written in C++ and Python, and provides interfaces in both languages for the user interaction. The focus of felicitaX is on extensibility, modularity and rapid prototyping.

4.5.1 Dogma and Fundamentals

Making use of the Python interface of FEniCS, felicitaX provides a modularized, object-oriented approach to generate the weak form of the governing equations for thermo- and aeroacoustics, including LEE, LNSE and LRF. This includes the appropriate treatment of the mean flow via interpolation, as well as providing boundary conditions in strong and weak forms. The aim of the development was to abstract the numerical details of the implementation from the

user, such that minimal input is required, albeit the user should stay in full control over the form of the governing equations and boundary conditions. Therefore, the required inputs are:

- A **mesh** for the linearized computations. The open-source mesher GMSH [49] was found to be well suited for all geometries and cases encountered in connection to this thesis. FEniCS provides easy interfacing for GMSH meshes.
- **Mean flow fields** in the form of a comma-separated-value (`.csv`) file. The spatial resolution provided here is usually (but not necessarily) higher than that of the mesh for the linearized computations. The interpolation of the mean flow values to the mesh is then handled by `felicitaX` via a multi-dimensional unstructured interpolation algorithm provided in the Python package `scipy`. First, triangulation with the Quickhull algorithm is performed [50]. Afterwards, the mean flow values at the nodes of the target mesh are computed via piecewise linear barycentric interpolation on the input data.
- A **study type** (time-domain, frequency response or eigenvalues) with appropriate parameters, e.g. the time-step width and the total simulation time, or the frequencies to be solved for.
- A **flux scheme**. Currently, the local Lax-Friedrichs flux as well as flux difference splitting are implemented. Note that the user can choose the flux, but does not need to provide details about the implementation.
- The **order of the basis functions**.
- The **physical model**, from which the parameters used for **simplifications** of the governing equations can be derived. This includes whether viscous terms and the fluctuation of the material values such as μ' and λ' should be included, whether the perturbed flow is isentropic, and whether a reacting flow is present.
- An **optional FTF** in state-space representation, stored in `.csv` files. If an FTF is provided, a reference position as well as the field of the mean heat release rate needs to be defined by the user as well.

After these inputs are made by the user, `felicitaX` returns the according weak form of the governing equations in a symbolic representation that is not yet discretized. Subsequently, boundary conditions are set either in the strong or the weak form. Boundary conditions in the strong form can only be applied to the unknown variables of the perturbed flow, i.e. $\left(\rho', u_i', p', Y_k'\right)^T$. Weak boundary conditions are required for isothermal walls and characteristics based conditions, such as arbitrary acoustic reflection coefficients. However, many of the physical boundary conditions such as an acoustically open end ($p' = 0$) or a slip-wall ($\boldsymbol{u}' \cdot \boldsymbol{n} = 0$) can be prescribed both in the strong or weak form. To make it easier for the user to provide the correct flux in the weak form, common cases are already pre-defined in flux functions, e.g. `set_flux_pressure` (allows for pressure fluctuations at a boundary, should be omitted at an acoustically open end) or `set_flux_heat_conduction` (admits a flux through heat conduction at the boundary, should be set for isothermal and omitted for adiabatic walls). In this way, the weak boundary conditions are set in an additive way, i.e. adding the flux expressions for the mechanisms that occur at a certain boundary, rather in a subtractive way, which would be to provide the full flux and then

eliminate the mechanisms that should not be present. This step requires knowledge of the governing equations as well as physically sensible boundary conditions from the user. Providing an incomplete or inconsistent flux can lead to spurious artifacts in the solution of the problem.

Once the weak form, including boundary conditions, is fully set up, the discretization is performed with a FEniCS built in function. The resulting system of linear equations can subsequently be solved with direct solvers (based on a lower/upper decomposition of the system matrix) or through iterative solvers employing Krylov subspace methods, such as GMRES or BiCGStab [51].

For post-processing, felicitaX provides functionality to visualize full-period animations for complex solutions stemming from studies in the Laplace domain, such as eigenmodes.

4.5.2 Usage Examples

The following code snippets are intended to give the reader an impression of the usage of felicitaX. They do not serve as a documentation and are not executable on their own, as they are embedded in a bigger script.

```
# Read meanflow from .csv file and interpolate to mesh.
fieldnames = {
        "U:0":"uMean_axial", "U:1":"uMean_radial", "rho":"rhoMean",
        "T":"TMean", "p":"pMean", "h":"hSensMean"
    }
meanflow = ctf.interpolate_all_meanfields_from_csv(
        meanflow_file, fieldnames, mesh, order=2, parallel=True
    )
```

One of the first steps after loading the mesh (not shown here) is the interpolation of the meanflow fields onto the computation mesh. The first expression defines a dictionary of the fields to be read from .csv file via their column header name as key and their name in the workspace as value. Then, the interpolation routine is called in a second step with parallel execution via threading being requested.

```
# Options class for felicitaX.
DGOpts = felicitax.fem.opts.Opts()
DGOpts.viscous = 'viscousfluctuation'
DGOpts.isentropic = 'nonisentropic'
DGOpts.reacting = 'nonreacting'
DGOpts.physical_space = 'frequency'
DGOpts.flux_scheme = 'LFF'
DGOpts.lagrange_multiplier = 'none'
DGOpts.order = 2
DGOpts.mesh = mesh
DGOpts.ds = ds
DGOpts.meanflow = meanflow
DGOpts.lff_prefactor = 1.0

# Create an instance of the LNSE that contains the equations,
# the mean flow as well as the finite element spaces.
LNSE = felicitax.fem.weakform.WeakForm(DGOpts)
```

This part of the code illustrates the options the user sets for the flow, as described in the previous subsection. Note that the `ds` holds the boundaries of `mesh` and is defined earlier in this script from an imported mesh file generated with GMSH. The Python dictionary `meanflow` is the result of mean-field interpolation from the previous step. The local Lax-Friedrichs flux prefactor `lff_prefactor` controls the amount of upwinding. The class `felicitax.fem.opts.Opts` serves as a container for the options and includes parameter checks to ensure sensible settings. The weak form is generated when an instance of the class `felicitax.fem.weakform.WeakForm` is generated with the `DGOpts` object as input.

```
# Set the flux and implicitly account for weak boundary conditions.
LNSE.set_flux_pressure([boundary["inflow"], boundary["walls"],
                        boundary["lower_symmetry"],
                        boundary["upper_symmetry"]])
LNSE.set_flux_normal_velocity([boundary["inflow"],
                               boundary["outflow"]])
LNSE.set_flux_convection([boundary["outflow"]])
LNSE.set_flux_convection_isothermal([boundary["inflow"]])
LNSE.set_flux_viscous([boundary["inflow"], boundary["walls"]])
LNSE.set_flux_viscous([boundary["outflow"]], penalty=False)
LNSE.set_flux_viscosity_fluctuation([boundary["lower_symmetry"],
                                     boundary["upper_symmetry"],
                                     boundary["outflow"]])
LNSE.set_flux_viscous_slip([boundary["lower_symmetry"],
                            boundary["upper_symmetry"]])
LNSE.set_flux_heat_conduction([boundary["inflow"], boundary["walls"]])
```

The above code gives an example for setting boundary conditions in the weak form. Due to the choice of flux contributions, and the intentional omission of some parts on specific boundaries, the conditions are enforced. `boundary` is a dictionary relating the human readable boundary specifiers (like `inflow`) to their respective internal representations as integers.

```
# Dirichlet boundary conditions in strong form.
BCmethod = "geometric"
bcs = [
    DirichletBC(LNSE.V.sub(LNSE.get_field_id("uR")), (u_forcing, 0.0),
                boundaries, boundary["inflow"], BCmethod),
    DirichletBC(LNSE.V.sub(LNSE.get_field_id("uI")), (0.0, 0.0),
                boundaries, boundary["inflow"], BCmethod),
    DirichletBC(LNSE.V.sub(LNSE.get_field_id("uR")).sub(1), 0.0,
                boundaries, boundary["lower_symmetry"], BCmethod),
    DirichletBC(LNSE.V.sub(LNSE.get_field_id("uI")).sub(1), 0.0,
                boundaries, boundary["lower_symmetry"], BCmethod),
    DirichletBC(LNSE.V.sub(LNSE.get_field_id("uR")).sub(1), 0.0,
                boundaries, boundary["upper_symmetry"], BCmethod),
    DirichletBC(LNSE.V.sub(LNSE.get_field_id("uI")).sub(1), 0.0,
                boundaries, boundary["upper_symmetry"], BCmethod),
    DirichletBC(LNSE.V.sub(LNSE.get_field_id("uR")), (0.0, 0.0),
                boundaries, boundary["walls"], BCmethod),
    DirichletBC(LNSE.V.sub(LNSE.get_field_id("uI")), (0.0, 0.0),
                boundaries, boundary["walls"], BCmethod),
    DirichletBC(LNSE.V.sub(LNSE.get_field_id("pR")), 0.0,
                boundaries, boundary["outflow"], BCmethod),
    DirichletBC(LNSE.V.sub(LNSE.get_field_id("pI")), 0.0,
                boundaries, boundary["outflow"], BCmethod)
]
```

Boundary conditions the user wants to enforce in the strong form are handled via a list (called bcs here), which is later applied to the weak form during assembling of the matrices. The variables of the LNSE, e.g. uR as the real part of the perturbed velocity field, are chosen, as well as the respective boundaries, for which the values should be constrained.

```
for sol in frequency_sweep(LNSE, bcs, freqvec):
    # Post-processing loop.
    # Retrieve solution.
    uR = project(sol.sub(LNSE.get_field_id("uR")), V_mean)
    uI = project(sol.sub(LNSE.get_field_id("uI")), V_mean)

    # Write phase animation of velocity perturbation to file.
        postproc.save_phase_animation_xdmf(
        filename=resultFolder + f"/{freq}Hz_phi.xdmf",
        mesh=mesh, u={"u": (uR, uI), n_phi=60
    )
```

Finally, the assembling and solution of the equation system happens in the Python generator expression frequency_sweep, which takes as input parameters the weak form, boundary conditions in the strong form as well as a list of frequencies to be solved for. The solution step, which is typically by far the computationally most expensive part of the whole procedure, can be run in serial, threaded or in parallel on multiple machines, depending on how FEniCS was compiled. Note that the weak form already comprises the weakly imposed boundary conditions. In the loop created by the generator, the user can access the solution fields sol for post-processing purposes. In this case, the real and imaginary parts of the velocity perturbations are extracted and a phase animation, dividing the period into 60 steps, is saved to .xdmf file. This functionality is provided from the postproc module of felicitaX.

5 Modular Systems in the State-Space Framework

Hybrid thermoacoustic models require the interconnection of several submodels to form a representation that encompasses all physical aspects governing combustion instabilities. In general, the connections are formulated as (usually algebraic) equations to relate a subset of the degrees of freedom between the submodels. The state-space representation, as a unifying modeling framework, has shown to be well suited to define the interfaces between the submodels and offers a strongly formalized procedure to establish the connections.

5.1 State-Space Systems

The state-space framework is a formalized representation for a system of linear time-invariant (LTI) ordinary differential equations.

$$\mathbf{E}\frac{\mathrm{d}\mathbf{x}(t)}{\mathrm{d}t} = \mathbf{A}\mathbf{x}(t) + \mathbf{B}\mathbf{u}(t) \tag{5.1}$$

$$\mathbf{y}(t) = \mathbf{C}\mathbf{x}(t) + \mathbf{D}\mathbf{u}(t) \tag{5.2}$$

The matrices $\mathbf{A}, \mathbf{B}$ and $\mathbf{E}$ govern the temporal evolution of the state vector $\mathbf{x}$ under the influence of inputs $\mathbf{u}$. The output $\mathbf{y}$ of the system is defined as a linear combination of the states and the inputs via $\mathbf{C}$ and $\mathbf{D}$. Due to their LTI nature, both the linear acoustic (ranging from network to LNSE) as well as the flow-flame models can be represented in state-space form. This is also possible for models emerging from the discretization of the LRF equations.

5.1.1 Solution Procedures

Equation (5.1) is formulated in the time domain and can be solved non-iteratively due to linearity. However, most linear thermoacoustic studies are not carried out in the time-domain. Applying the Laplace transformation, Eq. (2.14), to the state vector results in the state-space formulation in the Laplace domain:

$$\mathbf{E}s\hat{\mathbf{x}}(s) = \mathbf{A}\hat{\mathbf{x}}(s) + \mathbf{B}\hat{\mathbf{u}}(s) \tag{5.3}$$

$$\hat{\mathbf{y}}(s) = \mathbf{C}\hat{\mathbf{x}}(s) + \mathbf{D}\hat{\mathbf{u}}(s) \tag{5.4}$$

In this form, the input-output transfer behavior $\hat{\mathbf{G}}(s)$ of a state-space system can be computed for a given frequency s.

$$\hat{\mathbf{G}}(s) = \hat{\mathbf{y}}(s)\hat{\mathbf{u}}(s)^{-\top} = \mathbf{C}\left(\mathbf{E}s - \mathbf{A}\right)^{-1}\mathbf{B} + \mathbf{D} \tag{5.5}$$

When no input signal is present, eigenvalues and -vectors of the autonomous system can be computed. For small systems, where the degrees of freedom are approximately lower than 10^4, it is viable to compute all the eigenvalues. However, the computational demand increases rapidly for larger systems and higher order eigenvalues are deemed irrelevant in thermoacoustic stability analysis, such that it is common practice to only compute a few of the eigenvalues for those systems. One of the most popular algorithms is the *implicitly restarted iterative Arnoldi* algorithm [52]. In order to control, which of the eigenvalues the algorithm will converge to, a shift-invert procedure can be applied to the eigenvalue problem. Therefore, a complex shift frequency s_{shift} is chosen around which the inversion is constructed. This leads to the shift-inverted eigenvalue problem formulation,

$$(\mathbf{A} - s_{\text{shift}}\mathbf{E})^{-1}\,\mathbf{E}\hat{\mathbf{v}}(s) = \frac{1}{s - s_{\text{shift}}}\hat{\mathbf{v}}(s) \tag{5.6}$$

The shift can be interpreted as the new origin of the complex plane, in which the eigenvalues lie and consequently the algorithm can be set to find eigenvalues closest to the shift. Choosing the shift correctly requires some a priori knowledge about the system, e.g. the frequency band of interest, which can be guessed from the gain of the FTF, or a network model approximation of the large system, which allows to have an estimate of the relevant eigenvalues.

5.1.2 Interconnection of State-Space Systems

The matrices **A** to **E** of two systems 1 and 2 are appended block-diagonally to form the basis of the respective matrices for the connected system. The link is then established by feeding an output signal $\mathbf{y}_1$ of system 1 into the input $\mathbf{u}_2$ of system 2 and vice versa. This is realized by a feedback equation with the binary feedback matrix **F** [53].

$$\tilde{\mathbf{u}} = \mathbf{F}\tilde{\mathbf{y}} + \mathbf{u} \tag{5.7}$$

This feedback equation represents the intermediate input vector $\tilde{\mathbf{u}}$ as the sum of fed back internal outputs $\tilde{\mathbf{y}}$ and true external inputs **u** to the connected system, which originate from the original systems and are not interconnected. Resolving Eq. (5.7) by applying the output equation, Eq. (5.2) to it, yields the new, connected system matrices.

5.2 Use Cases of State-Space Interconnect Models

The most common use of the state-space interconnect approach is the connection of a flow-flame submodel to an acoustic submodel in hybrid models. However, there are other fields of application where this strategy is advantageous. A technique described and applied in [19] is aimed at reducing the overall computational cost of thermoacoustic stability analysis while accurately accounting for the interactions between perturbations and the mean flow. This is achieved by representing the crucial parts of the combustor (in this case the swirl generator as well as the combustion zone) with high-fidelity governing equations, e.g. the LNSE, while other parts, such as the plenum and the combustion chamber extension, are approximated by 1D network models. This shows the generality and potential of the state-space interconnect

approach: it is possible to seamlessly combine linear submodels of different complexity, making use of the respective advantages of all modeling approaches employed.

Beyond the connection of models emerging from discretization of governing equations, it is also possible to represent non-trivial, frequency dependent impedances and scattering matrices, e.g. from experimental measurements, in state-space form. To this end, a rational complex polynomial in s is fitted to the discrete data points of the measured frequency response, thus yielding a continuous transfer function. This transfer function can be converted analytically to a state-space model, thus making it suited for interconnection.

6 Contextualization and Discussion of Publications

This chapter clarifies the context between individual publications and provides their relation to literature.

The goal of the series of publications encompassed in this thesis is the development of linear thermoacoustic models with increased prediction accuracy, while remaining in the region of affordable computational cost. Throughout the series of papers, less and less simplifications are made to the governing equations, thus increasingly accounting for effects that strongly simplified models do not take into account. This yields not only more accurate predictions of thermoacoustic instabilities, but also provides more consistency with real combustion devices. As a result, spurious effects, which stem from simplified modeling, can be eliminated by more comprehensive approaches. Thus, results are more reliable and the numerical models are more robust, because there is less impact of modeling decisions on the results. However, more knowledge about the numerical treatment, especially concerning boundary conditions, is required.

The first important step towards the general framework for multi-dimensional linear thermoacoustic models starts with the extension of the state-space interconnect approach from one-dimensional to two/three-dimensional models. Compared to the first appearance of the state-space interconnect approach in thermoacoustics by Schuermans et al. [54], the flow-flame interaction model is also formulated in the state-space formalism, allowing for a linear instead of a non-linear eigenvalue problem. While the state-space interconnect methodology is presented mainly in PAPER-CONNECT, the seamless inclusion of an $n-\tau$ flow-flame model in state-space form as well as a comparison to a state-of-the-art Helmholtz solver is detailed in PAPER-EFFICIENT. Retaining the linearity of the physical problem in the numerical representation leads to significantly less computational cost, equaling a shorter turnaround time for stability predictions compared to other approaches with similar accuracy [55, 56]. Beyond this, the unifying modeling strategy provided by the state-space approach allows for interconnection of models with different governing equations resulting from varying degrees of simplification to the physics of fluid dynamics and combustion. This is a cornerstone of subsequent papers, in which simple parts of the burner under investigation are modeled by one-dimensional network models, while swirl generator and combustion zone are represented by highly resolved three-dimensional models stemming from DG-FEM discretization of governing equations that account for mean-flow and (thermo-)viscous effects. A similar approach, well known in literature, is to connect acoustic transfer-matrices to domains modeled by discretized acoustic governing equations [57–61]. In these studies, segments of the system under investigation were modeled by transfer matrices, which the discretized governing equations could not represent well enough, e.g. because of strong interaction between acoustics and hydrodynamics. While this approach typically yields a strong reduction of degrees of freedom, it requires a source for

the transfer matrices – usually experimental measurements or costly CFD simulations. Coupling of discretized models based on different governing equations, as done in the studies of this thesis, can yield additional information: the interaction between acoustics and hydrodynamics, which can often contribute to the growth or dampening of thermoacoustic instabilities, is resolved and can thus be analyzed in the context of eigenmodes, rather than being hidden in a lumped model like a transfer matrix.

A Discontinuous Galerkin Finite Element approach for solving the Linearized Navier-Stokes Equations in conservative form, or any simplifications thereof, is presented in PAPER-DGFEM. The paper suggests application of this numerical method in thermoacoustics. Strengths of DG-FEM are the physically motivated stabilization via an upwind flux between elements, as well as the straightforward extension to higher order schemes. Compared to a stabilized continuous Finite Element Method for the LNSE that has previously been applied to thermoacoustic problems, DG-FEM proved to be more accurate and reliable for semi-analytical validation cases [62]. Alongside the validation case, the paper shows the capability of this approach to determine thermoacoustic eigenvalues with increased accuracy compared to a network model. As a novelty, a single state-space model comprises the combustion device under investigation that is split into a core of the combustion chamber including the swirl generator, an upstream and a downstream section. While the core is modeled by three-dimensional LNSE discretized with DG-FEM, the dimensionality of other sections is reduced to only the longitudinal aspect, and thus they can be modeled by a network approach. This divide and conquer ansatz yields accurate predictions of the thermoacoustic instabilities, while remaining in the affordable computational regime. A cross-comparison to a pure network representation of the complete burner shows that the three-dimensional LNSE discretization of the burner core influences the predicted growth-rates of thermoacoustic eigenvalues. Strong interaction between the unsteady heat-release rate of the flame, the acoustics and the hydrodynamics can be seen during instability in the combustion region as well as the flow directly downstream of the swirl generator. The resolution of this interplay allows to reason about the role of convective time-delays between swirler and flame in the eigenfrequency of intrinsic thermoacoustic instabilities – an advantage that is missing in modeling approaches that represent regions of complex geometry and flow with a lumped way, e.g. with a transfer matrix [57–61].

PAPER-SCATTERING compares the differences in acoustic scattering behavior predictions of two swirl generators, when various approaches with varying simplifications are employed. While PAPER-DGFEM focused on numerical methodology and a comparison between two extremes – one-dimensional network-model versus three-dimensional LNSE – PAPER-SCATTERING demonstrates the differences on a more fine-grained scale of simplifications to governing equations. Three approaches, namely Helmholtz, Linearized Euler Equations and Linearized Navier-Stokes Equations are employed to discretize the swirl generators under investigation. Reference results as well as the mean-flow fields are provided by Large Eddy Simulation. Results of the linearized methods show increasingly good agreement, when more physical mechanisms, such as mean-flow (Linearized Euler Equations) and viscous effects (Linearized Navier-Stokes Equations), are accounted for. The paper also confirms an effect seen by Kierkegaard et al. [63], that Linearized Euler Equations generate unphysical amounts of vorticity in the boundary layers near walls, which seems to be connected to the discrepancy in boundary conditions between the mean-flow (no-slip) and the linearized perturbation approach (slip). Therefore, it is concluded that accounting for viscous effects, which allows to prescribe

no-slip boundary conditions, not only increases the accuracy but also the robustness of this methodology.

The last major step in methodological development in the frame of this thesis is published in PAPER-LRF. It represents the first publication of an analytically Linearized Reactive Flow solver and is mainly concerned with validation against results from CFD. The numerical Discontinuous Galerkin Finite Element methodology developed in PAPER-DGFEM is successfully employed. This paper marks the first publication, in which a thermoacoustic system was investigated by an analytically linearized fully compressible reactive flow solver. The goal was to demonstrate quantitative accuracy without use of tunable parameters, by comparing to reference solutions computed with CFD, from which also the mean-flow was extracted. Albayrak et al. [64] demonstrated earlier, that the behavior of a swirl flame subject to inertial wave forcing could be represented by a similar approach with a continuous Finite Element Method in the low Mach number regime. Weakly compressible Linearized Navier-Stokes Equations with a one-step chemistry were solved, based on a mean-flow obtained by solving the non-linear set of equations with Newton's method. Although it is possible to reproduce and investigate the flame response with this methodology, thermoacoustic eigenmodes can not be computed because the weakly compressible LNSE do not support the correct propagation of acoustic waves. Blanchard et. al [65] investigated the response of a laminar premixed flame to acoustic perturbations by means of a numerically linearized reactive flow solver, though without quantitative agreement to reference data. The emphasis of this study was to reproduce the flame behavior on a qualitative level, in order to investigate the spatially resolved perturbations in heat-release rate as well as their feedback on the unsteady flow field. Opposed to the numerical linearization, the analytical linearization used in the LRF approach in this thesis allows for flexible choice of numerical scheme and spatial discretization of the computations. As no simplifications to the governing equations (beside linearization) are made, the highest degree of consistency to the simulation for the mean-flow is guaranteed. Computational efficiency is achieved because it is no longer necessary to identify the flow-flame model a priori through CFD in the time-domain. These savings can typically more than compensate for the added degrees of freedom in the linearized simulations stemming from the discretized species transport equations, which are not necessary if a flow-flame model is used. Beyond the gain in prediction accuracy, the resolution of the linearized reaction mechanism allows investigation of the physical processes in the combustion region during a thermoacoustic instability. The results show that a perturbed flame front is not a monopole, but rather a dipole source of acoustic waves. This dipole pattern forms due to the movement of the flame, which is strongly influenced by convective effects. A synchronization between the acoustic forcing and the convective displacement can lead to intrinsic thermoacoustic instabilities. In a lumped framework that models the flame as a discontinuity in the flow, rather than a spatially resolved flame front, this lock-on between flame and forcing is expressed in the π-criterion [66–68].

PAPER-ENTROPY employs the same fundamental governing equations and numerical methodology as in PAPER-LRF. The only difference is that a partly reversible two-step chemical mechanism is used to model the lean methane-air combustion in closer agreement to experimental data, rather than a one-step mechanism. The focus of this work is to demonstrate the spurious results that are obtained when simplifications in the governing equations or the overall approach are made in the context of linearized combustion dynamics. The response of a laminar flame subject to acoustic forcing is investigated with a hybrid model, consisting of Linearized Navier-

Stokes Equations coupled to a lumped flame transfer function, and the monolithic Linearized Reactive Flow. While the perturbed heat-release rate due to acoustic forcing is correctly represented by both models, the ensuing response of the flow, especially generated entropy waves, differ significantly. It is reasoned that due to the lack of flame movement in the hybrid model, excessive amounts of spurious entropy are generated in the combustion zone, which contradict first principles as well as reference results from CFD. This entropy is not only per se a wrong representation of physical mechanisms, but can additionally deteriorate the prediction of thermoacoustic modes due to a feedback mechanism between accelerated entropy waves and acoustics. The LRF on the other hand is in good agreement to reference data and behaves as expected from first principles, because the locally resolved linearized reaction mechanism accounts for movement of the flame due to an interplay between perturbations in flow, temperature and transported species. This spurious entropy production has already been derived by Strobio Chen et al. [69] for a framework, in which the spatial extent of the flame is neglected. Results given in a theoretical analysis by Yoon [70] also show that regarding the flame as a fixed heat-source, rather than a moving flame front in kinematic balance with the approaching flow, leads to spurious entropy production. PAPER-ENTROPY sheds more light on the processes that are happening in the combustion zone itself, both when flame movement is correctly represented, and when a fixed flame is considered. These findings continue the train of thought found throughout the whole thesis, which is that simplifying the overall approach or the governing equations not only reduces the accuracy of results, but also gives rise to inconsistencies between CFD (mean-flow, reference results) and the linearized models. Beyond that, the apparent savings in computational effort due to simplified approaches, like the hybrid one using a flow-flame interaction model, often turn out to be outperformed by a monolithic approach like the LRF.

7 Summary and Discussion of Papers

In this chapter, the core finding of individual publications is laid out. Beyond this, the respective contribution of the authors to each paper is stated. The publications are not sorted strictly chronologically, but rather in a way that underlines the progress made in the methodology.

7.1 Linear State-Space Interconnect Modeling of Acoustic Systems

Label: PAPER-CONNECT

Outcome: Linear state-space models of various origin, i.e. one-dimensional acoustic network models, three-dimensional perturbation equations, as well as flow-flame interaction models identified from Computational Fluid Dynamics, are connected in a state-space interconnect framework. The connected system is represented as a single state-space model. The resulting eigenvalue problem is linear in the Laplace variable, facilitating non-iterative, robust and accurate solution procedures.

Relevance for the thesis: This publication provides the backbone of the interconnect framework, demonstrating how sub-models of various spatial dimensionality and based on different governing equations can be merged to form a single model of the thermoacoustic system.

Contribution: The research topic was jointly defined by Wolfgang Polifke, Thomas Emmert, Stefan Jaensch and me. The state-space interconnect algorithm was implemented by Thomas Emmert in the in-house thermoacoustic network tool `taX`, which is written in Matlab. I contributed the state-space models for the full as well as the segregated three-dimensional annular combustor. The manuscript was prepared by Thomas Emmert, proof reading and suggestions for improvement were given by all co-authors.

Status: Published in *Acta Acoustica united with Acoustica*.

Review process: Peer-reviewed, Scopus listed.

Reference: Thomas Emmert, Max Meindl, Stefan Jaensch, and Wolfgang Polifke. Linear State Space Interconnect Modeling of Acoustic Systems. *Acta Acustica United with Acustica* 102, no. 5 (2016): 824–33. doi: 10.3813/AAA.918997, reproduced on p.59f.

7.2 Efficient Calculation of Thermoacoustic Modes utilizing State-Space Models

Label: PAPER-EFFICIENT

Outcome: In this publication, the state-space interconnect approach is employed to form a model based on a sub-model for the acoustic propagation in an annular combustor as well as a flow-flame interaction sub-model. The acoustic perturbations are governed by the Linearized Euler Equations, the flow-flame interaction is modeled by a simplistic $n-\tau$ ansatz. The latter is formulated in terms of a discretized advection equation for the time delay, yielding a state-space model linear in the Laplace variable. The comparison to a Finite Volume solver of the Helmholtz equation based on fixed-point iteration shows good agreement for the eigenfrequencies. The computational cost is significantly lower, which is attributed to the linear eigenvalue problem emerging from the state-space approach with the discretized time-delay.

Relevance for the thesis: This paper uses the interconnect framework of PAPER-CONNECT and applies it to a case including flow-flame interaction, rather than pure acoustic perturbations. The efficiency of formulating a linear eigenvalue problem by means of discretizing the time delay of the flow-flame model is presented.

Contribution: Conceptualization of the topic was done in collaboration with all co-authors. Wolfgang Polifke supervised the work and gave critical feedback on both the methodology as well as the manuscript. Thomas Emmert implemented the state-space interconnect algorithm as well as the discretization of the $n-\tau$ flame model via an advection equation. I contributed the Finite Element models, set up the case of the annular combustor and conducted all the computations. The manuscript was written by me, feedback and suggestions for improvement were made by all co-authors.

Status: Presented at the *23rd International Congress on Sound & Vibration*, published in *Proceedings of the 23rd International Congress on Sound & Vibration*.

Review process: Peer-reviewed, Scopus listed.

Reference: Max Meindl, Thomas Emmert and Wolfgang Polifke. Efficient Calculation of Thermoacoustic Modes Utilizing State-Space Models. *In 23nd Int. Congress on Sound and Vibration (ICSV23)*. Athens, Greece, 2016. reproduced on p.69ff.

7.3 A State-Space Formulation of a Discontinuous Galerkin Method for Thermoacoustic Stability Analysis

Label: PAPER-DGFEM

Outcome: A Discontinuous Galerkin Finite Element Discretization for the Linearized Navier-Stokes Equations is presented. The approach is based on a formulation for the non-linear Navier-Stokes and Euler Equations by Baumann et al. [47]. Compared to previously published results by a Galerkin Least Squares stabilized continuous Finite Element Method [62], the presented approach showed improved agreement with semi-analytical results for a one-dimensional validation case first investigated by Dowling [71]. Subsequent analysis of a turbulent swirled combustion test rig demonstrated that the interaction between acoustic, hydrodynamic and entropic perturbations as well as the influence of spatial gradients in the mean-flow can impact thermoacoustic eigenvalues both in their oscillation frequency as well as their growth rate. It is important to note that those mechanisms can have a stabilizing as well as a destabilizing effect on the eigenmodes. Throughout the studies of this paper, state-space formulations as well as interconnection algorithms developed in PAPER-CONNECT are employed to connect models of varying spatial dimensionality, governing equations as well as the acoustic and the flow-flame sub-models.

Relevance for the thesis: This publication validates the numerical approach – a Discontinuous Galerkin Finite Element Method – for the discretization of non self-adjoint governing equations like such as Linearized Navier-Stokes Equations. It is thus the second staple, next to the state-space framework, on which the methodology presented in this thesis is based on.

Contribution: The research topic was defined by me. The implementation of the numerical methods as well as the setup of the linear models was done by me. Alp Albayrak set up and ran the Large Eddy Simulation of the turbulent swirl combustor, which is required for the provision of the mean-flow as well as identification of the flow-flame interaction model. The manuscript was written in major parts by me, feedback, suggestions and improvements were given by all co-authors. Wolfgang Polifke contributed significantly in writing of the introduction, abstract and conclusion, Alp Albayrak wrote the section on the Large Eddy Simulations.

Status: Published in *Journal of Sound and Vibration*.

Review process: Peer-reviewed, Scopus listed.

Reference: Max Meindl, Alp Albayrak and Wolfgang Polifke. A State-Space Formulation of a Discontinuous Galerkin Method for Thermoacoustic Stability Analysis. *Journal of Sound and Vibration* 481 (2020): 115431. doi: 10.1016/j.jsv.2020.115431, reproduced on p.104ff.

7.4 Determination of Acoustic Scattering Matrices from Linearized Compressible Flow Equations with Application to Thermoacoustic Stability Analysis

Label: PAPER-SCATTERING

Outcome: The acoustic scattering behavior of two swirl generators for combustion test rigs is investigated via Large Eddy Simulation, Helmholtz Equation, Linearized Euler Equations and Linearized Navier-Stokes Equations. The latter two governing equations are solved with the Discontinuous Galerkin Finite Element Method introduced in PAPER-DGFEM. Results from Large Eddy Simulation and Linearized Navier-Stokes Equations agree well. The Linearized Euler Equations perform similar for most frequencies, but suffer from spurious unstable eigenmodes, which spoil the scattering behavior. The Helmholtz Equation underestimates the magnitude of reflected waves significantly. Accounting for this acoustic scattering in a network model of a combustor test rig is shown to impact the predicted eigenfrequencies.

Relevance for the thesis: This publications shows that simplifications that are commonly made in aeroacoustics, e.g. non-viscous perturbations or neglect of the mean-flow velocity, should not be employed when treating ducted flows, ubiquitous in combustors.

Contribution: The idea to investigate acoustic scattering of swirl generators was given by Wolfgang Polifke. The Large Eddy Simulation for the radial swirl generator was conducted by Malte Merk. The linearized simulations were carried out by Fabian Fritz for the radial and by me for the axial swirl generator. The network model analysis was conducted by me. The section on the radial swirl generator was written by Fabian Fritz, except for the description of the Large Eddy Simulation, which was written by Malte Merk. The rest of the manuscript was written by me. Wolfgang Polifke contributed through discussion, feedback and improvements of the manuscript.

Status: Published in *Journal of Theoretical and Computational Acoustics*.

Review process: Peer-reviewed, Scopus listed.

Reference: Max Meindl, Malte Merk, Fabian Fritz and Wolfgang Polifke. Determination of Acoustic Scattering Matrices from Linearized Compressible Flow Equations. *J. Theoretical and Computational Acoustics* 27, no. 3 (June 5, 2018): 1850027-1-1850027–27. doi: 10.1142/S2591728518500275, reproduced on p.77ff.

7.5 Thermoacoustic Analysis of a Laminar Premixed Flame using a Linearized Reactive Flow Solver

Label: PAPER-LRF

Outcome: This paper is mainly concerned with the validation of a Linearized Reactive Flow Solver employing the Discontinuous Galerkin Finite Element Method introduced in PAPER-DGFEM. The subject of investigation is a small laminar flame forced acoustically. The flame response is compared to the flame dynamics computed from an OpenFOAM time series post-processed with system identification. Good agreement for both adiabatic and isothermal flame anchoring plates is observed. An eigenvalue analysis of the intrinsic thermoacoustic mode shows differences between the Linearized Reactive Flow solver and a hybrid approach consisting of Linearized Navier-Stokes Equations coupled to a Flame Transfer Function. Not only the resonance frequency, but also the mode shape differs.

Relevance for the thesis: The publication introduces the Linearized Reactive Flow solver, furthering the development of linear thermoacoustic models towards higher accuracy in the prediction of instabilities.

Contribution: The idea of linearizing – beyond the Navier-Stokes Equations – also the species transport equations and the reaction mechanism stems from Alexander Avdonin. The implementation of the governing equations was conducted by me, with Alexander Avdonin contributing valuable ideas on discretization and formulation of the governing equations. OpenFOAM simulations were carried out by Alexander Avdonin, the linearized simulations were carried out in parts by Alexander Avdonin and me. The manuscript was written by Alexander Avdonin, all co-authors gave feedback and suggestions for improvement. Wolfgang Polifke supervised the whole process, providing valuable ideas and feedback on technical as well as conceptual aspects.

Status: Published in *Proceedings of the Combustion Institute*.

Review process: Peer-reviewed, Scopus listed.

Reference: Alexander Avdonin, Max Meindl and Wolfgang Polifke. Thermoacoustic Analysis of a Laminar Premixed Flame Using a Linearized Reacting Flow Solver. *Proceedings of the Combustion Institute* 37 (2019): 5307–14. doi: 10.1016/j.proci.2018.06.142, reproduced on p.125ff.

7.6 On the Spurious Entropy Generation Encountered in Hybrid Linear Thermoacoustic Models

Label: PAPER-ENTROPY

Outcome: This paper shows the ramifications of employing the hybrid approach commonly used in thermoacoustic. The split of the acoustic and flow-flame sub-model is investigated for a one- and a two-dimensional flame with both a global and a local flow-flame model identified from non-linear OpenFOAM simulations. To this end, Linearized Navier-Stokes equations are employed as the acoustic sub-model. For both flames, significant generation of spurious entropy in the combustion zone is observed if a global flow-flame model is employed. The local flow-flame model remedies this problem. Additionally, it is shown that the Linearized Reactive Flow does not suffer from this problem, as the combustion dynamics is inherently accounted for locally. The spurious generation of entropy is explained by the lack of a global flow-flame model to account for flame movement. The numerical discretization for the linear models is entirely done with the Discontinuous Galerkin Finite Element Method described in PAPER-DGFEM.

Relevance for the thesis: This publication shows that the Linearized Reactive Flow is not only more accurate than hybrid models, but also less error prone in terms of modeling mistakes. Additionally, it demonstrates how flame movement – a critical property of an acoustically forced flame – can be accounted for in a spatially resolved combustion region.

Contribution: Wolfgang Polifke conceptualized the idea that flame movement needs to be accounted for in spatially resolved combustion regions. All the simulations as well as the writing of the first version of the manuscript were done by me. Camilo Silva contributed the idea to investigate hybrid models with a locally resolved flow-flame model. Wolfgang Polifke formulated the explanation for the spurious entropy in terms of lack of flame movement. Major contributions to the manuscript were made by Wolfgang Polifke and Camilo Silva through numerous internal revisions, suggestions and editing.

Status: Published in *Combustion and Flame*.

Review process: Peer-reviewed, Scopus listed.

Reference: Max Meindl, Camilo F. Silva and Wolfgang Polifke. On the Spurious Entropy Generation Encountered in Hybrid Linear Thermoacoustic Models. *Combustion and Flame* 223 (January 2021): 525–40. doi: 10.1016/j.combustflame.2020.09.018, reproduced on p.133ff.

8 Outlook

The Discontinuous Galerkin Finite Element Method described in this thesis is the basis for the development of hybrid and monolithic thermoacoustic models governing the full spectrum of perturbations in the linear regime. A strong foundation is set for future research to build on.

Progress can be aimed at both new numerical schemes as well as varying the formulation of the governing equations. Chances for improvement in the numerical treatment are to be seen in the various new flux formulations emerging rapidly in the Finite Element context. For the pure hyperbolic parts of the flux, exact flux difference splitting by means of diagonalization of the flux matrix is the optimum. However, when the number of equations increases, e.g. due to several species accounted for in the Linearized Reactive Flow, this is not a trivial task. The best choice for discretization of the diffusive terms is much more controversial, as stabilization or penalty methods have to be employed due to the discontinuous basis functions. Due to the prominent role of heat and species diffusion in combustion, studying the impact on accuracy and computational effort of newly emerging schemes for thermoacoustic problems should be aimed at.

In the field of governing equations, the main challenge lies in the modeling of linearized turbulent combustion with the Linearized Reactive Flow. Due to the unsteady nature of turbulence, there is no steady-state of the mean flow computations, and thus – strictly speaking – no valid linearization point. However, practical cases showed that a time averaged mean field of the unsteady flow can still yield good results in terms of a non-reacting flow stability analysis. Once combustion is added on top of turbulence, the main complication becomes that applying the reaction mechanism to the averaged mean fields, one does not recover the averaged mean heat release rate, i.e. the mean flow itself is inconsistent. It is still an open question how to account for or circumvent this fundamental problem.

Beyond the challenges that lie in modeling linearized turbulent combustion, the compute effort will also be significantly larger than for the cases tackled in the scope of this thesis research. While solving small cases is a matter of minutes with a direct solver on a typical desktop computer, the use of iterative methods to solve the linear system of equations resulting for larger cases is a necessity. Preliminary studies, however, showed that the structure of the resulting matrix in the frequency domain, even for small cases, poses a problem for combinations of preconditioners and solvers that are typically employed in the field of fluid mechanics. Convergence towards the correct solution is either very slow, or not possible at all. Deriving a suitable preconditioning matrix is therefore essential to expand the applicability of the Linearized Reactive Flow approach towards realistic combustion configurations. As an alternative way, employing model order reduction to large systems can significantly reduce computational cost.

A topic that seems less challenging with the current state of the method is the treatment of acoustically non-compact flames, as they often occur in high frequency transversal thermoa-

coustic instabilities. No essential modifications or additions to the methodology presented in the scope of this thesis are needed to account for this phenomenon.

As a result of future implementations, and based on the currently existing method, the investigation of the physics of perturbed flames could be of great use to broaden the understanding of thermoacoustic instabilities. The Linearized Reactive Flow allows to vary the boundary conditions for thermal perturbations while keeping the mean flow unchanged. This could be used to investigate the influence of flame anchoring at a plate that behaves adiabatic or isothermal in terms of the perturbations, thus reflecting a negligible or infinitely high thermal inertia of the plate, respectively. First numerical experiments in this direction showed that the excess of gain in the Flame Transfer Function could be tightly connected to the thermal boundary conditions. Beyond this rather simplistic approach, the perturbed heat conduction in the plate itself could be included in the linearized simulation, to closer model the actual physics. Due to the symmetric nature of the Fourier's equation for heat conduction, the discretization with the Finite Element Method is straight forward and no stabilization is required.

The modular nature of the method developed in this thesis – on the one hand due to its implementation `felicitaX`, on the other hand due to the state-space interconnect approach – lends itself to make additions to the functionality, while keeping flexibility and compatibility of the sub-modules. This is an approach that has proven valuable in the past, as demonstrated by state-space based thermoacoustic network models. Thus, the approach can be deemed future-prove and enables further research in this area.

Bibliography

[1] G. A. Jones and K. J. Warner. "The 21st century population-energy-climate nexus". *Energy Policy*, 93:206–212, June 2016. ISSN 03014215. doi: 10.1016/j.enpol.2016.02.044.

[2] M. Götz, J. Lefebvre, F. Mörs, A. McDaniel Koch, F. Graf, S. Bajohr, R. Reimert, and T. Kolb. "Renewable Power-to-Gas: A technological and economic review". *Renewable Energy*, 85:1371–1390, January 2016. ISSN 09601481. doi: 10.1016/j.renene.2015.07.066.

[3] T. Lieuwen and V. Yang, editors. *Combustion Instabilities in Gas Turbine Engines: Operational Experience, Fundamental Mechanisms and Modeling*. Number v. 210 in Progress in Astronautics and Aeronautics. American Institute of Aeronautics and Astronautics, Reston, VA, 2005. ISBN 978-1-56347-669-3.

[4] S. Candel. "Combustion Dynamics and Control: Progress and Challenges". *Proceedings of the Combustion Institute*, 29(1):1–28, 2002.

[5] T. Poinsot. "Prediction and Control of Combustion Instabilities in Real Engines". *Proceedings of the Combustion Institute*, 36:1–28, 2017. ISSN 1540-7489. doi: 10.1016/j.proci.2016.05.007.

[6] T. C. Lieuwen. *Unsteady Combustor Physics*. Cambridge University Press, New York, N.Y., USA, 2012. ISBN 978-1-107-01599-9.

[7] J. W. S. Rayleigh. "The Explanation of Certain Acoustical Phenomena". *Nature*, 18:319–321, 1878. doi: 10.1038/018319a0.

[8] L. Crocco and S. I. Cheng. *Theory of Combustion Instability in Liquid Propellant Rocket Motors*. Number 8 in AGARDograph. Butterworths Science Publications, New York, 1956.

[9] B.-T. Chu. "On the generation of pressure waves at a plane flame front". *Symposium (International) on Combustion*, 4(1):603–612, January 1953. doi: 10.1016/S0082-0784(53)80081-0.

[10] M. Bauerheim, F. Nicoud, and T. Poinsot. "Progress in Analytical Methods to Predict and Control Azimuthal Combustion Instability Modes in Annular Chambers". *Physics of Fluids (1994-present)*, 28(2):021303, February 2016. ISSN 1070-6631, 1089-7666. doi: 10.1063/1.4940039.

[11] A. Avdonin, M. Meindl, and W. Polifke. “Thermoacoustic analysis of a laminar premixed flame using a linearized reacting flow solver”. *Proceedings of the Combustion Institute*, 37:5307–5314, 2019. doi: 10.1016/j.proci.2018.06.142.

[12] C. K. Westbrook and F. L. Dryer. “Simplified Reaction Mechanisms for the Oxidation of Hydrocarbon Fuels in Flames”. *Combustion Science and Technology*, 27(1-2):31–43, December 1981. ISSN 0010-2202. doi: 10.1080/00102208108946970.

[13] M. Meindl, C. F. Silva, and W. Polifke. “On the spurious entropy generation encountered in hybrid linear thermoacoustic models”. *Combustion and Flame*, 223:525–540, January 2021. ISSN 00102180. doi: 10.1016/j.combustflame.2020.09.018.

[14] J. Bibrzycki, T. Poinsot, and A. Zajdel. “Investigation of Laminar Flame Speed of CH4/N2/O2 and CH4/CO2/O2 Mixtures Using Reduced Chemical Kinetic Mechanisms”. *Archivum combustionis*, 30(4):287–296, 2010.

[15] M. Fosas de Pando, D. Sipp, and P. J. Schmid. “Efficient evaluation of the direct and adjoint linearized dynamics from compressible flow solvers”. *Journal of Computational Physics*, 231(23):7739–7755, October 2012. ISSN 0021-9991. doi: 10.1016/j.jcp.2012.06.038.

[16] J. Gikadi, S. Föller, and T. Sattelmayer. “Impact of turbulence on the prediction of linear aeroacoustic interactions: Acoustic response of a turbulent shear layer”. *Journal of Sound and Vibration*, 333(24):6548–6559, December 2014. ISSN 0022-460X. doi: 10.1016/j.jsv.2014.06.033.

[17] T. L. Kaiser, T. Poinsot, and K. Oberleithner. “Stability and Sensitivity Analysis of Hydrodynamic Instabilities in Industrial Swirled Injection Systems”. In *ASME Turbo Expo 2017: Turbomachinery Technical Conference and Exposition*, GT2017-63649, page V04AT04A043. American Society of Mechanical Engineers, 2017. doi: 10.1115/GT2017-63649.

[18] T. L. Kaiser, L. Lesshafft, and K. Oberleithner. “Prediction of the Flow Response of a Turbulent Flame to Acoustic Pertubations Based on Mean Flow Resolvent Analysis”. *Journal of Engineering for Gas Turbines and Power*, 141(11):111021, November 2019. ISSN 0742-4795, 1528-8919. doi: 10.1115/1.4044993.

[19] M. Meindl, A. Albayrak, and W. Polifke. “A state-space formulation of a discontinuous Galerkin method for thermoacoustic stability analysis”. *Journal of Sound and Vibration*, 481:115431, 2020. doi: 10.1016/j.jsv.2020.115431.

[20] L. Tay-Wo-Chong, S. Bomberg, A. Ulhaq, T. Komarek, and W. Polifke. “Comparative Validation Study on Identification of Premixed Flame Transfer Function”. *Journal of Engineering for Gas Turbines and Power*, 134(2):021502–1–8, 2012. doi: 10.1115/1.4004183.

[21] R. MacCormack. “Numerical solution of a shock wave with a laminar boundary layer.”. *Lecture Notes in Physics*, 8:151–163, 1971.

[22] M. Meindl, M. Merk, F. Fritz, and W. Polifke. "Determination of acoustic scattering matrices from linearized compressible flow equations". *J. Theoretical and Computational Acoustics*, 27(3):1850027–1 – 1850027–27, June 2018. doi: 10.1142/S2591728518500275.

[23] A. Kierkegaard, S. Allam, G. Efraimsson, and M. Åbom. "Simulations of whistling and the whistling potentiality of an in-duct orifice with linear aeroacoustics". *Journal of Sound and Vibration*, 331(5):1084–1096, 2012. ISSN 0022-460X. doi: 10.1016/j.jsv.2011.10.028.

[24] F. Nicoud, L. Benoit, C. Sensiau, and T. Poinsot. "Acoustic Modes in Combustors with Complex Impedances and Multidimensional Active Flames". *AIAA Journal*, 45(2):426–441, 2007. doi: 10.2514/1.24933.

[25] M. Zhu, A. P. Dowling, and K. N. C. Bray. "Flame Transfer Function Calculations for Combustion Oscillations". In *Volume 2: Coal, Biomass and Alternative Fuels; Combustion and Fuels; Oil and Gas Applications; Cycle Innovations*, page V002T02A055, New Orleans, Louisiana, USA, June 2001. American Society of Mechanical Engineers. ISBN 978-0-7918-7851-4. doi: 10.1115/2001-GT-0374.

[26] K. Truffin, B. Varoquié, and T. Poinsot. "Measurements of transfer functions in reacting flows using Large Eddy Simulations". In *10th International Congress on Sound and Vibration,*, pages 785–793, Stockholm, Sweden, 2003.

[27] C. A. Armitage, A. J. Riley, R. S. Cant, A. P. Dowling, and S. R. Stow. "Flame Transfer Function for Swirled LPP Combustion from Experiments and CFD". In *ASME Turbo Expo 2004: Power for Land, Sea, and Air*, GT2004-53820, pages 527–537, Vienna, Austria, June 2004. ASME. doi: 10.1115/GT2004-53820.

[28] S. Kato, T. Fujimori, A. P. Dowling, and H. Kobayashi. "Effect of heat release distribution on combustion oscillation". *Proceedings of the Combustion Institute*, 30(2):1799–1806, January 2005. ISSN 1540-7489. doi: 10.1016/j.proci.2004.08.154.

[29] D. Kang, F. Culick, and A. Ratner. "Combustion dynamics of a low-swirl combustor". *Combustion and Flame*, 151(3):412–425, November 2007. doi: 10.1016/j.combustflame.2007.07.017.

[30] K. T. Kim, J. G. Lee, B. D. Quay, and D. A. Santavicca. "Spatially distributed flame transfer functions for predicting combustion dynamics in lean premixed gas turbine combustors". *Combustion and Flame*, 157(9):1718–1730, 2010. ISSN 0010-2180. doi: 10.1016/j.combustflame.2010.04.016.

[31] R. Leandro and W. Polifke. "Low-Order Modelling of Distributed Heat Release". In *19th Int. Congress on Sound and Vibration*, Vilnius, Lithuania, 2012. Int'l Inst. of Acoustics and Vibration.

[32] M. Schulze and T. Sattelmayer. "Eigenvalue Analysis for the Prediction of Initial Growth Rates of Thermoacoustic Instability in Rocket Motors". In *53rd AIAA Aerospace Sciences Meeting*, Kissimmee, Florida, USA, 2015. American Institute of Aeronautics and Astronautics. doi: 10.2514/6.2015-1606.

[33] J. Li, Y. Xia, A. S. Morgans, and X. Han. "Numerical prediction of combustion instability limit cycle oscillations for a combustor with a long flame". *Combustion and Flame*, 185: 28–43, November 2017. ISSN 0010-2180. doi: 10.1016/j.combustflame.2017.06.018.

[34] J. S. Hesthaven and T. Warburton. *Nodal Discontinuous Galerkin Methods: Algorithms, Analysis, and Applications*, volume 54 of *Texts in Applied Mathematics*. Springer New York, New York, NY, 2008. ISBN 978-0-387-72065-4 978-0-387-72067-8. doi: 10.1007/978-0-387-72067-8.

[35] J. Donéa and A. Huerta. *Finite Element Methods for Flow Problems*. Wiley, Chichester ; Hoboken, NJ, 2003. ISBN 978-0-471-49666-3.

[36] R. Costa, S. Clain, R. Loubère, and G. J. Machado. "Very high-order accurate finite volume scheme on curved boundaries for the two-dimensional steady-state convection–diffusion equation with Dirichlet condition". *Applied Mathematical Modelling*, 54: 752–767, February 2018. ISSN 0307904X. doi: 10.1016/j.apm.2017.10.016.

[37] A. N. Brooks and T. J. Hughes. "Streamline upwind/Petrov-Galerkin formulations for convection dominated flows with particular emphasis on the incompressible Navier-Stokes equations". *Computer Methods in Applied Mechanics and Engineering*, 32(1-3):199–259, September 1982. ISSN 00457825. doi: 10.1016/0045-7825(82)90071-8.

[38] T. J. Hughes, L. P. Franca, and G. M. Hulbert. "A new finite element formulation for computational fluid dynamics: VIII. The Galerkin/least-squares method for advective-diffusive equations". *Computer Methods in Applied Mechanics and Engineering*, 73(2):173–189, May 1989. ISSN 00457825. doi: 10.1016/0045-7825(89)90111-4.

[39] T. Hofmeister, T. Hummel, B. Schuermans, and T. Sattelmayer. "Quantification of Energy Transformation Processes Between Acoustic and Hydrodynamic Modes in Non-Compact Thermoacoustic Systems via a Helmholtz-Hodge Decomposition Approach". In *Volume 4A: Combustion, Fuels, and Emissions*, page V04AT04A013, Phoenix, Arizona, USA, June 2019. American Society of Mechanical Engineers. ISBN 978-0-7918-5861-5. doi: 10.1115/GT2019-90240.

[40] T. Hofmeister, T. Hummel, B. Schuermans, and T. Sattelmayer. "Modeling and Quantification of Acoustic Damping Induced by Vortex Shedding in Noncompact Thermoacoustic Systems". *Journal of Engineering for Gas Turbines and Power*, 142(3):031016, March 2020. ISSN 0742-4795, 1528-8919. doi: 10.1115/1.4044936.

[41] A. Birkefeld. *Computational Aeroacoustics with a High Order Discontinuous Galerkin Scheme*. PhD thesis, Universität Stuttgart, January 2013.

[42] A. Beck and C.-D. Munz. "Direct Aeroacoustic Simulations Based on High Order Discontinuous Galerkin Schemes". In M. Kaltenbacher, editor, *Computational Acoustics*, volume 579, pages 159–204. Springer International Publishing, Cham, 2018. ISBN 978-3-319-59037-0 978-3-319-59038-7. doi: 10.1007/978-3-319-59038-7_4.

[43] M. Dumbser and C.-D. Munz. "ADER discontinuous Galerkin schemes for aeroacoustics". *Comptes Rendus Mécanique*, 333(9):683–687, September 2005. ISSN 16310721. doi: 10.1016/j.crme.2005.07.008.

[44] C. Blom. *Discontinuous Galerkin Methods on Tetrahedral Elements for Aeroacoustics*. PhD thesis, University of Twente, Enschede, 2003.

[45] I. Babuška, C. Baumann, and J. Oden. "A discontinuous hp finite element method for diffusion problems: 1-D analysis". *Computers & Mathematics with Applications*, 37(9): 103–122, May 1999. ISSN 08981221. doi: 10.1016/S0898-1221(99)00117-0.

[46] C. E. Baumann and J. T. Oden. "A discontinuous hp finite element method for convection—diffusion problems". *Computer Methods in Applied Mechanics and Engineering*, 175(3-4):311–341, July 1999. ISSN 00457825. doi: 10.1016/S0045-7825(98)00359-4.

[47] C. E. Baumann and J. T. Oden. "A discontinuous hp finite element method for the Euler and Navier-Stokes equations". *International Journal for Numerical Methods in Fluids*, 31(1):79–95, September 1999. ISSN 0271-2091, 1097-0363. doi: 10.1002/(SICI)1097-0363(19990915)31:1.

[48] M. Alnæs, J. Blechta, J. Hake, A. Johansson, B. Kehlet, A. Logg, C. Richardson, J. Ring, M. E. Rognes, and G. N. Wells. "The FEniCS Project Version 1.5". *Archive of Numerical Software*, Vol 3:Starting Point and Frequency: Year: 2013</p>, 2015. doi: 10.11588/ANS.2015.100.20553.

[49] C. Geuzaine and J.-F. Remacle. "Gmsh: A 3-D finite element mesh generator with built-in pre- and post-processing facilities: THE GMSH PAPER". *International Journal for Numerical Methods in Engineering*, 79(11):1309–1331, September 2009. ISSN 00295981. doi: 10.1002/nme.2579.

[50] C. B. Barber, D. P. Dobkin, and H. Huhdanpaa. "The quickhull algorithm for convex hulls". *ACM Transactions on Mathematical Software*, 22(4):469–483, December 1996. ISSN 0098-3500, 1557-7295. doi: 10.1145/235815.235821.

[51] Y. Saad. *Iterative Methods for Sparse Linear Systems: Second Edition*. Society for Industrial and Applied Mathematics, April 2003. ISBN 978-0-89871-534-7.

[52] Y. Saad. *Numerical Methods for Large Eigenvalue Problems*. Number 66 in Classics in Applied Mathematics. Society for Industrial and Applied Mathematics, Philadelphia, rev. ed edition, 2011. ISBN 978-1-61197-072-2.

[53] T. Emmert, M. Meindl, S. Jaensch, and W. Polifke. "Linear State Space Interconnect Modeling of Acoustic Systems". *Acta Acustica united with Acustica*, 102(5):824–833, 2016. doi: 10.3813/AAA.918997.

[54] B. Schuermans, V. Bellucci, D. Nowak, and C. O. Paschereit. "Modelling of Complex Thermoacoustic Systems: A State-Space Approach". In *Ninth Int. Congress on Sound and Vibration, ICSV9*, Orlando, FL, U.S.A., May 2002. IIAV.

[55] M. Bauerheim, J.-F. Parmentier, P. Salas, F. Nicoud, and T. Poinsot. "An analytical model for azimuthal thermoacoustic modes in an annular chamber fed by an annular plenum". *Combustion and Flame*, 161(5):1374–1389, May 2014. ISSN 0010-2180. doi: 10.1016/j.combustflame.2013.11.014.

[56] M. Meindl, T. Emmert, and W. Polifke. "Efficient calculation of thermoacoustic modes utilizing state-space models". In *23nd Int. Congress on Sound and Vibration (ICSV23)*, Athens, Greece, 2016.

[57] S. M. Camporeale, B. Fortunato, and G. Campa. "A Finite Element Method for Three-Dimensional Analysis of Thermo-acoustic Combustion Instability". *Journal of Engineering for Gas Turbines and Power*, 133(1):011506, 2011. ISSN 07424795. doi: 10.1115/1.4000606.

[58] G. Campa and S. Camporeale. "Eigenmode analysis of the thermoacoustic combustion instabilities using a hybrid technique based on the finite element method and the transfer matrix method". *Advances in Applied Acoustics (AIAAS)*, 1(1):1–14, 2012.

[59] G. Campa and S. M. Camporeale. "Prediction of the Thermoacoustic Combustion Instabilities in Practical Annular Combustors". *J. Eng. Gas Turbines and Power*, 136(9): 091504–091504, 2014. ISSN 0742-4795. doi: 10.1115/1.4027067.

[60] M. Schulze and T. Sattelmayer. "A Comparison of Time and Frequency Domain Descriptions of High Frequency Acoustics in Rocket Engines with Focus on Dome Coupling". *Aerospace Science and Technology*, 45:165–173, 2015. doi: 10.1016/j.ast.2015.05.007.

[61] F. Ni, M. M. Brebion, F. Nicoud, and T. Poinsot. "Accounting for Acoustic Damping in a Helmholtz Solver". *AIAA Journal*, 55(4):1205–1220, 2017. ISSN 0001-1452. doi: 10.2514/1.J055248.

[62] J. Gikadi, T. Sattelmayer, and A. Peschiulli. "Effects of the mean flow field on the thermoacoustic stability of aero-engine combustion chambers". In *ASME Turbo Expo 2012: Turbine Technical Conference and Exposition*, pages 1203–1211, Copenhagen, Denmark, 2012. American Society of Mechanical Engineers. doi: 10.1115/GT2012-69612.

[63] A. Kierkegaard, S. Boij, and G. Efraimsson. "Simulations of the scattering of sound waves at a sudden area expansion". *Journal of Sound and Vibration*, 331(5):1068–1083, February 2012. doi: 10.1016/j.jsv.2011.09.011.

[64] A. Albayrak, D. A. Bezgin, and W. Polifke. "Response of a Swirl Flame to Inertial Waves". *Int. J. Spray and Combustion Dynamics*, 10(4):277–286, 2018. ISSN 1756-8277, 1756-8285. doi: 10.1177/1756827717747201.

[65] M. Blanchard, T. Schuller, D. Sipp, and P. J. Schmid. "Response Analysis of a Laminar Premixed M-Flame to Flow Perturbations Using a Linearized Compressible Navier-Stokes Solver". *Physics of Fluids*, 27(4):043602, April 2015. ISSN 1070-6631, 1089-7666. doi: 10.1063/1.4918672.

[66] M. Hoeijmakers, V. Kornilov, I. Lopez Arteaga, P. de Goey, and H. Nijmeijer. "Intrinsic Instability of Flame-Acoustic Coupling". *Combustion and Flame*, 161(11):2860–2867, November 2014. doi: 10.1016/j.combustflame.2014.05.009.

[67] T. Emmert, S. Bomberg, and W. Polifke. "Intrinsic Thermoacoustic Instability of Premixed Flames". *Combustion and Flame*, 162(1):75–85, 2015. ISSN 0010-2180. doi: 10.1016/j.combustflame.2014.06.008.

[68] E. Courtine, L. Selle, and T. Poinsot. “DNS of Intrinsic Thermoacoustic Modes in Laminar Premixed Flames”. *Combustion and Flame*, 162(11):4331–4341, 2015. doi: 10.1016/j.combustflame.2015.07.002.

[69] L. Strobio Chen, S. Bomberg, and W. Polifke. “Propagation and Generation of Acoustic and Entropy Waves Across a Moving Flame Front”. *Combustion and Flame*, 166:170–180, April 2016. doi: 10.1016/j.combustflame.2016.01.015.

[70] M. Yoon. “The entropy wave generation in a heated one-dimensional duct”. *Journal of Fluid Mechanics*, 883:A44, January 2020. ISSN 0022-1120, 1469-7645. doi: 10.1017/jfm.2019.901.

[71] A. P. Dowling. “The Calculation of Thermoacoustic Oscillation”. *Journal of Sound and Vibration*, 180(4):557–581, 1995. doi: 10.1006/jsvi.1995.0100.

List of Figures

Supervised Students

In the frame of this Ph.D. thesis several student theses have been conducted and written under supervision of the author. Some of these were connected to one or multiple topics discussed in this thesis, others were tied to different research topics of the department or were supervised in cooperation with industry. The author would like to express his sincere gratitude towards all the students and appreciates the effort they put into their work.

Student	Thesis/Work packages
Nadin Sarajlic	Bachelor's Thesis Efficient Simulation of Conjugate Heat Transfer based on State-Space Models
Mehdi Hammami	Bachelor's Thesis Hybride numerische Untersuchung des Transferverhaltens von verlustbehafteten Düsen für Akustik und Entropiewellen
Thomas Hofmeister	Term Paper Investigation of uniform heat flux thermal boundary conditions for local heat transfer measurements
Felix Thomann	Term Paper Modellordnungsreduktion von gekoppelten thermoakusitschen Problemen
Isabella Stellwag	Term Paper Process Strategy for Lowering Solvent Degradation in CO2 Capture Systems
Jonas Eichelsdörfer	Term Paper Large Eddy Simulation of Turbulent Pipe Flow (08.19), Zusammenarbeit mit UniBW
Christian Maier	Master's Thesis Development of an algorithm for the optimization of a high-voltage-battery cooling
Lucien Panetta	Master's Thesis Application and modelling of FTM/FTF of kerosene spray flames in low order network models
Moudather Chelbi	Research Assistant Implementation of a Galerkin Least-Squares Finite Element procedure for the Linearized Euler Equations.
Fabian Fritz	Research Assistant Development and testing of the Discontinuous Galerkin Finite Element framework for thermoacoustics in both Comsol Multiphysics and FEniCS. Co-authorship of [22]

Appendices

Acta Acustica united with Acustica
Vol. 102 (2016) 824 – 833
DOI 10.3813/AAA.918997

Linear State Space Interconnect Modeling of Acoustic Systems

Thomas Emmert, Max Meindl, Stefan Jaensch, Wolfgang Polifke
Professur für Thermofluiddynamik, Technische Universität München, 85747 Garching, Germany.
polifke@tfd.mw.tum.de

Summary
Linear, low-order network models, constructed from a set of interconnected acoustic subsystem elements, are an established tool in acoustic analysis. This paper introduces a generalized linear modeling framework for acoustic systems that is based on a state space formalism and linear system theory. It is shown how subsystem models retrieved from 1D low order modeling, 3D linearized perturbation equations as well as computational fluid dynamics or experiment can be translated into state space models. This translation does not involve any approximations beyond those made by the acoustic modeling in the first place. An algorithm to interconnect state space models is presented, which results in a single, joint state space model for the complete acoustic system. The resulting eigenvalue problem is linear, thus eigenvalues and eigenvectors can be determined for small and moderate problem sizes with very little effort, using standard numerical routines. In order to make possible the solution of larger problem sizes, as they result from 3D models, the framework exploits the sparse structure of the models. The methods and algorithms are exemplified and validated using simplistic configurations, but also a generic annular combustor test case with non trivial topology.

PACS no. 43.20.Bi, 43.20.-f, 43.20.Fn, 43.20.Hq, 43.20.Ks, 43.28.Kt, 43.20.Mv, 43.28.Py

1. Introduction

Prediction and optimization of generation, propagation and attenuation of sound as well as aero- or thermoacoustic stability, are important objectives in a wide range of applications such as ventilation systems or gas turbines. Typically such systems are of considerable spatial extent, but involve small scale phenomena such as turbulence or combustion. This causes a need for very detailed models with complex physics in large domains. Therefore the simulation of models derived from first principles is very expensive, even though the propagation of acoustic waves may still be modeled in a linear manner.

A strategy to cope with this modeling complexity due to the multi-scale nature is to divide the entire system into several interconnected parts. Linear models of the acoustic dynamics of the different parts of the system are retrieved using suitable methods according to complexity and physical phenomena involved. In the simplest case, there are low order models assuming 1D plane wave propagation, which may be solved analytically. Such models are either algebraic relations due to acoustically compact discontinuities in area and temperature or (linear) Green's functions of ducts [1, 2]. If the propagation of acoustic waves is not one dimensional, but the mean flow is still unaffected by acoustic perturbations, CAA tools can be used to retrieve acoustic models of the domain. Such tools model the acoustic dynamics by 2D or 3D linearized partial differential equations (e.g. Helmholtz, LEE, APE, LNSE) against the background of a given mean field [3, 4]. In case of two-way interactions between mean flow and acoustic perturbations, a full LES computation or an experiment are needed. In this case, linearized models of the acoustic dynamics may be inferred from time series data by system identification [5] or fitting polynomials to the frequency responses of the system.

The resulting set of interconnected linear models may be called a linear acoustic *network model*. Such network models are well established and have proven to predict the dynamics of acoustic systems. Typically, those models are either coupled in the time domain and solved, in a simultaneous, but segregated manner [6], or in the frequency domain by individual evaluation and multiplicative coupling [7, 8, 9, 10, 11]. In order to compute the stability properties of such models, a nonlinear eigenvalue problem needs to be solved, as the model coefficients depend on frequency.

In this paper we present the application of linear system theory and unified state space modeling to acoustic network systems. The generic state space structure allows to incorporate models of varying modeling depth, such as 1D low order models, as well as models retrieved from linearized PDEs on complex geometries, or even data driven models from LES or experiments. In addition, multi-physics modeling is easily incorporated in the

Received 3 February 2016,
accepted 16 July 2016.

framework by means of e.g. flame transfer functions for combustion processes or active control. As we will show, the state space modeling is numerically very efficient as it is based on matrices with constant, frequency independent coefficients. Therefore, the search for eigenvalues is a standard or generalized linear eigenvalue problem. For small to moderate model sizes, it is possible to directly solve for all eigenvalues. The efficient computation of eigenvalues of large models requires an iterative algorithm. We will demonstrate that it is numerically simpler and much more efficient to solve such a linear eigenvalue problem than the nonlinear eigenvalue problems that result from traditional formulation.

The core concepts are introduced using the example of the 1D scattering matrix of a duct section. Subsequently, we show how all kinds of linear acoustic models can be translated into state space formulation. This translation does not involve any approximation beyond those already made by the linear acoustic modeling.

Based on the unified modeling, we demonstrate a generic algorithm for the interconnection of state space models, which results in a single joint state space model. Similar algorithms are implemented by Matlab and Octave control toolboxes. In contrast to those, our implementation takes advantage of the sparse structure of acoustic models, which makes possible the solution of very large acoustic network systems. The concept is illustrated using a bare bones example of a quarter-wave resonator composed by two duct sections.

As the resulting interconnected network model is again a state space model, the eigenvalues and vectors can be determined by solving a standard or generalized linear eigenvalue problem. We present a memory and time efficient iterative eigenvalue solver based on a direct method for the LU decomposition [14] and an Arnoldi algorithm [15].

Eventually the modeling strategy developed is applied to a cavity problem, where two annular chambers are connected by multiple tubes. This topology is representative of plenum, burners and combustion chamber of a gas turbine. The annuli are modeled using 3D linearized PDEs, whereas the ducts are modeled by a low order 1D model. Results are validated with a CAA model, where the entire system including the ducts is modeled by linearized PDEs, and against results from the literature

All methods and algorithms are publicly available as a (thermo-) acoustic network modeling framework called taX [13].

2. State space modeling

Acoustic network systems are composed of interconnected subsystems, which are often called *elements*. These individual subsystems model internal sources of acoustic waves and how incident waves are transmitted or reflected. Sources of acoustic waves are, for example, aero-acoustic noise due to turbulence [5] or actuators such as loudspeakers.

We are assuming that on the interfaces between the subsystems only plane waves are propagating, whereas inside of the subsystems arbitrary e.g. 3D wave propagation is possible. This assumption is valid if the wave length of the highest frequency of interest is large compared to the diameter of the interface.

The models that describe the scattering of acoustic waves are typically characterized by frequency responses of the scattering matrix or transfer matrix. The scattering matrix relates incident and emitted characteristic wave amplitudes, whereas the transfer matrix relates pressure and velocity perturbation amplitudes at the different interfaces of the system. It is important to note that in system theory one distinguishes the frequency responses from the subsystem models. Frequency responses are not models, but rather the results of the models evaluated at discrete frequencies.

Linear dynamic models are described by a set of ordinary differential equations relating inputs u (e.g. incident acoustic waves) and outputs y (emitted acoustic waves). They are given either by high order one dimensional transfer functions,

$$b_0 y(t) + b_1 \dot{y}(t) + b_2 \ddot{y}(t) + \ldots + b_m \frac{\partial^m y(t)}{\partial t^m} = a_0 u(t) + a_1 \dot{u}(t) + a_2 \ddot{u}(t) + \ldots + a_n \frac{\partial^n u(t)}{\partial t^n}, \quad (1)$$

or as a generic high dimensional first order state space system,

$$\dot{x} = Ax + Bu, \quad (2)$$

$$y = Cx + Du. \quad (3)$$

In the following sections we show how linear acoustic subsystem models (elements) from different sources can be translated into a state space formulation. At first, a minimal, 1D example of plan wave propagation in a duct is provided in order to motivate and introduce the state space models. Following this, we generalize the result to models retrieved from linearized PDEs in 3D. Subsequently, we indicate how state space models may be retrieved from experimental or LES data.

Eventually, an algorithm to compute the eigenvalues of large sparse state space systems is presented.

2.1. State space duct model

Acoustic wave propagation in a duct is in the simplest case governed by a 1D wave equation

$$\frac{1}{c^2}\frac{\partial^2 p'}{\partial t^2} = \frac{\partial^2 p'}{\partial x^2}. \quad (4)$$

The solution can be written as the superposition of characteristic waves,

$$\frac{p'(x,t)}{\rho c} = f\left(t - \frac{x}{c}\right) + g\left(t + \frac{x}{c}\right), \quad u' = f - g. \quad (5)$$

The propagation of the characteristic wave amplitudes f and g is described by an advection equation,

$$\frac{\partial f}{\partial t} = -c\frac{\partial f}{\partial x}, \qquad \frac{\partial g}{\partial t} = c\frac{\partial g}{\partial x}. \quad (6)$$

Acta Acustica united with Acustica
Vol. 102 (2016)

The Laplace transform of the analytic solution of the spatial integral over a duct of length L with non-reflecting boundary conditions is known as the scattering matrix

$$\begin{bmatrix} g_u(s) \\ f_d(s) \end{bmatrix} = \underbrace{\begin{bmatrix} 0 & \mathrm{e}^{-s\tau} \\ \mathrm{e}^{-s\tau} & 0 \end{bmatrix}}_{\text{Scattering matrix } S(s)} \begin{bmatrix} f_u(s) \\ g_d(s) \end{bmatrix}. \tag{7}$$

During time $\tau = L/c$, the waves travel through the duct. The formulation is using the Laplace variable $s = j\omega + \sigma$ with the angular frequency ω and growth rate σ.

Instead of analytically integrating the propagation of the characteristic waves, we can spatially discretize the PDE with a first order upwind scheme to obtain an ordinary differential equation (ODE)

$$\frac{df_j}{dt} = -c\frac{f_j - f_{j-1}}{\Delta x}. \tag{8}$$

For simplicity, we choose $\Delta x = L/4$. With $a \equiv c/\Delta x$ the propagation of f waves in the duct section is described by a system of ODEs

$$\frac{d}{dt}\begin{bmatrix} f_2 \\ f_3 \\ f_4 \\ f_5 \end{bmatrix} = \begin{bmatrix} -a & 0 & 0 & 0 \\ a & -a & 0 & 0 \\ 0 & a & -a & 0 \\ 0 & 0 & a & -a \end{bmatrix}\begin{bmatrix} f_2 \\ f_3 \\ f_4 \\ f_5 \end{bmatrix} + \begin{bmatrix} a \\ 0 \\ 0 \\ 0 \end{bmatrix}\begin{bmatrix} f_u \end{bmatrix}$$
$$\begin{bmatrix} f_d \end{bmatrix} = \begin{bmatrix} 0 & 0 & 0 & 1 \end{bmatrix} x + \begin{bmatrix} 0 \end{bmatrix} f_u. \tag{9}$$

The wave amplitudes f_j at the positions j inside the duct and on its interfaces are collected in a state vector $x = \begin{bmatrix} f_2 & f_3 & f_4 & f_5 \end{bmatrix}^T$. The wave at the left boundary is an input $u = f_u = f_1$ to the system and is not part of the acoustic state, whereas the wave leaving on the right boundary is an output $y = f_d = f_5$ and a state. The same derivation can be done for the g waves. "Stacking" of state vectors (see below) and block diagonal appending of the evolution matrices leads to a generalized state space model

$$\dot{x} = Ax + Bu, \tag{10}$$
$$y = Cx + Du, \tag{11}$$

with inputs $u = \begin{bmatrix} f_u & g_d \end{bmatrix}^T$, outputs $y = \begin{bmatrix} g_u & f_d \end{bmatrix}^T$ and without feed through $D = 0$. Laplace transform is used to solve the model for its scattering matrix $S(s)$

$$y = \underbrace{C(sI - A)^{-1}B}_{S(s)}u, \tag{12}$$

with I the identity matrix.

Figure 2 shows the frequency responses of the analytical (crosses) and the first order upwind (dashed) state space models. In addition, a state space duct model resulting from third order upwind discretization with the same resolution $\Delta x = L/4$ is displayed (circles). We observe that all three models have the same low frequency properties. The damping of the first order upwind model increases for high frequencies, whereas the third order model is matching the analytical model very well within the given frequency range. By increasing the spatial resolution, the discretized models approach the analytical solution for yet higher frequencies.

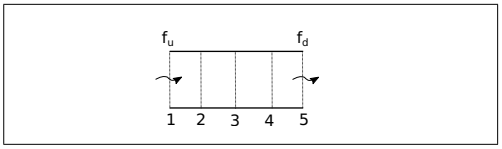

Figure 1. Discretized duct section.

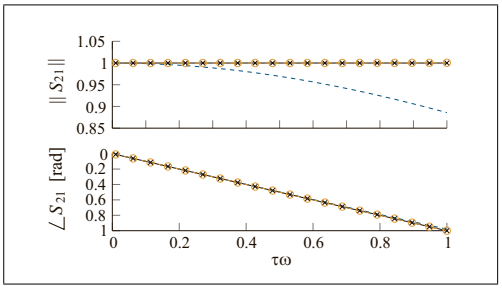

Figure 2. Frequency response of f_u to f_d: First order upwind (dashed), third order upwind (circles) and analytic solution (crosses).

2.2. Generalization to linearized partial differential equations

Instead of modeling acoustic propagation by 1D wave equations as in the previous section, various 2D or 3D linearized PDEs (LEE, LNSE, APE, reactive LNSE) may be considered [9, 3, 4]. This gives the opportunity to incorporate complex geometry, the effects of mean flow, dissipation and even acoustic-vortex interaction with all its advantages and issues [16]. As demonstrated above, the partial differential equation may be spatially discretized using a finite volume or finite element method, which results in a system of ordinary differential equations. On the interfaces, boundary conditions need to be implemented, which excite and receive plane waves. This is achieved by averaging across the surface of the interface and to excite for instance either p' or the incident wave and to measure the remaining free variable u' or the outgoing wave. Depending on the discretization scheme, the translation to state space formulation may require a so called mass or descriptor matrix E,

$$E\dot{x} = Ax + Bu,$$
$$y = Cx + Du. \tag{13}$$

Note that this translation to state space formulation is achieved by merely a rearrangement of the system of equations. Most notably it does not introduce any approximations other than the ones made by choosing the type of PDE and the discretization scheme.

As the relation between the states x and the field variables on the computational grid are known, the state vector of such models may be interpreted physically and visualized.

The procedure of defining the perturbation equations, geometry, boundary conditions, grid and discretization

scheme may be supported by tools such as freeFEM or COMSOL Multiphysics. COMSOL is facilitating the process by providing a default set of LEE and LNSE equations, as well as an export interface to directly obtain the state space matrices A, B, C, D, E.

Note that there are alternative methods to create state space systems from the eigenmodes of a linearized field system [17, 18]. However this method is a reduced order approximation of the original field based system, whereas the direct method presented above is not.

2.3. Application to experimental and LES data

Instead of deriving acoustic models directly from linearized PDEs, they may be given in the form of scattering or transfer matrices. Such models may for instance be derived from experiment using the multi-microphone method. Typically harmonic excitation is used and the time series of acoustic waves up- and downstream of the system are measured. Subsequently, polynomials are fitted to the measured frequency response [11].

When carrying out LES computations, it is more convenient to excite the system with broadband acoustic perturbations, as this reduces the necessary computational time compared to harmonic forcing [5]. Discrete time models are inferred by system identification from the input and output time series of the system. Eventually, the discrete time models can be transformed to continuous time.

For a system with two interfaces (upstream, downstream) this is expressed by either the scattering matrix S or the transfer matrix T

$$\begin{bmatrix} g_u(s) \\ f_d(s) \end{bmatrix} = \begin{bmatrix} S_{11}(s) & S_{12}(s) \\ S_{21}(s) & S_{22}(s) \end{bmatrix} \begin{bmatrix} f_u(s) \\ g_d(s) \end{bmatrix}, \tag{14}$$

$$\begin{bmatrix} p'_u(s) \\ u'_u(s) \end{bmatrix} = \begin{bmatrix} T_{11}(s) & T_{12}(s) \\ T_{21}(s) & T_{22}(s) \end{bmatrix} \begin{bmatrix} p'_d(s) \\ u'_d(s) \end{bmatrix}. \tag{15}$$

In this case, the transfer functions $G = S_{ij}, T_{ij}$ between either incident, emitted waves or pressure, velocity perturbations at the interfaces of the system are known. In general, each transfer function $G(s)$ may be represented as a rational polynomial in s, which relates the corresponding input variable u and the output y,

$$y(s) = G(s)u(s), \tag{16}$$

$$G(s) = \frac{b_n s^n + \ldots + b_1 s + b_0}{s^m + a_{m-1}s^{m-1} + \ldots + a_1 s + a_0}, \tag{17}$$

and corresponds to a linear differential equation in time,

$$\frac{d^m y(t)}{dt^m} + a_{m-1}\frac{d^{m-1} y(t)}{dt^{m-1}} + \ldots + a_1 \dot{y}(t) + a_0 y(t) = b_n \frac{d^n u(t)}{dt^n} + \ldots + b_1 \dot{u}(t) + b_0 u(t). \tag{18}$$

All transfer functions $G(s)$ can be translated into state space models, see Equation (25) in [19] or Lunze [20]:

$$\dot{x} = \begin{bmatrix} 0 & 1 & & \\ & \ddots & \ddots & \\ & & 0 & 1 \\ -a_0 & -a_1 & \ldots & -a_{m-1} \end{bmatrix} x + \begin{bmatrix} 0 \\ \vdots \\ 0 \\ 1 \end{bmatrix} u, \tag{19}$$

$$y = \begin{bmatrix} b_0 - b_n a_0, & b_1 - b_n a_1, & \ldots, & b_{n-1} - b_n a_{m-1} \end{bmatrix} x + b_n u.$$

However, compared with the linearized PDE based models, these state space models do not establish a direct relation between acoustic perturbations inside the domain and the state x of the model. Therefore, the state vector of such models cannot be physically interpreted or visualized.

3. Interconnection of state space models

Network models for duct acoustics are constructed by interconnecting a set of sub-system models, which represent various model elements. In the state-space framework, such interconnect algorithms are provided by the control toolboxes of Matlab and Octave. Both are based on full matrices, which restricts them to small systems due to memory restrictions. Therefore we have re-implemented the interconnect functionality, which will be described in the following, in a sparse state space toolbox. This toolbox, which is part of taX [13], exploits the sparse structure of acoustic network systems and allows the efficient solution of very large systems with $\mathcal{O}(10^5)$ degrees of freedom on standard personal computer [12].

The interconnection of a set of state space systems is achieved in three steps: At first all subsystems are appended, then the interconnections are evaluated and a feedback equation is formulated. Finally, the feedback equation is eliminated and a joint state space model of the interconnected sub-systems is retrieved.

3.1. Appending of SS models

State space systems are appended by the block diagonal collection of the system matrices A_i, B_i, C_i, D_i, E_i of each of the state space models $i = 1, 2, \ldots, n$. Exemplary for $\tilde{A}$,

$$\tilde{A} = \begin{bmatrix} A_1 & 0 & 0 & 0 \\ 0 & A_2 & 0 & 0 \\ 0 & 0 & \ddots & 0 \\ 0 & 0 & 0 & A_n \end{bmatrix}. \tag{20}$$

This implies that the state vectors and the input and output vectors of the sub-systems are stacked on top of each other to form the corresponding vectors of the interconnected system,

$$x = \begin{bmatrix} x_1 \\ x_2 \\ \vdots \\ x_n \end{bmatrix}, \quad \tilde{u} = \begin{bmatrix} u_1 \\ u_2 \\ \vdots \\ u_n \end{bmatrix}, \quad \tilde{y} = \begin{bmatrix} y_1 \\ y_2 \\ \vdots \\ y_n \end{bmatrix}. \tag{21}$$

ACTA ACUSTICA UNITED WITH ACUSTICA
Vol. 102 (2016)

3.2. Evaluation of feedback

The input of the appended system $\tilde{u}$ consists of true external inputs u and internal feedbacks $\tilde{y}$. External inputs of the connected system are for example internal sources of acoustic waves such as noise or loudspeakers or perturbations at plane wave interfaces that are not connected internally. The latter case applies if the network system is not terminated at all ends, but left open. The internal feedbacks are due to the plane wave connections between the appended models. For example, waves that are leaving one subsystem model $\tilde{y}_j$ may enter another subsystem $\tilde{u}_k$. This is expressed by a feedback matrix F that contains binary $(0, 1)$ entries corresponding to the topology of the network.

$$\tilde{u} = F\tilde{y} + u. \tag{22}$$

The modelling package taX [13] retrieves the feedback matrix by evaluating the names that are assigned to the inputs and outputs of the system elements.

3.3. Solve for the connected SS model

Using the feedback equation (22), the connected system is expressed by

$$\tilde{E}\dot{x} = \tilde{A}x + \tilde{B}\tilde{u}, \tag{23}$$
$$\tilde{y} = \tilde{C}x + \tilde{D}\tilde{u}, \tag{24}$$
$$\tilde{u} = F\tilde{y} + u. \tag{25}$$

In order to obtain a state space model with the generic structure as in Equation (13), the feedback equation needs to be eliminated. This is achieved by replacing $\tilde{y}$ in the feedback equation (25) using the output equation (24) and then solve for $\tilde{u}$

$$\tilde{u} = (1 - F\tilde{D})^{-1}F\tilde{C}x + (1 - F\tilde{D})^{-1}u. \tag{26}$$

Subsequently $\tilde{u}$ can be eliminated in the system equation (23) and the output equation (24) and the state space system matrices of the connected system are

$$\begin{aligned} A &= \tilde{A} + \tilde{B}(1 - F\tilde{D})^{-1}F\tilde{C}, \\ B &= \tilde{B}(1 - F\tilde{D})^{-1}, \\ C &= \tilde{C} + \tilde{D}(1 - F\tilde{D})^{-1}F\tilde{C}, \\ D &= \tilde{D}(1 - F\tilde{D})^{-1}, \quad E = \tilde{E}. \end{aligned} \tag{27}$$

Eventually, the internally connected outputs in $\tilde{y}$ can be eliminated, and only the relevant outputs y are retained. Thus the interconnected state space model has the generic form shown in Equation (13).

3.4. Invertibility of feedback

Evaluating the feedback needs an inversion of $1-F\tilde{D}$. This operation is typically very cheap as both F and $\tilde{D}$ are very sparse. In fact $F\tilde{D}$ has non zero entries only where a feed through ($\tilde{D}$) is internally connected. Such a feed through occurs in low order models of acoustically compact elements. Examples are duct singularities such as discontinuities in area or temperature, and plane wave boundary interfaces defined in primitive acoustic variables u', p'.

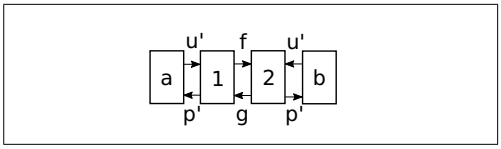

Figure 3. Interconnection of incompatible system interfaces (a,b) by Connectors (1,2).

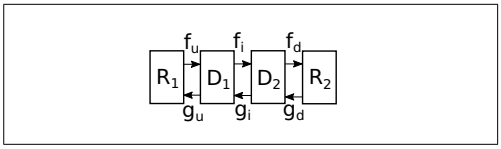

Figure 4. Interconnection of two duct sections and two reflective ends.

There are rare cases when the inversion is not possible. This happens if there is a connection between two interfaces, which implicitly connects two inputs. If both systems (a,b) have for example u' as an output and p' as an input, it is not possible to connect them directly. However, it is possible to convert the interface to wave amplitudes f, g on both sides, and subsequently connect the two systems as shown in Figure 3.

The connectors (1,2) represent algebraic relations, so-called "feed through" between inputs and outputs,

$$\begin{bmatrix} f \\ p' \end{bmatrix} = \begin{bmatrix} 1 & 1 \\ 2 & 1 \end{bmatrix} \begin{bmatrix} g \\ u' \end{bmatrix}, \quad \begin{bmatrix} g \\ p' \end{bmatrix} = \begin{bmatrix} 1 & -1 \\ 2 & -1 \end{bmatrix} \begin{bmatrix} f \\ u' \end{bmatrix}. \tag{28}$$

The connection of the converted interfaces leads to an algebraic equation linking two inputs ($p'_a = p'_b$), which results in a rank deficiency of $1 - F\tilde{D}$. The solution to this is to append the feed back equation (26) to the system equation (23), instead of inverting it. Then the state vector becomes $\tilde{x} = \begin{bmatrix} x & \tilde{u} \end{bmatrix}^T$ and the resulting system matrices are

$$\begin{aligned} A &= \begin{bmatrix} \tilde{A} & \tilde{B} \\ F\tilde{C} & F\tilde{D} - I \end{bmatrix}, \quad B = \begin{bmatrix} 0 \\ I \end{bmatrix}, \\ C &= \begin{bmatrix} \tilde{C} & \tilde{D} \end{bmatrix}, \quad D = \begin{bmatrix} 0 \end{bmatrix}, \quad E = \begin{bmatrix} \tilde{E} & 0 \\ 0 & 0 \end{bmatrix}. \end{aligned} \tag{29}$$

4. A bare bones example

This section explicates and illustrates by way of example the algorithm to connect several state space sub-models into a joint state space system model.

A simplistic configuration is selected: two identical duct sections of length $L' = L/2$ (see section 2.1) are terminated by a closed end ($R_1 = 1$) upstream and an open end ($R_2 = -1$) downstream boundary condition, as depicted in Figure 4. Both the frequency domain and the state space formulations will be presented.

4.1. Frequency domain interconnection

The analytic solution for the scattering matrices of the two duct sections are according to Equation (7)

$$\begin{bmatrix} g_u(s) \\ f_i(s) \end{bmatrix} = \begin{bmatrix} 0 & \mathrm{e}^{-s\tau} \\ \mathrm{e}^{-s\tau} & 0 \end{bmatrix} \begin{bmatrix} f_u(s) \\ g_i(s) \end{bmatrix}, \tag{30}$$

$$\begin{bmatrix} g_i(s) \\ f_d(s) \end{bmatrix} = \begin{bmatrix} 0 & \mathrm{e}^{-s\tau} \\ \mathrm{e}^{-s\tau} & 0 \end{bmatrix} \begin{bmatrix} f_i(s) \\ g_d(s) \end{bmatrix}, \tag{31}$$

with $\tau = L/(2c)$. The reflection coefficients $R_1 = 1$ and $R_2 = -1$ imply that

$$f_u = g_u, \quad g_d = -f_d. \tag{32}$$

By appending all the scattering matrices and reflection coefficients, we obtain a multiple input, multiple output system of open loop transfer functions,

$$\begin{bmatrix} f_u \\ g_u \\ f_i \\ g_i \\ f_d \\ g_d \end{bmatrix} = \underbrace{\begin{bmatrix} 0 & 1 & 0 & 0 & 0 & 0 \\ 0 & 0 & 0 & \mathrm{e}^{-s\tau} & 0 & 0 \\ \mathrm{e}^{-s\tau} & 0 & 0 & 0 & 0 & 0 \\ 0 & 0 & 0 & 0 & 0 & \mathrm{e}^{-s\tau} \\ 0 & 0 & \mathrm{e}^{-s\tau} & 0 & 0 & 0 \\ 0 & 0 & 0 & 0 & -1 & 0 \end{bmatrix}}_{G(s)} \begin{bmatrix} f_u \\ g_u \\ f_i \\ g_i \\ f_d \\ g_d \end{bmatrix}. \tag{33}$$

The system is closed on the left hand side by subtracting the matrix of transfer functions from unity,

$$\begin{bmatrix} 1 & -1 & 0 & 0 & 0 & 0 \\ 0 & 1 & 0 & -\mathrm{e}^{-s\tau} & 0 & 0 \\ -\mathrm{e}^{-s\tau} & 0 & 1 & 0 & 0 & 0 \\ 0 & 0 & 0 & 1 & 0 & -\mathrm{e}^{-s\tau} \\ 0 & 0 & -\mathrm{e}^{-s\tau} & 0 & 1 & 0 \\ 0 & 0 & 0 & 0 & 1 & 1 \end{bmatrix} \begin{bmatrix} f_u \\ g_u \\ f_i \\ g_i \\ f_d \\ g_d \end{bmatrix} = I - G(s) = 0. \tag{34}$$

Note that this is a generalized, *nonlinear* eigenvalue problem, because the coefficients of the matrix G depend on the eigenvalue s.

Non trivial solutions for f_x, g_x exist if the resulting closed loop transfer function matrix is rank deficient. Values s that lead to rank deficiency are eigenvalues of the system,

$$\det\left(I - G(s)\right) = 0. \tag{35}$$

The characteristic equation of the system is also called dispersion relation,

$$1 + \mathrm{e}^{4s\tau} = 0. \tag{36}$$

Using the definition of the Laplace variable $s = \mathrm{j}\omega + \sigma$, we can solve for the real and imaginary part independently:

$$1 + \cos(\omega 4\tau)\mathrm{e}^{\sigma 4\tau} = 0, \quad \sin(\omega 4\tau)\mathrm{e}^{\sigma 4\tau} = 0. \tag{37}$$

According to the first condition, the system is a quarter wave resonator $\omega_n/(2\pi) = (n + 1/2)/(4\tau) = (1/4 + n/2)c/l$ with $\sigma_n = 0$ for all whole numbers $n = 0, 1, 2, \ldots$. The second equation does not impose further restrictions as $\omega_n/2\pi = (n/2)/(4\tau)$ is part of the first condition.

It is important to note that in general it is not possible to directly solve for the eigenvalues analytically. In this case, a nonlinear eigenvalue would need to be solved, which is even for moderately small systems a numerically expensive operation.

4.2. Interconnection of SS models

Now the interconnection of state space models is considered. The coefficients of the f-wave propagation of the two discretized duct section state space models are identical,

$$\frac{d}{dt}\begin{bmatrix} f_2 \\ f_3 \end{bmatrix} = \begin{bmatrix} -a & 0 \\ a & -a \end{bmatrix}\begin{bmatrix} f_2 \\ f_3 \end{bmatrix} + \begin{bmatrix} a \\ 0 \end{bmatrix}\begin{bmatrix} f_u \end{bmatrix}, \tag{38}$$

$$\begin{bmatrix} f_i \end{bmatrix} = \begin{bmatrix} 0 & 1 \end{bmatrix}\begin{bmatrix} f_2 \\ f_3 \end{bmatrix} + \begin{bmatrix} 0 \end{bmatrix}\begin{bmatrix} f_u \end{bmatrix}, \tag{39}$$

$$\frac{d}{dt}\begin{bmatrix} f_4 \\ f_5 \end{bmatrix} = \begin{bmatrix} -a & 0 \\ a & -a \end{bmatrix}\begin{bmatrix} f_4 \\ f_5 \end{bmatrix} + \begin{bmatrix} a \\ 0 \end{bmatrix}\begin{bmatrix} f_i \end{bmatrix}, \tag{40}$$

$$\begin{bmatrix} f_d \end{bmatrix} = \begin{bmatrix} 0 & 1 \end{bmatrix}\begin{bmatrix} f_4 \\ f_5 \end{bmatrix} + \begin{bmatrix} 0 \end{bmatrix}\begin{bmatrix} f_i \end{bmatrix}, \tag{41}$$

just as the coefficients for the g-waves:

$$\frac{d}{dt}\begin{bmatrix} g_1 \\ g_2 \end{bmatrix} = \begin{bmatrix} a & -a \\ 0 & a \end{bmatrix}\begin{bmatrix} g_1 \\ g_2 \end{bmatrix} + \begin{bmatrix} 0 \\ -a \end{bmatrix}\begin{bmatrix} g_i \end{bmatrix}, \tag{42}$$

$$\begin{bmatrix} g_u \end{bmatrix} = \begin{bmatrix} 1 & 0 \end{bmatrix}\begin{bmatrix} g_1 \\ g_2 \end{bmatrix} + \begin{bmatrix} 0 \end{bmatrix}\begin{bmatrix} g_i \end{bmatrix}, \tag{43}$$

$$\frac{d}{dt}\begin{bmatrix} g_3 \\ g_4 \end{bmatrix} = \begin{bmatrix} a & -a \\ 0 & a \end{bmatrix}\begin{bmatrix} g_3 \\ g_4 \end{bmatrix} + \begin{bmatrix} 0 \\ -a \end{bmatrix}\begin{bmatrix} g_d \end{bmatrix}, \tag{44}$$

$$\begin{bmatrix} g_i \end{bmatrix} = \begin{bmatrix} 1 & 0 \end{bmatrix}\begin{bmatrix} g_3 \\ g_4 \end{bmatrix} + \begin{bmatrix} 0 \end{bmatrix}\begin{bmatrix} g_d \end{bmatrix}. \tag{45}$$

Due to the numbering scheme, the acoustic states on the interfaces correspond to: $f_u = f_1$, $g_u = g_1$, $f_i = f_3$, $g_i = g_3$,$f_d = f_5$, $g_d = g_5$. States 2, 4 are internal states of duct D_1 respectively D_2. In addition to that, the boundaries are just feed-through conditions,

$$\begin{bmatrix} f_u \end{bmatrix} = \begin{bmatrix} 1 \end{bmatrix}\begin{bmatrix} g_u \end{bmatrix}, \quad \begin{bmatrix} g_d \end{bmatrix} = \begin{bmatrix} -1 \end{bmatrix}\begin{bmatrix} f_d \end{bmatrix}. \tag{46}$$

We can block diagonally append the systems

$$\tilde{A} = \begin{bmatrix} -a & 0 & 0 & 0 & 0 & 0 & 0 & 0 \\ a & -a & 0 & 0 & 0 & 0 & 0 & 0 \\ 0 & 0 & -a & 0 & 0 & 0 & 0 & 0 \\ 0 & 0 & a & -a & 0 & 0 & 0 & 0 \\ 0 & 0 & 0 & 0 & a & -a & 0 & 0 \\ 0 & 0 & 0 & 0 & 0 & a & 0 & 0 \\ 0 & 0 & 0 & 0 & 0 & 0 & a & -a \\ 0 & 0 & 0 & 0 & 0 & 0 & 0 & a \end{bmatrix}, \; x = \begin{bmatrix} f_2 \\ f_3 \\ f_4 \\ f_5 \\ g_1 \\ g_2 \\ g_3 \\ g_4 \end{bmatrix}, \tag{47}$$

Acta Acustica united with Acustica
Vol. 102 (2016)

$$\tilde{B} = \begin{bmatrix} a & 0 & 0 & 0 & 0 & 0 \\ 0 & 0 & 0 & 0 & 0 & 0 \\ 0 & a & 0 & 0 & 0 & 0 \\ 0 & 0 & 0 & 0 & 0 & 0 \\ 0 & 0 & 0 & 0 & 0 & 0 \\ 0 & 0 & 0 & 0 & -a & 0 \\ 0 & 0 & 0 & 0 & 0 & 0 \\ 0 & 0 & 0 & 0 & 0 & -a \end{bmatrix}, \quad \tilde{u} = \begin{bmatrix} f_u \\ f_i \\ f_d \\ g_u \\ g_i \\ g_d \end{bmatrix}, \tag{48}$$

$$\tilde{C} = \begin{bmatrix} 0 & 0 & 0 & 0 & 0 & 0 & 0 & 0 \\ 0 & 1 & 0 & 0 & 0 & 0 & 0 & 0 \\ 0 & 0 & 0 & 1 & 0 & 0 & 0 & 0 \\ 0 & 0 & 0 & 0 & 1 & 0 & 0 & 0 \\ 0 & 0 & 0 & 0 & 0 & 0 & 1 & 0 \\ 0 & 0 & 0 & 0 & 0 & 0 & 0 & 0 \end{bmatrix}, \quad \tilde{y} = \begin{bmatrix} f_u \\ f_i \\ f_d \\ g_u \\ g_i \\ g_d \end{bmatrix}, \tag{49}$$

$$\tilde{D} = \begin{bmatrix} 0 & 0 & 0 & 1 & 0 & 0 \\ 0 & 0 & 0 & 0 & 0 & 0 \\ 0 & 0 & 0 & 0 & 0 & 0 \\ 0 & 0 & 0 & 0 & 0 & 0 \\ 0 & 0 & 0 & 0 & 0 & 0 \\ 0 & 0 & -1 & 0 & 0 & 0 \end{bmatrix}. \tag{50}$$

Eventually, the system is closed by the feedback equation (22):

$$\tilde{u} = \begin{bmatrix} 1 & 0 & 0 & 0 & 0 & 0 \\ 0 & 1 & 0 & 0 & 0 & 0 \\ 0 & 0 & 1 & 0 & 0 & 0 \\ 0 & 0 & 0 & 1 & 0 & 0 \\ 0 & 0 & 0 & 0 & 1 & 0 \\ 0 & 0 & 0 & 0 & 0 & 1 \end{bmatrix} y + \begin{bmatrix} 0 \end{bmatrix} u. \tag{51}$$

Due to the arrangement of $\tilde{u}$ and $\tilde{y}$, the feedback matrix F is unity in this particular case. It is an autonomous system, therefore there are no remaining external in- or outputs u, y. Subsequently, the feedback equation is solved as given by Equation (26) and the system matrix is retrieved from Equation (27):

$$A = \begin{bmatrix} -a & 0 & 0 & 0 & a & 0 & 0 & 0 \\ a & -a & 0 & 0 & 0 & 0 & 0 & 0 \\ 0 & a & -a & 0 & 0 & 0 & 0 & 0 \\ 0 & 0 & a & -a & 0 & 0 & 0 & 0 \\ 0 & 0 & 0 & 0 & a & -a & 0 & 0 \\ 0 & 0 & 0 & 0 & 0 & a & -a & 0 \\ 0 & 0 & 0 & 0 & 0 & 0 & a & -a \\ 0 & 0 & 0 & a & 0 & 0 & 0 & a \end{bmatrix}. \tag{52}$$

The interconnected system of this simplistic example is of order $n = 8$. We are using the same duct resolution as in section 2.1, therefore the upper left 4x4 sub matrix, which is modeling the f wave dynamics, is identical to Equation (9).

We emphasize that the coefficients of the matrix A do not depend on the eigenvalues of the problem, i.e. we have a standard *linear* eigenvalue problem. The determination of eigenvalues and eigenvectors is much easier than for the nonlinear eigenvalue problem Equation (35) that results from the frequency domain formulation. This is discussed in the next section,

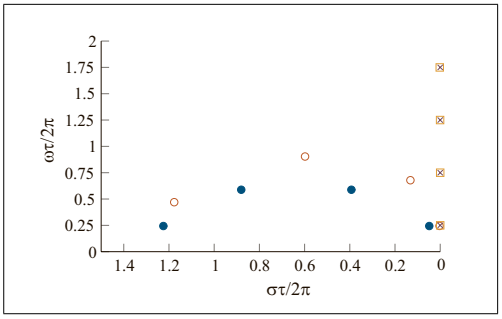

Figure 5. Eigenvalues of the bare bones example system. Analytic solution (crosses), first order upwind n=8 (filled circles), third order upwind n=8 (circles) and high resolution third order upwind n=80 (squares).

5. Computation of eigenvalues

The eigenvalues and eigenvectors of a state space system are computed by Laplace transformation of the system equation (13). Depending on whether $E = I$ or not, a standard or generalized eigenvalue problem

$$sEx = Ax \tag{53}$$

needs to be solved.

For small and moderate problem sizes of order $n < \mathcal{O}(10^3)$ standard MATLAB routines can be employed for this purpose. As an example, we compute eigenfrequencies of the quarter-wave resonator considered in the previous section, with the first order upwind scheme $n = 8$ (see sub-section 4.2), a third order upwind of the same order, and a high resolution third order upwind $n = 80$, respectively. Results for the first four eigenmodes are compared against the analytical solution (crosses in Figure 5).

The first quarter-wave eigenvalue is approximated fairly well by all three state space systems. Whereas the highly resolved system (squares) matches all four eigenvalues in the given frequency range, the two systems of order $n = 8$ (filled circles, circles) exhibit highly damped modes. This corresponds well to the general behavior of the state space models in the frequency response plots of the duct section let alone as shown in Figure 2, where the gain decreases at high frequencies. The most important feature of the discretization scheme is that it is conservative in the sense that the resulting models are stable for analytically marginally stable systems.

For large systems such as the annular combustor example presented in the next section, eigenvalues and eigenvectors are determined with the shift and invert method in combination with an Arnoldi algorithm. It involves an LU decomposition of the matrix pencil $A - s_o E$ at a shift frequency s_o. As this decomposition involves only constant coefficients, it needs to be performed only once. This is a fundamental difference compared to other acoustic network codes, where the system matrices are functions of the frequency. Subsequently the implicitly restarted Arnoldi

method (IRAM) is executed using ARPACK [15] in order to retrieve eigenvalues and vectors close the the shift frequency. The LU decomposition is the bottleneck of the computation. Therefore we perform this decomposition using the MUMPS algorithm [14], which is very efficient for large sparse systems that result from the FEM discretization of linearized PDEs.

6. Eigenmodes of an annular combustor

In order to demonstrate the functionality and effectiveness of the connection algorithm, we consider an annular combustor geometry which was previously investigated by Evesque *et al.* [9]. The system is shown in Figure 6 and consists of an annular plenum (P) and combustion chamber (C), which are connected by 12 burner tubes (B).

The geometrical parameters of the system are listed in Table I. The plenum and combustion chamber have equal middle radii R and widths δ. For the purpose of comparability with the work of Evesque *et al.* [9], we consider a cold case of the combustion system, where there is no reaction or temperature gradients in the field. Furthermore, low Mach number is assumed and mean flow is neglected.

Evesque *et al.* [9] have investigated this configuration with two different types of models. One was a classical frequency domain low order network code and the other a FEM code which discretized the linearized acoustic equations on the full geometry. Here we will refer only to the results of the full linearized FEM computations.

In addition to this reference, we will investigate the system with two different models. The first model discretizes the entire system using linearized Navier-Stokes equations (LNSE) and a FEM scheme built with the commercial tool Comsol[1]. Thus it is basically reproducing the reference case of Evesque with higher resolution. Especially the duct sections need to be highly refined in order to avoid numerical issues in this area. The total order of the full system is $n = 152547$.

The second model discretizes just the plenum and combustion chamber in Comsol and uses a 1D third order upwind scheme as introduced in the minimal example for the tubes. This corresponds to the hybrid method of Campa and Camporeale [23], who combined a high order FEM model with low order transfer matrix models. The length of the tubes is $L = 0.13\,\mathrm{m}$, speed of sound $c = 350\,\mathrm{m/s}$ and the maximum frequency of interest is up to $f = 400\,\mathrm{Hz}$. Therefore, the non-dimensionalized frequency $\tau\omega = 2\pi f L/c = 0.93$ is within the range where the model is performing well (circles in Figure 2).

The state space system matrices (A,B,C,D,E) of the plenum and combustion chamber sub-models are exported from Comsol. Subsequently input and output names of the subsystems may either be manually assigned or the system is assembled using the graphical interface of the taX package [13], as shown in Figure 7.

[1] https://www.comsol.de/

Table I. Geometrical parameters of the combustor in [m].

l_P	l_B	l_C	$R_{P,C}$	$\delta_{P,C}$	r_B
0.1	0.13	0.35	0.22	0.12	0.03

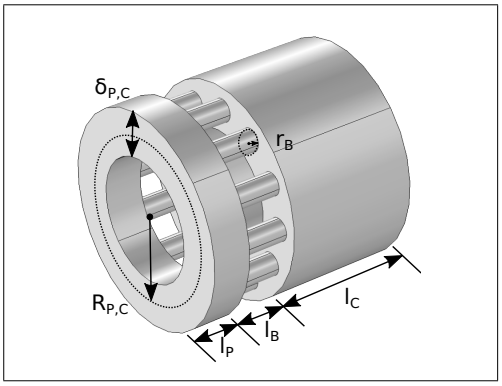

Figure 6. Geometry of the annular combustion system.

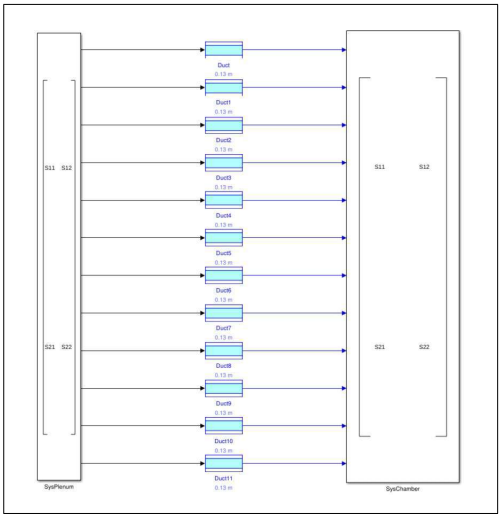

Figure 7. Screenshot of the taX Simulink gui.

Finally all 12 duct models of the tubes and the plenum and combustion chamber models are connected with the algorithm presented in the previous section. The total order of the connected system is $n = 136702$, which is approximately 90% of the full model.

Table II shows the first four physical eigenvalues of the full model, which was entirely computed in Comsol ("Full"), the eigenvalues computed by the connected system ("Connected") and the eigenvalues reported by [9] ("Evesque"). We can see that there is very good agreement between the three computational models. However, it appears that the connected model and the Evesque FEM

ACTA ACUSTICA UNITED WITH ACUSTICA
Vol. 102 (2016)

Table II. Eigenfrequency of the first four eigenmodes.

	Full	Connected	Evesque [9]
1. Mode	139.3	144.6	≈ 143
2. Mode	274.8	276.7	≈ 278
3. Mode	274.8	277.0	≈ 278
4. Mode	293.2	305.6	≈ 305

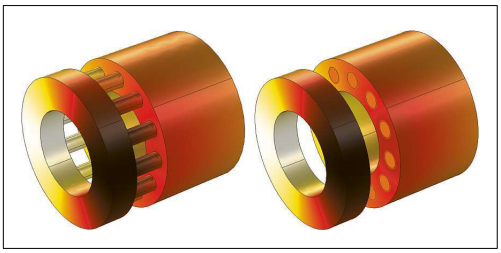

Figure 8. Pressure fields of the second acoustic eigenmode of the full system (left) and connected system (right).

model are matching better than the highly resolved full FEM model. We attribute this to modeling errors respectively the coarser mesh of the computations by Evesque *et al.* [9].

The mode shapes of the second mode of the "Full" and "Connected" models are shown in Figure 8. As the tube sections are not part of the Comsol mesh in the connected model, only the plenum and combustion chamber are shown there. The mode shapes show very good agreement and we conclude that the connection algorithm is working well for state space models retrieved from linearized PDEs.

Note that the computation of five eigenvalues around one shift frequency for the "Connected" annular combustor model of order $n = 10e5$ takes about 38 s and 1.5 GB of RAM on a PC workstation. The MATLAB eigs() command is more than 6.5 times slower (248 s) and needs 4.3 times more RAM (6.5 GB). The same computation for the "Full" model takes about 180 s and 4.2 GB of RAM, whereas the MATLAB eigs() command takes more than 28 GB and runs out of memory after 15 minutes.

For models of this size, the solution of the nonlinear eigenvalue problem corresponding to Equation (35) that results from a frequency domain formulation is orders of magnitudes more expensive [12].

7. Conclusion

The methods presented in this paper allow for a unified state space modeling of acoustic systems. This applies to models retrieved from analytical low order derivations, from linearized partial differential equations for aero-acoustic field variables and also from experimental or LES data. The respective translation to a generic state space formulation does not invoke any approximations beyond those introduced by the acoustic modeling in the first place. This distinguishes the procedure from methods that retrieve state space models from modal reduction techniques [11].

There is a generic algorithm to connect networks of interconnected state space models that results in one joint state space model of the interconnected system.

Due to the unified state space formulation, we can compute the eigenvalues and vectors of acoustic network models very efficiently by solving a standard or generalized linear eigenvalue problem. If one exploits the sparse structure of linear acoustic network models and an iterative eigenvalue solver, solving even very large models is entirely feasible.

Therefore, we can determine stability, optimize using adjoint eigenvectors, carry out parameter studies or perform uncertainty quantification. Furthermore, power spectral density of noise emissions and acoustic wave scattering dynamics can be evaluated directly, without sampling, in frequency domain. At the same time, the simulation in time domain is possible, which is necessary for nonlinear simulations. For example limit cycles of a combustion test rig can be simulated by coupling a linear acoustic network model with an incompressible LES of the flame [22].

There are still some areas for improvements of this state space acoustic network modeling framework. Instead of appending all inputs to the state vector if the feedback is not entirely invertible, it would be better to partially invert the feedback and append only those inputs that may not be inverted. On behalf of the interfaces between subsystems it would be possible to resolve non-planar waves. Such higher order interfaces would enable to divide domains into subsystems even if there are no acoustically compact regions for placing a planar-wave interface. Furthermore, multi physics systems can be easily included. For example, flame transfer functions or active flow control can be incorporated into the interconnected state space model [12] without essential difficulty. The latter may be connected directly by means of a sensor and actor model and a state space controller.

Acknowledgment

Financial support for S. Jaensch by the Research Association for Combustion Engines (Forschungsvereinigung Verbrennung e.V - FVV, project: 6011150) is gratefully acknowledged. We also thank A. Castagnotto, M. Cruz and B. Lohmann for the fruitful cooperation in developing the sparse state space toolbox.

References

[1] M. L. Munjal: Acoustics of Ducts and Mufflers. John Wiley & Sons, 1986.

[2] S. W. Rienstra, A. Hirschberg: An Introduction to Acoustics. Tech. Rept. IWDE 92-06, Eindhoven University of Technology, 2006.

[3] F. Nicoud, L. Benoit, C. Sensiau, T. Poinsot: Acoustic modes in combustors with complex impedances and multidimensional active flames. AIAA J. **45** (2007) 426–441.

[4] G. Campa, S. M. Camporeale: Prediction of the Thermoacoustic Combustion Instabilities in Practical Annular Com-

bustors. J. of Eng. for Gas Turbines and Power **136** (2014) 091504–091504.

[5] C. Sovardi, S. Jaensch, W. Polifke: Concurrent Identification of Aero-acoustic Scattering and Noise Sources at a Flow Duct Singularity in low Mach Number Flow. J. Sound Vib. **377**, (2015) 90-105.

[6] J. Li, A. S. Morgans: Time domain simulations of nonlinear thermoacoustic behaviour in a simple combustor using a wave-based approach. J. Sound Vib. **346** (Juni 2015) 345–360.

[7] J. J. Keller: Thermoacoustic Oscillations in Combustion Chambers of Gas Turbines. AIAA J. **33** (1995) 2280–2287.

[8] A. P. Dowling: The calculation of thermoacoustic oscillation. J. Sound Vib. **180** (1995) 557–581.

[9] S. Evesque, W. Polifke: Low-Order Acoustic Modelling for Annular Combustors: Validation and Inclusion of Modal Coupling. Int'l Gas Turbine and Aeroengine Congress & Exposition, ASME **GT-2002-30064** Amsterdam, NL, (2002).

[10] T. Elnady, M. Åbom: SIDLAB: New 1D sound propagation simulation software for complex duct networks. 13th Int'l Congress on Sound and Vibration (ICSV13), 2006, 4262–4269.

[11] M. Bothien, J. Moeck, A. Lacarelle, C. O. Paschereit: Time domain modelling and stability analysis of complex thermoacoustic systems. Proc. Inst. Mech. Eng. Part J. Power Energy **221** (Jan. 2007) 657–668.

[12] M. Meindl, T. Emmert, W. Polifke: Efficient calculation of thermoacoustic modes utilizing state-space models. 23rd Int'l Congress on Sound and Vibration, ICSV23, Athens, Greece, July 11-14 2016 IIAV

[13] Professur für Thermofluiddynamik: taX. https://tax.wiki.tum.de/.

[14] P. R. Amestoy, I. S. Duff, J.-Y. L'Excellent, J. Koster: MUMPS: A General Purpose Distributed Memory Sparse Solver. – In: Applied Parallel Computing. New Paradigms for HPC in Industry and Academia. T. Sørevik, F. Manne, A. H. Gebremedhin, R. Moe (eds.). Springer Berlin Heidelberg, Juni 2000, 121–130.

[15] R. Lehoucq, D. Sorensen, C. Yang: ARPACK Users Guide. Society for Industrial and Applied Mathematics, Jan. 1998 (Software, Environments and Tools).

[16] R. Ewert, W. Schröder: Acoustic perturbation equations based on flow decomposition via source filtering. J. Comput. Phys. **188** (Juli 2003) 365–398.

[17] B. Schuermans, V. Bellucci, C. O. Paschereit: Thermoacoustic Modeling and Control of Multi-Burner Combustion Systems. Int'l Gas Turbine and Aeroengine Congress & Exposition, Atlanta, GA, U.S.A., ASME **GT2003-38688** (2003) 509–519.

[18] T. Hummel, M. Schulze, B. Schuermans, T. Sattelmayer: Reduced-Order Modeling of Transversal and non-compact Combustion Dynamics. 22nd Int'l Congress on Sound and Vibration (ICSV22), Juli 2015.

[19] S. Jaensch, C. Sovardi, W. Polifke: On the obust, flexible and consistent Implementation of time domain Impedance Boundary Conditions for compressible Flow Simulations. J. Comp. Phys. **314** (2015) 145-159.

[20] J. Lunze: Regelungstechnik 1. Springer Vieweg, Berlin, 2014.

[21] V. Duindam, A. Macchelli, S. Stramigioli, H. Bruyninckx: Modeling and Control of Complex Physical Systems. Springer, Berlin, Heidelberg, 2009.

[22] S. Jaensch, M. Merk, E. Gopalakrishnan, S. Bomberg, T. Emmert, R. I. Sujith, W. Polifke: Hybrid CFD/ low-order modeling of nonlinear thermoacoustic oscillations. 36th Symposium of the Combustion Institute, Seoul, Korea, 2016.

[23] G. Campa, S.M. Camporeale: Eigenmode analysis of the thermoacoustic combustion instabilities using a hybrid technique based on the finite element method and the transfer matrix method. Advances in Applied Acoustics (AIAAS) **1**(1) (2012).

23rd International Congress on Sound & Vibration
Athens, Greece 10-14 July 2016
ICSV23

EFFICIENT CALCULATION OF THERMOACOUSTIC MODES UTILIZING STATE-SPACE MODELS

Max Meindl, Thomas Emmert and Wolfgang Polifke
Technische Universität München, Professur für Thermofluiddynamik, 85747 Garching, Germany
email: meindl@tfd.mw.tum.de

This paper describes a framework for the efficient computation of thermoacoustic modes in annular combustors. It is based on state-space models for coupling both the linearized acoustics and the flame dynamics. The state space models for the acoustics are exported from COMSOL Multiphysics. The Finite Element Method for the linearized Euler equations yields very sparse system matrices. The acoustic and the flame models are connected by network model routines. Due to the state-space modeling, thermoacoustic modes can be computed by solving a generalized non-Hermitian linear eigenvalue problem instead of a nonlinear eigenvalue problem. The Arnoldi algorithm is used to calculate selected eigenvalues in case the systems are too big to compute a direct solution for all the eigenvalues. Validation is carried out for a plenum-burner-chamber configuration with four burners. Simplistic n-τ models are chosen for the flame-acoustic interaction, which are represented in state space form utilizing an advection equation for representing the time delay. The results show good agreement with a full three-dimensional Finite Volume Helmholtz solver in mode shape, frequency and growth rates. Coupling between the plenum and the chamber is observed to be dependent on the interaction index and the characteristic time delay of the flame models.

1. Introduction

Premixed flames in gas turbines are widely used, since they feature high efficiency paired with low emissions. However, they are susceptible to self excited thermoacoustic instabilities, which occur due to interactions between fluctuating heat release of the flame and acoustic waves. These waves are reflected by the combustion chamber walls. In the design stage, analytical and numerical methods can be used to predict the stability of a gas turbine. Compressible LES simulations are very expensive and thus low-order models are often utilized to predict stability. So called network models have become very popular, in which the acoustic behavior and the flame-acoustic coupling are captured in modular blocks, which can be connected to build a complete thermoacoustic system [1]. Though being very affordable, low-order models are mostly limited to quasi 1-D wave propagation [2], which often assumes azimuthal compactness of annular geometries. Models for more complex geometries are based on a modal reduction technique [3, 4]. The latter procedure requires a priori knowledge of the system, because the modal basis strongly influences the behavior of the deduced model.

A different approach to thermoacoustic stability is the calculation of the system eigenmodes on a perturbation equation for describing the acoustics (e.g. Helmholtz [5] or linearized Navier-Stokes [6] equations). The flame's response to acoustic fluctuations is typically accounted for by the frequency response of a flame transfer function (FTF). Then the eigenvalue problem needs to be solved iteratively due to the nonlinear coupling of the FTF, which again leads to high computational cost.

In this paper, a method for the efficient stability analysis of gas turbine combustion chambers is introduced, which is based on state-space models for both the acoustic and the flame response. No

a priori knowledge of the system acoustics is required, because the acoustic is only based on the governing equations deduced from first principles instead of a modal reduction.

The paper is organized as follows: Section 2 shows the methods for acquiring state-space models for the acoustic and the FTF, section 3 outlines the validation case setup. In section 4, the results for the validation case are presented. Section 5 concludes with a discussion and provides an outlook on the potential of this method.

2. State-Space Models

State-Space Models are a compact and efficient way to represent a set of linear coupled differential equations. The state vector $\mathbf{x}$ contains the states retained to represent the system. Matrix $\mathbf{A}$ and $\mathbf{E}$ describe the full dynamic of the system and $\mathbf{B}$ models the effect of the inputs $\mathbf{u}$, see Eq. (1). Equation (2) defines an output-vector $\mathbf{y}$, which is a linear combination of the states and the inputs, determined by the output-matrix $\mathbf{C}$ and the feedthrough-matrix $\mathbf{D}$.

$$\mathbf{E}\frac{d\mathbf{x}}{dt} = \mathbf{A}\mathbf{x} + \mathbf{B}\mathbf{u} \tag{1}$$

$$\mathbf{y} = \mathbf{C}\mathbf{x} + \mathbf{D}\mathbf{u} \tag{2}$$

Time domain simulation is straight forward by discretization of the time derivative of $\mathbf{x}$. From the Laplace-transfomred system, the in-/output transfer functions as well as the eigenvalues can be calculated.

2.1 Acoustic state-space model

In this study, the linearized Euler equations (LEE) are employed for the acoustic modeling [7]. Only the source term $\dot{q}'_v$ for the unsteady heat release in the linearized conservation of energy, Eq. (5), is kept.

$$\frac{\partial \rho'}{\partial t} + \nabla\rho' \cdot \bar{\mathbf{u}} + \rho'\nabla \cdot \bar{\mathbf{u}} + \nabla\bar{\rho} \cdot \mathbf{u}' + \bar{\rho}\nabla \cdot \mathbf{u}' = 0 \tag{3}$$

$$\bar{\rho}\frac{\partial \mathbf{u}'}{\partial t} + \bar{\rho}(\bar{\mathbf{u}} \cdot \nabla)\mathbf{u}' + \bar{\rho}(\mathbf{u}' \cdot \nabla)\bar{\mathbf{u}} + \rho'(\bar{\mathbf{u}} \cdot \nabla)\bar{\mathbf{u}} + \nabla p' = 0 \tag{4}$$

$$\frac{\partial p'}{\partial t} + \bar{\mathbf{u}} \cdot \nabla p' + \mathbf{u}' \cdot \nabla\bar{p} + \gamma(\bar{p}\nabla \cdot \mathbf{u}' + p'\nabla \cdot \bar{\mathbf{u}}) = (\gamma - 1)\dot{q}'_v \tag{5}$$

Here, $\bar{(\cdot)}$ are the mean values and $(\cdot)'$ are the acoustic perturbations. Equations (3) - (5) are spatially discretized using a Finite Element Method (FEM). Together with boundary conditions, a linear set of equations results from the FEM.

$$\mathbf{E}\frac{d\mathbf{x}}{dt} + \mathbf{K}\mathbf{x} = \mathbf{L} \tag{6}$$

Here, $\mathbf{E}$ is the mass matrix, $\mathbf{K}$ is the stiffness matrix and the load vector $\mathbf{L}$ contains entries which originate from Dirichlet boundary conditions and source terms. The state-vector $\mathbf{x}$ contains the acoustic variables at all spatial discretization points, which have not been eliminated by boundary conditions. The length N_A of the state vector equals the degrees of freedom of the acoustic system.

Equation (6) can be transformed to state-space representation by choosing $\mathbf{A} = -\mathbf{K}$ and splitting the load vector in two factors, a matrix $\mathbf{B}$ with constant coefficients and a vector $\mathbf{u}$ which contains the time dependent input signals, e.g. unsteady heat release. By means of the output matrix $\mathbf{C}$, the user can define output variables which are linear combinations of the states. These outputs can be chosen arbitrarily as they do not effect the dynamics of the system.

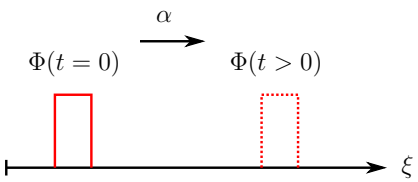

Figure 1: Illustration of a signal Φ being advected along ξ.

2.2 Flame state-space model

A flame transfer function with a single time-lag, e.g. the $n-\tau$ model, represents a flame that reacts to an acoustic perturbation after a time-lag τ. A linear model for the time-lag, which is the crucial part of the $n-\tau$ model, can be derived e.g. by means of a Padé-approximation ([1]). For increasing τ however, the Padé-approximation requires an increased number of coefficients which become ill conditioned. The approach taken in this paper is the utilization of the 1D advection differential equation to model the time-lag.

$$\frac{\partial \Phi}{\partial t} + \alpha \frac{\partial \Phi}{\partial \xi} = 0 \tag{7}$$

In Eq. (7), the property Φ is transported with the constant advection speed $\alpha > 0$ in positive ξ direction (compare Fig. 1). Assume an advection along a fixed interval of length T in ξ direction. Subsequently, the time τ it takes for a signal Φ to be transported is $\tau = T/\alpha$.

For the $n-\tau$ model, a signal Φ is imposed at the upstream boundary ($\xi = 0$). At the downstream boundary ($\xi = T$), the time-lagged signal is measured and amplified by the factor n.

To obtain the state-space form, the interval T is discretized in $N_F - 1$ elements of size ΔT by means of an upwind difference scheme which yields N_F degrees of freedom. The input signal to this model is the acoustic velocity perturbation u' at a reference position, the measured output $\dot{q}'_V$ is the time delayed input signal, amplified by the flame-gain n. The states correspond to the advected property at the respective discretization nodes between the elements. Equations (8) and (9) illustrate a state-space model with $N_F = 4$ degrees of freedom, discretized with a first order upwind scheme. The input acts only on the first state (upstream boundary), whereas the output vector $\mathbf{C}$ uses the last state only (downstream boundary). For this case, the coefficients in $\mathbf{A}$ and $\mathbf{B}$ are $a = \alpha/\Delta T$.

$$\frac{d\mathbf{x}}{dt} = \underbrace{\begin{bmatrix} -a & 0 & 0 & 0 \\ a & -a & 0 & 0 \\ 0 & a & -a & 0 \\ 0 & 0 & a & -a \end{bmatrix}}_{\mathbf{A}} \mathbf{x} + \underbrace{\begin{bmatrix} a \\ 0 \\ 0 \\ 0 \end{bmatrix}}_{\mathbf{B}} u' \tag{8}$$

$$\dot{q}'_V = \underbrace{\begin{bmatrix} 0 & 0 & 0 & n \end{bmatrix}}_{\mathbf{C}} \mathbf{x} \tag{9}$$

By modeling the time-lag with an advection equation, a well conditioned, linear system in time-domain results. Using higher order upwind schemes or more discretization points increases the accuracy of the model for higher frequencies. Figure 2 (left) shows the step responses for two models of order $N_F = 100$ and $N_F = 30$, both discretized with a third order upwind scheme. Slight under- and overshoots are observed close to the step. The higher order model has a steeper response, whereas the overshoot amplitude remains constant. However, for harmonic excitations, which are important in acoustics, the model performs excellent up to a certain frequency, which depends on the model order (Figure 2 (right)). As intended, the gain remains at a constant value of 1 up to a certain frequency, while the phase decreases linearly, which implies a constant time-lag.

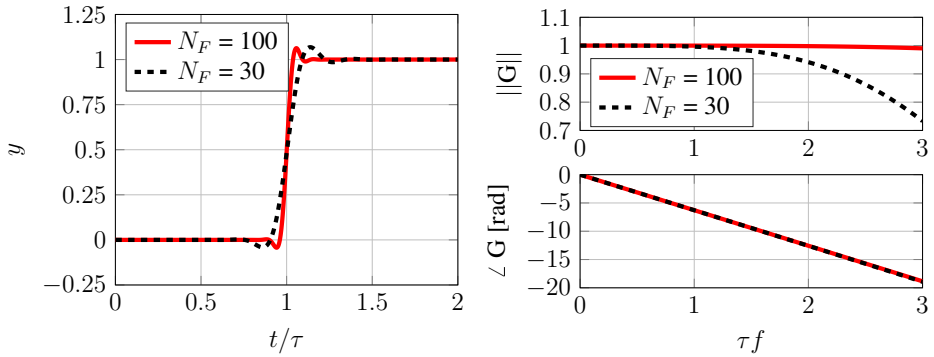

Figure 2: Step response (left) and transfer function $G(\omega)$ (right) of a $n-\tau$ state-space model, $\tau = 1$ ms, $n = 1$.

The implementation of a linear FTF with multiple time-delays, which is the more accurate and generic way to describe the flame-acoustic interaction, is also straightforward ([8]). This allows for incorporation of FTFs which were measured from experiments or identified from CFD simulations.

2.3 Connection of state-space models

For the validation case in this paper, the outputs of the acoustic system have been chosen to be velocity perturbations u' at the flame reference positions upstream of the heat release zones. The inputs to the acoustic system are the volumetric heat-release fluctuations $\dot{q}'_V$ in these zones, which appear as a source term in Eq. (5). The $n-\tau$ flame model provides the time-lagged volumetric heat-release as a function of the velocity perturbations u' at the reference positions.

The connection of the acoustic and the flame models are accomplished using a state-space connection algorithm described in [9]. This is done by feeding back the output of the acoustic system u' to the input of the flame system and vice versa with $\dot{q}'_V$. This way, a closed loop is created and the connected model has no more in- or outputs. Due to the linearity of both acoustic and flame model, the resulting thermoacoustic model is also linear, which yields efficient computations both in time- and frequency-domain.

2.4 Calculation of eigenmodes

The connection of the acoustic and the flame model yields a state-space model, which incorporates the complete thermoacoustic dynamics. The stability of this system can be investigated by solving for the eigenmodes. For smaller systems (up to $N \sim 3 \times 10^4$), it is feasible to directly calculate all the eigenmodes of the system. Due to limitations in memory and computational effort, only some modes of interest are calculated for bigger systems. In order to solve for modes around a specific shift-frequency σ, the generalized, non-Hermitian eigenvalue problem in Eq. (10) has to be solved, where σ is the complex shift, λ is the complex eigenfrequency and $\mathbf{v}$ is the right-eigenvector [10].

$$(\mathbf{A} - \sigma\mathbf{E})^{-1}\mathbf{E}\mathbf{v} = \nu\mathbf{v} \quad \text{with} \quad \nu = \frac{1}{\lambda - \sigma} \tag{10}$$

The eigenfrequencies, which are closest to the shift, get moved close to zero. After inverting the problem, these are the eigenfrequencies ν with largest magnitude and can be found efficiently by the iterative Arnoldi algorithm. The eigenfrequencies λ of the original problem can then be computed with knowledge of the shift σ (Eq. (10)).

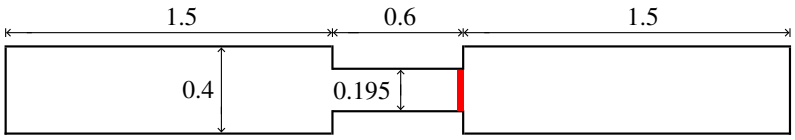

Figure 3: Annular combustor cut through one burner, all measures in m.

LU-factorizations of the stencil $(\mathbf{A} - \sigma\mathbf{E})$ are computed using the multifrontal solver MUMPS ([11], version 5.0.1), because the direct inversion would be too expensive. This factorization step takes up most of the computational time and working memory, but can be parallelized. The eigenvalue calculation is very efficient, because the matrices obtained for the state-space models of the acoustic and the FTF system are very sparse, which speeds up the vector matrix products significantly and requires little working memory. The system which was used to create the results of this paper consists of $\sim$ 203,000 states and requires $\sim$ 4 Gigabyte of RAM to solve for an eigenvalue.

3. Validation Case Setup

The capabilities of the state-space method have been validated for a well researched plenum-burner-chamber configuration [12]. This simplified model of an annular gas turbine combustion chamber consists of a plenum and a chamber of equal geometry, connected by four burner ducts, see Fig. 3 for a cross-section through one burner. The acoustic-flame interaction has been taken into account with $n - \tau$ models. Volumetric heat-release fluctuations $\dot{q}'_V$ of the flames are assumed to be localized at the burner-chamber interface in a volume which amounts to 5 % of the duct volume. The configuration has zero mean-flow velocity and exhibits a temperature jump from 700 K in the plenum and the burners to 1800 K in the chamber. Further parameters can be found in Table 1 of [12].

The numerical setup has been done in COMSOL Multiphysics. A tetrahedral spatial discretization with refinements in proximity to the heat-release areas was employed. For this mesh with $\sim$ 225,000 Elements, a state-space model with $N_A \sim$ 206,000 degrees of freedom was exported. The mesh size is similar to the AVSP mesh used in [12]. All the boundaries were modeled as hard slip-walls and linear testfunctions were used. Note that in three dimensions, each node will result in 5 degrees of freedom (p', ρ', $\mathbf{u}'$), but Dirichlet boundary conditions will eliminate some of these states.

Conversion from non-dimensional to dimensional heat-release rate fluctuations $\dot{q}'_{V,i}$ for the i-th burner (Eq. (11)) is done through incorporating a constant factor in the output-matrix $\mathbf{C}$ of the flame state-space system.

$$\dot{q}'_{V,i} = \frac{\gamma \bar{p} S_i}{\gamma - 1} n_i u'(t - \tau) \tag{11}$$

Here, γ is the ratio of specific heats, $\bar{p}$ is the mean pressure and S_i is the burner cross-section. For the mode calculation in this paper, the same n and τ were chosen for all four burners.

4. Results

Validation of this method is carried out against the results of the Finite-Volume Solver AVSP reported in [12] by comparing the azimuthal eigenmodes. Azimuthal modes appear in pairs with opposite rotational directions (clockwise and counter-clockwise), which can exhibit different eigenfrequencies. However, if the case is perfectly rotational symmetric, both modes become standing modes and coincide on the same frequency. Subsequently, these modes are called degenerate. The investigated plenum-burner-chamber configuration features coupling between the azimuthal eigenmodes of the cold plenum and the hot chamber. The strength of this coupling depends, for a given n, on the time delay τ of the flame model.

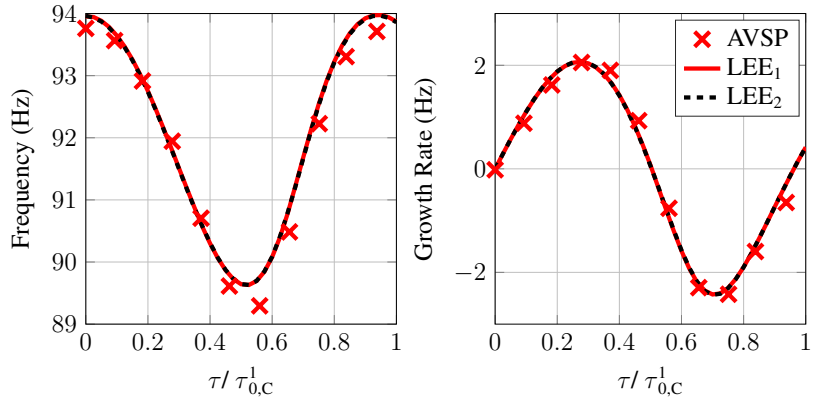

Figure 4: Eigenfrequencies and growth rates for WCC1 of the presented state-space method compared to AVSP results reported in [12].

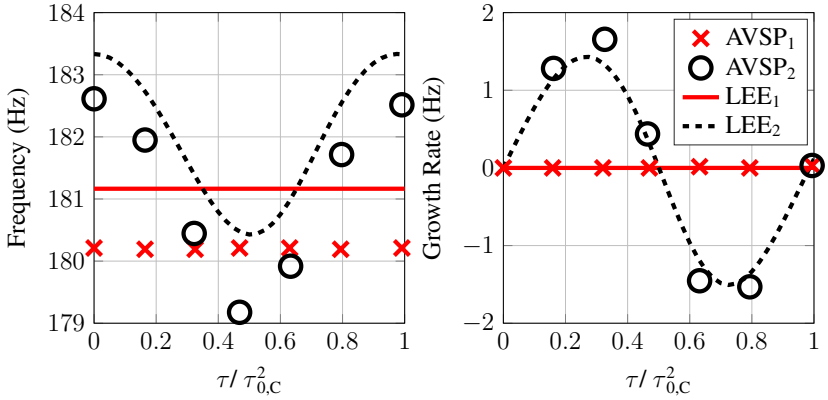

Figure 5: Eigenfrequencies and growth rates for WCC2 of the presented state-space method compared to AVSP results reported in [12].

Figures 4 and 5 show the frequencies and the growth rates of the first (WCC1) and second (WCC2) **W**eakly **C**oupled azimuthal **C**hamber modes. The indices 1 and 2 denote the first and second mode of the azimuthal mode pair. Note that τ has been non-dimensionalized by the respective decoupled chamber mode time period $\tau^1_{0,C}$ and $\tau^2_{0,C}$. The period times for the m-th chamber mode is given by Eq. (12), L_C and c^0 are the half-perimeter and the speed of sound in the chamber [12].

$$\tau^m_{0,C} = \frac{2L_C}{mc^0} \tag{12}$$

The increasing time-delay of the FTF changes the relative phase between the heat release and the acoustic velocity perturbations of the mode. For $\tau/\tau_{0,C} < 0.5$, the interference between these perturbations leads to a net increase in perturbation energy. As neither damping mechanisms nor energy loss at the domain boundaries are present, the mode becomes unstable. With further increase in τ, the shift in phase angle leads to a destructive interference between heat release and acoustic pressure, the mode stabilizes and thus exhibits negative growth-rates. Both the WCC1 and WCC2 modes show this behavior.

Very good agreement between the results of the state-space method and AVSP can be found for the WCC1 mode. The two modes are degenerate and have identical frequencies and growth-rates. For

Figure 6: WCC1 (left) and WCC2 (right) eigenmodes for $n = 1.57$ and $\tau/\tau_{0,C} = 0.5$.

the WCC2 mode frequencies, an almost constant off-set of ~ 1 Hz compared to AVSP can be found for both modes. However, the basic nature of the WCC2 modes is present in both compared models: The first WCC2 mode exhibits pressure nodes at the burners and thus doesn't excite any acoustic velocity perturbations in the burner ducts. Consequently, there is no influence of the time delay τ on this mode. The second mode (Fig. 6) right) strongly depends on the time delay of the flame due to the pressure anti-nodes at the burners.

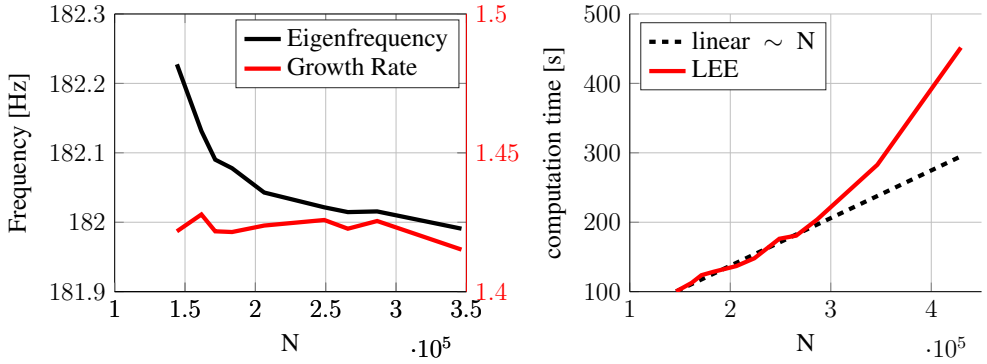

Figure 7: WCC2 eigenfrequency convergence (left, $n = 1.57$, $\tau/\tau_{0,C}^2 = 0.25$) and computation time (right) with increasing system order N.

Computational efficiency and convergence are shown in Fig. 7. As can be seen, the eigenfrequency is only slightly mesh dependent for $N > 2 \times 10^5$. For simplicity, only the WCC2 mode is shown. This convergence behavior is similar for all investigated modes and growth rates.

The computation time for the eigenmodes scales linearly for small to medium systems, then takes a superlinear trend for larger N. Notice that all the computations have been carried out on a single core of a desktop PC. It is assumed, that a better scaling for large systems can be achieved by parallel processing. The calculation of an eigenmode using AVSP takes 5 to 30 minutes on 14 cores for a mesh containing $\sim$ 57,000 cells and depends on the thermoacoustic coupling between plenum and chamber. For strong coupling, convergence is significantly slower. The same calculations for a state-space model with $\sim$ 206,000 degrees of freedom ($\sim$ 225,000 cells in the FEM discretized mesh) take around 2 minutes. The presented state space eigenvalue solver has no convergence issues depending on the mode-shape or the coupling strength and shows superior performance because, compared to AVSP, no iterations for the flame coupling are required.

5. Conclusion

The gap in terms of computational effort and complexity between (analytical) low-order models and very costly LES can be closed based on linearized acoustic equations. Following this idea, state-space models offer great efficiency and robustness when combined with very sparse system matrices, as obtained from discretized LEE or FTFs. The ability to connect these models yields a closed

description of thermoacoustic systems in complex geometries, while retaining the linear eigenvalue problem. Network models, which are based on state-space descriptions, such as taX ([9]), can be used to combine FEM models with low-order acoustic elements to increase their range of application. As shown in this paper, state-space models can make the stability analysis in complex geometries affordable.

6. Acknowledgement

We thank M. Bauerheim for his cooperation and making his results available.

REFERENCES

1. Emmert, T., Jaensch, S., Sovardi, C. and Polifke, W. taX - a Flexible Tool for Low-Order Duct Acoustic Simulation in Time and Frequency Domain, *7th Forum Acusticum*, Krakow, Sep., (2014).

2. Evesque, S. and Polifke, W. Low-Order Acoustic Modelling for Annular Combustors: Validation and Inclusion of Modal Coupling, *Int'l Gas Turbine and Aeroengine Congress & Exposition*, Amsterdam, NL, ASME GT-2002-30064, (2002).

3. Schuermans, B., Bellucci, V. and Paschereit, C. O. Thermoacoustic Modeling and Control of Multi-Burner Combustion Systems, *Int'l Gas Turbine and Aeroengine Congress & Exposition*, Atlanta, GA, U.S.A., pp. 509–519, GT2003-38688, ASME, (2003).

4. Bothien, M., Moeck, J., Lacarelle, A. and Paschereit, C. O. Time domain modelling and stability analysis of complex thermoacoustic systems, *Proceedings of the Institution of Mechanical Engineers, Part A: Journal of Power and Energy*, **221** (5), 657–668, (2007).

5. Nicoud, F., Benoit, L., Sensiau, C. and Poinsot, T. Acoustic modes in combustors with complex impedances and multidimensional active flames, *AIAA Journal*, **45** (2), 426–441, (2007).

6. Gikadi, J., *Prediction of Acoustic Modes in Combustors using Linearized Navier-Stokes Equations in Frequency Space*, Phd thesis, Technische Universität München, Garching, Germany, (2013).

7. Lieuwen, T. and Yang, V. Eds., *Combustion Instabilities in Gas Turbine Engines: Operational Experience, Fundamental Mechanisms, and Modeling*, vol. 210 of *Progress in Astronautics and Aeronautics*, AIAA (2005).

8. Subramanian, P., Blumenthal, R. S., Sujith, R. and Polifke, W. Distributed time lag response functions for the modelling of combustion dynamics, *Combustion Theory and Modelling*, **19** (2), 223–237, (2015).

9. Emmert, T., Meindl, M., Jaensch, S. and Polifke, W. Linear State Space Network Modeling of Acoustic Systems, *submitted to Acta Acustica united with Acustica*, (2016).

10. Lehoucq, R., Sorensen, D. and Yang, C., *ARPACK Users' Guide*, Software, Environments and Tools, Society for Industrial and Applied Mathematics (1998).

11. Amestoy, P. R., Duff, I. S., L'Excellent, J.-Y. and Koster, J., (2000), MUMPS: A General Purpose Distributed Memory Sparse Solver. Sørevik, T., Manne, F., Gebremedhin, A. H. and Moe, R. (Eds.), *Applied Parallel Computing. New Paradigms for HPC in Industry and Academia*, pp. 121–130, no. 1947 in Lecture Notes in Computer Science, Springer Berlin Heidelberg.

12. Bauerheim, M., Parmentier, J.-F., Salas, P., Nicoud, F. and Poinsot, T. An analytical model for azimuthal thermoacoustic modes in an annular chamber fed by an annular plenum, *Combustion and Flame*, **161** (5), 1374–1389, (2014).

Journal of Theoretical and Computational Acoustics
Vol. 27, No. 3 (2019) 1850027 (27 pages)

DOI: 10.1142/S2591728518500275

Determination of Acoustic Scattering Matrices from Linearized Compressible Flow Equations with Application to Thermoacoustic Stability Analysis

Max Meindl*, Malte Merk, Fabian Fritz and Wolfgang Polifke
Technical University of Munich, 85747 Garching, Germany
**meindl@tfd.mw.tum.de*

Received 20 December 2017
Accepted 29 March 2018
Published 5 June 2018

The acoustic transmissions and reflections of plane waves at duct singularities can be represented with so-called scattering matrices. This paper shows how to extract scattering matrices utilizing linearized compressible flow equations and provides a comparative study of different governing equations, namely the Helmholtz, linearized Euler and linearized Navier–Stokes equations. A discontinuous Galerkin finite element method together with a two-source forcing is employed. With this method, the scattering matrix for a radial swirler of a combustion test-rig is computed and validated against the results of a fully compressible Large-Eddy-Simulation. Analogously, the scattering behavior of an axial swirler is investigated. The influence of acoustic-hydrodynamic interactions, viscous effects as well as unsteady boundary layers on the results is investigated for both configurations. A thermoacoustic stability analysis of the combustion test-rig housing the axial swirler is carried out, utilizing the scattering matrix of the swirler. Major influence of the reflections coming from the swirler on the thermoacoustic eigenfrequencies is found.

Keywords: Scattering matrix; discontinuous Galerkin; thermoacoustic.

1. Introduction

Under lean premixed operation conditions, required for low pollutant emissions, gas turbines are susceptible to thermoacoustic combustion instabilities, which arise due to an interaction of acoustic and hydrodynamic perturbations with the flame.[1] When the flow field is perturbed by acoustic waves, which are ubiquitous in gas turbines, the heat-release of the flame oscillates, leading to unsteady volumetric expansion. This mechanism acts as a monopole source of sound.[2] When the generated acoustic waves are reflected back to the combustion zone, a feedback cycle establishes, which can become unstable, i.e. grow in amplitude. The high sound pressure levels as well as the oscillating temperature of the burnt gas are detrimental to stable operation and might even destroy the engine. Additionally, thermoacoustic instabilities limit the operability and increase noise, pollutant emission and material wear.[3]

Due to the high cost of experiments, numerical simulations are an important complement to investigate and predict instabilities. In order to achieve accurate predictions, the scattering and dissipation of acoustic waves in complex combustor geometries has to be captured. This is a challenging task, especially in the regions where significant interaction between hydrodynamics and acoustics is present.[4,5]

Swirl generators are essential in gas turbines due to their support of stable combustion and improvement of the fuel–air mixing process. The resulting complex rotational flow-field featuring shear- and boundary-layers is an important zone, in which acoustic-hydrodynamic interactions take place.[6,7] Effects like acoustic-vorticity interaction similar to those at orifices[8,9] and trailing edges[10] are expected to have a major influence on the acoustic transmission and reflection as well as dissipation behavior. Due to the proximity of the swirl generator to the combustion area, this interaction can impact thermoacoustic stability.[11] The development of reduced order models that can represent the effect of such singularities in tools for thermoacoustic stability assessment is an ongoing process.[7,12–14] It was already shown that accounting for a swirler directly in a Helmholtz solver, which neglects mean-flow effects, is insufficient.[13]

Frequency dependent scattering matrices, which relate the plane acoustic waves at both sides to each other, are often employed for characterization of duct singularities in the plane wave region.[15] Once determined, these acoustic two-ports can conveniently incorporate the complex interaction between acoustics and hydrodynamics in transmission and reflection coefficients. Their deduction has been done experimentally,[15–19] from nonlinear CFD[13,19–22] as well as by means of hybrid approaches.[6,8,9,23–28] The latter is usually based on the computation of a steady-state or time averaged mean-flow field with Reynolds-Averaged Navier–Stokes (RANS) or Large-Eddy-Simulations (LES), respectively. Employing a linear perturbation ansatz to the governing equations around this mean-flow yields linearized compressible flow equations, from which the scattering matrix can be computed. Based on assumptions about the perturbed flow, i.e. isentropic or inviscid, different levels of detail and computational efficiency can be achieved. Due to the linearity of this hybrid approach, the computational effort is significantly lower than employing a nonlinear CFD simulation. While the pure CFD approach is pursued in the time domain, the hybrid methods typically take advantage of a transformation into the frequency domain, where the perturbed flow field can be evaluated with a single computational step for each frequency, which makes them well suited to compute a scattering matrix.

The aim of the present study is to investigate the impact of different linearized compressible governing equations within the hybrid approach on the scattering matrix of two swirlers. Special attention is put to the quantification of viscous effects, acoustic-vortex interaction and the augmentation of acoustic wave propagation by mean-flow velocities. To this end, the scattering matrices of an axial and a radial swirler are computed with the linearized Navier–Stokes equations (LNSE), linearized Euler equations (LEE) and the Helmholtz equation (HHE). A discontinuous Galerkin finite element method (DG-FEM,[29,30] derived for LNSE in Ref. 31) is applied to solve the LNSE and LEE, while a continuous approach is pursued for the HHE. The perturbation energy norm defined by Myers[32] is

employed to investigate loss mechanisms specific to both swirler configurations. By comparing the scattering matrices for the different governing equations, the dominant physical effects will be identified and the required level of modeling detail can be deduced.

To quantify the impact of the acoustic scattering and dissipation by the axial swirler on thermoacoustic stability, the scattering matrix is implemented into a 1D thermoacoustic network model.[33] A linear stability analysis is conducted with scattering matrices obtained from the different governing equations.

Section 2 introduces the different linearized compressible flow equations employed in this study. The numerical method for computation of the scattering matrices based on FEM is presented in Sec. 3. A validation case for a radial swirler is conducted in Sec. 4. In the same manner, the acoustic scattering behavior is deduced for an axial swirl generator and the computed matrices are utilized in linear thermoacoustic stability analysis in Sec. 5, which is followed by a conclusion, Sec. 6.

2. Linear Acoustics

In the mathematical modeling of aeroacoustic problems, the phenomena governing the propagation of acoustic waves are often assumed to be linear and the influence of small perturbations on the mean-flow field is neglected. This means, that the mean-flow can influence the perturbations, but not vice versa. Applying these simplifications, linear time-invariant models that facilitate fast numerical computations can be derived. These models are then restricted to linear phenomena, like the onset of instabilities, and cannot represent the nonlinear interactions which dominate the flow-field when developed instabilities with high amplitudes are present.

2.1. *Linearized compressible flow equations*

Under the assumption of small perturbations, the Navier–Stokes equations can be linearized around a mean-flow state. Therefore, the field variables for pressure p, velocity $\mathbf{u}$ and density ρ are separated into a steady-state mean flow part (denoted by $\bar{\cdot}$) and time-dependent, fluctuating quantities (denoted by $\cdot'$).

The linearized Navier–Stokes equations (LNSE) in conservative form, which are employed in this study, read (without source terms):

$$\frac{\partial \rho'}{\partial t} + \frac{\partial}{\partial x_j}(\bar{u}_j \rho' + \bar{\rho} u_j') = 0, \tag{1}$$

$$\frac{\partial}{\partial t}(\bar{u}_i \rho' + \bar{\rho} u_i') + \frac{\partial}{\partial x_j}(\bar{\rho}\bar{u}_i u_j' + \bar{\rho}\bar{u}_j u_i' + \bar{u}_i \bar{u}_j \rho' - \tau_{ij}') + \frac{\partial p'}{\partial x_i} = 0, \tag{2}$$

$$\begin{aligned}\frac{\partial}{\partial t}((\rho E)') + \frac{\partial}{\partial x_j}(\bar{u}_j (\rho E)' + \overline{(\rho E)} u_j') - \frac{\partial}{\partial x_j}\left(\bar{k}\frac{\partial T'}{\partial x_j}\right) \\ + \frac{\partial}{\partial x_j}(\bar{u}_j p' + \bar{p} u_j') - \frac{\partial}{\partial x_j}(\bar{\tau}_{ij} u_i' + \bar{u}_i \tau_{ij}') = 0,\end{aligned} \tag{3}$$

with the expressions for the internal energy,

$$\overline{(\rho E)} = \frac{\bar{p}}{\bar{\gamma}-1} + \frac{\bar{\rho}\bar{u}_i\bar{u}_i}{2}, \quad (\rho E)' = \frac{p'}{\bar{\gamma}-1} + \frac{\bar{u}_i\bar{u}_i\rho'}{2} + \bar{\rho}\bar{u}_i u_i', \tag{4}$$

and the viscous stress tensor,

$$\bar{\tau}_{ij} = \bar{\mu}\left(\frac{\partial \bar{u}_i}{\partial x_j} + \frac{\partial \bar{u}_j}{\partial x_i} - \frac{2}{3}\frac{\partial \bar{u}_k}{\partial x_k}\delta_{ij}\right), \quad \tau_{ij}' = \bar{\mu}\left(\frac{\partial u_i'}{\partial x_j} + \frac{\partial u_j'}{\partial x_i} - \frac{2}{3}\frac{\partial u_k'}{\partial x_k}\delta_{ij}\right), \tag{5}$$

using the dynamic viscosity $\bar{\mu}$ of the mean-flow and the Kronecker–Delta δ_{ij}. The fluctuating temperature is calculated via the linearized ideal gas law,

$$T' = \bar{T}\left(\frac{p'}{\bar{p}} - \frac{\rho'}{\bar{\rho}}\right). \tag{6}$$

Note that the LNSE are the most general form of linearized compressible flow equations, because the least assumptions and simplifications are made. The LNSE are therefore able to capture the damping effects of acoustic and thermal boundary layers[34] as well as eddy generation and dissipation. The latter is important for acoustic characterization, because vortical structures can act as a secondary source of sound when interacting with solid surfaces.

Neglecting viscous effects and thermal conduction, i.e. $\bar{\mu} = 0$ and $\bar{k} = 0$, the linearized Euler equations (LEE) are obtained from the LNSE. This assumption is often employed in aeroacoustics because for most applications, the influence of viscous damping and heat conduction on the perturbation field is minor.

Assuming isentropic behavior, i.e. $p' = \bar{c}^2\rho'$, with the speed of sound $\bar{c}$, and neglecting mean-flow velocities, i.e. $\bar{\mathbf{u}} = \mathbf{0}$, the LEE can further be reduced to the scalar wave equation,

$$\frac{1}{\bar{\rho}\bar{c}^2}\frac{\partial^2 p'}{\partial t^2} - \frac{\partial}{\partial x_j}\left(\frac{1}{\bar{\rho}}\frac{\partial p'}{\partial x_j}\right) = 0. \tag{7}$$

After Fourier transformation, the wave equation is also known as Helmholtz equation (HHE). Extending the HHE to the convected Helmholtz equation, the correct propagation speed of the acoustic waves, which is the speed of sound augmented by the local mean-flow velocities, can be accounted for. The LNSE/LEE formulations inherently represent this behavior. In the scope of this work, the standard HHE without accounting for mean-flow velocities has been employed.

While the LNSE and the LEE support the propagation of acoustic, vortical and entropy waves, the HHE can only describe the irrotational acoustic part of the field. Therefore, all dissipation mechanisms for perturbation energy within the computational domain are omitted.

2.2. *Perturbation energy*

The quantification of different physical effects, which generate or dissipate perturbation energy, can be a helpful procedure to understand the dominant mechanics that influence

the acoustic characteristics of a system. This methodology has already been applied, e.g. for a transonic nozzle flow.[35] The conservation of energy contained in first-order perturbations of the flow field according to Myers[32] reads (for a domain Ω bounded by Γ with the normal vector $\mathbf{n}$):

$$\int_\Omega \frac{\partial E'}{\partial t} d\Omega + \int_\Gamma W_i' n_i d\Gamma = \int_\Omega D' d\Omega. \tag{8}$$

Here, E' is the perturbation energy, W_i' is the flux in the ith coordinate direction and D' is the source term. Neglecting fluctuations in entropy, unsteady heat-release as well as thermal diffusion, the perturbation energy is defined as

$$E' = \frac{p'^2}{2\bar{\rho}\bar{c}^2} + \frac{1}{2}\bar{\rho}u_j'u_j' + \rho'\bar{u}_j u_j', \tag{9}$$

the flux is

$$W_i' = \dot{m}_i' \left(\frac{p'}{\bar{\rho}} + \bar{u}_j u_j' \right) - \dot{m}_i' \left(\frac{\tau_{ij}}{\rho} \right)' \tag{10}$$

and the source term is

$$D' = \underbrace{\bar{\rho}\bar{\mathbf{u}} \cdot (\boldsymbol{\Omega}' \times \mathbf{u}') + \rho'\mathbf{u}' \cdot (\bar{\Omega} \times \bar{\mathbf{u}})}_{D_\Omega'} - \underbrace{\left(\frac{\tau_{ij}}{\rho} \right)' \frac{\partial \dot{m}_i'}{\partial x_i} + \dot{m}_i' \left(\frac{\tau_{ij}}{\rho^2} \frac{\partial \rho}{\partial x_i} \right)'}_{D_\tau'}, \tag{11}$$

where $\boldsymbol{\Omega} = \nabla \times \mathbf{u}$ is the vorticity. The first term on the right-hand side of Eq. (11) is the source term due to vorticity perturbations, while the second term is the interaction of perturbations with vorticity of the mean-flow. The other terms are sinks due to viscous dissipation, both in the perturbed field and by interaction of perturbations with mean-flow shear- and boundary-layers. The evaluation of these terms allows the quantification of different loss mechanisms for a configuration, giving insight into the validity of assumptions for the perturbed flow, like inviscid or irrotational flow.

Although present in the LNSE, the source terms due to thermal diffusion and entropy waves have been neglected because these effects are orders of magnitude smaller than viscous and vortical losses for the cases investigated in this study.

2.3. *Scattering matrices for plane acoustic waves*

In the frequency band below the cut-on frequency of a configuration, where plane acoustic waves are dominant, an acoustic element can be characterized with a frequency dependent scattering matrix $\mathbf{S}(\omega)$,

$$\begin{pmatrix} f_\mathrm{d} \\ g_\mathrm{u} \end{pmatrix} = \underbrace{\begin{bmatrix} T_\mathrm{ud} & R_\mathrm{dd} \\ R_\mathrm{uu} & T_\mathrm{du} \end{bmatrix}}_{\mathbf{S}(\omega)} \begin{pmatrix} f_\mathrm{u} \\ g_\mathrm{d} \end{pmatrix}. \tag{12}$$

Here, the plane acoustic waves f propagating downstream and g propagating upstream parallel to the x_1 axis are defined as

$$f = \frac{1}{2}\left(\frac{p'}{\bar{\rho}\bar{c}} + u_1'\right), \quad g = \frac{1}{2}\left(\frac{p'}{\bar{\rho}\bar{c}} - u_1'\right). \tag{13}$$

The coefficients of $\mathbf{S}$ govern the transmission and reflection behavior for upstream (T_{ud} and R_{uu}) and downstream (T_{du} and R_{dd}) plane wave forcing via complex-valued coefficients. These coefficients also include the losses present in the system, e.g. due to acoustic-hydrodynamic interactions. This representation is not only useful to get physical insight, but also for implementation in low-order models, which are based on a plane wave description of a whole system.[33,36] An application to a thermoacoustic network model is discussed in Sec. 5.3.1.

3. Numerical Method

The hybrid approach employed in this study to obtain scattering matrices is based on a time-averaged mean-field from Large-Eddy-Simulations and subsequent solving of the compressible flow equations presented in Sec. 2, linearized around this pseudo steady-state. The numerical scheme employed for the LNSE and LEE is the discontinuous Galerkin finite element method (DG-FEM) described in Ref. 31. In conjunction with the local Lax-Friedrichs flux, a stable scheme for the convective terms is obtained, even for the nonviscous LEE. Numerous studies have shown high accuracy for DG-FEM applied to aero-acoustics, e.g. Refs. 29, 37–39. In the absence of convective terms, i.e. for the HHE, a standard FEM approach with continuous test- and ansatz-functions is used.

A Fourier transformation of the linearized equations is employed which allows for direct evaluation of the matrix coefficients in the frequency domain, significantly reducing the computational effort. Applying a two-source-location method,[23] i.e. acoustic plane wave forcing at the upstream and downstream end of the computational domain, the scattering matrix can be obtained from two computations at each frequency. This is done by retrieving the plane wave amplitudes exiting the domain, which are caused by the forced wave. The ratio of the outgoing and the forced wave amplitudes yields the scattering matrix coefficients. Compared to a time-domain simulation, this is very efficient because it requires only two matrix inversions per computed frequency. As a downside, the evaluated transmission and reflection coefficients are only valid for acoustic waves without growth rate. For small growth or damping rates however, the scattering behavior can be extrapolated in the complex plane, see Ref. 40. This is done by fitting a continuous function to the transfer behavior computed at single frequencies. The derivatives of the resulting holomorph transfer function in the direction of the imaginary and the real axes are then inherently coupled via the Cauchy–Riemann equations. This allows the extrapolation of the transfer function to complex frequencies away from the imaginary axis, i.e. for inputs with nonzero growth-rate.

Linear stability of a system is often assessed by the computation of the eigenvalues. By employing the Laplace transformation and assuming harmonic oscillating time dependence,

the system variables $\mathbf{\Phi}'$ (e.g. pressure and velocity perturbations) can be written as

$$\mathcal{L}\{\mathbf{\Phi}'(x,t)\} = \hat{\mathbf{\Phi}}(x,s)e^{st} \tag{14}$$

with the Laplace variable

$$s = s_r + is_{\text{im}}. \tag{15}$$

While the imaginary part s_{im} of an eigenvalue denotes the oscillation frequency, the real part s_r corresponds to the growth-rate. Thus, a positive real part means that the mode is unstable. This stability analysis will be performed for the perturbed field of the radial swirler, Sec. 4, to expand on the scattering behavior as well as for a thermoacoustic model of the whole combustion test-rig housing the axial swirler, Sec. 5.

4. Validation Case: Scattering Matrix for a Radial Swirler

Swirl generators are an essential part of turbulent swirl combustors. The induced swirling flow motion upstream of the turbulent flame avoids blow-off of the flame and allows thus a controlled combustion process. However, the complex geometry and flow through swirlers also influence the scattering of acoustic waves in a nontrivial way.

This study of the swirler is conducted with two objectives: First, to gain an understanding of the (aero-)acoustic phenomena present in the swirler, which lead to the acoustic scattering behavior. To this end, different linearized compressible flow equations are employed in a comparative study. Second, to derive a low order model, represented as scattering matrix, which can describe the transmission and reflection of plane acoustic waves at the swirler. This model may then be employed in 1D thermoacoustic stability analysis to increase the accuracy with which instabilities can be predicted.

Acoustic waves are partially reflected at the cross-section changes within a swirler. However, accounting for this effect only yields only a crude estimate of the overall scattering behavior as it neglects complex parts of the geometry and the mean-flow interaction.

When a longitudinal acoustic wave propagates through a swirler, the local swirl number is mainly modulated by two mechanisms: the acoustic wave perturbs the axial flow velocity and generates fluctuations in tangential velocity due to interactions with the boundaries and the mean-flow.[11,41–43] The tangential perturbations are convected by the mean-flow and therefore propagate slower than the acoustic wave. The spatial separation of these perturbations becomes more evident for increased distances between the swirler and the observer. The scattering matrix, which — in this study — is limited to describe plane acoustic waves, does not directly represent the convected tangential velocity fluctuations. The energy transfer from the acoustics to the convected wave at the swirler however influences the gain.

The tangential mean-velocity component leads to a rotation in the acoustic wave propagation. Due to the low circumferential Mach number and the short distance between the swirler and the outlet of the computational domain however, this effect is negligible for the two swirlers investigated in this study. In fact, due to the circumferential averaging of

the acoustic wave leaving the domain at the in- and outlet, the rotation of the acoustic wave is not represented in the scattering matrix.

The isolated computation of a swirler scattering matrix and the subsequent use in a 1D thermoacoustic network model limits the interaction between the swirler and the rest of the modeled thermoacoustic system to plane acoustic waves. In particular, the interaction of hydrodynamic perturbations generated by acoustic forcing in the swirler with downstream components cannot be represented by this model. The model neglects, for example, that swirl perturbations might be convected to the combustion chamber and influence the thermoacoustic oscillations due to interaction with the edges at cross-section changes. The direct influence on the flame in terms of heat-release perturbation is however accounted for in the flame transfer function.

Before deducing the scattering matrix for an axial swirler and investigating its impact on the thermoacoustic stability of the combustor, see Sec. 5, the numerical methods applied are validated for a radial swirler geometry, see Fig. 1.

The radial swirl generator bypasses the flow through off-centered swirler vanes yielding a swirling flow motion. For this swirler design validation data from a compressible LES is available. Consequently, the scattering matrices deduced from the linearized equations are compared against the results from the compressible LES. The compressible LES can be seen as a validation tool, as it directly resolves the transient, nonlinear acoustic-flow interactions within the swirler geometry. This validation highlights the potential of the linearized equations for the acoustic characterization of complex geometries and puts any subsequent investigations on a solid basis.

The radial swirler investigated is part of a turbulent swirl combustor test-rig, see Fig. 1, located at the EM2C, Paris.[44] Upstream of the swirler, the cross-section area of the round duct section has a diameter $D = 0.022\,\mathrm{m}$, the inlet velocity here is $u_{\mathrm{in}} = 5.4\,\mathrm{m/sec}$. The combustor is operated with a perfectly premixed methane/air mixture with an equivalence

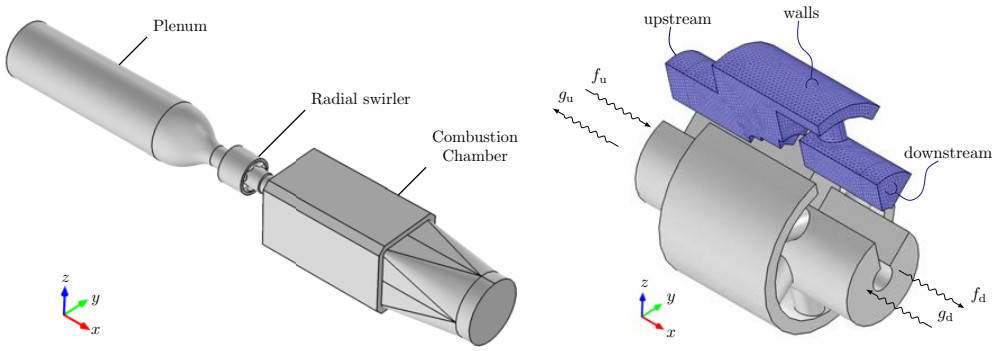

(a) (b)

Fig. 1. Model of the turbulent combustion test-rig (a) and radial swirler (b). The sector with opening angle $\vartheta = 60^\circ$ illustrates the reduced computational domain with periodic boundary conditions on the joint faces.

ratio of $\phi = 0.82$. In the test-rig the swirler is located upstream of the combustion zone and the mixture is not preheated such that the temperature within the swirler flow is constantly equal to an ambient temperature of $T = 293\,\mathrm{K}$. This results in a density of $\rho = 1.204\,\mathrm{kg/m^3}$ and a sound speed of $c = 343\,\mathrm{m/sec}$.

4.1. *LES*

The main idea of an LES is to directly resolve the larger turbulent structures and to model the small scaled turbulent motions. Whereas the larger turbulent structures often depend on the geometry of the configuration studied, the small-scaled turbulence is more universal and can be modeled. The LES numerically solves the fully compressible Navier–Stokes equations which means that the hydrodynamics as well as the acoustics are fully described within the LES.

The compressible LES is performed with AVBP[45] developed by CERFACS & IFPEN. Within the swirler geometry, the fully compressible Navier–Stokes equations are solved on an unstructured grid[46,47] by using the Lax–Wendroff scheme that is second-order accurate in time and space. Consisting of approximately 2 million tetrahedral cells, the unstructured grid has a maximum cell edge length of 0.7 mm and is refined toward the wall. Subgrid stresses are modeled by the WALE model.[48] Isothermal no-slip conditions with a temperature of $T = 293\,\mathrm{K}$ are applied for all swirler walls. Nonreflective acoustic boundary conditions are prescribed at the in- and outlet of the computational LES domain by making use of the Plane-Wave-Masking technique.[49]

In order to deduce from LES values of the acoustic scattering matrix at discrete frequencies, acoustic forcing in form of a sine-sweep signal is induced at the inlet and the outlet of the LES domain. The sine sweep signal consists of seven mono frequent parts $f = [200, 400, 600, 800, 1000, 1200, 1400\,\mathrm{Hz}]$ that are concatenated. Every mono frequent part consists of eight periods. By imposing at the inlet of the LES an acoustic wave, gain and phase values of the transmission coefficient from upstream to downstream T_{ud} and the upstream reflection coefficient R_{uu} can be computed. This is done by measuring the resulting acoustic signals f_{d} and g_{u} and relating the amplitude and the phase of the signals to the forcing signal f_{u}. The remaining two scattering matrix coefficients may be deduced analogously by acoustically forcing the system from downstream, via g_{d}. Note that this simple approach only works with nonreflecting boundary conditions.

4.2. *Linearized compressible flow*

In this section, the acoustic scattering matrix for the radial swirler is derived from linearized compressible flow equations with DG-FEM. Therefore, the transmission and reflection coefficients are obtained by solving the governing equations in the frequency-domain with a two-source method explained previously in Sec. 2.3.

The investigated radial swirler exhibits a geometry, which allows to be divided into six identical $\vartheta = 60°$ sectors due to cyclic symmetry, see Fig. 2. Assuming periodicity of mean and fluctuating fields leads to a significant reduction in computational cost. The mean

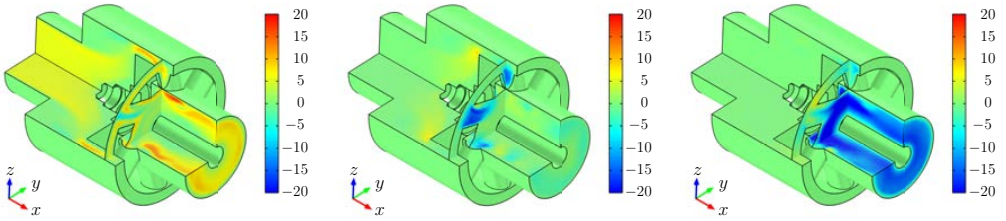

(a) Axial mean velocity (b) Radial mean velocity (c) Azimuthal mean velocity

Fig. 2. Mean velocity fields in m/sec, obtained by time-averaging the transient velocity fields from LES.

fields are obtained by time-averaging the transient fields from the LES used to obtain the reference scattering matrix. The axial, radial and azimuthal mean velocities are shown in Fig. 2.

Inviscid and viscid linearized compressible flow equations, namely HHE, LEE and LNSE, are employed. Boundary conditions for walls in the (aero-)acoustic computations are prescribed as adiabatic slip ($n_i u_i' = 0$) or no-slip ($\mathbf{u}' = 0$) walls. The no-slip boundary condition is forcing velocity fluctuations to vanish at walls, which leads to the development of acoustic boundary layers, governed by viscous effects.[34] Therefore, in the (aero-)acoustic computations, no-slip boundary conditions are only employed for the LNSE. On the upstream and downstream boundaries, the plane acoustic waves f_u and g_d are prescribed. Incoming vorticity and entropy waves are set to zero at the inlet. No boundary conditions for these convective waves are given at the outlet, which allows for propagation out of the domain without interference with the acoustic field.

For the subsequent computation of LEE and LNSE with DG-FEM, three different meshes are employed, see Table 1. The fine mesh for the periodic geometry is also shown in Fig. 1. The shortest acoustic wavelength at 1400 Hz is 0.245 m, i.e. even the coarse mesh resolves this wave with more than 120 elements, guaranteeing mesh independence for the acoustics. The hydrodynamic boundary layer of the mean-flow has an average thickness of 5 mm. The fine mesh fully resolves this boundary layer and therefore captures its influence on the acoustics.[50,51] The unsteady boundary layer $\delta_u = \sqrt{2\nu/\omega}$ forming on no-slip walls becomes very thin for increasing frequencies ω.[52] Due to the high computational cost associated with

Table 1. Mesh statistics of the radial swirler. Degrees of freedom (DOFs) are for LNSE/LEE.

Mesh	No. of Elements	No. of DOFs	$\Delta h_{\max}$
Coarse Mesh	$2 \cdot 10^4$	$5 \cdot 10^5$	2.0 mm
Medium Mesh	$5 \cdot 10^4$	$1 \cdot 10^6$	1.3 mm
Fine Mesh	$1 \cdot 10^5$	$2 \cdot 10^6$	1.0 mm

mesh refinement in a discontinuous Galerkin method in 3D, the unsteady boundary layers were not resolved.

4.3. *Scattering matrix of the radial swirler*

The acoustic scattering matrices for the radial swirler deduced from LES, linearized compressible flow equations with DG-FEM and HHE with continuous FEM, respectively, are shown in Fig. 3.

The scattering behavior of the radial swirler is expected to be largely determined by reflection and transmission at the cross-sectional changes along the swirler. The gain in transmission for upstream excitation yields larger amplitudes than for downstream excitation, especially for HHE, where the magnitude exceeds one for low frequencies. This behavior is expected, because the area ratio between the inlet and outlet is larger than one and continuity equation constrains the mass turnover.

The transmission and reflection coefficients derived from LEE and LNSE yield convincing qualitative agreement compared to LES. The HHE can predict qualitatively the trend of the scattering coefficients. However, qualitative errors of up to 25% arise compared to the LES results. For all coefficients and frequencies, the HHE produces higher transmission and lower reflection coefficients than LEE, LNSE and LES — only the reflection coefficient R_{dd} for downstream forcing shows different behavior. The reflection of an acoustic wave g_{d} coming from the downstream end of the domain is strongly influenced by the vortices formed at the outlets of the off-centered swirler vanes. These vortices generate sound while being convected by the swirled mean-flow,[53] which partially contributes to the acoustic wave f_{d} leaving the domain at the outlet. The propagation of acoustic waves through the sheared mean-flow also generates losses of perturbation energy,[54] which explain the overall significantly lower reflection coefficient obtained by the governing equations which account for these phenomena (LES, LEE and LNSE) compared to the HHE. Figure 4 clearly shows that the dominant loss term for the radial swirler is D'_{Ω}, which includes the formation and dissipation of vortical perturbations as well as the interaction of acoustic waves with vorticity in the mean-flow. The viscous losses D'_{τ}, which occur in the LNSE computations, are of minor importance.

The augmentation of the characteristic speed of acoustic waves through convection by the mean flow is negligible for this configuration, which shows in the fact that the phase diagrams for the scattering coefficients are almost identical for all governing equations. The only noticeable deviation of the HHE results is in the frequency range of 200 Hz to 600 Hz in the downstream reflection coefficient. As already discussed above, vortices strongly contribute to this mechanism, which are not described by the HHE.

For an increased mesh resolution, the scattering matrix deduced by the LEE starts to deviate from the coefficients computed with the LES, especially in the low-frequency range. Figure 4 shows vastly increased vortex perturbations, two orders of magnitude higher compared to the LNSE simulations. In order to further examine this behavior, the linearized compressible flow equations are solved for their complex eigenmodes. The eigenvalues closest to the stability limit for LEE and LNSE on the mid-sized mesh are shown in Fig. 5(a). Two

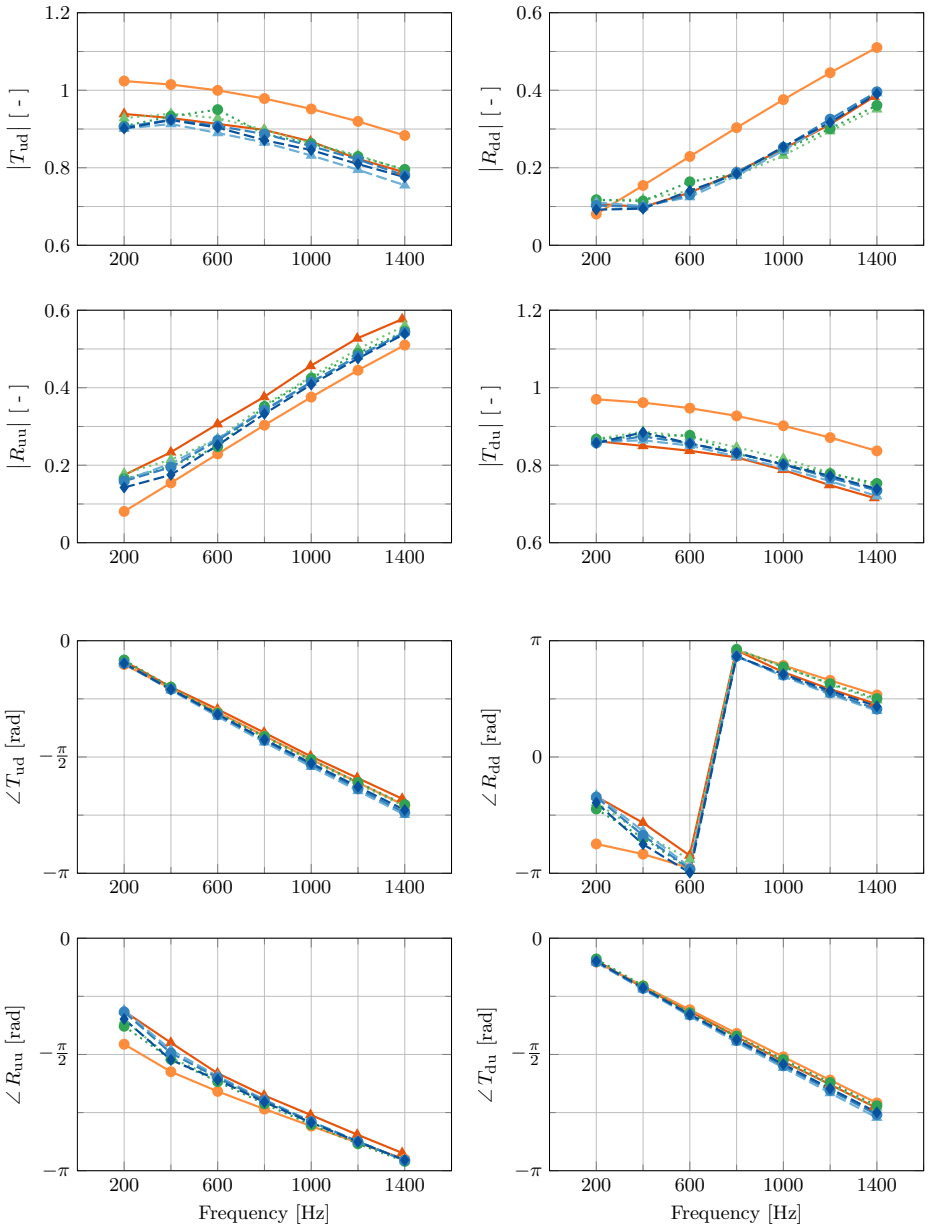

Fig. 3. Acoustic scattering matrix for the radial swirler, which was obtained by solving the linearized compressible flow by LES (—▲—), HHE (—●—), LEE on the coarse (···▲···) and mid-sized (···●···) mesh , and LNSE on the coarse (–▲–), mid-sized (–●–) and fine (–◆–) mesh.

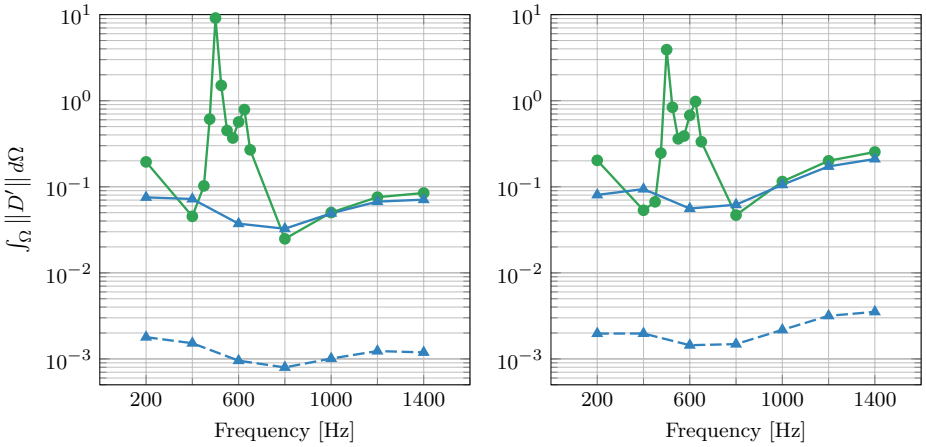

(a) Upstream excitation (b) Downstream excitation

Fig. 4. Acoustic energy dissipation for the radial swirler, integrated over the whole computational domain and one period of the forcing frequency. Dissipation due to vorticity D'_Ω deduced by LEE (—●—) and LNSE (—▲—) and viscous diffusion D'_τ for LNSE (–▲–).

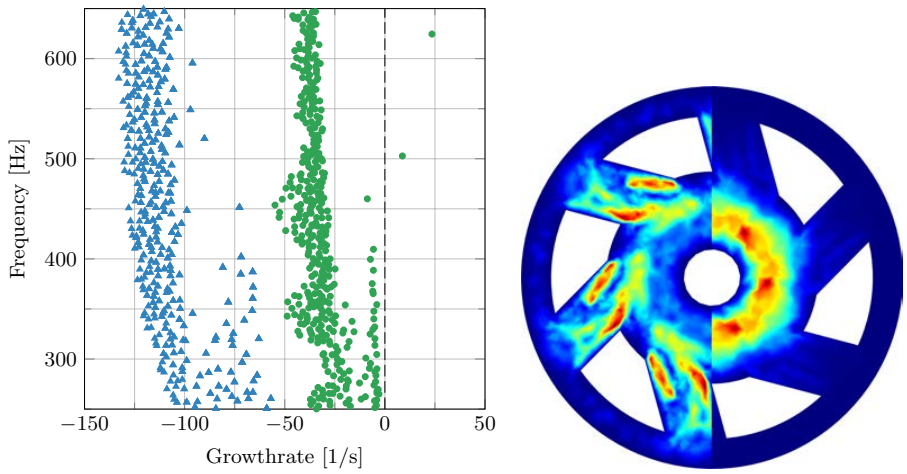

(a) (b)

Fig. 5. Eigenvalue spectrum (a) and eigenmode (b) for the radial swirler on the mid-size mesh, both for LEE and LNSE. (a) Eigenvalue spectrum for the radial swirler around the region of interest, both for LEE (●) and LNSE (▲) and (b) eigenmode in the magnitude of the radial velocity fluctuation $|u'_r|$ for LNSE (left half plane) and LEE (right half plane).

unstable eigenmodes are discovered for LEE at 502.8 Hz and 624.5 Hz, which spoil the scattering matrix at frequencies close to the eigenfrequencies. On the contrary, all eigenmodes for LNSE are stable for the chosen mesh in the investigated frequency spectrum. Figure 5(b) shows eigenmodes in terms of the absolute radial velocity field in a plane, perpendicular to the x-axis and cutting through the off-centered swirler vanes, again both for LEE and LNSE. For LEE the unstable eigenmode at 624.5 Hz is shown, whereas for LNSE a stable eigenmode at 607.4 Hz is depicted. Here, the unstable eigenmodes are not damped by viscous effects or no-slip boundary conditions in the vicinity of solid surfaces and lead to unphysical solutions. The high vorticity present in the unstable LEE eigenmodes leads to sound emission, which is predominantly leaving the domain at the downstream end. This explains the surplus gain of the coefficients T_{ud} and R_{dd} computed with the LEE on the medium mesh. Results of the LEE computations on the fine mesh suffer even stronger from this instability and are therefore not shown. The coarse mesh does not show these problems, because the vortices in this region are not resolved well, which suppresses the instability.

A similar observation was made by Kierkegaard *et al.* for the whistling potentiality of an orifice, where the employment of slip boundary conditions at the orifice yielded "*an excessive amount of vorticity*".[8]

Carnevale *et al.* state, that in the nonlinear, inviscid case, a vortex dipole impinging on a slip wall leads to a separation of the vortices, which will then slip along the wall without decaying.[55] In the linearized case, i.e. the LEE, a vortex propagates with the mean-flow only, which is not augmented by induced velocity of other vortices. Therefore, the vortex trajectory differs from the nonlinear case, but it may still be assumed that no major decay mechanism for vortical perturbations is present at a slip wall. For no-slip walls in the nonlinear case however, vorticity with opposing rotation is generated in the boundary layer, when a vortex dipole approaches the wall.[55] This behavior needs to be present in the linear LNSE computations as well, because it is required to fulfill the no-slip boundary condition.

The results of the computations for the radial swirler suggest that no-slip boundary conditions are required for the correct interaction between vortices and solid surfaces in linearized compressible flow computations. This also leads to a higher degree of consistency between the perturbed and the mean-flow field from LES, which was also computed with no-slip boundary conditions at the walls. If slip walls are enforced in the aeroacoustic computations, unphysical instabilities can develop in regions where strong interaction between vortices and surfaces occurs. When the LEE are employed in a thermoacoustic model of the full combustor, these unphysical vortical perturbations and the associated sound radiation may lead to erroneous growth-rate calculations.

5. Application Case: Axial Swirler

The scattering behavior of an axial swirler, placed in the combustion test-rig shown in Fig. 6, is investigated in the same manner as the radial swirler of the validation case. The annular duct housing the swirler has an inner diameter of $D_i = 0.016\,\mathrm{m}$ and an outer diameter of

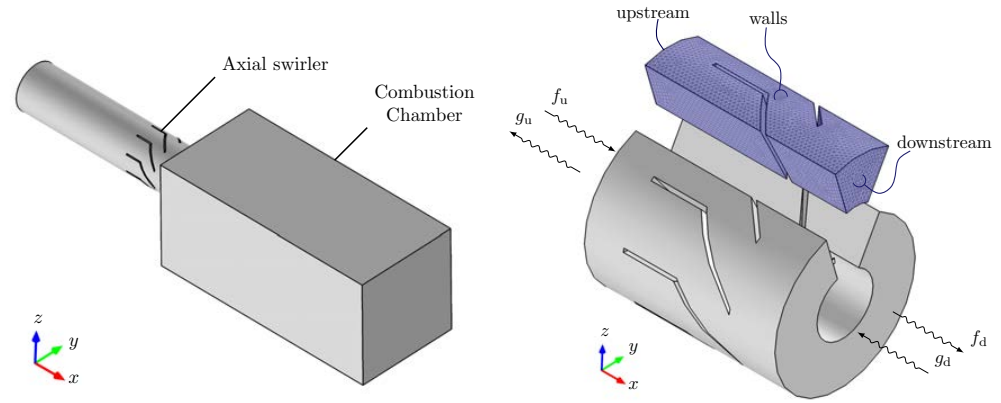

(a) (b)

Fig. 6. Model of combustion test-rig (a) and the axial swirler (b). The sector with opening angle $\vartheta = 45°$ illustrates the reduced computational domain with periodic boundary conditions on the joint faces. (a) Annular duct and combustion chamber of the turbulent combustion test-rig. Upstream plenum not shown and (b) Axial swirler.

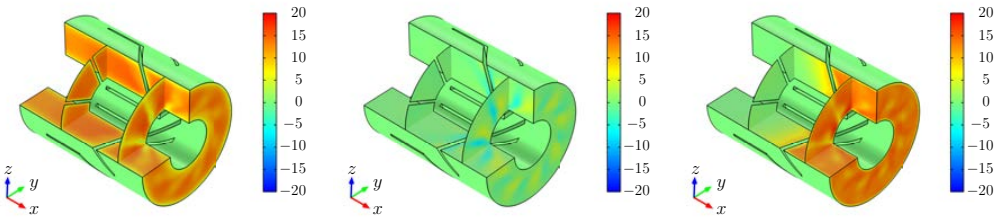

(a) Axial mean velocity (b) Radial mean velocity (c) Azimuthal mean velocity

Fig. 7. Mean velocity fields in m/sec, obtained by time-averaging the transient velocity fields from LES.

$D_o = 0.04\,\mathrm{m}$. The axial mean-flow velocity at the swirler inlet amounts to $u_{\mathrm{in}} = 11.3\,\mathrm{m/sec}$, the temperature is almost constant at $T = 293\,\mathrm{K}$ throughout the swirler domain. The spatially resolved mean-flow field is shown in Fig. 7.

5.1. *Numerical setup*

The mean-flow fields for the axial swirler were obtained from a time-averaged LES of the whole combustor, similar to Sec. 4.1. The 45° periodicity of the geometry and the flow is exploited with periodic boundary conditions. The mesh is chosen analogously to the fine mesh of the radial swirler, with a maximum cell length of $\Delta h = 1\,\mathrm{mm}$, which amounts to $1 \cdot 10^5$ elements and $2 \cdot 10^6$ degrees of freedom, see Fig. 6. The boundary conditions as well as

the two-source method to obtain the scattering matrix are equivalent to the radial swirler case.

5.2. *Scattering matrix of the axial swirler*

Magnitude and phase of the obtained plane wave scattering matrix for the axial swirler are shown in Fig. 8. Consistently throughout all the coefficients and frequencies, the HHE produces higher transmission and lower reflection than the LEE and LNSE. The LNSE show lower transmission and higher reflection. The reason for this are the unsteady boundary layers, that constrict the flow cross-section between the blades and are not represented by LEE and HHE. The effect is similar to an increased area jump when the acoustic wave propagates through the blades of the swirler. This results in increased reflection and reduced transmission of acoustic waves.[52,56,57] For very high frequencies, the unsteady boundary layer becomes thinner.[34,52] As already stated in Sec. 4.2, the mesh used could not resolve the unsteady boundary layers, especially at higher frequencies. Therefore, the unsteady boundary layer thickness is overestimated, which over predicts the effect of the flow constriction. In the frequency range of the thermoacoustic unstable mode around 100 Hz however, which will be shown in Sec. 5.3, the scattering matrix showed only minor changes when the grid was refined near the no-slip walls. Under this premise, the scattering coefficients of LNSE and LEE, which over predict and neglect unsteady boundary layers respectively, can be seen as upper and lower boundaries for the prediction of transmission and reflection of plane acoustic waves at the swirler.

Compared to the phase of a 1D duct, computed with convected HHE, all the governing equations yield larger phase lags for the transmission. This can partly be accounted to the longer path for the acoustic waves through the swirler geometry (HHE) and the inertia resulting from contractional acceleration. For the LEE and LNSE, the augmentation of the acoustic propagation speed by the locally resolved mean-flow velocity yields a smaller phase lag for T_{ud} with the flow and an increased phase lag for T_{du} against the flow compared to the HHE.

In contrast to the radial swirler, where vortical losses were dominant, the dissipation mechanisms in the axial swirler, Fig. 9, show that viscous and vortical dissipation are in the same order of magnitude. This is in agreement with the different reflection and transmission coefficients for LEE and LNSE, which also results from viscous boundary layer effects. It is also apparent, that in the low frequency band below 200 Hz, vortical losses are overestimated by the LEE compared to the LNSE, which also leads to high viscous dissipation of the vortices. Above this frequency band, the viscous losses are rather independent of the forcing frequency and are higher for the LNSE.

Figure 10 shows the absolute value of the perturbed axial velocity field in a plane directly after the blades normal to the x_1-axis. It is clearly visible at 100 Hz (a)–(c), that high non-physical perturbation magnitudes at the outer bearing of the swirler occur, when LEE with slip walls are employed. This relates to the strong vortical effects in the low frequency band, Fig. 9. Opposed to this, boundary layers form for the LNSE computation. Due to the neglect of the swirl in the mean-flow field, the HHE solution is turned slightly clockwise compared

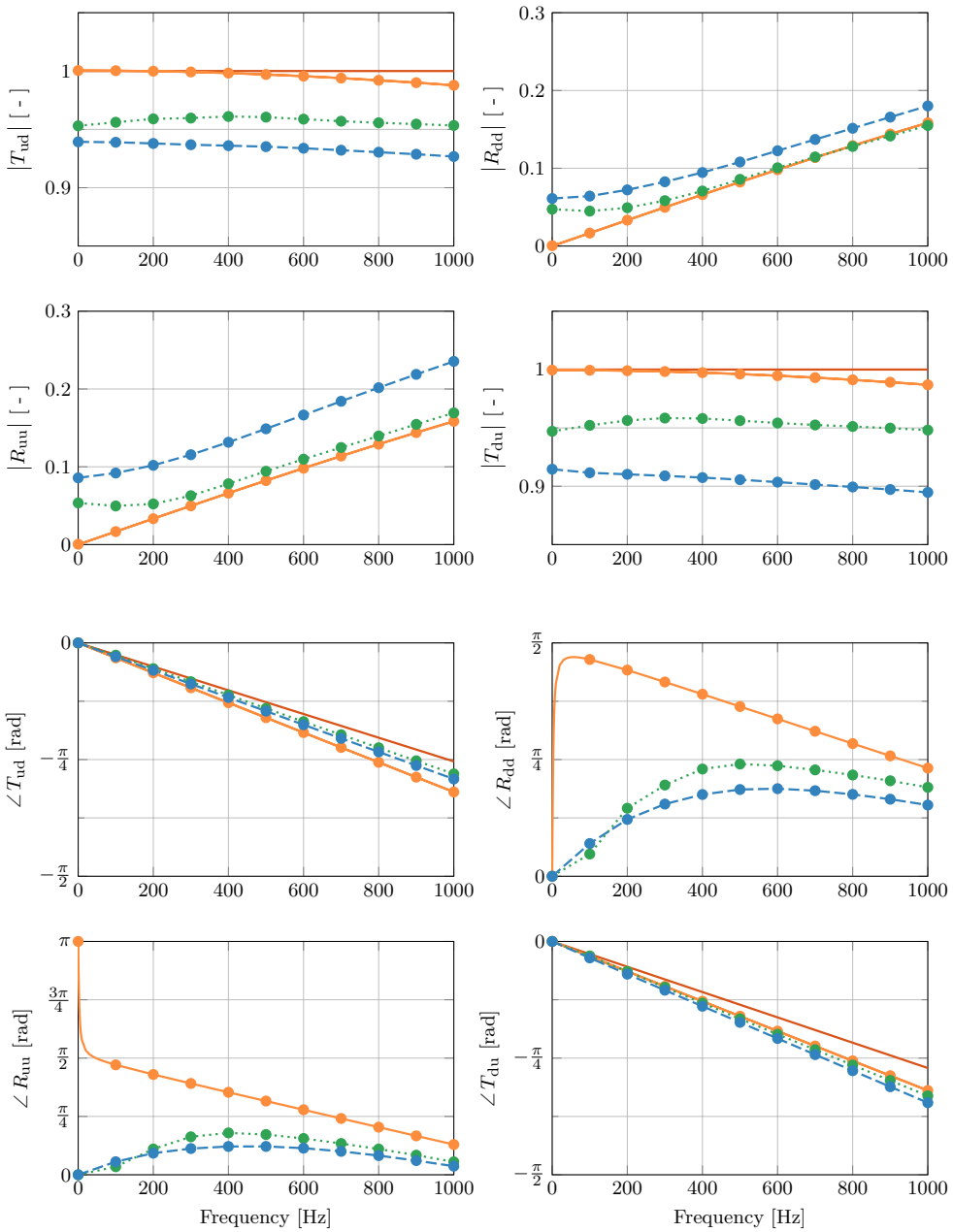

Fig. 8. Acoustic scattering matrix for the axial swirler, which was obtained by solving HHE (—●—), LEE (···●···) and LNSE (– – ●– –). The transmission behavior of a duct (——) is shown for comparison.

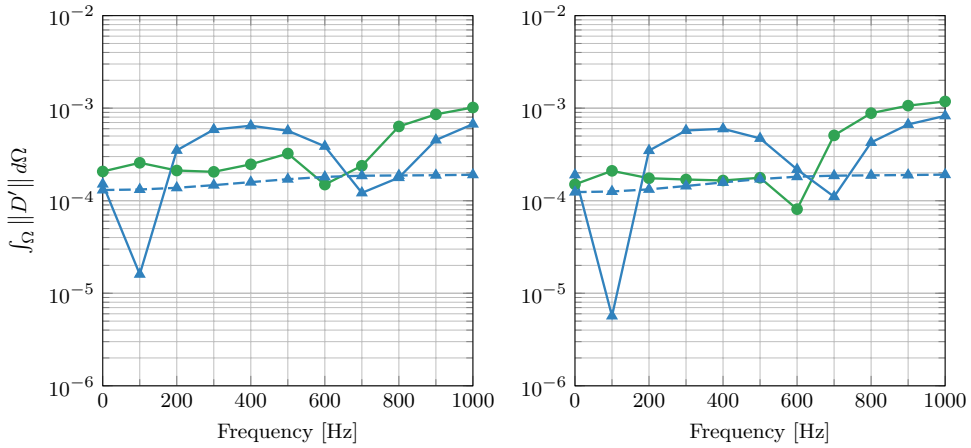

(a) Upstream excitation (b) Downstream excitation

Fig. 9. Acoustic energy dissipation for the axial swirler, integrated over the whole computational domain and one period of the forcing frequency. Dissipation due to vorticity D'_Ω deduced by LEE (—●—) and LNSE (—▲—) and viscous diffusion D'_τ for LNSE (--▲--).

to the LEE and LNSE solution. At 1000 Hz (d)–(f), the velocity fields look very similar for both LEE and LNSE, implying that the no-slip walls have major influence only in the low frequency range.

5.3. *Linear thermoacoustic stability analysis*

The linear thermoacoustic stability of a 1D network model of the combustor test-rig including the axial swirler is assessed by computing the eigenvalues. In this model, the scattering

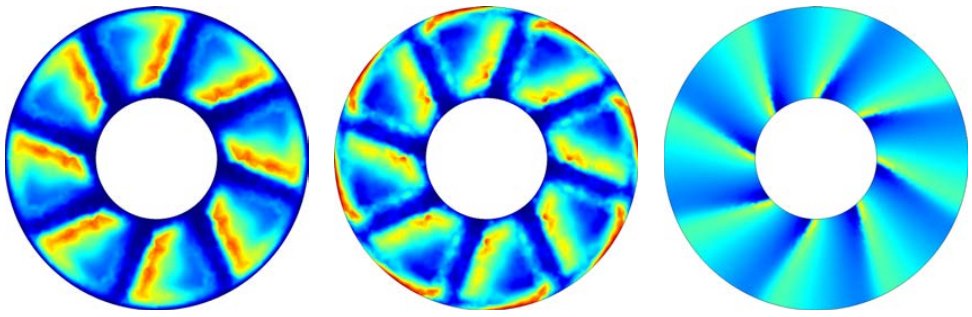

(a) LNSE, 100 Hz (b) LEE, 100 Hz (c) HHE, 100 Hz

Fig. 10. Magnitude of the axial velocity fluctuations $|u'_1|$ for harmonic upstream forcing with 100 Hz (a)–(c) and 1000 Hz (d)–(e) at the blade ends. Normalized by the maximum amplitudes across the different governing equations for each frequency, $\max(|u'_1|)(100\,\text{Hz}) = 3.03\,\text{m/sec}$, $\max(|u'_1|)(1000\,\text{Hz}) = 3.86\text{m/sec}$.

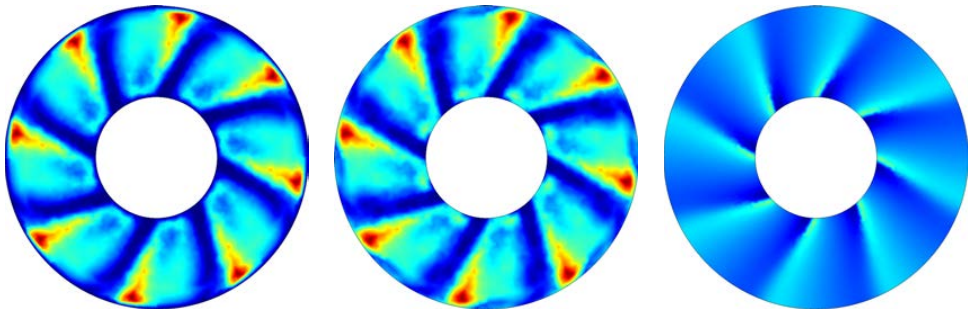

(d) LNSE, 1000 Hz (e) LEE, 1000 Hz (f) HHE, 1000 Hz

Fig. 10. (*Continued*)

matrix of the swirler obtained with the different governing equations is included to quantify the sensitivity of growth-rates of the thermoacoustic eigenmodes to the swirler model.

5.3.1. *Thermoacoustic network models*

Thermoacoustic models for linear stability analysis exist in a wide range from (semi-)analytical approaches (e.g. Refs. 58 and 59), to hybrid methods based on LNSE/LEE/HHE (e.g. Refs. 31, 60–63), which are applicable to complex geometries and model different degrees of acoustic-flow-flame interaction. Thermoacoustic network models (e.g. Refs. 33 and 64) are applicable if plane, 1D acoustic waves are a sufficient representation within the frequency range of interest, i.e. below cut-on frequencies of transversal modes. Due to the reduction in dimensionality, the computation of all eigenmodes of a network model takes only seconds.

Network models rely on a decomposition and abstraction of the combustion system into simple 1D two-port and one-port elements, for which analytical solutions of the convected HHE for propagation, transmission and reflection of the acoustic waves are known. Examples are ducts with constant cross-section, acoustically compact area jumps and reflecting terminations. The latter is characterized by a complex-valued reflection coefficient, R, that relates the plane wave entering the domain to the outgoing wave. This would read

$$R_\mathrm{u} = \frac{f_\mathrm{u}}{g_\mathrm{u}} \quad \text{and} \quad R_\mathrm{d} = \frac{g_\mathrm{d}}{f_\mathrm{d}} \tag{16}$$

for an upstream and downstream termination, respectively. The reflective behavior of the terminations is of great importance for system stability, as they can contribute major loss mechanisms of perturbation energy due to flux over the system boundaries.

In order to account for the acoustic-flow-flame interaction, which cannot be resolved in a 1D model, a so-called Flame Transfer Function (FTF, see e.g. Ref. 65) is often employed. For velocity sensitive flames — as they are found in gas turbines — an appropriate ansatz for the FTF is to relate the heat-release fluctuations $\dot{Q}'$ to axial velocity perturbations u'_ref

at a reference position upstream of the flame. By use of the linearized Rankine–Hugoniot jump conditions,[66] the unsteady heat-release is converted to acoustic plane waves, which are fed back into the acoustic part of the network model at the flame position. In this study, the open-source thermoacoustic network tool *taX*[33,a] is used for linear stability analysis.

5.3.2. *Network model of the axial swirler test-rig*

A thermoacoustic network model (Table 2) proposed in Ref. 68 and extended by a perforated plate model for the outlet in Ref. 31 is utilized to investigate the linear stability of the turbulent swirl burner featuring the axial swirler (see Fig. 11). It consists of duct elements of constant cross-section for the plenum and the combustion chamber, which are connected via area jumps to the annular duct housing the swirler. The parts of the annular duct up- and downstream of the swirler are also modeled with duct elements (D_1 and D_2). Note that in the original work of Emmert *et al.*,[68] the swirler is replaced by a lossless duct, i.e. the reflections and dissipation are neglected. The inlet of the plenum is a fully reflecting sound-hard wall, i.e. $u' = 0,\ R_u = 1$, while the downstream termination of the combustion

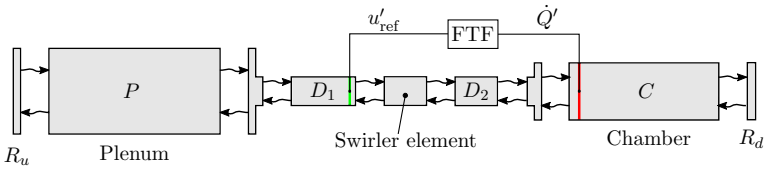

Fig. 11. (Color online) Thermoacoustic network model of the test-rig containing the axial swirler including markers for the reference (green) and flame position (red). Representation not to scale.

Table 2. Parameters for the thermoacoustic network model.[68]

Parameter	Variable	Value
Plenum length	l_P	0.17 m
Plenum cross-section area	A_P	0.0314 m^2
Duct lenght of D_1	l_{D1}	0.098 m
Swirler element length	l_S	0.045 m
Duct lenght of D_2	l_{D2}	0.025 m
Duct cross-section area	A_D	0.0011 m^2
Chamber length	l_C	0.7 m
Chamber cross-section area	A_C	0.0081 m^2
Upsteam reflection coefficient	R_u	1
Downstream reflection coefficient	R_d	see Fig. 12(b)
Ratio of speed of sound across flame	$\bar{c}_d/\bar{c}_u$	2.405
Upstream speed of sound	$\bar{c}_u$	343.14 m/sec
Upstream Mach number	$M_u = \frac{\bar{u}_u}{\bar{c}_u}$	0.0011

[a]The code for the software package *taX* can be found at http://gitlab.lrz.de/tfd/tax.

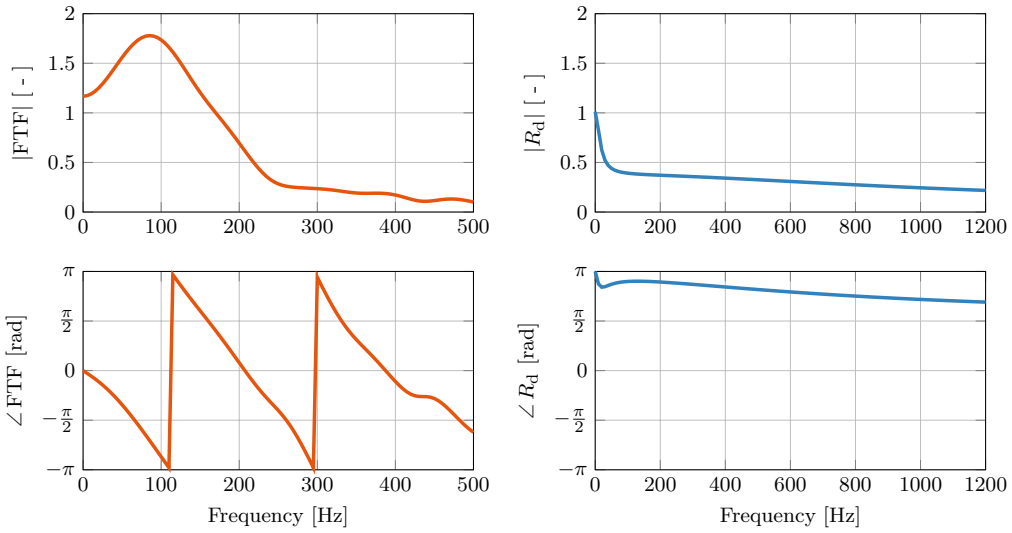

(a) FTF

(b) Outlet reflection coefficient

Fig. 12. Gain and phase of the FTF (a) and the reflection coefficient of the perforated plate model[65,67] (b).

chamber, a perforated plate, shows frequency dependent reflection behavior, see Fig. 12(b). In the frequency band of interest between 50 Hz and 500 Hz, the reflection coefficient is $R_d \lesssim -0.4$, i.e. the perforated plate behaves like a partly reflecting open end. The frequency dependent FTF used in this study was identified from LES,[65] see Fig. 12(a).

In order to obtain a continuous model of the scattering matrices, which were sampled at discrete frequencies, a fifth-order polynomial is fitted to the scattering coefficients. This continuous polynomial is then included in the network model in the position of the swirler element, see Fig. 11.

The spectrum of the computed eigenvalues is shown in Fig. 13, left. A difference in oscillation frequency and growth-rate can be seen for the two cases applying the LNSE swirler scattering matrix versus a lossless duct. Note that the latter option is often employed due to lack of a better model, when an acoustic characterization of the swirler has not been conducted. The only unstable mode is at $\sim$ 100 Hz. Investigations have shown that this mode is not based on reflections of the acoustic waves at the domain terminations but on a direct intrinsic feedback from the sound generated by the unsteady flame to the velocity perturbations at the reference position.[68,69] Note that the swirler has a major influence on this mode, because it introduces reflections exactly in this feedback path. The two modes at 1000 Hz, that are close to instability, have high pressure amplitudes in the annular duct housing the swirler. Again, strong influence of the scattering matrix especially on the growth-rates can be seen for these modes. The rest of the (already strongly damped) modes show only minor sensitivity for reflections from the swirler. The right part

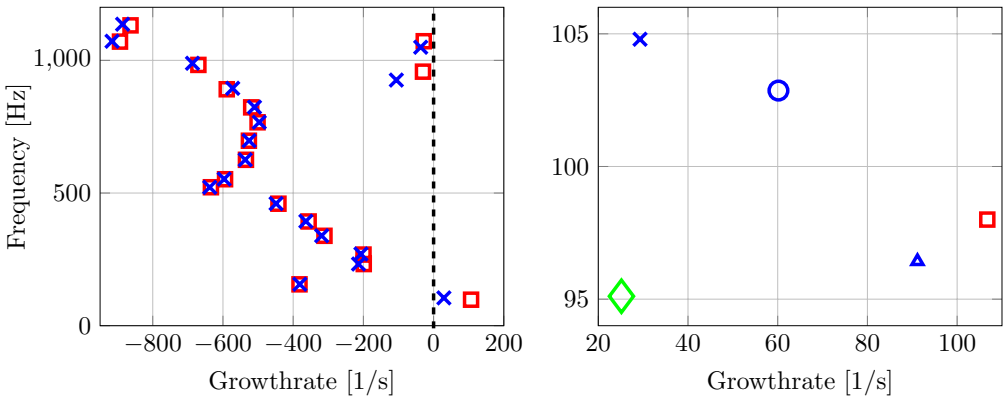

Fig. 13. Left: Eigenvalue spectrum of the model with a duct in the swirler position (□) and with the LNSE swirler scattering matrix (×). Right: Unstable ITA eigenmode for the network model with different swirler scattering matrices: duct (□), HHE (△), LEE (○) and LNSE (×). ITA eigenfrequency of the model used in Ref. 31 with resolved swirler and combustion chamber (◇).

of the plot quantifies the influence of the swirler scattering matrices obtained by different governing equations on the unstable mode. For the scattering matrix with HHE, the main influence is the greater phase shift for transmission from downstream to upstream acoustic waves, T_{du}, compared to the duct. Therefore, the feedback mechanism is slower and the oscillation frequency decreases. If nonnegligible reflections of upstream waves, R_{uu}, are present, as it is the case for the LEE and LNSE scattering matrices, the early feedback of reflected waves back to the reference position introduces a comparatively small time-scale to the eigenmode and thus the frequency increases. The lower amplitude in the transmission coefficient T_{du}, compared to a duct, contributes to a weaker overall feedback which leads to a smaller growth-rate of the mode for all swirler models. The difference between the influence of the scattering matrices (HHE/LEE/LNSE) is significant, especially in terms of the growth-rate. Therefore, care has to be taken regarding the validity of assumptions for the flow through the swirler, like neglect of unsteady boundary layers and mean-flow influence.

The result obtained for the unstable mode from the network model including the swirler is comparable to a stability analysis conducted in Ref. 31, where a part of the combustion chamber and the annular duct including the swirler were resolved with LNSE in 3D, see Fig. 13, right. This shows, that the acoustic behavior of the swirler is a major influence in linear thermoacoustic stability analysis and is in the same order of magnitude like losses at area expansions and dissipative acoustic-flow interactions in the combustion zone.

6. Conclusion

Scattering matrices for a radial and an axial swirler have been computed by means of the Helmholtz, linearized Euler and linearized Navier–Stokes equations, respectively with a

two-source methodology in the frequency domain. The discontinuous Galerkin finite element discretization was utilized to obtain a stable and accurate numerical scheme. Good agreement to the scattering matrix retrieved with a Large-Eddy-Simulation was found for the linearized Navier–Stokes equations. The linearized Euler equations showed similar agreement for most frequencies, but featured unstable modes due to the interaction between vortices and slip walls. For the radial swirler, vortices have been found to be the main loss mechanism, while the scattering behavior of the axial swirler is governed by viscous and vortical effects. The Helmholtz equation, which neglects mean-flow acoustic interaction, overestimates the transmission in both cases. A linear 1D thermoacoustic stability analysis of the combustor test-rig including the axial swirler was conducted. Taking into account the scattering matrices from different governing equations significantly influences the growth-rate of the unstable mode of the system, which leads to the conclusion that reflections coming from the swirler cannot be neglected.

Acknowledgments

The authors thank Alp Albayrak for providing the mean-fields of the axial swirler from his LES computation and acknowledge financial support by the German Research Foundation DFG, project PO 710/16-1. The Gauss Centre for Supercomputing e.V. is gratefully acknowledged for funding this project by providing computing time on the GCS Supercomputer SuperMUC at Leibniz Supercomputing Centre.

References

1. T. Poinsot and D. Veynante, Flame-acoustics interactions, in *Theoretical and Numerical Combustion*, 2nd edn. (R. T. Edwards, Inc., Philadelphia, PA, 2012), pp. 375–431.
2. S. L. Bragg, Combustion noise, *J. Inst. Fuel* **36** (1963) 12–16.
3. A. H. Lefebvre, *Gas Turbine Combustion*, 2nd edn. (Taylor & Francis, Philadelphia, PA, USA, 1999).
4. M. S. Howe, Dissipation of sound at an edge, *J. Sound Vib.* **70** (1980) 407–411.
5. D. W. Bechert, Sound absorption caused by vorticity shedding, demonstrated with a jet flow, *J. Sound Vib.* **70**(3) (1980) 389–405, doi: 10.1016/0022-460X(80)90307-7.
6. J. Gikadi, W. C. Ullrich, T. Sattelmayer and F. Turrini, Prediction of the acoustic losses of a swirl atomizer nozzle under non-reactive conditions, in *ASME Turbo Expo* 2013: *Turbine Technical Conf. and Exposition* (ASME, 2013).
7. M. Zahn, M. Schulze, C. Hirsch, M. Betz and T. Sattelmayer, Frequency domain predictions of acoustic wave propagation and losses in a swirl burner with linearized Navier–Stokes equations (ASME, 2015).
8. A. Kierkegaard, S. Allam, G. Efraimsson and M. Åbom, Simulations of whistling and the whistling potentiality of an in-duct orifice with linear aeroacoustics, *J. Sound Vib.* **331**(5) (2012) 1084–1096, doi: http://dx.doi.org/10.1016/j.jsv.2011.10.028.
9. A. Kierkegaard, S. Boij and G. Efraimsson, Simulations of the scattering of sound waves at a sudden area expansion, *J. Sound Vib.* **331**(5) (2012) 1068–1083, doi: 10.1016/j.jsv.2011.09.011.
10. Y. Fukumoto and M. Takayama, Vorticity production at the edge of a slit by sound waves in the presence of a low-Mach-number bias flow, *Phys. Fluids A*: *Fluid Dyn.* **3** (1991) 3080.

11. T. Komarek and W. Polifke, Impact of swirl fluctuations on the flame response of a perfectly premixed swirl burner, *J. Eng. Gas Turbines Power* **132**(6) (2010) 061503, doi: 10.1115/1.4000127.
12. G. Campa and S. M. Camporeale, Prediction of the thermoacoustic combustion instabilities in practical annular combustors, *J. Eng. Gas Turbines Power* **136**(9) (2014) 091504–091504, doi: 10.1115/1.4027067.
13. F. Ni, M. Miguel-Brebion, F. Nicoud and T. Poinsot, Accounting for acoustic damping in a Helmholtz solver, *AIAA J.* **55**(4) (2017) 1205–1220, doi: 10.2514/1.J055248.
14. G. Campa and S. M. Camporeale, Eigenmode analysis of the thermoacoustic combustion instabilities using a hybrid technique based on the finite element method and the transfer matrix method, *Adv. Appl. Acoust.* **1**(1) (2012) 1–14.
15. M. Åbom, Measurement of the scattering matrix of acoustical two-ports, *Mech. Syst. Signal Proces.* **5**(2) (1991) 89–104.
16. C. O. Paschereit, B. B. H. Schuermans, W. Polifke and O. Mattson, Measurement of transfer matrices and source terms of premixed flames, *J. Eng. Gas Turbines Power* **124**(2) (2002) 239–247, doi: 10.1115/1.1383255.
17. A. Fischer, C. Hirsch and T. Sattelmayer, Comparison of multi-microphone transfer matrix measurements with acoustic network models of swirl burners, *J. Sound Vib.* **298**(1–2) (2006) 73–83, doi: 10.1016/j.jsv.2006.04.040.
18. Y. Aurégan and R. Starobinski, Determination of acoustical energy dissipation/production potentiality from the acoustical transfer functions of a multiport, *Acta Acust. United with Acust.* **85**(6) (1999) 788–792.
19. A. Gentemann, A. Fischer, S. Evesque and W. Polifke, Acoustic transfer matrix reconstruction and analysis for ducts with sudden change of area, in *9th AIAA/CEAS Aeroacoustics Conf.*, AIAA-2003-3142, Hilton Head, SC, USA (2003), doi: 10.2514/6.2003-3142.
20. W. Polifke, A. Poncet, C. O. Paschereit and K. Döbbeling, Reconstruction of acoustic transfer matrices by instationary computational fluid dynamics, *J. Sound Vib.* **245**(3) (2001) 483–510, doi: 10.1006/jsvi.2001.3594.
21. S. Föller and W. Polifke, Identification of aero-acoustic scattering matrices from large eddy simulation: Application to a sudden area expansion of a duct, *J. Sound Vib.* **331**(13) (2012) 3096–3113, doi: 10.1016/j.jsv.2012.01.004.
22. C. Sovardi, S. Jaensch and W. Polifke, Concurrent identification of aero-acoustic scattering and noise sources at a flow duct singularity in low Mach number flow, *J. Sound Vib.* **377** (2016) 90–105, doi: 10.1016/j.jsv.2016.05.025.
23. A. Kierkegaard, S. Boij and G. Efraimsson, A frequency domain linearized Navier–Stokes equations approach to acoustic propagation in flow ducts with sharp edges, *J. Acoust. Soc. Am.* **127** (2010) 710–719.
24. C. Pankiewitz, A. Fischer, C. Hirsch and T. Sattelmayer, Computation of transfer matrices for gas turbine combustors including acoustics/flame interaction, in *9th AIAA/CEAS Aeroacoustics Conf. and Exhibit*, Hilton Head, SC, USA (2003).
25. C.-I. J. Young and M. J. Crocker, Prediction of transmission loss in mufflers by the finite-element method, *J. Acoust. Soc. Am.* **57**(1) (1975) 144–148, doi: 10.1121/1.380424.
26. K. S. Peat, The acoustical impedance at discontinuities of ducts in the presence of a mean flow, *J. Sound Vib.* **127**(1) (1988) 123–132.
27. P. P. Rao and P. J. Morris, Use of finite element methods in frequency domain aeroacoustics, *AIAA J.* **44**(7) (2006) 1643–1652, doi: 10.2514/1.12932.
28. J. Gikadi, S. Föller and T. Sattelmayer, Impact of turbulence on the prediction of linear aeroacoustic interactions: Acoustic response of a turbulent shear layer, *J. Sound Vib.* **333**(24) (2014) 6548–6559, doi: 10.1016/j.jsv.2014.06.033.

29. B. Cockburn, G. E. Karniadakis and C.-W. Shu (eds.), *Discontinuous Galerkin Methods*: *Theory, Computation and Applications*, Lecture Notes in Computational Science and Engineering, Vol. 11 (Springer, Berlin, 2000).
30. J. S. Hesthaven and T. Warburton, *Nodal Discontinuous Galerkin Methods*, Texts in Applied Mathematics, Vol. 54 (Springer, New York, 2008), doi: 10.1007/978-0-387-72067-8.
31. M. Meindl, A. Albayrak and W. Polifke, A discontinuous Galerkin finite element method for thermoacoustic stability analysis based on the linearized Navier–Stokes equations, Submitted to *J. Comp. Phys.* (2018) JCOMP-D-17-01782.
32. M. K. Myers, Transport of energy by disturbances in arbitrary steady flows, *J. Fluid Mech.* **226** (1991) 383–400, doi: 10.1017/S0022112091002434.
33. T. Emmert, State space modeling of thermoacoustic systems with application to intrinsic feedback, Ph.D. thesis, TU München, München, Germany (2016).
34. A. D. Pierce, *Acoustics*: *An Introduction to Its Physical Principles and Applications* (Acoustical Society of America, Woodbury, NY, 1989).
35. W. C. Ullrich, M. Schulze and T. Sattelmayer, Fundamental indirect noise generation by interactions between entropy, vorticity and acoustic waves in the context of aero engine applications, Inter-Noise 2014, Melbourne, Australia (16–19 November, 2014).
36. M. L. Munjal, *Acoustics of Ducts and Mufflers* 2nd edn. (Wiley, Chichester, West Sussex, United Kingdom, 2014).
37. K. Hamiche, G. Gabard, H. Bériot, A high-order finite element method for the linearised Euler equations, *Acta Acustica united with Acustica* **102** (2016) 813–823. https://doi.org/10.3813/AAA.918996.
38. N. Chevaugeon, K. Hillewaert, X. Gallez, P. Ploumhans and J.-F. Remacle, Optimal numerical parameterization of discontinuous Galerkin method applied to wave propagation problems, *J. Comput. Phys.* **223**(1) (2007) 188–207, doi: http://dx.doi.org/10.1016/j.jcp.2006.09.005.
39. L. Liu, X. Li and F. Q. Hu, Nonuniform time-step Runge–Kutta discontinuous Galerkin method for computational aeroacoustics, *J. Comput. Phys.* **229**(19) (2010) 6874–6897, doi: 10.1016/j.jcp.2010.05.028.
40. M. Schmid, R. Blumenthal, M. Schulze, W. Polifke and T. Sattelmayer, Quantitative stability analysis using real frequency response data, *J. Eng. Gas Turbines Power* **135**(12) (2013) 121601, doi: 10.1115/1.4025299.
41. S. Wang and V. Yang, Unsteady flow evolution in swirl injector with radial entry, II-external excitation, *Phys. Fluids* **17** (2005).
42. A. Albayrak, T. Steinbacher, T. Komarek and W. Polifke, Convective scaling of intrinsic thermoacoustic eigenfrequencies of a premixed swirl combustor, *J. Eng. Gas Turbines Power* **140**(4) (2017) 041510–041510–9, doi: 10.1115/1.4038083.
43. P. Palies, D. Durox, T. Schuller and S. Candel, The combined dynamics of swirler and turbulent premixed swirling flames, *Combust. Flame* **157**(9) (2010) 1698–1717, doi: 10.1016/j.combustflame.2010.02.011.
44. M. Merk, R. Gaudron, M. Gatti, C. Mirat, T. Schuller and W. Polifke, Measurement and simulation of combustion noise and dynamics of a confined swirl flame, *AIAA J.* **56**(5) (2018) 1930–1942, doi: 10.2514/1.J056502.
45. CERFACS and IMFT, *The AVBP HandBook*, http://www.cerfacs.fr/avbp6x/. (2008).
46. L. Selle, G. Lartigue, T. Poinsot, R. Koch, K.-U. Schildmacher, W. Krebs, B. Prade, P. Kaufmann and D. Veynante, Compressible large eddy simulation of turbulent combustion in complex geometry on unstructured meshes, *Combust. Flame* **137**(4) (2004) 489–505, doi: 10.1016/j.combustflame.2004.03.008.

47. L. Y. M. Gicquel, G. Staffelbach and T. Poinsot, Large eddy simulations of gaseous flames in gas turbine combustion chambers, *Prog. Energy Combust. Sci.* **38**(6) (2012) 782–817, doi: 10.1016/j.pecs.2012.04.004.
48. F. Nicoud and F. Ducros, Subgrid-scale stress modelling based on the square of the velocity gradient tensor, *Flow Turbulence Combust.* **62**(3) (1999) 183–200, doi: 10.1023/A:1009995426001.
49. W. Polifke, C. Wall and P. Moin, Partially reflecting and non-reflecting boundary conditions for simulation of compressible viscous flow, *J. Comput. Phys.* **213** (2006) 437–449, doi: 10.1016/j.jcp.2005.08.016.
50. A. Michalke, On spatially growing disturbances in an inviscid shear layer, *J. Fluid Mech.* **23**(03) (1965) 521, doi: 10.1017/S0022112065001520.
51. J. Gikadi, M. Schulze, S. Föller, J. Schwing and T. Sattelmayer, Linearized Navier–Stokes and Euler equations for the determination of the acoustic scattering behaviour of an area expansion, in *18th AIAA/CEAS Conf.* (Colorado Springs, CO, USA, 2012).
52. S. W. Rienstra and A. Hirschberg, An introduction to acoustics, Technical Report IWDE 92-06, Eindhoven University of Technology (2015).
53. M. S. Howe, *Theory of Vortex Sound*, Series: Cambridge Texts in Applied Mathematics (Cambridge University Press, New York, 2003). Library Catalog: Library of Congress ISBN, Call Number: TA357.H69 2003.
54. M. Howe, *Acoustics and Aerodynamic Sound* (Cambridge University Press, Cambridge, 2015), doi: 10.1017/CBO9781107360273.
55. G. F. Carnevale, O. U. Velasco Fuentes and P. Orlandi, Inviscid dipole-vortex rebound from a wall or coast, *J. Fluid Mech.* **351** (1997) 75–103, doi: 10.1017/S0022112097007155.
56. H. Schlichting and K. Gersten, *Boundary-Layer Theory* (Springer, Berlin, NY, 2016).
57. M. S. Howe, The role of displacement thickness fluctuations in hydroacoustics, and the jet-drive mechanism of the flue organ pipe, *Proc. Roy. Soc. London. Series A, Math. Phys. Sci.* **374** (1981) 543–568.
58. A. P. Dowling, The calculation of thermoacoustic oscillation, *J. Sound Vib.* **180**(4) (1995) 557–581, doi: 10.1006/jsvi.1995.0100.
59. M. Bauerheim, J.-F. Parmentier, P. Salas, F. Nicoud and T. Poinsot, An analytical model for azimuthal thermoacoustic modes in an annular chamber fed by an annular plenum, *Combust. Flame* **161**(5) (2014) 1374–1389, doi: 10.1016/j.combustflame.2013.11.014.
60. F. Nicoud, L. Benoit, C. Sensiau and T. Poinsot, Acoustic modes in combustors with complex impedances and multidimensional active flames, *AIAA J.* **45**(2) (2007) 426–441, doi: 10.2514/1.24933.
61. J. Gikadi, Prediction of acoustic modes in combustors using linearized Navier–Stokes equations in frequency space, Phd thesis, Technische Universität München, Garching, Germany (2013).
62. M. Schulze, T. Hummel, N. Klarmann, F. M. Berger, B. Schuermans and T. Sattelmayer, Linearized Euler equations for the prediction of linear high-frequency stability in gas turbine combustors, *J. Eng. Gas Turbines Power* **139**(3) (2016) 031510, doi: 10.1115/1.4034453.
63. A. Avdonin, M. Meindl and W. Polifke, Thermoacoustic analysis of a laminar premixed flame using a linearized reacting flow solver, in *Submitted to 37th Int. Symp. on Combustion*, Dublin, Ireland (2018).
64. B. B. H. Schuermans, W. Polifke, C. O. Paschereit and J. H. van der Linden, Prediction of acoustic pressure spectra in combustion systems using swirl stabilized gas turbine burners, in *IGTI TE2000*, ASME 2000-GT-105, Munich, Germany (2000).
65. L. Tay-Wo-Chong, S. Bomberg, A. Ulhaq, T. Komarek and W. Polifke, Comparative validation study on identification of premixed flame transfer function, *J. Eng. Gas Turbines Power* **134**(2) (2012) 021502-1–8, doi: 10.1115/1.4004183.

66. B. T. Chu, On the generation of pressure waves at a plane flame front, in *4th Symp.* (*Int.*) *on Combustion*, Vol. 4 (Cambridge, Massachusetts, USA, 1953), pp. 603–612. Combustion Institute. doi: 10.1016/S0082-0784(53)80081-0.
67. E. P. Wanke, FE-VerfahrenZur Analyse Der Thermoakustischen Stabilität Nichtisentroper Strömungen, Phd thesis (2010).
68. T. Emmert, S. Bomberg, S. Jaensch and W. Polifke, Acoustic and intrinsic thermoacoustic modes of a premixed combustor, in *36th Int. Symp. on Combustion*, Seoul, Korea (2016), doi: 10.1016/j.proci.2016.08.002.
69. M. Hoeijmakers, V. Kornilov, I. L. Arteaga, P. de Goey and H. Nijmeijer, Intrinsic instability of flame-acoustic coupling, *Combust. Flame* **161**(11) (2014) 2860–2867, doi: 10.1016/j.combustflame.2014.05.009.

Journal of Sound and Vibration 481 (2020) 115431

Contents lists available at ScienceDirect

Journal of Sound and Vibration

journal homepage: www.elsevier.com/locate/jsvi

A state-space formulation of a discontinuous Galerkin method for thermoacoustic stability analysis

M. Meindl, A. Albayrak, W. Polifke *

Technical University of Munich, 85747, Garching, Germany

ARTICLE INFO

Article history:
Received 6 September 2019
Revised 20 February 2020
Accepted 30 April 2020
Available online 8 May 2020
Handling Editor: O. Guasch

Keywords:
Discontinuous Galerkin
State-space
Eigenvalues
Linearized Navier-Stokes
Thermoacoustics

ABSTRACT

A hybrid approach for thermoacoustic stability analysis is formulated in a state-space framework. The approach distinguishes between regions of the computational domain with and without important interactions between acoustics and mean flow or unsteady heat release, respectively. The former regions are modeled by a discontinuous Galerkin finite element method (DG-FEM) for the linearized Navier-Stokes equations in conservative form. The latter are represented by reduced-order models of acoustic wave propagation or dissipation, and provide complex-valued, frequency dependent impedance boundary conditions for the DG-FEM domain. The flow-flame coupling is modeled by a flame transfer function that governs a volumetric source term for the fluctuating heat release rate.

The respective (sub-)models are formulated and interconnected in a state-space framework, which facilitates the monolithic formulation of hybrid thermoacoustic models. Moreover, the state-space interconnect framework makes it possible to formulate thermoacoustic stability analysis as a linear eigenvalue problem – even if flame transfer function or acoustic boundary conditions depend in a non-trivial manner on frequency.

The approach is first verified against analytical solutions for a duct with mean flow across a thin heat source, similar to a Rijke tube. Then the thermoacoustic eigenmodes of a premixed, swirl-stabilized combustor are computed in order to validate the method against experimental data for a configuration of applied interest. For this second validation case, a detailed comparison against predictions of a low-order network-model is also presented.

1. Introduction

Thermoacoustic instabilities are a phenomenon that results from interactions between heat release (e.g. by combustion) and acoustic waves. Many industrial configurations, such as rocket engines or aero-engines as well as stationary gas turbines are subject to these instabilities. In particular, with the introduction of lean premixed combustion, gas turbines have become very susceptible to combustion instabilities. Limited operational range, increased emissions and even fatal damage to an engine are undesirable possible consequences. Due to the high costs and difficulty of measurements in experimental setups, analytical and numerical investigations are the method of choice to assess thermoacoustic stability. High-fidelity simulation of compressible, reactive, turbulent flow requires high spatial and temporal resolution [1–3] and demands very significant computational effort. In this situation, reduced order models (ROM) constitute a useful alternative or complement, in particular for parameter studies.

* Corresponding author.
E-mail address: polifke@tum.de (W. Polifke).

https://doi.org/10.1016/j.jsv.2020.115431
0022-460X/

ROMs range from low-order network models that make use of analytical solutions for simple elements such as ducts and area jumps [4–11], to methods for solving linearized 2D/3D compressible flow equations [12–23].

Typically, ROMs for thermoacoustic stability analysis are *hybrid methods* inasmuch as they do not resolve the flame dynamics. For example, the intricacies of vortex generation by acoustic waves or perturbations of flame shape and the consequential modulation of flame heat release rate [24–27] were not explicitly represented in the studies [4–21,28]. Instead, flow-flame interaction was taken into account by flame transfer functions (FTF) based on analytical models, experimental or simulation data.

Reliable prediction of thermoacoustic stability requires not only accurate representation of the flow-flame-acoustic interactions that drive thermoacoustic oscillations, but also adequate models for other acoustic-hydrodynamic interactions that contribute to the balance of perturbation energy. For example, vortex shedding may occur whenever an acoustic wave propagates through a shear layer in the mean flow. In combustors, shear layers are often found between the flame and a recirculation zone, where they support stable combustion. Viscous dissipation of vorticity then results in an overall reduction of perturbation energy. On the other hand, secondary sources of sound may emerge when vortical structures collide with a solid surface. Furthermore, non-uniformities of entropy (so-called "hot spots" or "entropy waves") are typically generated by inhomogeneities in the fuel/air mixture that occur when the mixing process is disturbed by acoustic waves. When accelerated (e.g. in a downstream nozzle), these hot spots generate acoustic waves that can contribute to an unstable thermoacoustic system [7,29–32]. A major challenge for ROMs based on the wave or Helmholtz equation lies in the reproduction of these interactions between acoustic waves and hydrodynamic phenomena [23]. Fortunately, linear acoustic-hydrodynamic interactions are inherently taken into account by the linearized Navier-Stokes equations (LNSE) [13–15,18–21]. This set of equations supports vorticity and entropy waves, which are convected by the mean flow, as well as acoustic waves, which propagate with the speed of sound augmented by the mean flow velocity [25]. Note that the change of acoustic propagation velocity and the corresponding changes in eigenfrequencies are comparatively small for low Mach-numbers, the important mean flow effect is the transfer of perturbation energy between acoustic, vorticity and entropy waves that results from the interaction between perturbations and mean flow.

To conclude, it is crucial for thermoacoustic stability analysis to account for flow-flame-acoustic interactions that generate perturbation energy. This can be achieved, for example, with an accurate flame transfer function. Moreover, it is equally important that acoustic-hydrodynamic interactions, such as vortex shedding or dissipation, be taken into account in order to properly balance generation against losses of perturbation energy. Provided that mean flow fields are available—typically generated by computational fluid dynamics—the LNSE framework represents these interactions from first principles, which motivates the use of the LNSE as the basis for the modeling approach presented in this study.

The finite element method (FEM) is often employed to discretize the aeroacoustic governing equations in non trivial geometries [13–16,18–21]. Advantages over the finite volume and finite difference methods are the straightforward extensibility to higher order schemes (pFEM) and the applicability to unstructured meshes. On the other hand, a major challenge lies with the discretization of the convective terms of the aeroacoustic governing equations, which is numerically unstable if standard, continuous basis functions are applied [33]. In the last decades, discontinuous Galerkin finite element methods (DG-FEM) have become popular as a numerical approach to discretize linear and non-linear partial differential equations (e.g. Ref. [34–36]), especially for convectively dominated problems. For this type of problems the DG method has shown to constitute a framework in which stable numerical schemes can be derived that feature high accuracy and convergence potential due to *hp* convergence [37–41].

In this paper, a DG-FEM method for the compressible LNSE is formulated following the discretization approach of Baumann and Oden [35] for the non-linear Navier-Stokes equations. We demonstrate by means of comparison with semi-analytical solutions for a simplistic model of a Rijke tube that this discretization leads to highly accurate numerical results—in contrast to a well established method employing a streamline upwind/Petrov Galerkin ansatz [15]. Other than previous implementations in thermoacoustics [18–21], we keep the LNSE in conservative form. This eliminates the need for an explicit evaluation of mean flow gradients on the FEM grid and thereby avoids inconsistencies that might emerge from that procedure.

Eventually, in continuation of previous efforts in our group [10,42,43], the discretized DG-LNSE models are integrated in a seamless manner into a "state-space interconnect" framework for thermoacoustic stability analysis. Following the established hybrid approach for thermoacoustic problems, flow-flame interaction is accounted for by an FTF that relates a volumetric source term, resulting from fluctuating heat release of the flame, to the upstream acoustic velocity at earlier times.

Fundamentally, thermoacoustic systems with a time-delayed heat source represent a nonlinear eigenvalue problem (NLEVP). The non-linearity emerges from the representation of time delay terms in the Laplace domain, which results in matrix coefficients that depend on the eigenvalue, even if the governing equations per se are linear. State-of-the-art methods [12,44] employ fixed-point iterations to compute one eigenvalue at a time. Whether a given eigenvalue is actually found depends on the initial guess of the iterative solver, on the basin of attraction of the eigenvalue sought, and on the proximity of other eigenvalues, as highlighted in a recent paper by Buschmann et al. [45]. The number of iterations required for convergence also depends on these factors. In some circumstances, converging to a given eigenvalue is near impossible unless a priori knowledge of its location in the complex plane is available. Fortunately, the state-space approach facilitates a representation of time delays in terms of an advection equation. At the expense of a moderate increase in the number of degrees of freedom, the time delay can be discretized with sufficient accuracy for the frequency range of interest. This leads to models that do not explicitly depend on the frequency, such that a linear eigenvalue problem is obtained. For small to moderate problem sizes, such linear eigenvalue problems may be solved non-iteratively for multiple eigenfrequencies and without the hazards that come with initial guesses. Overall, significantly reduced computational effort may result.

With the state-space interconnect framework, parts of the configuration where acoustic-flow or flow-flame-acoustic interactions are not important may be represented by low order thermoacoustic network models [10,42], which provide complex-valued, frequency-dependent impedance boundary conditions for the LNSE domain. Again, in contrast to state-of-the-art methods [12,44], any time delays in the impedance boundary conditions are discretized utilizing an advection equation, which eliminates the explicit dependence on frequency and results in a linear eigenvalue problem. Further significant reductions in computational effort and increased flexibility in modeling complex (thermo-)acoustic systems may be realized in this way, as demonstrated in the second validation case presented in this paper.

In summary, the state-space formulation of a discontinuous Galerkin method (ssDG) introduced and validated in the present study brings significant improvement in robustness, accuracy, efficiency and flexibility for thermoacoustic stability analysis. The DG discretization of the LNSE assures robustness and accuracy. The state space interconnect framework makes possible the flexible integration of a variety of sub-models into a monolithic numerical model. The concomitant reformulation of thermoacoustic stability analysis as a linear eigenvalue problem occasions computational efficiency.

The paper is structured as follows: in the next section, the linearized Navier-Stokes equations in conservative form and the discretization with DG-FEM are presented. State-space modeling is introduced as a unified framework for thermoacoustic simulations in section 3, and it is demonstrated how the DG-FEM model is interconnected to impedance and flow-flame interaction models. Section 4 is concerned with validation of the DG-LNSE method against analytical solutions for a 1D duct case with and without unsteady heat release by comparison of eigenvalues. In section 5, the thermoacoustic stability of a turbulent swirl burner is assessed, employing interconnected state-space models originating from DG-LNSE, network model, FTF and a frequency dependent impedance boundary condition at the burner outlet. The paper concludes with a summary of the results and provides limitations as well as an outlook. Details on the vector/matrix notation of the LNSE are presented in an Appendix.

2. Discontinuous Galerkin discretization for the linearized Navier-Stokes equations

The flow perturbations considered in aeroacoustic simulations are often assumed small compared to mean flow quantities. Based on this assumption, a linearization of the governing equations around a steady-state mean flow can be employed. The resulting linear system of equations requires significantly less effort to solve than the full non-linear equations. In addition, various simplifications can be imposed on the linearized equations, e.g. isentropic or non-viscous flow. In the general case, however, the full Navier-Stokes equations are the basis for the linearization.

2.1. Linearized Navier-Stokes equations

The primitive flow field variables (pressure p, velocity u_i in x_i direction and Temperature T)

$$\mathbf{\Phi}(x_i,t)=\begin{pmatrix} p \\ u_i \\ T \end{pmatrix}, \qquad i=1\dots 3, \tag{1}$$

can be separated into a mean flow field $\overline{\mathbf{\Phi}}(x_i)$ that satisfies the steady-state Navier-Stokes equations and unsteady fluctuations $\mathbf{\Phi}'(x_i,t)$:

$$\mathbf{\Phi}(x_i,t)=\overline{\mathbf{\Phi}}(x_i)+\mathbf{\Phi}'(x_i,t) \tag{2}$$

Inserting this ansatz into the Navier-Stokes equations and assuming small perturbations $\mathbf{\Phi}'$, all except the linear terms in the fluctuating variables can be omitted. This yields the linearized Navier-Stokes equations (LNSE) in conservative form. Only the following assumptions have been made: ideal gas, Newtonian fluid and Stokes' hypothesis for the viscous terms. Viscous heating in the linearized energy conservation equation is neglected:

$$\frac{\partial \rho'}{\partial t}+\frac{\partial}{\partial x_j}\left(\overline{u}_j\rho'+\overline{\rho}u_j'\right)=0, \tag{3}$$

$$\frac{\partial}{\partial t}\left(\overline{u}_i\rho'+\overline{\rho}u_i'\right)+\frac{\partial}{\partial x_j}\left(\overline{\rho u}_i u_j'+\overline{\rho u}_j u_i'+\overline{u}_i\overline{u}_j\rho'\right)+\frac{\partial p'}{\partial x_i}=\frac{\partial \tau_{ij}'}{\partial x_j}, \tag{4}$$

$$\frac{\partial}{\partial t}(\rho e)'+\frac{\partial}{\partial x_j}\left(\overline{u}_j(\rho e)'+\overline{(\rho e)}u_j'+\overline{u}_j p'+\overline{p}u_j'\right)=\frac{\partial}{\partial x_j}\left(k\frac{\partial T'}{\partial x_j}\right)+\dot{q}_V', \tag{5}$$

with the thermal conductivity k and the volumetric heat release perturbations $\dot{q}_V'$. This source term is of prime importance in thermoacoustics as it constitutes the influence of the unsteady heat release on the perturbation field. A closure model that relates $\dot{q}_V'$ to the perturbation variables of the LNSE is discussed in section 3.6. The terms containing the total mass-specific energy e are expressed in terms of the primitive variables and the ratio of specific heats γ via

$$\overline{(\rho e)}=\frac{\overline{p}}{\gamma-1}+\frac{\overline{\rho u}_k\overline{u}_k}{2}, \qquad (\rho e)'=\frac{p'}{\gamma-1}+\frac{\overline{u}_k\overline{u}_k\rho'}{2}+\overline{\rho u}_k u_k'. \tag{6}$$

The viscous stresses are defined via Stokes' hypothesis as

$$\tau'_{ij} = \mu \left(\frac{\partial u'_i}{\partial x_j} + \frac{\partial u'_j}{\partial x_i} - \frac{2}{3} \frac{\partial u'_k}{\partial x_k} \delta_{ij} \right) \tag{7}$$

with the dynamic viscosity μ and the Kronecker-Delta δ_{ij}:

$$\delta_{ij} \equiv \begin{cases} 1 & \text{for } i = j, \\ 0 & \text{else.} \end{cases} . \tag{8}$$

This set of equations can be closed with the linearized equation of state for an ideal gas,

$$\frac{T'}{\overline{T}} = \frac{p'}{\overline{p}} - \frac{\rho'}{\overline{\rho}}, \tag{9}$$

which yields the five unknowns p', T' and u'_i with $i = 1 \dots 3$ in three dimensions. Fluctuations in entropy s' can be derived via

$$s' = c_p \frac{T'}{\overline{T}} - R \frac{p'}{\overline{p}}, \tag{10}$$

where c_p is the isobaric specific heat capacity and R is the gas-constant of the medium.

Following Baumann and Oden [35], the LNSE can be formulated in vector notation similarly to the Navier-Stokes equations:

$$\mathbf{M} \frac{\partial \mathbf{\Phi}'}{\partial t} + \frac{\partial \mathbf{F}_j(\mathbf{\Phi}')}{\partial x_j} = \frac{\partial \mathbf{F}_j^{\nu}(\mathbf{\Phi}')}{\partial x_j} + \mathbf{S}. \tag{11}$$

$\mathbf{M}$ is a matrix containing the mean flow prefactors of the time derivative terms, $\mathbf{F}_j$ and $\mathbf{F}_j^{\nu}$ are the non-viscous and viscous flux in direction x_j, respectively. $\mathbf{S}$ contains the fluctuating heat release source term for the linearized conservation of energy. Further details on the vector notation is given in the Appendix.

2.2. Discontinuous Galerkin FEM

Assuming isentropic perturbations and neglecting the mean flow velocities as well as viscous effects, the wave equation can be deduced from the LNSE. Many numerical schemes are well suited to solve the wave equation, e.g. the standard finite element [46] or the finite volume method (FVM) [12]. However, when mean flow velocities are taken into account, the application of a standard, unstabilized finite element method with continuous basis functions leads to a numerically unstable discretization scheme in cases with high cell Péclet numbers. The reason for the instability is as follows: symmetric test functions that span the neighboring elements of a node lead to a discretization similar to a central difference scheme of the finite difference method. It is known that for convection dominated problems, this scheme introduces negative numerical diffusivity, which may exceed the physical one and thus result in unstable behavior [33]. To remedy this situation, a number of stabilized finite element methods have been developed. Two well-known approaches are the streamline upwind Petrov-Galerkin method (SUPG) [47], which introduces additional numerical viscosity in streamline direction and the Galerkin Least Squares (GLS) [48] formulation, which minimizes the error of the residuum in a least squares sense to produce stable solutions. Both approaches require a stabilization parameter that controls the weighting of the correction terms in the weak form. An exact analytical expression for this parameter is in general not known for the LNSE in three dimensions, it is thus often chosen based on the characteristic wave speed, the cell size and a case-dependent pre-factor that is a priori unknown [15,21]. It has been shown that the growth rates of thermoacoustic eigenmodes depend on the choice of this parameter [21,49]. The parameter has been varied over several orders of magnitude between $\alpha_\tau = 1.0 \cdot 10^{-3}$ [18,19], $\alpha_\tau = 1.00$ [20,50] and $\alpha_\tau \in [0, 50]$ [49] for different application cases.

The problem of the symmetric discretization of the convective terms can be avoided by the use of basis functions that are discontinuous at the mesh nodes and only span one element. This makes non-symmetric discretization possible. The discontinuous Galerkin method has been applied to aeroacoustic problems of sound propagation, where excellent performance was observed [40]. This suggests the application to thermoacoustic problems, where the aeroacoustics is a crucial part of the model.

In contrast to the continuous FEM, the discontinuous nature of the discretization does not allow the integration of the governing equations over the whole domain when deriving the weak form. Instead, an element-wise derivation is pursued. A partition $\mathcal{P}_h$ of the computational domain Ω with outer boundary $\partial\Omega = \Gamma$ into $N(\mathcal{P}_h)$ non overlapping elements Ω_e is employed,

$$\Omega = \bigcup_{\Omega_e \in \mathcal{P}_h}^{N(\mathcal{P}_h)} \Omega^e. \tag{12}$$

The union of all element boundaries $\partial\Omega_e$ consists of the true outer boundary Γ of the domain as well as the internal boundaries between the elements, Γ_{Int}. The outer domain boundary is separated into Dirichlet and Neumann partitions, Γ_D and Γ_N. With $V(\mathcal{P}_h)$ being a space of nodal discontinuous trial functions, the solution vector is sought from this space,

$$\mathbf{\Phi}' = \left(\Phi'_1, \dots, \Phi'_5 \right), \qquad \Phi'_i \in V(\mathcal{P}_h). \tag{13}$$

Due to the discontinuous nature of the trial functions, two solution values are present at internal boundaries, one within the cell under consideration, $\mathbf{\Phi'}^{-}$, as well as the value of the neighboring cell, $\mathbf{\Phi'}^{+}$. For ease of representation, the following shorthand notations for any two quantities at opposing sides of internal boundaries are introduced as the average and jump operator, respectively:

$$< (\,) >= \frac{(\,)^{-} + (\,)^{+}}{2}, \qquad [(\,)] = (\,)^{-} - (\,)^{+} \tag{14}$$

Multiplication of Eq. (11) with a vector of discontinuous test functions from the same space $V(\mathcal{P}_h)$ as the trial functions

$$\mathbf{W} = \left(w_1, \dots, w_5\right), \qquad w_i \in V(\mathcal{P}_h) \tag{15}$$

and element-wise integration over the domain $\Omega = \sum_{\Omega_e \in \mathcal{P}_h} \Omega^e$ yields the variational formulation of the LNSE. Subsequent integration by parts constructs the form required for the discontinuous Galerkin finite element method. From this step, the non-viscous flux $\mathbf{F}_n = \mathbf{F}_j n_j$ as well as the viscous flux $\mathbf{F}_n^v = \mathbf{F}_j^v n_j = \mathbf{D}_n \mathbf{\Phi'}$ normal to the element boundary $\partial\Omega^e$ with outward facing normal vector components n_j arises. The weak form of the LNSE in vector notation, again following Baumann and Oden [35], reads:

$$\begin{aligned} &\sum_{\Omega_e \in \mathcal{P}_h} \int_{\Omega_e} \mathbf{W}^T \mathbf{M} \frac{\partial \mathbf{\Phi'}}{\partial t} \mathrm{d}\mathbf{x} \quad + \quad \sum_{\Omega_e \in \mathcal{P}_h} \int_{\Omega_e} \frac{\partial \mathbf{W}^T}{\partial x_j} \left(\mathbf{F}_j^v - \mathbf{F}_j\right) \mathrm{d}\mathbf{x} + \quad \sum_{\Omega_e \in \mathcal{P}_h} \int_{\partial\Omega_e} \mathbf{W}^T \mathbf{F}_n^{\star} \mathrm{d}\mathbf{s} \\ &+ \int_{\Gamma_{\mathrm{Int}}} \left(< \mathbf{W}^T \mathbf{D}_n^T > \left[\mathbf{\Phi'}\right] - \left[\mathbf{W}^T\right] < \mathbf{F}_n^v > \right) \mathrm{d}\mathbf{s} + \quad \int_{\Gamma_D} \left(\mathbf{W}^T \mathbf{D}_n^T \mathbf{\Phi'} - \mathbf{W}^T \mathbf{F}_n^v \right) \mathrm{d}\mathbf{s} \\ &= \sum_{\Omega_e \in \mathcal{P}_h} \int_{\Omega_e} \mathbf{W}^T \mathbf{S} \mathrm{d}\mathbf{x} \quad + \quad \int_{\Gamma_D} \mathbf{W}^T \mathbf{D}_n^T \widetilde{\mathbf{\Phi'}} \mathrm{d}\mathbf{s} \quad + \quad \int_{\Gamma_N} \mathbf{W}^T \widetilde{\mathbf{F}}_{\mathbf{n}^v} \mathrm{d}\mathbf{s} \quad , \end{aligned} \tag{16}$$

where $\widetilde{\mathbf{\Phi'}}$ and $\widetilde{\mathbf{F}_n^v}$ are known values of Dirichlet and Neumann boundary conditions, respectively. The linearized Euler equations can be retrieved from the LNSE by neglecting the viscous flux $\mathbf{F}_n^v$. Details on the flux formulations and their use to impose boundary conditions in the weak form are given in Appendix A.

By choosing an appropriate numerical non-viscous flux $\mathbf{F}_n^{\star}$ on internal boundaries Γ_{Int}, similar to FVM, a stable discretization can be obtained. Thus, the DG-FEM approach is often referred to as a hybrid FEM/FVM method that combines the advantages of both approaches [34,36]. Due to the choice to represent the solution with discontinuous trial functions, the numerical flux between elements may depend on the solutions on both sides of the element boundary. It is highly desirable to introduce a local flux, i.e. a flux formulation that only depends on the solution of the adjacent cells to the element boundary, in order to guarantee a very sparse equation system after discretization. Furthermore, we seek a formulation that is inherently numerically stable, independent of the time-stepping scheme. This second requirement arises from the need of computations in the frequency as well as the Laplace domain. For this study, the local Lax-Friedrichs flux has been chosen, which blends between a central and an upwind flux, based on the parameter C [40,51]:

$$\mathbf{F}_n^{\star,\mathrm{LF}} = < \mathbf{F}_n > + \frac{C}{2} \left[\mathbf{M} \mathbf{\Phi'}\right]. \tag{17}$$

Setting C equal to the maximum characteristic wave speed normal to the boundary of two neighboring elements results in a stable scheme [40]. For the LNSE, the characteristic propagation velocities are defined by the speed of sound $\overline{c} = \sqrt{\gamma \overline{RT}}$ in the mean flow field and the mean flow velocities. The maximum value results if an acoustic wave propagates in mean flow direction, which implies:

$$C = \overline{c} + \left|\overline{u}_i n_i\right|. \tag{18}$$

This expression for the parameter C is physically motivated and known before run time, as it only depends on the mean fields.

The viscous flux on internal boundaries, compare Eq. (16), is discretized with a scheme first presented by Babuŝka et al. [52] for pure diffusion problems. This scheme was also applied to convection-diffusion problems [53] as well as the Navier-Stokes equations [35]. The scheme is element-wise conservative, does not require a hybrid basis function approach and leads to a block diagonal mass matrix with uncoupled blocks [52].

A problem emerging due to the perturbation ansatz is the need for steady-state mean flow fields as a basis for the LNSE. The interpolation of mean field variables $\overline{\mathbf{\Phi}}$ from a highly resolved large eddy simulation (LES), say, to a more coarse mesh as typically used in aeroacoustic computations gives rise to inconsistencies: Spatial derivatives of $\overline{\mathbf{\Phi}}$ can be obtained either by interpolation of the gradients computed on the LES mesh, or by evaluation on the computational aeroacoustic (CAA) grid based on the interpolated mean field variables. The derivatives obtained by these approaches will in general differ. This effect contributes to the mesh dependence of CAA results. The advantage of integration by parts of the conservative formulation shows in the fact that no explicit evaluation of spatial derivatives of the mean field variables is required. This contributes to high reliability in the prediction of thermoacoustic instabilities, especially regarding the correct representation of dissipation mechanisms.

The described DG-LNSE method has been implemented within the commercial FEM software COMSOL Multiphysics version 5.3 [54]. Throughout this study, a numerical quadrature of the flux terms with order adapted to the highest polynomial degree of the integrand is employed to ensure accurate integration.

3. Thermoacoustic state-space modeling

A wide range of models for thermoacoustic stability analysis exists. The DG-FEM model based on the LNSE presented in the previous section describes propagation and dissipation of acoustic waves in the presence of mean flow (and mean temperature gradients), but does not resolve the response of a flame to acoustic perturbations and the ensuing fluctuations of heat release rate, which generate sound. In other words, a closure model for flow-flame-acoustic interaction is required. Additionally, non-trivial boundary conditions such as impedances that depend on frequency, are often required, e.g. for up- and downstream boundaries of a combustion chamber or damping devices. In order to couple models for unsteady heat release rate and non-trivial boundary conditions to a DG-FEM model, a unifying representation is desired. A robust and efficient framework for linear, time-invariant systems, which also facilitates coupling of sub-models, is the state-space formalism. Indeed, a variety of state-space models for thermoacoustic stability analysis have been proposed and employed in several prior studies [9,55–59].

The following sections focus on the representation of the various elements of a thermoacoustic model in state-space form with the goal in mind of retaining a linear eigenvalue problem. This includes the DG-FEM model, the flame transfer function that connects the fluctuating heat release to acoustic perturbations, as well as non-trivial acoustic boundary conditions. The connection of these models creates a monolithic state-space/DG-FEM (ssDG) model which comprises the complete thermoacoustic dynamics.

3.1. State-space representation

State-space models are a well researched, flexible and robust representation of coupled, linear, first order ordinary differential equations in time. The generalized formulation reads

$$\mathbf{E}\frac{\mathrm{d}\mathbf{x}(t)}{\mathrm{d}t} = \mathbf{A}\mathbf{x}(t) + \mathbf{B}\mathbf{u}(t), \tag{19}$$

$$\mathbf{y}(t) = \mathbf{C}\mathbf{x}(t) + \mathbf{D}\mathbf{u}(t). \tag{20}$$

The time-dependent state-vector $\mathbf{x}(t)$ contains N unknown variables, $\mathbf{u}(t)$ and $\mathbf{y}(t)$ are vectors of in- and outputs respectively. Due to the constant coefficient matrices $\mathbf{A}$ to $\mathbf{E}$, state-space models are linear time-invariant (LTI). Equation (19) is called the system equation and determines the autonomous dynamics of the system through the mass matrix $\mathbf{E}$ and the system matrix $\mathbf{A}$, as well as the impact of inputs $\mathbf{u}(t)$ on the system via $\mathbf{B}$. Equation (20) defines the outputs $\mathbf{y}(t)$ as linear combinations of the states $\mathbf{x}(t)$ and the inputs $\mathbf{u}(t)$ through the output matrix $\mathbf{C}$ and the feed-through matrix $\mathbf{D}$. Note that for a single system, the output equation does not contribute to the system dynamics and can therefore be chosen to define any outputs.

3.2. Eigenvalue computation in the Laplace domain

We assume that a quantity $a(t)$ in the time domain behaves like a harmonically oscillating, exponentially growing or decaying signal, i.e.

$$a(t) \;\rightarrow\; \widehat{a}(s)e^{st}. \tag{21}$$

Here $s = s_r + is_{im}$ is the Laplace variable with the growth rate s_r as the real part and the oscillation frequency s_{im} as the imaginary part. The hat $\widehat{(\,)}$ denotes a complex amplitude. When applied to a state-space model, a system that is linearly dependent on s is retrieved,

$$\mathbf{E}s\widehat{\mathbf{x}}(s) = \mathbf{A}\widehat{\mathbf{x}}(s) + \mathbf{B}\widehat{\mathbf{u}}(s), \tag{22}$$

$$\widehat{\mathbf{y}}(s) = \mathbf{C}\widehat{\mathbf{x}}(s) + \mathbf{D}\widehat{\mathbf{u}}(s). \tag{23}$$

Based on this state-space system in the Laplace domain, the eigenvalues can be computed, which is a common approach to linear thermoacoustic stability analysis. The system is called linearly stable if all eigenvalues have a negative real part, $s_r < 0$, i.e. the eigenmodes decay in amplitude. For state-space models with a moderate number of degrees of freedom, $N \lessapprox 10^4$, say, the full set of eigenvalues can be computed non-iteratively in one single computation, e.g. by means of the QR algorithm. For larger systems, this is not feasible due to excessive memory demands. Instead, assumptions about the frequency range in which instabilities might occur are made. Then, a number of eigenmodes are computed in the vicinity of complex shift frequencies $\sigma = \sigma_r + i\sigma_{im}$. The implicitly restarted iterative Arnoldi algorithm may be employed to solve the shift-and-invert eigenvalue problem for a state-space system [60], until a set number of eigenvalues and corresponding eigenvectors are converged within a given tolerance:

$$(\mathbf{A} - \sigma\mathbf{E})^{-1}\mathbf{E}\widehat{\mathbf{v}} = \nu\widehat{\mathbf{v}} \quad \text{with} \quad \nu = \frac{1}{s-\sigma}. \tag{24}$$

The complex-valued eigenvectors $\widehat{\mathbf{v}}(s)$ of the state variables correspond to the shape of the eigenmode.

In order to solve Eq. (24), this study employs an LU decomposition of $(\mathbf{A} - \sigma\mathbf{E})$ in a lower and an upper triangular matrix with the parallel direct solver MUMPS [61], which is well suited for sparse systems as they typically result from FEM discretization.

Note that the state-space method does not necessarily rely on these algorithms, both the iterative Arnoldi as well as MUMPS could be replaced by other suitable methods. On the other hand, if the fixed-point iteration method is employed for a NLEVP, an outer loop is added to this procedure because the system matrices explicitly depend on the eigenvalue. For every iteration (around 25 per eigenvalue, as reported by Buschmann et al. [45]), the matrices have to be reconstructed and newly factorized. Conversely, if time-delays are discretized in order to obtain a linear eigenvalue problem, only one decomposition of $(\mathbf{A} - \sigma\mathbf{E})$ – which is the main computational effort for large systems – is required.

As an alternative to the state-space approach or fixed-point iteration, Beyn's method [62] of computing the eigenvalues in a given region of the complex plane can be employed. By means of a contour integration, it is ensured that all eigenvalues within this region are indeed found, without the hazards of initial guesses. The contour integral is computed by numerical integration, utilizing several sampling points on the chosen contour. For example, Buschmann et al. [45] report the use of 256 sampling points for a thermoacoustic system. The completeness of eigenvalues comes at the cost of multiple solutions of linear systems with dimensionality of the original problem on the contour. Additionally, one is advised to confirm that eigenvalues are indeed actual solutions of the problem by employing a small number of fixed-point iterations on the results of the contour integration [45].

3.3. Discretized DG-FEM models

The spatial discretization of the LNSE using the DG method as detailed in section 2 leads to a linear system of ordinary differential equations:

$$\mathbf{E}\frac{\mathrm{d}\boldsymbol{\Phi}'_h(t)}{\mathrm{d}t} + \mathbf{K}\boldsymbol{\Phi}'_h(t) = \mathbf{L}(t). \tag{25}$$

$\mathbf{E}$ is the mass matrix, $\mathbf{K}$ is the stiffness matrix, $\mathbf{L}$ is the load vector and $\boldsymbol{\Phi}'_h(t)$ contains the unknowns $\boldsymbol{\Phi}'$ at the mesh nodes. The generation of the state-space system, Eq. (19), from (25) is straight forward: We choose $\mathbf{x}(t) = \boldsymbol{\Phi}'_{\boldsymbol{h}}(t)$, $\mathbf{A} = -\mathbf{K}$ and the load vector $\mathbf{L}(t)$ is split into a matrix with constant coefficients $\mathbf{B}$ and a vector containing the time-dependent input signals $\mathbf{u}(t)$. These input signals emerge from the inhomogeneous terms of the LNSE, e.g. boundary conditions or source terms. As stated before, $\mathbf{C}$ and $\mathbf{D}$ can be chosen arbitrary without changing the system dynamics. Section 3.7 will show that an appropriate choice of outputs of the LNSE state-space model will facilitate coupling to an FTF on the one hand and to network models for non-trivial acoustic impedance boundary conditions on the other.

3.4. Network modeling

Network-models, also called characteristic wave models, are modular, 1D tools that allow inexpensive thermoacoustic analysis. The method is based on elements for which the acoustic transmission and reflection behavior of characteristic waves is known from analytical expressions. Some examples are ducts, area jumps or (partially) reflective terminations. By combination and connection of multiple elements, a full thermoacoustic system can be modeled [4–11].

All elements except for ducts are treated as acoustically compact and do not need spatial discretization. The wave propagation in ducts is governed by the 1D convected Helmholtz equation with constant mean flow velocity. An analytical diagonalization of the convected Helmholtz equation yields two advection equations for the acoustic plane waves f and g with the characteristic velocity $\overline{u} + \overline{c}$ and $\overline{u} - \overline{c}$, respectively [10],

$$f = \frac{1}{2}\left(\frac{p'}{\overline{\rho c}} + u'_1\right), \qquad g = \frac{1}{2}\left(\frac{p'}{\overline{\rho c}} - u'_1\right), \tag{26}$$

$$\frac{\partial f}{\partial t} + (\overline{u} + \overline{c})\frac{\partial f}{\partial x} = 0, \qquad \frac{\partial g}{\partial t} + (\overline{u} - \overline{c})\frac{\partial g}{\partial x} = 0. \tag{27}$$

These equations are only coupled at specific locations, i.e. the "nodes" of the network model, which represent boundaries or duct singularities such as area jumps or changes of the specific impedance of the mean flow. In ducts with constant cross-sectional area and mean flow however, they can be treated separately. Higher order finite difference upwinding schemes are employed for the spatial discretization of the advection equations for f and g in the thermoacoustic network tool *taX* [42]. Due to the nature of the advection equation (first order in time, LTI), the semi-discrete, spatially discretized equation can be represented in state-space form [10,42]. A connection between multiple elements is established by matching the characteristic acoustic waves at the nodes, see also section 3.7.

For single or multiple connected network elements in the state-space framework, a transfer function $\mathbf{G}(s)$ between selected in- and outputs can be computed via

$$\mathbf{G}(s) = \frac{\widehat{\mathbf{y}}(s)}{\widehat{\mathbf{u}}(s)} = \mathbf{C}(\mathbf{E}s - \mathbf{A})^{-1}\mathbf{B} + \mathbf{D}. \tag{28}$$

By way of example, let us consider the connection of a duct to a partially reflecting termination at the downstream end of a combustion chamber. For this model, the characteristic wave entering and exiting the duct at the upstream end are the respective in- and outputs for the state-space model. The transfer function of this connected model represents a complex impedance that

is also valid for signals with non-zero growth rate, $s_r \neq 0$. This fact plays an important role in thermoacoustic stability analysis, because the growth rate of the eigenmodes is the desired result.

3.5. Discretization of single time lags and complex impedances

Time lags, e.g. between an acoustic disturbance and the fluctuating heat release of the heat source, can be represented in pseudo-space using an advection equation,

$$\frac{\partial \beta}{\partial t} + \frac{\partial \beta}{\partial \xi} = 0. \tag{29}$$

Here, β is the quantity transported along ξ with speed 1.00. Assuming a domain $[0, \tau]$ along the ξ direction, a signal entering the domain at time $t = 0$ will arrive at the end of the domain at time $t = \tau$. Discretizing Eq. (29) in ξ direction, again utilizing a finite difference upwinding scheme, a linear, time-invariant system of equations is obtained that can be represented in the state-space framework [42,43]. Note that the discretized system of equations does not depend explicitly on the time lag τ. As a consequence, when represented in the Laplace domain, the state-space system, Eq. (19), remains linear in the Laplace variable s. On the contrary, if the time delay is not discretized, a non-linear term $e^{-s\tau}$ emerges that leads to a NLEVP [12,45], which can be solved e.g. by fixed-point iteration in s:

$$a(t-\tau) \;\rightarrow\; \hat{a}(s)e^{st}e^{-s\tau}. \tag{30}$$

A validation for an FTF with a single time delay within the state-space framework, i.e. the so-called n-τ model, was conducted in Ref. [43] and showed reasonable agreement with results produced with the FVM Helmholtz solver AVSP [12,63], which relies on fixed-point iteration for solution of the non-linear eigenvalue problem.

The discretization of the time lag however adds additional degrees of freedom, equal to the number of discretization points chosen. In order to adequately represent the time delay in a given frequency band, best practice rules suggest at least 20 points per wavelength for the highest frequency of interest. When less points are used, errors due to aliasing can be expected. As an example, a time delay of $\tau = 1$ ms should be discretized with at least 40 points to be accurately represented in the frequency band of up to 2000 Hz. The increased number of degrees of freedom for thermoacoustic models due to time lag discretization is usually small compared to those emerging from FEM models. Therefore, the savings in computational cost by avoiding multiple factorizations of the full system matrix by far outweigh the costs due to the increased size of the system.

3.6. Representation of an FTF with distributed time lags

The interaction between the heat release of a flame and acoustic waves is a key element in thermoacoustic systems. This mechanism is the main driver of instabilities and thus, care has to be taken to accurately include the dynamics in the thermoacoustic model. The most accurate description can be retrieved by locally accounting for the influence of acoustic perturbations on the combustion mechanism [64]. This is very expensive as it adds linearized transport equations for the chemical species to the LNSE and requires a highly refined numerical mesh in the flame area to correctly model the unsteady heat release via a linearized combustion mechanism. The typical low-order models used to represent the flow-flame interaction are so called flame transfer functions (FTF). These models often link the overall unsteady heat release $\dot{Q}'$ to the fluctuation of the axial velocity u'_{ref} at a reference position, which is the main cause for unsteady combustion of premixed flames. The FTF model in the Laplace domain reads

$$\frac{\hat{\dot{Q}}}{\bar{\dot{Q}}} = \frac{\hat{u}_{1,\text{ref}}}{\bar{u}_{1,\text{ref}}}\text{FTF}(s). \tag{31}$$

In the LNSE model, $\hat{\dot{Q}}$ is represented by the integral of the spatially distributed source term, $\int_\Omega \hat{\dot{q}}_V(x_i)d\Omega$, while in the network model, the spatial extent of acoustically compact flames is neglected and $\hat{\dot{Q}}$ is a global quantity.

Subramanian et al. [65] showed that distributed time-lag response functions (DTL) can capture the flame dynamics very well in the context of linear stability assessment. Typically, the frequency response function of a flame can be deduced either experimentally or numerically. A DTL can be derived from this data by fitting a rational polynomial to the frequency response function and applying the inverse Fourier transformation to obtain the impulse response as a sum of exponential functions in the time domain [65]. The convolution of this impulse response function with the time-lagged velocity fluctuations u'_{ref} then produces a representation in state-space form. For details on this procedure, the reader is referred to Ref. [65]. As already discussed in section 3.2, state-space models are linear in the Laplace variable after transformation and therefore DTL FTF models retain the linearity of the eigenvalue problem.

3.7. Interconnection of state-space models

The connection of two FEM models for acoustic governing equations via a transfer matrix, relating the plane acoustic waves between both model interfaces, was originally proposed, implemented and validated by Camporeale and co-workers [16,28].

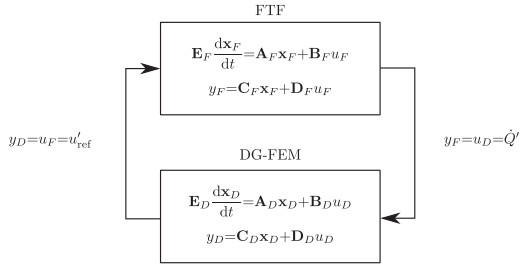

Fig. 1. Schematic representing the connection of the FTF to the DG-FEM state-space model with scalar in- and outputs.

The transfer matrix is usually used for elements of a (thermo-) acoustic system where the acoustic governing equations can not represent the complex flow or are too expensive to solve for. In a follow-up study, Campa et al. [17] used a transfer matrix to connect an annular plenum to a combustion chamber and incorporate the effects of acoustic time-delays, a variation in cross-section and damping. Similarly, Schulze and Sattelmayer [22] coupled FEM models of the dome and the nozzle of a rocket engine via the scattering matrix of a perforated plate, which relates the characteristic waves *f* and *g* at two interfaces, in order to reduce the degrees of freedom and correctly account for damping. Ni et al. [23] coupled transfer matrices for a diaphragm and a swirler, respectively, to a Helmholtz solver.

In the present study, a state-space model of the FTF is connected to the DG-FEM model to account for the flow-flame interaction. Furthermore, parts of the geometry in which one-dimensional acoustic waves with negligible mean flow interaction can be assumed, are represented by complex impedances derived from the network modeling tool *taX* instead of three-dimensional DG-FEM. The respective sub-models are then connected to the DG-FEM model in the same way as the FTF state-space model in order to reduce the degrees of freedom of the whole thermoacoustic model.

The preceding sections have shown that models for the acoustic governing equations as well as the flame response can be represented in state-space form. The interfaces of these models are the in- and outputs. Some of the inputs of one model match the output of another, compare e.g. the output $\dot{Q}'$ of the FTF, Eq. (31), which is the input to the acoustic LNSE model ($\dot{q}'_V$, which is the spatially resolved global fluctuating heat release rate $\dot{Q}'$, source term in Eq. (5)). Vice versa, the velocity fluctuation at the reference position, u'_{ref}, is an output of the LNSE and an input of the FTF, see Fig. 1.

In order to form a monolithic state-space model, these internal input-output relations need to be interconnected. To this end, the individual matrices $\mathbf{A}_i$ to $\mathbf{E}_i$ of the models are appended in block-diagonal matrices $\widetilde{\mathbf{A}}$ to $\widetilde{\mathbf{E}}$, following Emmert et al. [10]. In addition to the five matrices emerging from this procedure, a feedback equation is established for matching internal in- and output relations:

$$\widetilde{\mathbf{u}} = \mathbf{F}\widetilde{\mathbf{y}} + \mathbf{u}. \tag{32}$$

The vector of inputs $\widetilde{\mathbf{u}}$ of the connected system consists of internal outputs $\widetilde{\mathbf{y}}$, which are fed back into the system via a binary feedback matrix $\mathbf{F}$, and the true external inputs $\mathbf{u}$. Examples for the latter could, e.g., be external acoustic forcing at a boundary. By applying the output Eq. (20) to $\widetilde{\mathbf{y}}$, the feedback loop can be resolved and a monolithic state-space system is retrieved in the standard form, Eqs. (19) and (20). Details on this procedure are presented in Ref. [10]. This unifying state-space interconnect framework allows for efficient and robust algorithms to perform time and frequency domain computations as well as assessing the system stability by eigenvalues.

4. Validation case: duct with temperature discontinuity

A first validation of the DG-LNSE method is carried out against semi-analytical solutions presented by Dowling in Ref. [4] for a duct of length L with a discontinuity in the mean fields $\overline{\mathbf{\Phi}}(x)$ at the location $x = b$. The discontinuity is caused by an infinitely thin heat source and is characterized by the ratio of mean stagnation temperatures $\overline{T}_{0,d}/\overline{T}_{0,u}$, where the indices u and d refer to the upstream and downstream part of the duct, respectively. This validation case might appear simplistic, but indeed is challenging for FEM-based thermoacoustic solvers and has been exploited in previous studies [12,15].

The material properties of the gas are assumed constant throughout the domain. The inlet Mach number M_u is varied from 0 to 0.2. The full set of parameters is shown in Table 1. Two different cases regarding the unsteady heat release are considered for validation in this paper:

Case I: No unsteady heat release of the flame, $\dot{q}'_V = 0$.

Case II: No unsteady heat input per unit mass. This yields $\dot{q}'_V = c_p(\overline{T}_{0,d} - \overline{T}_{0,u})(\overline{\rho}_u u'_u + \overline{u}_u \rho'_u)/\delta_{\mathrm{Q}}$ [4], where δ_{Q} is the finite length of the heat release area for the numerical simulations. Note that this is required because of the volumetric source-term $\dot{q}'_V$. The fluctuating values of u'_u and ρ'_u for the numerical approach are evaluated at the reference position x_{ref} upstream of the discontinuity.

Table 1
Parameters for the validation case.

Parameter	Variable	Value
duct length	L	1 m
position of temperature discontinuity	b	0.5 m
thickness of numerical heat release area	δ_Q	cell width h
reference position for unsteady heat release	x_{ref}	$b - 1 \times 10^{-3} m$
heat capacity at constant pressure	c_p	1004.5 J/(kgK)
ratio of specific heats	γ	1.4
ratio of mean stagnation temperatures	$\overline{T}_{0,d}/\overline{T}_{0,u}$	6
inlet Mach number	M_u	0, 0.02, …, 0.2
dynamic viscosity	μ	0kg/(ms)
thermal conductivity	k	0 W/(mK)

Case II corresponds to an infinitely fast combustion chemistry, i.e. heat release without time delay, which is an assumption that will be dropped for the case of the premixed swirl stabilized burner (section 5).

Two flow-acoustic interaction mechanisms are present in this case. The first is the generation of entropy waves when an acoustic wave crosses the temperature discontinuity. In this process, disturbance energy is transferred from the acoustic wave to an entropy fluctuation that is then convected out of the domain. The second phenomenon contributing to the attenuation is the convection of acoustic energy across the outlet ($x = L$). Due to the fact that both mechanisms scale with the mean flow velocity, an increased net loss of perturbation energy, resulting in an increased damping rate, is expected for higher inlet Mach numbers. Viscous effects have been neglected for the numerical studies in order to achieve comparable results to the non-viscous semi-analytical model [4]. An important difference between the cases considered is that, while the analytical method employs jump conditions derived from first principles at the discontinuity, a continuous domain is considered in the numerical approach. Due to the very thin heat release area in case II, high spatial resolution of the FEM model with up to $1.0 \cdot 10^{+6}$ cells, corresponding to $9.0 \cdot 10^{+6}$ degrees of freedom with quadratic basis functions, is required.

The boundary conditions are an isentropic inlet with constant mass flow,

$$s' = 0 \qquad \text{and} \qquad \dot{m}' = \rho' \overline{u} + u' \overline{\rho} = 0, \tag{33}$$

as well as an acoustically open end at the outlet,

$$p' = 0. \tag{34}$$

The source-term for the unsteady heat release in case II is only present in the first cell of width h downstream of the discontinuity. The reference position x_{ref} of u'_u and ρ'_u has been chosen to be 1×10^{-3}m upstream of the temperature discontinuity to avoid direct feedback of the heat release.

Fig. 2 shows the computed eigenvalues of the semi-analytical and the DG-LNSE approach. The latter employed a cell width $h = 1 \times 10^{-4}$ m (case I) and $h = 1 \times 10^{-6}$m (case II) in conjunction with quadratic basis functions. Due to the high degrees of freedom emerging for discretizations with low cell widths, the shift-inverted eigenvalue problem is solved. The eigenvalues predicted by the semi-analytical model are used as shifts for the DG-LNSE model. All modes were computed using the direct solver MUMPS and the iterative Arnoldi algorithm with a relative tolerance of $1.0 \cdot 10^{-7}$. Mode shapes similar to a quarter wave resonator can be observed for the acoustic quantities u' and p' (not shown). In ascending oscillation frequency, these are the 1/4, 3/4 and 5/4 modes. As expected, the growth rate s_r as well as the oscillation frequency s_{im} of the eigenmodes decrease with an increase in inlet Mach number. Note that all of these modes are stable ($s_r < 0$) except for $M_u = 0$, where neutral stability ($s_r = 0$) occurs. The small deviation in case II can be attributed to the required distance between the measurement point x_{ref} for the heat release coupling as well as the finite thickness δ_Q of the heat release, while the semi-analytical model uses the reference values directly at the upstream side of the discontinuity with jump conditions to model the impact of the heat release.

Fig. 3 shows the relative error ϵ of the eigenfrequencies for increasing mesh refinement. For this convergence study, linear and quadratic, nodal discontinuous basis functions have been employed. ϵ is the relative error of the eigenfrequencies averaged over all three modes ($N_s = 3$) and all Mach numbers ($N_M = 11$) defined in Table 1,

$$\epsilon = \frac{1}{N_M N_s} \sum_{i=1}^{N_M} \sum_{j=1}^{N_s} \frac{\left\| s_{i,j,\text{DG}} - s_{i,j,\text{analytical}} \right\|_2}{\left\| s_{i,j,\text{analytical}} \right\|_2}. \tag{35}$$

For case I, convergence within the iterative Arnoldi tolerance is achieved both for linear and quadratic basis functions. The distance between the reference position as well as the finite thickness of the heat release zone limit the convergence for case II, a mesh refinement beyond $h = 1 \times 10^{-5}$m does not increase the accuracy of the results. Slower convergence compared to case I can be observed due to the decreasing size of the heat release zone (one cell).

This validation case shows that the DG-LNSE method can very accurately represent interactions between acoustics and mean flow as well as fluctuating heat release occurring in thermoacoustic systems. A similar study that employed the LNSE implemented with the GLS stabilization method showed noticeable deviations from the analytical results [15].

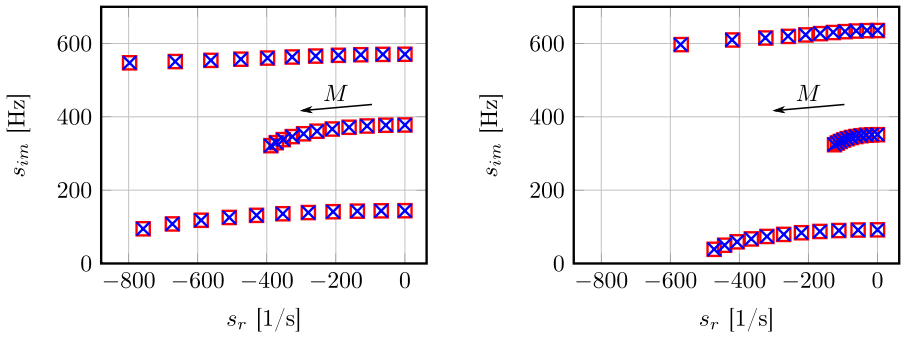

(a) Validation case I. (b) Validation case II.

Fig. 2. Analytical □ and DG-LNSE × results for the validation cases I and II.

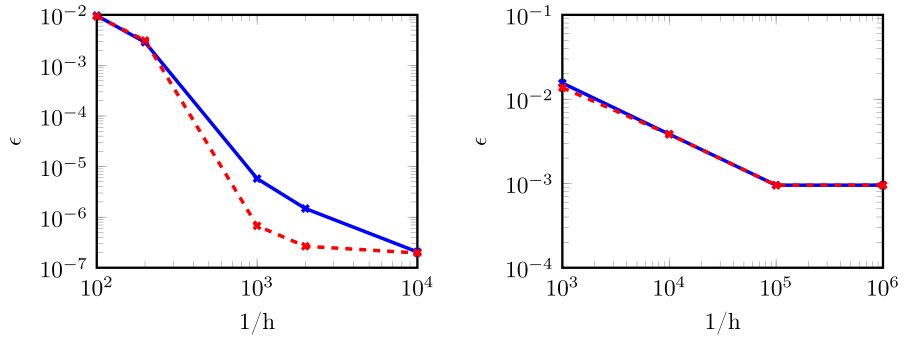

(a) Validation case I. (b) Validation case II.

Fig. 3. Relative errors of the eigenfrequencies for the validation cases I and II with linear —•— and quadratic - •- basis functions.

5. Application case: premixed, swirl-stabilized flame

In this section, the ssDG method is applied to a combustion test rig consisting of a plenum, an annular duct including an axial swirler and a combustion chamber with quadratic cross-section. A lean methane-air mixture is burned in a swirl-stabilized, V-shaped flame (see Fig. 4). The combustion chamber is terminated with a perforated plate to reduce reflections of acoustic waves. The geometrical and operating parameters of the swirl combustor are summarized in Table 2.

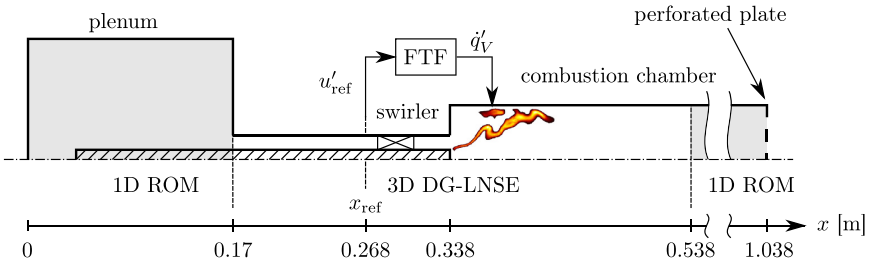

Fig. 4. Geometry and model partitions of the swirl combustor test rig [66].

Table 2
Geometrical and operating parameters of the swirl combustor.

Parameter	Variable	Value
nominal power rating	P	30 kW
plenum length	L_p	0.17 m
swirler duct length	L_d	0.168 m
combustion chamber length	L_c	0.7 m
combustion chamber length 3D domain	$L_{c,3D}$	0.2 m
plenum radius	r_p	0.1 m
bluff-body radius	r_b	0.008 m
swirler duct radius	r_d	0.02 m
combustion chamber side length	d_c	0.09 m
reference position for FTF	$x_{1,ref}$	$L_p + 0.098$ m
upstream speed of sound	$\bar{c}_u$	349.9 m/s
downstream speed of sound	$\bar{c}_d$	850.5 m/s

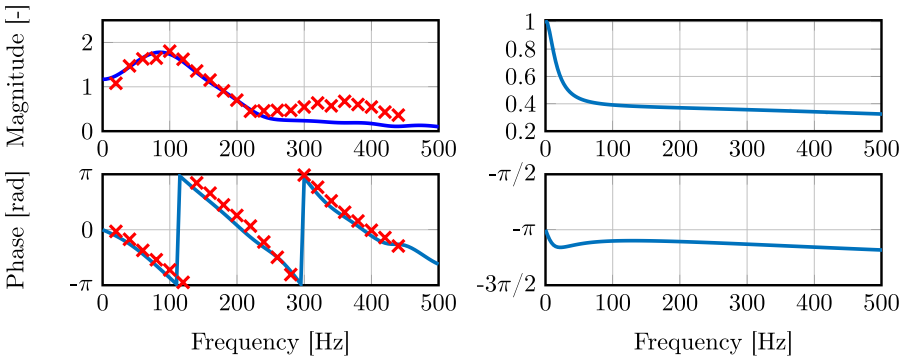

(a) Flame transfer function. (b) Perforated plate model.

Fig. 5. Left: Frequency response of the FTF identified from LES ▬ as well as from experimental measurements ✕ [67]. Right: Frequency response of the perforated plate model fitted to measurements in Ref. [68].

5.1. Overall ssDG model setup

Regions of the configuration where 3D effects, significant acoustic-flow interactions and fluctuating heat release are important are modeled using the DG-LNSE approach, with mean fields provided by time averaged large eddy simulation (LES) of turbulent, reacting flow (see section 5.2). In the present case of a premixed swirl combustor, the DG-LNSE domain comprises the annular duct including the swirler and the upstream part of the combustion chamber, where the flame is located (see Fig. 4). Acoustic damping effects are expected to be significant in these regions, where acoustic waves generate vortices at the swirler and at the area expansion into the combustion chamber. Thermoacoustic driving due to unsteady heat release by the flame is also located here. The flame dynamics is not resolved by the DG-LNSE, but instead provided in terms of a state-space representation of the FTF identified from LES data. This is detailed in sections 5.2 and 5.4.

Regions where the mean fields are nearly homogeneous and where only plane acoustic waves are expected in the frequency band of interest are represented by 1D, reduced-order network models formulated in state-space. Acoustic impedances derived from these models are coupled with the state-space interconnect approach to the DG-LNSE domain. In other words, the 1D reduced order models provide complex-valued, frequency dependent acoustic impedance boundary conditions for the DG-LNSE domain. Details are provided in section 5.5.

A state-space model deduced from experimental measurements is used to represent the acoustic reflection factor of the perforated plate at the combustion chamber outlet, see Fig. 5b. This model was suggested by Tay-Wo-Chong et al. [67], the experimental measurements were performed by Wanke [68]. For very low frequencies, the model behaves like a fully reflective open end. Above 50 Hz, the reflection amplitude drops, which leads to an increased loss of acoustic energy.

A sketch of the various state-space models and their interconnections is depicted in Fig. 6.

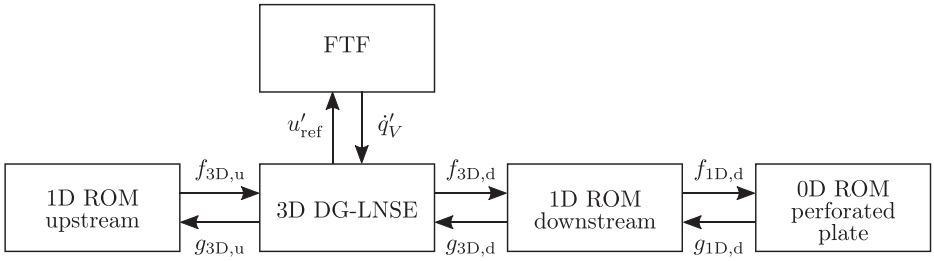

Fig. 6. Hybrid model of the swirl combustor built by state-space interconnect of sub-models.

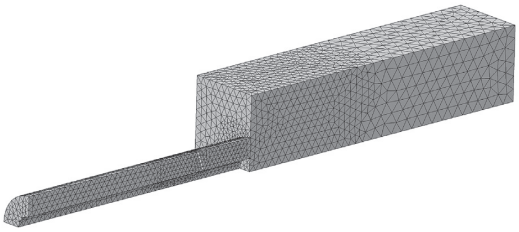

Fig. 7. Unstructured tetrahedral mesh used for the DG-LNSE computations.

5.2. LES and identification of the flame transfer function

Computations of the mean flow field and the FTF are based on an LES performed with the OpenFOAM toolbox [69]. A modified version of reactingFoam is employed, which is a solver for chemically reactive flows using Navier-Stokes equations with species transport. The low Mach number assumption is made, which omits the acoustic waves by use of the weakly compressible Navier-Stokes equations, i.e. the density only depends on the temperature. This is useful in a transient simulation, because possible thermoacoustic resonance structures enhanced by the acoustic reflections at the boundaries are ruled out.

The WALE model proposed by Nicoud and Ducros [70] is used for the sub-grid scale turbulence. Combustion of the methane-air mixture is modeled by a reduced two step chemical kinetic mechanism (2S-CM2) described in Ref. [71]. The dynamically thickened flame model proposed in Ref. [72] is employed to model the sub-grid scale turbulence-chemistry interaction.

The simulations are performed on a 90° sector of the geometry using periodic boundary conditions on a pure tetrahedral mesh. Refinement in the flame area and at the walls to an average edge length of 0.75 mm ensures a maximum thickening factor around 4. The PISO algorithm with five corrector steps is used and the time step for the integration is adjusted to the maximum Courant number of 0.7. Temporal averaging of the filtered variables over a period of 0.3s is employed to obtain the mean flow fields.

The FTF is computed via a system identification (SI) approach (for details see Ref. [73]) from the time series of excitation velocity at a reference position and the heat release fluctuations. To retain the linearity of the flame response, a maximum amplitude of 20% of the mean velocity was chosen for the broadband excitation signal [74]. The flame transfer function is identified as an ARX model, its frequency response is shown in Fig. 5a alongside the experimental measurements of Komarek [67].

5.3. 3D DG-LNSE element

The 3D DG-LNSE model comprises the annular duct that houses the swirler and the upstream part of the combustion chamber (see Fig. 4). The mean fields $\overline{\Phi}(x)$ are time-averaged LES data from the simulation that is used to identify the FTF. A 90° sector with periodic boundary conditions is investigated to stay consistent with the LES and to reduce computational costs.

Linear, nodal-discontinuous basis functions are chosen for the unstructured mesh consisting of 48,000 tetrahedral elements, cf. Fig. 7. This amounts to 932,000 degrees of freedom for the DG-LNSE model. The region including the swirler and the flame is refined to a maximum mesh size of 3 mm and 5 mm, respectively, to capture the damping effects and the unsteady heat release with increased resolution. The maximum mesh size in the downstream part of the combustion chamber is 8 mm.

At the boundaries of the combustion chamber, isothermal slip walls are employed,

$$u'_i n_i = 0 \qquad \text{and} \qquad T' = 0. \tag{36}$$

Slip walls are chosen because the mesh for the LNSE is not fine enough to resolve the unsteady Stokes boundary layer. The other walls (annular duct and swirler) are modeled as adiabatic slip walls,

$$u_i' n_i = 0 \qquad \text{and} \qquad \frac{\partial T'}{\partial x_i} n_i = 0. \tag{37}$$

At the inlet (index u, upstream) and outlet (index d, downstream) of the LNSE model, boundary conditions are given for the characteristic waves entering the domain in the following manner: the acoustic plane wave propagating downstream $f_{3D,u}$ is imposed at the inlet, all convective wave amplitudes that enter the domain (vorticity and entropy), are set to zero. No boundary condition is given for the characteristic wave exiting the domain, which is the upstream propagating acoustic plane wave $g_{3D,u}$. Following the same approach, only the upstream traveling plane wave $g_{3D,d}$ is imposed at the outlet, because the mean flow velocities are facing out of the domain. The convective waves at the outlet, namely entropy and vorticity, are neglected after they leave the 3D domain because they have no counterpart in the 1D network model. This implies the assumption that the convective waves will not interact with the acoustic characteristics in the downstream 1D part of the model. In order to generate the appropriate inputs for the 1D network models that represent the acoustic impedances at the boundary of the LNSE domain, the outgoing acoustic waves are determined as outputs. Note that the 1D models require a single complex-valued amplitude at the interfaces, whereas the inlet and the outlet of the LNSE domain are 2D surfaces. Therefore, the perturbed pressure and axial velocity are averaged over these surfaces to compute $g_{3D,u}$ and $f_{3D,d}$. Through this process, the perturbations in the axial velocity at the outlet through vortices cancel and the plane acoustic wave contribution is recovered.

For the FTF coupling, the axial velocity fluctuation $u'_{1,\mathrm{ref}}$, averaged over the reference plane, is provided as an output of the DG-LNSE model and the fluctuating heat release $\dot{q}'_V$ is kept as a parametric source term (input) to the DG-LNSE element. This results in a state-space model with the following in- and outputs:

$$\mathbf{u}_{3D} = \begin{pmatrix} f_{3D,u} \\ g_{3D,d} \\ \dot{q}'_V \end{pmatrix}, \qquad \mathbf{y}_{3D} = \begin{pmatrix} g_{3D,u} \\ f_{3D,d} \\ u'_{1,\mathrm{ref}} \end{pmatrix}. \tag{38}$$

5.4. FTF coupling

The FTF identified from the LES was used to couple the fluctuating heat release rate $\dot{q}'_V$ to the velocity fluctuations $u'_{1,\mathrm{ref}}$ at the reference plane at position $x_{1,\mathrm{ref}}$ upstream of the swirler. In the Laplace domain, the following relation for the heat release is established:

$$\hat{\dot{q}}_V(x_i, s) = \bar{\dot{q}}_V(x_i) \frac{\hat{u}_{1,\mathrm{ref}}}{\bar{u}_{1,\mathrm{ref}}} \mathrm{FTF}(s). \tag{39}$$

Equation (39) represents the spatially resolved source term $\hat{\dot{q}}_V(x_i, s)$. Amplitude and phase of the fluctuations are governed by the FTF, whereas the spatial distribution is proportional to the mean heat release interpolated to the DG-LNSE grid.

5.5. Complex-valued impedances from network models

The upstream and downstream boundary conditions of the DG-LNSE computational domain (see Fig. 4) are modeled as complex impedances with reduced order models utilizing the thermoacoustic network tool *taX* [10]. Therefore, constant mean flow values are assumed and the convected 1D Helmholtz equation is solved. Connecting the state-space models resulting from the DG-LNSE, *taX*, the perforated plate model and the FTF, a monolithic ssDG model is created for which the shift-inverted eigenvalue problem, Eq. (24), can be solved.

5.6. Pure network model

A model consisting only of network elements for the whole computational domain of the burner was set up by Emmert et al. [75]. In the presented study, this model is augmented by the perforated plate model at the combustion chamber outlet (see Fig. 5b). The same FTF as in the ssDG approach is used. The axial swirl generator is replaced by a duct of equal length, therefore any influence on the acoustic waves, e.g. reflection, is neglected. No loss coefficients have been introduced for the swirler or the area jumps.

5.7. Stability analysis

The stability of the swirl burner is assessed by computing the eigenvalues with the highest growth rates in the frequency band up to 1200 Hz. The ssDG model is compared to the full *taX* network model. The degrees of freedom as well as the points per wavelength for each sub-model are shown in Table 3. A maximum frequency of 1200 Hz is used to compute the points per

Table 3
Degrees of freedom and points per wavelength (PPW) of the various state-space models.

Model	degrees of freedom	PPW (s_{im} = 1200 Hz)
pure network model without FTF	368	84
ssDG 1D ROM upstream	98	84
ssDG 1D ROM downstream	120	84
ssDG 0D ROM perforated plate	2	–
3D DG-LNSE	932000	$\geq$ 73 (acoustic)
FTF	69	20 (s_{im} = 200 Hz)

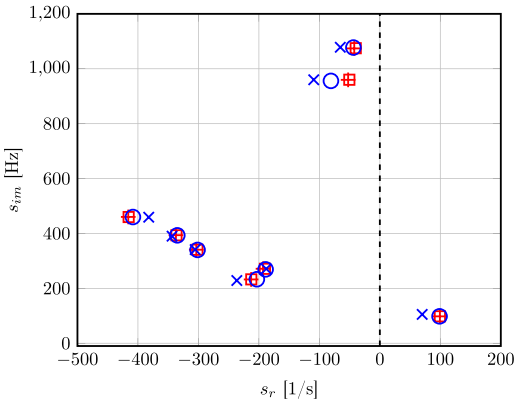

Fig. 8. Spectrum comparing the eigenvalues of the pure network (M ≠ 0:+, M = 0:□) and the ssDG model (M ≠ 0:×, M = 0:○).

wavelength for all elements except the FTF. Because the gain of the FTF is negligible beyond 200 Hz, the resolution was chosen to 20 points per wavelength at that frequency to avoid over-fitting during the SI procedure. The computations for the ssDG model were carried out in parallel on 8 CPUs. The iterative Arnoldi algorithm converges after approximately 30 min for 10 eigenmodes around one shift, using 90 GB of RAM. It is expected that the growth rates for both models differ due to the convective and viscous effects inherent to the ssDG approach, while the oscillation frequencies should be very similar due to the longitudinal nature of the eigenmodes in the investigated frequency band. The eigenfrequencies determined with the pure network model were therefore used as shifts for the eigenvalue computation of the ssDG model. The computation of eigenvalues was found to be insensitive to perturbations in the initial guess for the computation. Relative changes in eigenfrequency were below 1% when the mesh of the DG-LNSE domain was further refined to 60,000 tetrahedral cells.

Eigenvalues with both pure network and ssDG model have been computed with the mean flow velocities resulting from LES (M ≠ 0) as well as zero Mach number (M = 0). For the ssDG model in the latter case, the mean velocities in the DG-LNSE as well as the 1D ROM domains have been set to zero. The resulting spectrum of the eigenvalue analysis is shown in Fig. 8. All setups predict one unstable mode, i.e. the low-frequency intrinsic thermoacoustic (ITA) mode around 100 Hz, refer to Emmert et al. [75] and Albayrak et al. [76] for a discussion on the nature of this mode. This is in good agreement with experimental observations [67]. This mode is based on a direct feedback mechanism between the fluctuating heat release of the flame and the velocity fluctuations at the reference point, which does not require reflected acoustic waves at the system boundaries [77,78]. The first longitudinal mode (1L) at 260 Hz exhibits strong damping due to the losses at the perforated plate. Two other longitudinal, weakly damped acoustic modes at 950 Hz and 1050 Hz exhibit high pressure amplitudes only in the swirler duct. Due to the non trivial geometry, a strict classification of the modes is difficult. The other modes shown in Fig. 8 are higher order ITA modes which are strongly damped.

Comparing the results for both mean Mach number cases of the pure network model (+ and □), it is evident that the frequency shift due to mean flow velocity is negligible, as the eigenvalues almost coincide. For the ssDG approach (× and ○), the oscillation frequency s_{im} with and without mean Mach number is also very similar, the growth rate however differs significantly for some modes. Most of the eigenmodes are more damped when convective effects are present in the DG-LNSE domain, which can be attributed to the transfer of perturbation energy between acoustic and convective characteristics.

Compared to the pure network model, for which the computation takes only seconds, the computational cost of the ssDG model might seem high. However, the ssDG model inherently contains the fully resolved mean fields of flow velocity and speed of sound, accounting for flow-acoustic interactions that do not strictly increase damping for all modes, but can also have the adverse effect of increasing the growth rate, see e.g. the mode around 450 Hz. Some of the modes, on the other hand, are not influenced at all by this energy transfer, e.g. the longitudinal mode at 260 Hz. Therefore this study shows that the effects of

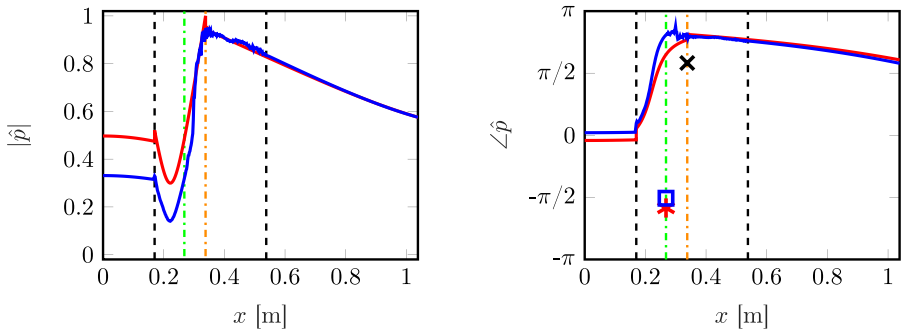

Fig. 9. Normalized magnitude and phase of $\hat{p}$ for the unstable intrinsic mode computed with the taX network model (—) and the hybrid ssDG approach (—) at M $\neq$ 0. The cross (×) indicates the phase of the unsteady heat release $\hat{Q}_V$ of the flame (position -.-.-) for both approaches. The markers (∗ and □) show the phase of the velocity fluctuations $\hat{u}_{\text{ref}}$ at the reference position (-.-.-).

perturbation energy transfer between acoustic and convective scales can not easily be estimated a priori. The inherent ability of the ssDG model to represent these mechanisms facilitates increased accuracy in the prediction of thermoacoustic eigenmodes. Including those effects in the pure network model is usually achieved by damping factors that are neither straight forward to determine, nor generally applicable for different geometries and mean flows. The mode shapes resulting in the LNSE part of the ssDG domain feature not only acoustic, but also hydrodynamic phenomena and can thus give more insight into the physics of the instability. Additionally, the DG-LNSE approach can also handle non-plane acoustics, such as transversal modes. This study, however, is limited to validation of the ssDG approach for longitudinal modes in the low-frequency band that can be represented well with a 1D approach.

Fig. 9 shows a comparison between the shapes (left: amplitude, right: phase) of the unstable ITA mode, computed with the pure network model (—) and the ssDG approach (—) with M $\neq$ 0. Note that the amplitude of the eigenvectors may be scaled arbitrarily. To facilitate a comparison, the amplitudes of both modes are normalized with the absolute value of the respective pressure at the downstream end of the combustion chamber, $x = 1.038$ m. The reference value of the phase is provided by the respective fluctuating heat release rate. It is apparent that the overall mode shapes agree well. Compared to the network model, a strong pressure gradient in the swirler area can be seen for the ssDG approach, which also exhibits a phase shift. This effect can be attributed to the reflections and the losses coming from the swirler, which are omitted in the network model. It is also worth noting that the network model converts all of the fluctuating heat release to axial acoustic waves, while the volumetric expansion due to heat release in the DG-LNSE domain also excites transversal velocity perturbations. This effect is expected to contribute to the damping, as transversal acoustic waves are mainly present in the flame region, where vortices form in the shear layer and dissipation occurs.

According to Rayleigh [79,80], the perturbation energy introduced into the acoustic waves is high when heat release and the pressure fluctuations in the flame area are in phase. This phase difference is very similar for both approaches, which favors an unstable thermoacoustic mode ($\angle(\hat{q}_V, \hat{p}_{\text{flame}})_{\text{network}} = 0.23\pi, \angle(\hat{q}_V, \hat{p}_{\text{flame}})_{\text{ssDG}} = 0.20\pi$). The phase between the heat release and the axial velocity fluctuations at the reference position is governed by the FTF (∗ and □) and shows only a minor discrepancy that stems from the slightly different oscillation frequencies of the modes ($s_{\text{im, network}} = 98.05$ Hz, $s_{\text{im, ssDG}} = 105.16$ Hz). This difference in frequency can be attributed to the spatially resolved mean fields of speed of sound and convective velocities in the DG-LNSE domain, which define the propagation velocity of the acoustic waves as well as the influence of hydrodynamic fluctuations on the eigenmode. Although the Rayleigh criterion is slightly more critical in the ssDG approach, the overall growth rate is smaller due to the damping effects by acoustic mean flow interactions that were not included in the pure network model. The real part of the mode shape ($\hat{p}$ and $\hat{u}_1$) computed with the ssDG approach in the DG-LNSE domain is shown in Fig. 10, clearly depicting the convective nature of the axial velocity perturbations that are mainly generated at the swirler and then dissipated or convected out of the domain.

6. Summary and conclusions

A state-space based framework was used to interconnect a discontinuous Galerkin discretization of the linearized, compressible Navier-Stokes equations with reduced-order representations of flame dynamics and acoustic impedance boundary conditions. This approach is conceptually a hybrid one, nevertheless the state-space framework makes possible the formulation of a monolithic model. At the expense of a comparatively small number of additional degrees of freedom, eigenvalue computa-

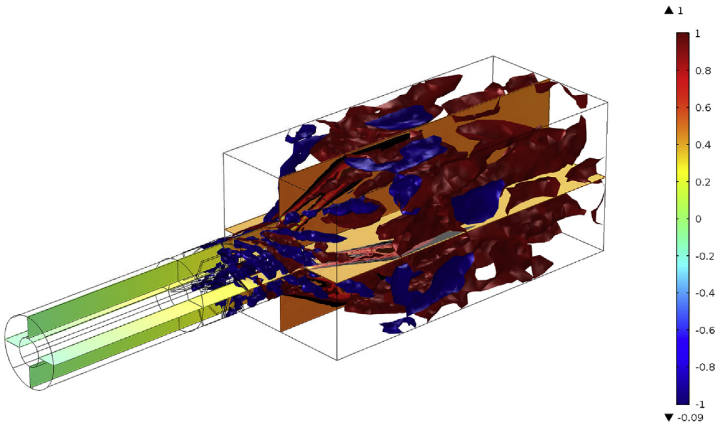

Fig. 10. Cutplanes show the normalized real part of the pressure fluctuations $\hat{p}$ of the unstable intrinsic eigenmode. Contours for the mean heat release $\overline{\dot{q}}_V$ are indicated in red to black. 3D iso-surfaces indicate positive (red) and negative (blue) fluctuations of the real part of the axial velocity $\hat{u}_1$. Full domain reconstructed from 90° sector. (For interpretation of the references to colour in this figure legend, the reader is referred to the Web version of this article.)

tions can be kept linear, even when time delay terms or non-trivial dependence of acoustic impedance on frequency must be taken into account.

The main advantages of the discontinuous Galerkin discretization are the high accuracy in the dispersion relation as well as the inherently stable discretization of the convective terms by means of a physically motivated upwinding parameter. These merits are accompanied by the drawback of the higher number of degrees of freedom compared to continuous finite element approaches. The presented state-space interconnect framework, however, allows to resolve parts of the computational domain, where flow-flame-acoustic or flow-acoustic interactions are not significant, with 1D reduced order network models to counterbalance the increased computational costs of the DG-LNSE. The discretization of time delays occurring in flow-flame models, as well as the representation of the reduced order network models as linear functions in the Laplace domain leads to a linear eigenvalue problem for which an efficient and robust solution algorithm is employed. Not reckoning the computational effort required to determine mean fields and FTF, the proposed state-space interconnect/discontinuous Galerkin scheme can thus yield accurate stability predictions within minutes for thermoacoustic systems featuring non trivial geometries and mean flow fields.

CRediT authorship contribution statement

M. Meindl: Conceptualization, Methodology, Software, Validation, Formal analysis, Data curation, Writing - original draft, Writing - review & editing, Visualization. **A. Albayrak:** Data curation, Writing - original draft. **W. Polifke:** Conceptualization, Methodology, Writing - original draft, Writing - review & editing, Supervision, Project administration, Funding acquisition.

Declaration of competing interest

The authors declare that they have no known competing financial interests or personal relationships that could have appeared to influence the work reported in this paper.

Acknowledgments

We gratefully acknowledge the financial support from the European Commission under call FP7-PEOPLE-ITN-2012 in the framework of the Marie Curie Initial Training Network *Thermo-acoustic and aeroacoustic nonlinearities in green combustors with orifice structures* (TANGO) and the Gauss Centre for Supercomputing e.V. (www.gauss-centre.eu) for funding this project by providing computing time on the GCS Supercomputer SuperMUC at Leibniz Supercomputing Centre (www.lrz.de) for the large eddy simulation. We thank Alexander Avdonin, Christian Lang and Felix Schily for fruitful discussions.

Appendix A. Vector matrix notation of the LNSE

The matrix containing the prefactors of the time derivatives in three dimensions is defined as

$$\mathbf{M} = \begin{bmatrix} \frac{\overline{\rho}}{\overline{p}} & 0 & 0 & 0 & -\frac{\overline{\rho}}{\overline{T}} \\ \overline{u}_1 \frac{\overline{\rho}}{\overline{p}} & \overline{\rho} & 0 & 0 & -\overline{u}_1 \frac{\overline{\rho}}{\overline{T}} \\ \overline{u}_2 \frac{\overline{\rho}}{\overline{p}} & 0 & \overline{\rho} & 0 & -\overline{u}_2 \frac{\overline{\rho}}{\overline{T}} \\ \overline{u}_3 \frac{\overline{\rho}}{\overline{p}} & 0 & 0 & \overline{\rho} & -\overline{u}_3 \frac{\overline{\rho}}{\overline{T}} \\ \frac{1}{\gamma - 1} + \overline{u}_k \overline{u}_k \frac{\overline{\rho}}{\overline{p}} & \overline{\rho u}_1 & \overline{\rho u}_2 & \overline{\rho u}_3 & -\overline{u}_k \overline{u}_k \frac{\overline{\rho}}{\overline{T}} \end{bmatrix}, \tag{A.1}$$

the vector of sources is

$$\mathbf{S} = \begin{pmatrix} 0 \\ 0 \\ 0 \\ 0 \\ \dot{q}'_V \end{pmatrix}. \tag{A.2}$$

On the domain boundary Γ, the non-viscous flux $\mathbf{F}_n^\star$ is chosen to weakly impose boundary conditions. This is done by inserting the boundary conditions into $\mathbf{F}_n$. Therefore, it is useful to decompose $\mathbf{F}_n$ into flux contributions due to different physical causes:

$$\mathbf{F}_n = \mathbf{F}_n^{\overline{u}_n} + \mathbf{F}_n^{u'_n} + \mathbf{F}_n^{p'_n} \tag{A.3}$$

- Flux due to convection by the mean-flow

$$\mathbf{F}_n^{\overline{u}_n} = n_j \overline{u}_j \begin{pmatrix} \rho' \\ \overline{\rho} u'_1 + \overline{u}_1 \rho' \\ \overline{\rho} u'_2 + \overline{u}_2 \rho' \\ \overline{\rho} u'_3 + \overline{u}_3 \rho' \\ (\rho e)' + p' \end{pmatrix}, \tag{A.4}$$

- Flux due to normal velocity perturbation

$$\mathbf{F}_n^{u'_n} = n_j u'_j \begin{pmatrix} \overline{\rho} \\ \overline{\rho u}_1 \\ \overline{\rho u}_2 \\ \overline{\rho u}_3 \\ \overline{(\rho e)} + \overline{p} \end{pmatrix}, \tag{A.5}$$

- Flux due to normal pressure perturbation

$$\mathbf{F}_n^{p'_n} = p' \begin{pmatrix} 0 \\ n_1 \\ n_2 \\ n_3 \\ 0 \end{pmatrix}. \tag{A.6}$$

Examples of weakly imposed boundary conditions are acoustically hard walls ($\mathbf{F}_n^{u'_n} = \mathbf{0}$) or open ends ($\mathbf{F}_n^{p'_n} = \mathbf{0}$). The boundary conditions of the mean flow can also be taken into account in the LNSE computation, e.g. by setting ($\mathbf{F}_n^{\overline{u}_n} = \mathbf{0}$) at hard walls of the mean flow. This proves useful when the mean flow velocity normal to the boundary, $\overline{u}_j n_j$, is not exactly zero due to interpolation errors from the CFD to the LNSE mesh.
Similarly, the viscous flux is decomposed:

$$\mathbf{F}_n^v = \mathbf{F}_n^{v,\mu} + \mathbf{F}_n^{v,k} = \left(\mathbf{D}_n^\mu + \mathbf{D}_n^k \right) \mathbf{\Phi}' \tag{A.7}$$

- Flux due to viscous stress perturbations, $\mathbf{F}_n^{v,\mu}$,

- Flux due heat conduction perturbations, $\mathbf{F}_n^{v,k}$.

  The viscous flux is also used to impose weak boundary conditions, e.g. adiabatic walls ($\mathbf{F}_n^{v,k} = \mathbf{0}$). The pre-factor matrices for the viscous flux are defined as:

$$\mathbf{D}_n^{\mu} = \mu \begin{bmatrix} 0 & 0 & 0 & 0 & 0 \\ 0 & \frac{4}{3}n_1\frac{\partial}{\partial x_1} + n_2\frac{\partial}{\partial x_2} + n_3\frac{\partial}{\partial x_3} & -\frac{2}{3}n_1\frac{\partial}{\partial x_2} + n_2\frac{\partial}{\partial x_1} & -\frac{2}{3}n_1\frac{\partial}{\partial x_3} + n_3\frac{\partial}{\partial x_1} & 0 \\ 0 & n_1\frac{\partial}{\partial x_2} - \frac{2}{3}n_2\frac{\partial}{\partial x_1} & n_1\frac{\partial}{\partial x_1} + \frac{4}{3}n_2\frac{\partial}{\partial x_2} + n_3\frac{\partial}{\partial x_3} & -\frac{2}{3}n_2\frac{\partial}{\partial x_3} + n_3\frac{\partial}{\partial x_2} & 0 \\ 0 & n_1\frac{\partial}{\partial x_3} - \frac{2}{3}n_3\frac{\partial}{\partial x_1} & n_2\frac{\partial}{\partial x_3} - \frac{2}{3}n_3\frac{\partial}{\partial x_2} & n_1\frac{\partial}{\partial x_1} + n_2\frac{\partial}{\partial x_2} + \frac{4}{3}n_3\frac{\partial}{\partial x_3} & 0 \\ 0 & 0 & 0 & 0 & 0 \end{bmatrix}, \tag{A.8}$$

$$\mathbf{D}_n^{k} = k \begin{bmatrix} 0 & 0 & 0 & 0 & 0 \\ 0 & 0 & 0 & 0 & 0 \\ 0 & 0 & 0 & 0 & 0 \\ 0 & 0 & 0 & 0 & 0 \\ 0 & 0 & 0 & 0 & n_j\frac{\partial}{\partial x_j} \end{bmatrix}. \tag{A.9}$$

References

[1] P. Wolf, R. Balakrishnan, G. Staffelbach, L. Gicquel, T. Poinsot, Using LES to study reacting flows and instabilities in annular combustion chambers, Flow, Turbul. Combust. 88 (2012) 191–206, https://doi.org/10.1007/s10494-011-9367-7.

[2] P. Wolf, G. Staffelbach, L.Y.M. Gicquel, J.-D. Mller, T. Poinsot, Acoustic and Large Eddy Simulation studies of azimuthal modes in annular combustion chambers, Combust. Flame 159 (11) (2012) 3398–3413, https://doi.org/10.1016/j.combustflame.2012.06.016.

[3] T. Poinsot, Prediction and control of combustion instabilities in real engines, Proc. Combust. Inst. 36 (2017) 1–28, https://doi.org/10.1016/j.proci.2016.05.007.

[4] A.P. Dowling, The calculation of thermoacoustic oscillation, J. Sound Vib. 180 (4) (1995) 557–581, https://doi.org/10.1006/jsvi.1995.0100.

[5] J.J. Keller, Thermoacoustic oscillations in combustion chambers of gas turbines, AIAA J. 33 (12) (1995) 2280–2287, https://doi.org/10.2514/3.12980.

[6] B.B.H. Schuermans, W. Polifke, C.O. Paschereit, J.H. van der Linden, Prediction of acoustic pressure spectra in combustion systems using swirl stabilized gas turbine burners, in: ASME Turbo Expo 2000: Power for Land, Sea, and Air, 2000-GT-0105, ASME, Munich, Germany, 2000https://doi.org/10.1115/2000-GT-0105.

[7] W. Polifke, C.O. Paschereit, K. Döbbeling, Constructive and destructive interference of acoustic and entropy waves in a premixed combustor with a choked exit, Int. J. Acoust. Vib. 6 (3) (2001) 135–146, https://doi.org/10.20855/ijav.2001.6.382.

[8] V. Bellucci, B. Schuermans, D. Nowak, P. Flohr, C.O. Paschereit, Thermoacoustic modeling of a gas turbine combustor equipped with acoustic dampers, J. Turbomach. 127 (2) (2005) 372–379, https://doi.org/10.1115/1.1791284.

[9] M. Bothien, J. Moeck, A. Lacarelle, C.O. Paschereit, Time domain modelling and stability analysis of complex thermoacoustic systems, Proc. IME J. Power Energy 221 (5) (2007) 657–668, https://doi.org/10.1243/09576509JPE384.

[10] T. Emmert, M. Meindl, S. Jaensch, W. Polifke, Linear state space interconnect modeling of acoustic systems, Acta Acustica united Acustica 102 (5) (2016) 824–833, https://doi.org/10.3813/AAA.918997.

[11] A. Orchini, M.P. Juniper, Linear stability and adjoint sensitivity analysis of thermoacoustic networks with premixed flames, Combust. Flame 165 (2016) 97–108, https://doi.org/10.1016/j.combustflame.2015.10.011.

[12] F. Nicoud, L. Benoit, C. Sensiau, T. Poinsot, Acoustic modes in combustors with complex impedances and multidimensional active flames, AIAA J. 45 (2) (2007) 426–441, https://doi.org/10.2514/1.24933.

[13] A. Kierkegaard, S. Boij, G. Efraimsson, A frequency domain linearized Navier-Stokes equations approach to acoustic propagation in flow ducts with sharp edges, J. Acoust. Soc. Am. 127 (2010) 710–719.

[14] A. Kierkegaard, S. Allam, G. Efraimsson, M. Åbom, Simulations of whistling and the whistling potentiality of an in-duct orifice with linear aeroacoustics, J. Sound Vib. 331 (5) (2012) 1084–1096, https://doi.org/10.1016/j.jsv.2011.10.028.

[15] J. Gikadi, T. Sattelmayer, A. Peschiulli, Effects of the mean flow field on the thermo-acoustic stability of aero-engine combustion chambers, in: ASME Turbo Expo 2012: Turbine Technical Conference and Exposition, American Society of Mechanical Engineers, Copenhagen, Denmark, 2012, pp. 1203–1211, https://doi.org/10.1115/GT2012-69612.

[16] S.M. Camporeale, B. Fortunato, G. Campa, A finite element method for three-dimensional analysis of thermo-acoustic combustion instability, J. Eng. Gas Turbines Power 133 (1) (2011) 011506https://doi.org/10.1115/1.4000606.

[17] G. Campa, S.M. Camporeale, Prediction of the thermoacoustic combustion instabilities in practical annular combustors, J. Eng. Gas Turbines Power 136 (9) (2014), https://doi.org/10.1115/1.4027067 091504091504.

[18] J. Gikadi, S. Föller, T. Sattelmayer, Impact of turbulence on the prediction of linear aeroacoustic interactions: acoustic response of a turbulent shear layer, J. Sound Vib. 333 (24) (2014) 6548–6559, https://doi.org/10.1016/j.jsv.2014.06.033.

[19] M. Zahn, M. Schulze, C. Hirsch, M. Betz, T. Sattelmayer, Frequency domain predictions of acoustic wave propagation and losses in a swirl burner with linearized Navier-Stokes equations, in: ASME Turbo Expo 2015: Turbine Technical Conference and Exposition, GT2015-42723, ASME, Montreal, Quebec, Canada, 2015https://doi.org/10.1115/GT2015-42723, p. V04AT04A055.

[20] M. Schulze, T. Hummel, N. Klarmann, F.M. Berger, B. Schuermans, T. Sattelmayer, Linearized Euler equations for the prediction of linear high-frequency stability in gas turbine combustors, J. Eng. Gas Turbines Power 139 (3) (2017) 031510https://doi.org/10.1115/1.4034453.

[21] M. Schulze, Linear Stability Assessment of Cryogenic Rocket Engines, PhD Thesis, TU München, Munich, Germany, 2016.

[22] M. Schulze, T. Sattelmayer, A comparison of time and frequency domain descriptions of high frequency acoustics in rocket engines with focus on dome coupling, Aero. Sci. Technol. 45 (2015) 165–173.

[23] F. Ni, M.M. Brebion, F. Nicoud, T. Poinsot, Accounting for acoustic damping in a Helmholtz solver, AIAA J. 55 (4) (2017) 1205–1220, https://doi.org/10.2514/1.J055248.

[24] T. Poinsot, A. Trouve, D. Veynante, S. Candel, E. Esposito, Vortex-driven acoustically coupled combustion instabilities, J. Fluid Mech. 177 (1987) 265–292, https://doi.org/10.1017/S0022112087000958.

[25] T.C. Lieuwen, Unsteady Combustor Physics, Cambridge University Press, New York, N.Y., USA, 2012.
[26] M. Blanchard, T. Schuller, D. Sipp, P.J. Schmid, Response analysis of a laminar premixed M-flame to flow perturbations using a linearized compressible Navier-Stokes solver, Phys. Fluids 27 (4) (2015) 043602https://doi.org/10.1063/1.4918672.
[27] T. Steinbacher, A. Albayrak, A. Ghani, W. Polifke, Response of premixed flames to irrotational and vortical velocity fields generated by acoustic perturbations, Proc. Combust. Inst. 37 (4) (2019) 5367–5375, https://doi.org/10.1016/j.proci.2018.07.041.
[28] G. Campa, S. Camporeale, Eigenmode analysis of the thermoacoustic combustion instabilities using a hybrid technique based on the finite element method and the transfer matrix method, Adv. Appl. Acoust. (AIAAS) 1 (1) (2012) 1–14.
[29] F.E. Marble, S.M. Candel, Acoustic disturbance from gas non-uniformities convected through a nozzle, J. Sound Vib. 55 (2) (1977) 225–243, https://doi.org/10.1016/0022-460X(77)90596-X.
[30] M.S. Bohn, Response of a subsonic nozzle to acoustic and entropy disturbances, J. Sound Vib. 52 (2) (1977) 283–297, https://doi.org/10.1016/0022-460X(77)90647-2.
[31] J.J. Keller, W. Egli, J. Hellat, Thermally induced low-frequency oscillations, Z. Angew. Math. Phys. (ZAMP) 36 (2) (1985) 250–274, https://doi.org/10.1007/BF00945460.
[32] E. Motheau, F. Nicoud, T. Poinsot, Mixed acousticentropy combustion instabilities in gas turbines, J. Fluid Mech. 749 (2014) 542–576, https://doi.org/10.1017/jfm.2014.245.
[33] J. Donéa, A. Huerta, Finite Element Methods for Flow Problems, Wiley, Chichester; Hoboken, NJ, 2003. oCLC: ocm48025024.
[34] J.S. Hesthaven, T. Warburton, Nodal Discontinuous Galerkin Methods, Vol. 54 of Texts in Applied Mathematics, Springer, New York, New York, NY, 2008https://doi.org/10.1007/978-0-387-72067-8.
[35] C.E. Baumann, J.T. Oden, A discontinuous hp finite element method for the Euler and Navier-Stokes equations, Int. J. Numer. Methods Fluid. 31 (1) (1999) 79–95, https://doi.org/10.1002/(SICI)1097-0363(19990915)31:1.
[36] B. Cockburn, Discontinuous Galerkin Methods: Theory, Computation and Applications, No. 11 in Lecture Notes in Computational Science and Engineering, Springer, Berlin, 2000. oCLC: 247733322.
[37] H. Atkins, Continued development of the discontinuous Galerkin method for computational aeroacoustic applications, in: 3rd AIAA/CEAS Aeroacoustics Conference, American Institute of Aeronautics and Astronautics, Atlanta, GA, USA, 1997https://doi.org/10.2514/6.1997-1581.
[38] H.L. Atkins, C.-W. Shu, Quadrature-free implementation of discontinuous galerkin method for hyperbolic equations, AIAA J. 36 (5) (1998) 775–782, https://doi.org/10.2514/2.436.
[39] L. Liu, X. Li, F.Q. Hu, Nonuniform time-step RungeKutta discontinuous galerkin method for computational aeroacoustics, J. Comput. Phys. 229 (19) (2010) 6874–6897, https://doi.org/10.1016/j.jcp.2010.05.028.
[40] C. Blom, Discontinuous Galerkin Methods on Tetrahedral Elements for Aeroacoustics, PhD Thesis, University of Twente, Enschede, 2003.
[41] M. Dumbser, C.-D. Munz, ADER discontinuous Galerkin schemes for aeroacoustics, Compt. Rendus Mec. 333 (9) (2005) 683–687, https://doi.org/10.1016/j.crme.2005.07.008.
[42] T. Emmert, State Space Modeling of Thermoacoustic Systems with Application to Intrinsic Feedback, Ph.D. Thesis, TU München, Munich, Germany, 2016.
[43] M. Meindl, T. Emmert, W. Polifke, Efficient calculation of thermoacoustic modes utilizing state-space models, in: 23nd Int. Congress on Sound and Vibration (ICSV23), Athens, Greece, 2016.
[44] M. Schulze, T. Sattelmayer, Eigenvalue analysis for the prediction of initial growth rates of thermoacoustic instability in rocket motors, in: 53rd AIAA Aerospace Sciences Meeting, American Institute of Aeronautics and Astronautics, Kissimmee, Florida, USA, 2015https://doi.org/10.2514/6.2015-1606.
[45] P.E. Buschmann, G.A. Mensah, F. Nicoud, J.P. Moeck, Solution of thermoacoustic eigenvalue problems with a non-iterative method, in: ASME Turbo Expo 2019: Turbomachinery Technical Conference & Exposition, GT2019-90834, ASME, Phoenix, USA, 2019.
[46] C. Pankiewitz, T. Sattelmayer, Time domain simulation of combustion instabilities in annular combustors, in: Int'l Gas Turbine and Aeroengine Congress & Exposition, GT-2002-30063, ASME, Amsterdam, NL, 2002.
[47] A.N. Brooks, T.J. Hughes, Streamline upwind/Petrov-Galerkin formulations for convection dominated flows with particular emphasis on the incompressible Navier-Stokes equations, Comput. Methods Appl. Mech. Eng. 32 (13) (1982) 199–259, https://doi.org/10.1016/0045-7825(82)90071-8.
[48] T.J. Hughes, L.P. Franca, G.M. Hulbert, A new finite element formulation for computational fluid dynamics: VIII. The galerkin/least-squares method for advective-diffusive equations, Comput. Methods Appl. Mech. Eng. 73 (2) (1989) 173–189, https://doi.org/10.1016/0045-7825(89)90111-4.
[49] T. Hofmeister, T. Hummel, B. Schuermans, T. Sattelmayer, Quantification of energy transformation processes between acoustic and hydrodynamic modes in non-compact thermoacoustic systems via a Helmholtz-Hodge decomposition approach, in: ASME Turbo Expo 2019: Turbomachinery Technical Conference and Exposition, 2019, pp. GT2019–90240.
[50] W.C. Ullrich, T. Sattelmayer, Transfer functions of acoustic, entropy and vorticity waves in an annular model combustor and nozzle for the prediction of the ratio between indirect and direct combustion noise, in: 21st AIAA/CEAS Aeroacoustics Conference, American Institute of Aeronautics and Astronautics, 2015https://doi.org/10.2514/6.2015-2972.
[51] B. Cockburn, S.-Y. Lin, C.-W. Shu, TVB Runge-Kutta local projection discontinuous Galerkin finite element method for conservation laws III: one-dimensional systems, J. Comput. Phys. 84 (1) (1989) 90–113, https://doi.org/10.1016/0021-9991(89)90183-6.
[52] I. Babuška, C. Baumann, J. Oden, A discontinuous hp finite element method for diffusion problems: 1-D analysis, Comput. Math. Appl. 37 (9) (1999) 103–122, https://doi.org/10.1016/S0898-1221(99)00117-0.
[53] C.E. Baumann, J.T. Oden, A discontinuous hp finite element method for convectiondiffusion problems, Comput. Methods Appl. Mech. Eng. 175 (34) (1999) 311–341, https://doi.org/10.1016/S0045-7825(98)00359-4.
[54] COMSOL, Inc, COMSOL Multiphysics Reference Manual, version 5.3.
[55] B. Schuermans, Modeling and Control of Thermoacoustic Instabilities, PhD Thesis, École Polytechnique Fédérale de Lausanne, Lausanne, Switzerland, 2003.
[56] B. Schuermans, V. Bellucci, D. Nowak, C.O. Paschereit, Modelling of complex thermoacoustic systems: a state-space approach, in: Ninth Int. Congress on Sound and Vibration, ICSV9, IIAV, Orlando, FL, U.S.A., 2002.
[57] B. Schuermans, V. Bellucci, C.O. Paschereit, Thermoacoustic modeling and control of multi-burner combustion systems, GT2003-38688, in: Int'l Gas Turbine and Aeroengine Congress & Exposition, ASME, Atlanta, GA, USA, 2003, pp. 509–519, https://doi.org/10.1115/GT2003-38688.
[58] H. Mangesius, W. Polifke, A discrete-time, state-space approach for the investigation of non-normal effects in thermoacoustic systems, Int. J. Spray Combust. Dyn. 3 (4) (2011) 331–350, https://doi.org/10.1260/1756-8277.3.4.331.
[59] A. Orchini, S.J. Illingworth, M.P. Juniper, Frequency domain and time domain analysis of thermoacoustic oscillations with wave-based acoustics, J. Fluid Mech. 775 (2015) 387–414, https://doi.org/10.1017/jfm.2015.139.
[60] Y. Saad, Numerical methods for large eigenvalue problems, rev, no. 66, in: Classics in Applied Mathematics, Society for Industrial and Applied Mathematics, Philadelphia, 2011.
[61] P.R. Amestoy, I.S. Duff, J.-Y. L'Excellent, J. Koster, MUMPS: a general purpose distributed memory sparse solver, in: T. Srevik, F. Manne, A.H. Gebremedhin, R. Moe (Eds.), Applied Parallel Computing. New Paradigms for HPC in Industry and Academia, no. 1947 in Lecture Notes in Computer Science, Springer Berlin Heidelberg, 2000, pp. 121–130, https://doi.org/10.1007/3-540-70734-416.
[62] W.-J. Beyn, An integral method for solving nonlinear eigenvalue problems, Lin. Algebra Appl. 436 (10) (2012) 3839–3863, https://doi.org/10.1016/j.laa.2011.03.030.
[63] M. Bauerheim, J.-F. Parmentier, P. Salas, F. Nicoud, T. Poinsot, An analytical model for azimuthal thermoacoustic modes in an annular chamber fed by an annular plenum, Combust. Flame 161 (5) (2014) 1374–1389, https://doi.org/10.1016/j.combustflame.2013.11.014.
[64] A. Avdonin, M. Meindl, W. Polifke, Thermoacoustic analysis of a laminar premixed flame using a linearized reacting flow solver, in: 37th Int'l Symposium on Combustion, Dublin, Ireland, 2018https://doi.org/10.1016/j.proci.2018.06.142.
[65] P. Subramanian, R.S. Blumenthal, R. Sujith, W. Polifke, Distributed time lag response functions for the modelling of combustion dynamics, Combust. Theor. Model. 19 (2) (2015) 223–237, https://doi.org/10.1080/13647830.2014.1001438.
[66] L.R. Tay Wo Chong Hilares, Numerical Simulation of the Dynamics of Turbulent Swirling Flames, Ph.D. Thesis, TU München, Munich, Germany, 2012.

[67] L. Tay-Wo-Chong, S. Bomberg, A. Ulhaq, T. Komarek, W. Polifke, Comparative validation study on identification of premixed flame transfer function, J. Eng. Gas Turbines Power 134 (2) (2012), https://doi.org/10.1115/1.4004183 02150218.
[68] E.P. Wanke, FE-Verfahren zur Analyse der thermoakustischen Stabilitt nichtisentroper Strmungen (FE methods for thermoacoustic stability analysis of nonisentropic flows), PhD Thesis, TU München, 2010.
[69] H. Weller, G. Tabor, H. Jasak, C. Fureby, A tensorial approach to computational continuum mechanics using object-oriented techniques, Comput. Phys. 12 (1998) 620, https://doi.org/10.1063/1.168744.
[70] F. Nicoud, F. Ducros, Subgrid-scale stress modelling based on the square of the velocity gradient tensor, Flow, Turbul. Combust. 62 (3) (1999) 183–200, https://doi.org/10.1023/A:1009995426001.
[71] J. Bibrzycki, T. Poinsot, A. Zajdel, Investigation of laminar flame speed of CH4/N2/O2 and CH4/CO2/O2 mixtures using reduced chemical kinetic mechanisms, Arch. Combust. 30 (4) (2010) 287–296.
[72] F. Charlette, C. Meneveau, D. Veynante, A power-law flame wrinkling model for LES of premixed turbulent combustion Part I: non-dynamic formulation and initial tests, Combust. Flame 131 (1) (2002) 159–180, https://doi.org/10.1016/S0010-2180(02)00400-5.
[73] W. Polifke, Black-box system identification for reduced order model construction, Ann. Nucl. Energy 67C (2014) 109–128, https://doi.org/10.1016/j.anucene.2013.10.037.
[74] S. Föller, W. Polifke, Advances in identification techniques for aero-acoustic scattering coefficients from large eddy simulation, in: 18th International Congress on Sound and Vibration, 4, ISCV18, Rio de Janeiro, Brazil, 2011, pp. 3122–3129.
[75] T. Emmert, S. Bomberg, S. Jaensch, W. Polifke, Acoustic and intrinsic thermoacoustic modes of a premixed combustor, Proc. Combust. Inst. 36 (3) (2017) 3835–3842, https://doi.org/10.1016/j.proci.2016.08.002.
[76] A. Albayrak, T. Steinbacher, T. Komarek, W. Polifke, Convective scaling of intrinsic thermo-acoustic eigenfrequencies of a premixed swirl combustor, J. Eng. Gas Turbines Power 140 (4) (2017) 041510https://doi.org/10.1115/1.4038083.
[77] M. Hoeijmakers, V. Kornilov, I. Lopez Arteaga, P. de Goey, H. Nijmeijer, Intrinsic instability of flame-acoustic coupling, Combust. Flame 161 (11) (2014) 2860–2867, https://doi.org/10.1016/j.combustflame.2014.05.009.
[78] S. Bomberg, T. Emmert, W. Polifke, Thermal versus acoustic response of velocity sensitive premixed flames, Proc. Combust. Inst. 35 (3) (2015) 3185–3192, https://doi.org/10.1016/j.proci.2014.07.032.
[79] J.W.S. Rayleigh, The explanation of certain acoustical phenomena, Nature 18 (1878) 319–321, https://doi.org/10.1038/018319a0.
[80] M.J. Brear, F. Nicoud, M. Talei, A. Giauque, E.R. Hawkes, Disturbance energy transport and sound production in gaseous combustion, J. Fluid Mech. 707 (2012) 53–73, https://doi.org/10.1017/jfm.2012.264.

Available online at www.sciencedirect.com

ScienceDirect

Proceedings of the Combustion Institute 37 (2019) 5307–5314

Proceedings of the Combustion Institute

www.elsevier.com/locate/proci

Thermoacoustic analysis of a laminar premixed flame using a linearized reactive flow solver

Alexander Avdonin*, Max Meindl, Wolfgang Polifke

Technical University of Munich, D-85747 Garching, Germany

Received 1 December 2017; accepted 18 June 2018
Available online 2 July 2018

Abstract

In this paper, the dynamics and thermoacoustic stability of a laminar premixed flame are analyzed using a linearized reactive flow (LRF) solver. The LRF solver is based on linearized compressible Navier-Stokes and reacting species transport equations and thereby includes a model for the dynamic response of the flame to flow perturbations in an inherent manner. The equations are discretized using the discontinuous Galerkin finite element method. By way of example, thermoacoustic characteristics of attached and lifted laminar premixed flames are investigated. First, the respective flame transfer functions (FTFs) are computed in the frequency domain with the LRF solver. The results are in agreement with reference FTFs identified from CFD time-series. Secondly, the LRF solver is employed for thermoacoustic stability analysis, i.e. computation of shape, frequency, and growth rate of eigenmodes. Results are compared to established hybrid methods that couple FTFs with a low-order thermoacoustic network-model or a linearized Navier-Stokes equations solver. All solvers capture the dominant thermoacoustic mode, but only the LRF resolves local flow-flame interaction, revealing e.g. the onset of the flame movement and the propagation of distortions along the flame.

Keywords: Thermoacoustics; Combustion dynamics; Discontinuous Galerkin finite element method; Linearized reacting flow; Linearized Arrhenius equation

1. Introduction

Modern, low-emission gas turbines are prone to thermoacoustic instabilities, which originate from a feedback between unsteady heat release and acoustics. It is essential to study thermoacoustic coupling mechanisms and to develop reliable tools for thermoacoustic analysis.

Prediction of thermoacoustic instabilities by means of high-fidelity simulations of the compressible reacting flow requires very considerable computational resources. Large-Eddy Simulation (LES) of a gas turbine combustor, say, may be unaffordable for industrial purposes. To reduce the problem size, a variety of modeling assumptions may be invoked to formulate *hybrid approaches*, which typically couple a model for the

* Corresponding author.
E-mail address: avdonin@tfd.mw.tum.de (A. Avdonin).

https://doi.org/10.1016/j.proci.2018.06.142
1540-7489

propagation and dissipation of acoustic waves with a flame transfer function (FTF). The FTF describes a flow-flame interaction and relates fluctuations of the global heat release rate to velocity fluctuations at a reference point upstream of the flame. Flame transfer functions can be derived analytically or obtained from experiments or CFD simulations, see for instance [1–3].

Thermoacoustic network-models (TNMs) represent a very popular, low-order hybrid approach. A TNM represents a combustor as a conjunction of elements, such as ducts and area jumps. Acoustic waves propagate through the resulting network of elements. The heat release fluctuations are modeled using an FTF and produce acoustic perturbations according to the linearized Rankine–Hugoniot jump conditions [4].

Due to increasing computing power and improved numerical algorithms, it has become possible to resolve the acoustic field in a combustor in two or three dimensions with the Helmholtz [5], the linearized Euler [6] or the *linearized Navier–Stokes equations* (LNSE) [7,8]. The spatial resolution of the mean and fluctuating flow field variables allows to investigate complex geometries and can yield an accurate prediction of dissipative effects. These approaches should also be categorized as hybrid models, as the flow-flame interaction is represented by an FTF.

Despite increased efforts to scrutinize nonlinear aspects of combustion dynamics [9], linear analysis remains extremely useful and important for fundamental studies of flow-flame-interaction mechanisms, for sensitivity or uncertainty analysis, for optimization, and for industrial application. This motivates the quest for more efficient, more accurate and more widely applicable methods for linear thermoacoustic stability analysis.

In this paper, we suggest an approach with an inherent description of the flame dynamics. Specifically, we analytically linearize the Navier-Stokes and reacting species transport equations to obtain *linearized reactive flow* (LRF) equations. With such a monolithic formulation, the linear flame dynamics is by design inherited from the governing equations; an external FTF is not required. The LRF equations are discretized using the discontinuous Galerkin finite element method. The LRF solver requires a CFD simulation to obtain mean fields, but no additional unsteady CFD simulations are needed to identify the FTF.

The works by van Kampen et al. [10] on the response of a premixed flame to fluctuations of equivalence ratio and by Blanchard et al. [11] on the effects of flow disturbances on the flame (and vice versa) may be regarded as precursors of the LRF approach. Those studies employ a numerical linearization of the governing equations and compute the flame transfer functions by simulating the step response in the time domain. In contrast, the LRF equations are derived analytically and the solver operates in the frequency domain, which allows to compute the FTF as well as thermoacoustic eigenmodes with high accuracy and efficiency.

The present paper introduces the LRF solver and verifies results by comparison with established hybrid approaches. By way of example, we study the flame dynamics and the dominant thermoacoustic eigenmodes of attached as well as lifted, compact, laminar, premixed flames. The full potential of the method - e.g. for non-compact flames - shall be exploited in further studies.

The paper is structured as follows: in the next section, we introduce the LRF and the two hybrid approaches, TNM and LNSE. Afterwards, we compare the FTFs computed by the LRF solver and deduced from CFD simulations, respectively, for two flame configurations. Then we compute and compare the dominant thermoacoustic eigenmodes. The paper closes with conclusions and an outlook for further investigations.

2. Linearized reacting flow

2.1. Nonlinear governing equations

Both the OpenFOAM solver , which computes the mean flow fields and the reference FTF, and the LRF solver are based on the nonlinear reactive flow equations:

$$\frac{\partial \rho}{\partial t} + \frac{\partial \rho u_j}{\partial x_j} = 0, \tag{1}$$

$$\frac{\partial \rho u_i}{\partial t} + \frac{\partial \rho u_i u_j}{\partial x_j} = -\frac{\partial p}{\partial x_i} + \frac{\partial \tau_{ij}}{\partial x_j}, \tag{2}$$

$$\frac{\partial}{\partial t}(\rho h - p) + \frac{\partial \rho u_j h}{\partial x_j} = \frac{\partial}{\partial x_j}\left(\alpha \frac{\partial h}{\partial x_j}\right) + \dot{\omega}_T, \tag{3}$$

$$\frac{\partial \rho Y_k}{\partial t} + \frac{\partial \rho u_j Y_k}{\partial x_j} = \frac{\partial}{\partial x_j}\left(D \frac{\partial Y_k}{\partial x_j}\right) + \dot{\omega}_i. \tag{4}$$

Variables ρ, u_i, and Y_k denote density, velocity component in the i-direction, and mass fraction of the species k. The viscous term is neglected in the conservation equation (3) for the sensible enthalpy h. The heat flux is approximated by $-\alpha\left(\partial h/\partial x_j\right)$ instead of Fourier's law[1], which is commonly done when the energy equation is written in terms of the sensible enthalpy. The sensible enthalpy for the species k is calculated from JANAF polynomials with coefficients a_j:

$$h_k(T) = \int_{T_{ref}}^{T} c_{p,k} d\tilde{T} = R_k \sum_{j=1}^{5} a_j \frac{T^j - T_{\text{ref}}^j}{j}, \tag{5}$$

[1] In this study we follow the OpenFOAM definitions of the thermal and mass diffusivities, α and D, with SI units kg/(ms).

with the specific gas constant R_k for the species k. The sensible enthalpy of the mixture is computed using the species mass fractions: $h = \sum_k h_k Y_k$. The viscous stress tensor τ_{ij} reads:

$$\tau_{ij} = \mu\left(\frac{\partial u_i}{\partial x_j} + \frac{\partial u_j}{\partial x_i}\right) - \frac{2}{3}\mu\frac{\partial u_l}{\partial x_l}\delta_{ij}, \tag{6}$$

where δ_{ij} is the Kronecker delta. The pressure p, the density ρ, and the temperature T are linked by the ideal gas law: $p = \rho RT$. The dynamic viscosity μ is given by Sutherland's law: $\mu = A_s T^{1/2}/(1 + T_S/T)$ with $A_s = 1.67212 \cdot 10^{-6}$ kg/(msK$^{1/2}$) and $T_S = 170.672$ K. To determine thermal diffusivity α a constant Prandtl number $\mathrm{Pr} = \mu/\alpha = 0.71$ is assumed. Similarly, with unity Lewis number for all species, Schmidt number Sc and mass diffusivity D^2 obey $\mathrm{Sc} = \mu/D = 0.71$.

We model the methane-air combustion using a one-step Westbrook and Dryer [12] chemistry mechanism with a progress rate $\mathcal{Q}$:

$$\mathcal{Q} = A\rho^{a+b}\frac{Y_{O_2}^a Y_{CH_4}^b}{W_{O_2}^a W_{CH_4}^b}\exp\left(-\frac{E_a}{T R_{\mathrm{univ}}}\right), \tag{7}$$

with $A = 6.7 \times 10^{12}$ cgs units, $E_a = 48.4$ kcal/mol, $R_{\mathrm{univ}} = 1.987 \times 10^3$ kcal/(molK), $a = 1.3$ and $b = 0.2$.

The methane consumption rate is $\dot{\omega}_{\mathrm{CH_4}} = -W_{\mathrm{CH_4}}\mathcal{Q}$ and the heat release rate is $\dot{\omega}_T = \Delta h^\circ \mathcal{Q}$, where $W_{\mathrm{CH_4}}$ is the molar mass of methane and Δh° is the standard enthalpy of reaction.

2.2. Linearized governing equations

We split field variables into time-averaged and fluctuating parts, indicated by the overline and the prime, respectively. Linearization of equations (1)–(4) yields:

$$\frac{\partial \rho'}{\partial t} + \frac{\partial}{\partial x_j}\left(\overline{\rho}u_j' + \rho'\overline{u}_j\right) = 0, \tag{8}$$

$$\frac{\partial}{\partial t}\left(\overline{\rho}u_i' + \rho'\overline{u}_i\right) + \frac{\partial}{\partial x_j}\left(\overline{\rho}\overline{u}_i u_j' + \overline{\rho}u_i'\overline{u}_j + \rho'\overline{u}_i\overline{u}_j\right) = -\frac{\partial p'}{\partial x_i} + \frac{\partial \tau_{ij}'}{\partial x_j}, \tag{9}$$

$$\frac{\partial}{\partial t}\left(\overline{\rho}h' + \rho'\overline{h} - p'\right) + \frac{\partial}{\partial x_j}\left(\overline{\rho}\overline{u}_j h' + \overline{\rho}u_j'\overline{h} + \rho'\overline{u}_j\overline{h}\right) = \frac{\partial}{\partial x_j}\left(\overline{\alpha}\frac{\partial h'}{\partial x_j} + \alpha'\frac{\partial \overline{h}}{\partial x_j}\right) + \dot{\omega}_T', \tag{10}$$

$$\frac{\partial}{\partial t}\left(\overline{\rho}Y_k' + \rho'\overline{Y}_k\right) + \frac{\partial}{\partial x_j}\left(\overline{\rho}\overline{u}_j Y_k' + \overline{\rho}u_j'\overline{Y}_k + \rho'\overline{u}_j\overline{Y}_k\right) = \frac{\partial}{\partial x_j}\left(\overline{D}\frac{\partial Y_k'}{\partial x_j} + D'\frac{\partial \overline{Y}_k}{\partial x_j}\right) + \dot{\omega}_k'. \tag{11}$$

Note that the enthalpy equation cannot be reduced to the pressure equation because c_p is not constant, see Eq. (5). Furthermore,

$$\tau_{ij}' = -\frac{2}{3}\delta_{ij}\left(\overline{\mu}\frac{\partial u_l'}{\partial x_l} + \mu'\frac{\partial \overline{u}_l}{\partial x_l}\right) + \overline{\mu}\left(\frac{\partial u_i'}{\partial x_j} + \frac{\partial u_j'}{\partial x_i}\right) + \mu'\left(\frac{\partial \overline{u}_i}{\partial x_j} + \frac{\partial \overline{u}_j}{\partial x_i}\right),$$

$$\mu' = \overline{\mu}\frac{\overline{T} + 3T_S}{2(\overline{T} + T_S)}\frac{T'}{\overline{T}}, \quad h' = \overline{c}_p T' + \sum_k \overline{h}_k Y_k',$$

$$\frac{T'}{\overline{T}} = \frac{p'}{\overline{p}} - \frac{\rho'}{\overline{\rho}},$$

$$\dot{\omega}_k' = \overline{\dot{\omega}}_k\left((a+b)\frac{\rho'}{\overline{\rho}} + \frac{T_a T'}{\overline{T}^2} + a\frac{Y_{\mathrm{O_2}}'}{\overline{Y}_{\mathrm{O_2}}} + b\frac{Y_{\mathrm{CH_4}}'}{\overline{Y}_{\mathrm{CH_4}}}\right),$$

D', α' and $\dot{\omega}_T'$ are computed in an analogous manner. Fuel mass fraction $\overline{Y}_{\mathrm{CH_4}}$ appears in the denominator of the equation for $\dot{\omega}_k'$, which can lead to numerical problems. Its value is thus limited to $\overline{Y}_{\mathrm{CH_4}} \geq \max(\overline{Y}_{\mathrm{CH_4}}) \times 10^{-4}$.

In this study, we consider premixed flames with the global one-step reaction. Thus, it suffices to transport a single species or a single progress variable. We choose to transport $Y_{\mathrm{CH_4}}'$; hence the mass-fraction of oxygen required for the computation of the reaction progress is given by $Y_{O_2}' = (2W_{\mathrm{O_2}}/W_{\mathrm{CH_4}})Y_{\mathrm{CH_4}}'$. The remaining linearized field variables are p', ρ', and u_i'. For the sake of compactness, we avoid rewriting the linearized Eqs. (8)–(11) in terms of the selected linearized variables, it can be done without essential difficulty using the expressions provided above.

In closing this section we point out that in order to make the linearized equations fully consistent with the original nonlinear problem, first-order fluctuations of flow variables as well as material properties are retained. Note that the latter was crucial to achieve quantitative agreement with established methods (see below). Somewhat surprisingly, no sophisticated treatment of the strongly nonlinear Arrhenius term was required.

2.3. Discretization

The linearized reacting flow equations are discretized using the discontinuous Galerkin finite element method with a local Lax-Friedrichs flux formulation [13]. This method, which has proven to be robust for convectively-dominated problems, is an established method in CFD [14] and was adopted only recently for a hybrid thermoacoustic solver [8]. The discretization with linear ansatz functions

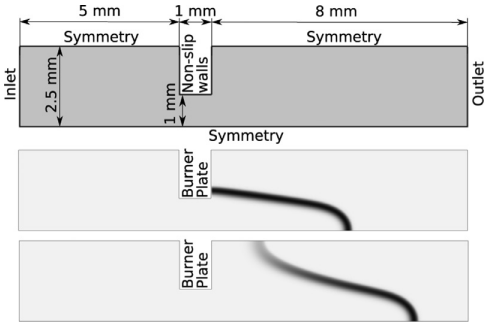

Fig. 1. Computational domain (top), mean heat release rate of the attached flame (middle) and of the lifted flame (bottom).

for all linearized variables is implemented in the commercial software COMSOL Multiphysics. The mean fields are provided by OpenFOAM simulations. The derivatives of the mean fields, such as $\partial\overline{u}_i/\partial x_j$, $\partial\overline{Y}_{CH_4}/\partial x_j$, and $\partial\overline{h}/\partial x_j$, are computed by the LRF solver internally.

In this study, the LRF solver computes the flame response in the frequency domain:

$$\hat{\dot{Q}} = \mathbf{C}(i\omega\mathbf{E} - \mathbf{A})^{-1}\mathbf{B}\hat{u}_{\text{ref}}, \tag{12}$$

where **A, B, C** and **E** are the system, input, output and mass matrices. Alternatively, the flame response may be deduced from a step response or broadband excitation in the time domain [3,15]. We solve for eigenvalues with an implicitly restarted Arnoldi algorithm [16]. All computations are performed with the direct parallel solver MUMPS [17].

3. Hybrid thermoacoustic models

The FTFs predicted by the LRF approach shall be verified by comparison with FTFs identified from CFD time-series, see Section 4.1 and [3,15]. Moreover, frequency and growth rate of the dominant thermoacoustic mode predicted by the LRF approach shall be compared to established hybrid approaches, which couple a model for the propagation and dissipation of acoustic waves with an FTF. In this section, the acoustic models are briefly described.

3.1. Thermoacoustic network-model

To represent the configurations under investigation (see Fig. 1), thermoacoustic network-models are built from simple elements such as ducts and sudden changes in cross-sectional area. The flame is assumed to be acoustically compact, so fluctuations of the global heat release rate $\dot{Q}'$ fully describe the flame dynamics and are related to the velocity fluctuations u'_{ref} at a reference point upstream of the flame through an FTF:

$$\frac{\hat{\dot{Q}}}{\overline{\dot{Q}}} = F(\omega)\frac{\hat{u}_{\text{ref}}}{\overline{u}_{\text{ref}}}, \tag{13}$$

where the circumflex denotes the complex fluctuation amplitude at frequency ω. The FTF is then coupled to the TNMs via linearized Rankine–Hugoniot jump conditions [4]. The network models are set up with the open source tool taX [18,19], which is based on a state-space formulation. The TNMs comprise no more than one thousand degrees of freedom; hence eigenvalues are computed within seconds. In the configuration investigated, the ducts are very short, so the corresponding viscous losses are negligible. Furthermore, loss coefficients at area jumps are not applied since semi-empirical approximations for the acoustic losses involve a high degree of uncertainty. Therefore, the reader should keep in mind that growth rates computed with the TNMs represent a worst-case result.

3.2. Linearized Navier–Stokes coupled with FTF

The hybrid model based on the linearized Navier-Stokes equations employs the same equations and discretization as the LRF, but without the transport equation for the fuel mass-fraction and the corresponding linearized reaction rate in the enthalpy equation. Instead, the unsteady heat release is represented by an FTF. The LNSE uses the same FTF as the TNM but additionally resolves the spatial extent of the flame. Thus, the fluctuating heat release rate results in a spatially distributed source term $\dot{\omega}'_T$. Following [5,8], we assume a distribution proportional to the local *mean* heat release rate:

$$\hat{\dot{\omega}}_T(\vec{x}) = \overline{\dot{\omega}}_T(\vec{x})F(\omega)\frac{\hat{u}_{\text{ref}}}{\overline{u}_{\text{ref}}}. \tag{14}$$

Using this formulation, the local fluctuations of the heat release rate are synchronized throughout the entire domain. This should be adequate for an acoustically compact flame, although it ignores any phase lag between the flame response at the root and the tip, say, and the consequential possibility of destructive interference.

Both the TNM and the LNSE models employed in this study employ a state-space formulation. The FTF is also converted to the state space representation and coupled with the acoustic system matrices, which yields a linear eigenvalue problem [8,19].

Note that the LNSE solver requires roughly 10% to 30% less computational resources than the LRF solver on the same mesh due to the reduced number of variables.

4. Investigation of a laminar premixed flame

4.1. Numerical setup

By way of example, we investigate a generic, laminar premixed flame that is stabilized on a slit as shown in Fig. 1 (top). Exploiting the symmetry along and across the slits reduces the simulation domain to one-half of the flame in two dimensions. If the burner plate is adiabatic, then the flame attaches to it, see Fig. 1 (middle). Setting a constant surface temperature $T_W = 375$ K at the burner plate results in a lifted flame as shown in Fig. 1 (bottom). The remaining flow parameters are identical for both configurations: the inlet velocity is 0.3 m/s, the equivalence ratio equals 0.8, the inlet temperature is 293 K, and the outlet pressure is 101325 Pa.

The CFD solver employs standard boundary conditions: isothermal inlet with fixed velocity and mixture, outlet with fixed static pressure, non-slip walls at the burner plate, symmetry at the top and bottom of the computational domain. A structured mesh with 53600 square cells of size of $\Delta x = 25\,\mu$m resolves the flame with 16 cells.

The LRF and LNSE solvers use corresponding linearized boundary conditions. Two meshes are used: a fine mesh that is identical to the CFD mesh, and a coarser mesh with $\Delta x = 40$ μm and 21100 cells (10 cells across the flame).

A flame transfer function as required for hybrid models is identified as a finite impulse response from time-series data generated by OpenFOAM simulations. A broadband velocity excitation with an amplitude of $0.05\overline{u}_{\text{inlet}}$ is imposed at the inlet. To ensure a robust simulation and reduce noise, a weakly compressible version of the reactive OpenFOAM solver is employed [20]. The CFL number is 0.1, and the simulation time is 0.15 s, which is sufficient for the accurate identification of the FTF in this study. The identification methodology is discussed in detail by Tay-Wo-Chong et al. [3] and Polifke [15]. The computation of the FTF is quite time consuming, since it requires a long time series for the identification process – typically 0.15 s to 0.3 s, which entails compute times of several days.

OpenFOAM simulations without excitation provide the flow parameters of the burnt and unburnt gas for the TNM as well as the mean fields for the LNSE and LRF. In these simulations, the CFL number was decreased to 0.01 to better resolve the chemical time scale and thus obtain a better flame-front resolution.

4.2. Flame transfer function

We use the inlet velocity of the computational domain as the reference velocity for the flame transfer functions, see Eq. (13).

The FTFs of the attached (left) and lifted (right) flames were identified from the OpenFOAM time-series with more than 95% accuracy, see Fig. 2. Due to a very high identification accuracy, the confidence intervals are negligibly small and therefore omitted. Both flames show a low-pass behavior. The lifted flame exhibits an excess gain at around 65 Hz, followed by a very rapid decline, such that its response is close to zero for frequencies above 200 Hz.

Figure 2 also shows the flame frequency responses computed by the LRF solver with two different meshes. For both the attached and lifted flames, the LRF solver yields similar results for mesh sizes $\Delta x = 40\,\mu$m and $25\,\mu$m, indicating discretization independence. Further reduction of the mesh size preserving the FTF quality is possible by coarsening the regions further away from the flame and the corners of the burner plate. In the following, we focus on results obtained on the fine mesh ($\Delta x = 25$ μm), which corresponds to the CFD mesh.

The LRF solver predicts the phase of the frequency response well. The gain of the frequency response is perfectly predicted for the attached flame and overestimated by up to 10% for the lifted flame. These results are achieved at significantly lower computational cost than running a transient CFD simulation for the FTF identification: 6 CPUh and 22 GB RAM for the computation of 16 frequency responses vs. 300 CPUh and 2Gb RAM for the CFD simulation on the same mesh. To reduce the RAM requirements, an iterative solver may be used – typically at the cost of longer computational time.

4.3. Thermoacoustic eigenmodes

In this section, we investigate the thermoacoustic eigenmodes and eigenvalues – i.e. frequencies and growth rates – of the two flame configurations. The simulation domain is very small (14 mm), such that acoustic cavity-modes can be found only at very high frequencies in the kHz range. Thus, we set the inlet and outlet boundaries to be nonreflecting and concentrate on intrinsic thermoacoustic (ITA) eigenmodes, which may be unstable for nonreflecting boundaries provided that the flame response is sufficiently strong [21,22]. Alternatively, impedance boundary conditions formulated as state space systems could be used, as suggested by Jaensch et al. [23]. The frequencies of ITA modes in an anechoic environment can be approximately determined by the "π criterion" [21]: *ITA modes may occur whenever the phase of the FTF is close to an odd multiple of* π. Inspecting Fig. 2, we see that ITA frequencies should be around 170 Hz for the attached flame and 100 Hz for the lifted flame.

Now, we compare predictions of the LRF solver with the two hybrid approaches described in Section 3. The TNM (○) and LNSE (▽) share the same FTF identified from CFD time-series as described in the previous subsection. All models predict the unstable thermoacoustic modes and yield

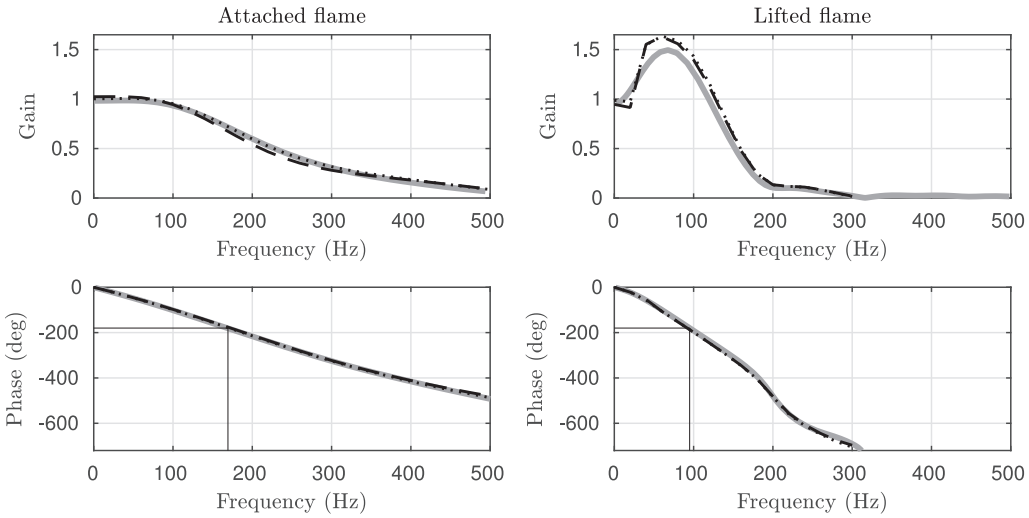

Fig. 2. Frequency response of the attached flame (left) and the lifted flame (right) identified using CFD time-series (▬) and computed using the LRF solver with mesh sizes $\Delta x = 40$ μm (- -) and 25 μm (....). Thin black lines (_) visualize the π criterion for ITA modes.

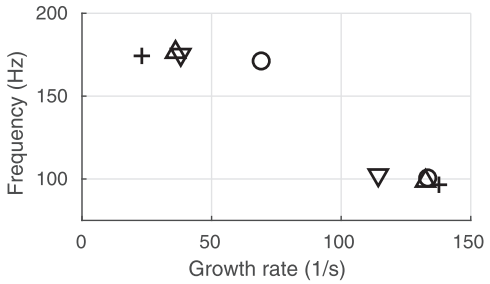

Fig. 3. Dominant thermoacoustic eigenvalues of the attached flame ($\approx$ 170 Hz) and the lifted flame ($\approx$ 100 Hz) predicted with LRF (+), LNSE with FTF_{LRF} (△), LNSE (▽) and TNM (○) with FTF identified from CFD time-series.

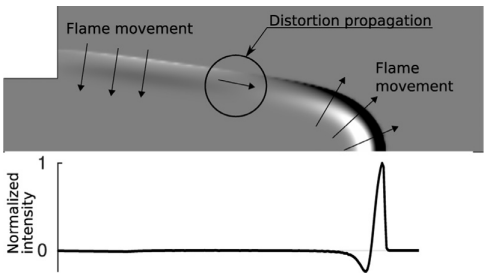

Fig. 4. Unstable eigenmode of the attached flame at 170 Hz: positive real part of the fluctuating heat release rate in black and negative in white at the top, its streamwise distribution at the bottom.

eigenfrequencies similar to the ones suggested by the π criterion.

The LRF solver requires most computational resources for the eigenvalue computation (0.4 CPUh and 22 GB RAM). The LNSE solver requires slightly less computational resources (0.4 CPUh and 18 GB RAM). The TNM solver computes eigenvalues within seconds due to the small number of degrees of freedom. Keep in mind, however, that even though the hybrid solvers are less costly than the LRF solver, they require to determine or measure an external FTF with considerable effort.

The LNSE as well as the LRF account for mean flow effects and allow for a linear energy transfer between acoustics, vorticity, and entropy waves. That results in a more accurate prediction of acoustic dissipation than using TNM and, typically, in smaller growth rates. The TNM (○) provides higher growth rates than the LNSE (▽), since the TNM neglects acoustic losses other than those associated with the nonreflecting in- and outlets.

The growth rates computed by the LRF (+) differ from those computed by the LNSE (▽). We offer two reasons for this discrepancy. Firstly, LRF slightly over-predicts the FTF gain of the lifted flame at its eigenfrequency, which should translate into an increase in growth rate [21].

Secondly, there are important differences in the modeling of flow-flame interactions by the LRF and LNSE. The LRF locally resolves the flow-flame interaction. This is demonstrated, for

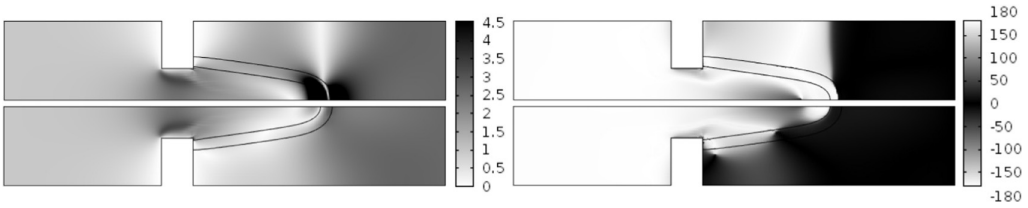

Fig. 5. Unstable eigenmode of the attached flame at 170 Hz: magnitude (left) and phase (right) of the fluctuating streamwise velocity normalized at the inlet for the LRF (top) and LNSE (bottom) models. Black lines indicate the mean flame position.

instance, for the attached flame[2] in Fig. 4. The figure shows the unstable mode at 170 Hz in terms of the real part of the fluctuating heat release rate. Only the flame tip yields a significant contribution to the global fluctuation of the heat release rate, since the local fluctuations upstream of the flame tip cancel out. The local fluctuations in heat release rate change from negative (white color) to positive (black) across the flame indicating the onset of the flame movement towards the burnt mixture (or vice versa). Furthermore, the LRF captures a distortion, initiated at the flame root and propagated downstream along the flame, changing the direction of the flame movement[3]

In contrast, the LNSE does not explicitly resolve the spatio-temporal evolution of flame movement and distortion along the length of the flame. Instead, the heat release rate fluctuation is synchronized along the length of the flame and is proportional to the mean heat release rate. Consequently, the fluctuating velocity fields that result from unsteady heat release differ for the LRF and LNSE formulations (see Fig. 5), which should contribute to the differences in predicted growth rates.

To facilitate further analysis, we introduce one additional model. We couple the LNSE with the flame transfer function that is computed using the linearized reactive flow solver[4] This new model is abbreviated as $\mathrm{LNSE_{LRF}}$. The LRF and $\mathrm{LNSE_{LRF}}$ share the same FTF, so these two models cannot show any discrepancies in their growth-rate predictions related to the gain of the FTF, but only related to the differences in the flow-flame modeling.

For the lifted flame, the growth rates provided by the LRF (+) and $\mathrm{LNSE_{LRF}}$ ($\triangle$) are in a much better agreement than those provided by the LRF (+) and LNSE ($\bigtriangledown$). Hence, the discrepancy between the LRF and LNSE originates mostly from the gain of the FTF at the eigenfrequency, which was overpredicted by the LRF.

For the attached flame, the gain of the FTF is perfectly captured by the LRF. Hence, the difference between the growth rates computed by the LRF (+) and LNSE ($\bigtriangledown$) is attributed solely to the differences in the flow-flame modeling.

5. Conclusion and outlook

This paper introduces a linearized reactive flow solver to analyze the flame dynamics of attached and lifted laminar premixed flames as well as their thermoacoustic stability. The LRF captures the dynamics of both flames quite well: the phase of the flame frequency response is accurately predicted, while its gain is very well predicted for the attached flame and only slightly overestimated for the lifted flame. The LRF solver also correctly predicts the dominant thermoacoustic modes and resolves the spatio-temporal evolution of the mode shapes, making explicit the local fluctuations of heat release, the onset of the flame movement, and the convective propagation of flame distortion. For the simplistic test cases considered here with compact, velocity-sensitive, premixed flames, established thermoacoustic models such as TNM and LNSE also capture the eigenmodes in terms of frequency and growth rate quite well, but they do not resolve local flow-flame interaction due to their coupling with a global FTF.

The LRF is a very promising approach because of its monolithic formulation with an inherent flow-flame-acoustic interaction. Admittedly, it is computationally more expensive than the LNSE approach due to one additional variable and possibly higher resolution in the flame region. On the other hand, the LRF approach does not require an external FTF, so an unsteady CFD simulation for the identification of the FTF is not required. The local flow-flame interaction resolved by the LRF is particularly important for the investigation of non-compact flames and/or non-plane acoustics, i.e. at higher frequencies, where a standard FTF that relates upstream velocity to overall heat release is inadequate [24–26]. Moreover,

[2] The detached flame shows a similar onset of movement.

[3] An animation of the propagating flame distortion is provided in supplementary materials.

[4] The $\mathrm{FTF_{LRF}}$ is fitted as a rational polynomial to a sampled frequency response and is valid over the entire frequency range.

configurations where fluctuations in equivalence ratio, pressure or temperature perturb the heat release require corresponding MISO or MIMO (multiple-input, single/multiple-output) formulations of hybrid models. In such cases, it is strictly speaking necessary to identify several flame transfer functions and couple them to an acoustic model, which can quickly become expensive and cumbersome. Conversely, LRF makes possible increased flexibility in the analysis of such systems: any combination of fluctuating variables may be chosen as "input" or "output", the respective transfer behavior or sensitivities may be studied in a MIMO framework with very favorable computational costs.

Future studies should extend the approach to turbulent, technically premixed flames at high frequencies and exploit advantages or identify limitations of the method.

Acknowledgments

The authors gratefully acknowledge funding provided by the German Federal Ministry for Economics and Energy (FKZ 03ET7021U) and GE Power. The investigations were conducted in the framework of the joint research program of AG Turbo (COOREFLEX-turbo 2.1.2c). The authors gratefully acknowledge the computational and data resources provided by the Leibniz Supercomputing Centre. We also thank Felix Schily for helping with the setup of network models in taX and Alp Albayrak for fruitful discussions about the LRF.

Supplementary material

Supplementary material associated with this article can be found, in the online version, at 10.1016/j.proci.2018.06.142

References

[1] L. Crocco, *J. Am. Rock. Soc.* (1951) 163–178.
[2] K. T. Kim, H. J. Lee, J. G. Lee, B. D. Quay, D. Santavicca (2009) 799–810. doi:10.1115/GT2009-60026.
[3] L. Tay-Wo-Chong, S. Bomberg, A. Ulhaq, T. Komarek, W. Polifke, *J. Eng. Gas Turbines Power* 134 (2) (2012) 021502–1–8, doi:10.1115/1.4004183.
[4] B.T. Chu, in: 4th Symposium (International) on Combustion, volume 4, Combustion Institute, Cambridge, Massachusetts, USA, 1953, pp. 603–612, doi:10.1016/S0082-0784(53)80081-0.
[5] F. Nicoud, L. Benoit, C. Sensiau, T. Poinsot, *AIAA J.* 45 (2) (2007) 426–441, doi:10.2514/1.24933.
[6] M. Zahn, M. Betz, M. Schulze, C. Hirsch, T. Sattelmayer (2017) V04AT04A081. doi:10.1115/GT2017-64238.
[7] J. Gikadi, T. Sattelmayer, A. Peschiulli, in: ASME Turbo Expo 2012: Turbine Technical Conference and Exposition, American Society of Mechanical Engineers, 2012, pp. 1203–1211.
[8] M. Meindl, A. Albayrak, W. Polifke, submitted to *J. Comput. Phys.* (2018).
[9] M.P. Juniper, R.I. Sujith, *Ann. Rev. Fluid Mech.* 50 (1) (2018) 661–689, doi:10.1146/annurev-fluid-122316-045125.
[10] J.F. van Kampen, J.B.W. Kok, T.H. van der Meer, *Int. J. Numer. Methods Fluids* 54 (9) (2007) 1131–1149, doi:10.1002/fld.1424.
[11] M. Blanchard, T. Schuller, D. Sipp, P.J. Schmid, *Phys. Fluids* 27 (4) (2015) 043602, doi:10.1063/1.4918672.
[12] C.K. Westbrook, F.L. Dryer, *Combust. Sci. Technol.* 27 (1–2) (1981) 31–43, doi:10.1080/00102208108946970.
[13] B. Cockburn, S.-Y. Lin, C.-W. Shu, *J. Comput. Phys.* 84 (1) (1989) 90–113, doi:10.1016/0021-9991(89)90183-6.
[14] B. Cockburn, G.E. Karniadakis, C.-W. Shu, in: Lecture Notes in Computational Science and Engineering, Springer, Berlin, Heidelberg, 2000, pp. 3–50, doi:10.1007/978-3-642-59721-3_1.
[15] W. Polifke, *Ann. Nuclear Energy* 67C (2014) 109–128, doi:10.1016/j.anucene.2013.10.037.
[16] R. Lehoucq, D. Sorensen, *SIAM J. Matrix Anal. Appl.* 17 (4) (1996) 789–821, doi:10.1137/S0895479895281484.
[17] P. R. Amestoy, I. S. Duff, J.-Y. L'Excellent, J. Koster, in: T. Sørevik, F. Manne, A. H. Gebremedhin, R. Moe (Eds.), Applied Parallel Computing. New Paradigms for HPC in Industry and Academia, number 1947 in Lecture Notes in Computer Science, Springer Berlin Heidelberg, 2000, pp. 121–130. doi:10.1007/3-540-70734-416.
[18] T. Emmert, S. Jaensch, C. Sovardi, W. Polifke, in: 7th Forum Acusticum, DEGA, Krakow, 2014.
[19] T. Emmert, M. Meindl, S. Jaensch, W. Polifke, *Acta Acust. United Acust.* 102 (5) (2016) 824–833, doi:10.3813/AAA.918997.
[20] S. Jaensch, M. Merk, E.A. Gopalakrishnan, et al., *Proc. Combust. Inst.* 36 (3) (2017) 3827–3834, doi:10.1016/j.proci.2016.08.006.
[21] M. Hoeijmakers, V. Kornilov, I. Lopez Arteaga, P. de Goey, H. Nijmeijer, *Combust. Flame* 161 (11) (2014) 2860–2867, doi:10.1016/j.combustflame.2014.05.009.
[22] C.F. Silva, T. Emmert, S. Jaensch, W. Polifke, *Combust. Flame* 162 (9) (2015) 3370–3378, doi:10.1016/j.combustflame.2015.06.003.
[23] S. Jaensch, C. Sovardi, W. Polifke, *J. Comput. Phys.* 314 (2016) 145–159, doi:10.1016/j.jcp.2016.03.010.
[24] M. Zellhuber, J. Schwing, B. Schuermans, T. Sattelmayer, W. Polifke, *Int. J. Spray Combust. Dyn.* 6 (2014) 1–34, doi:10.1260/1756-8277.6.1.1.
[25] T. Hummel, F. Berger, M. Hertweck, B. Schuermans, T. Sattelmayer, *J. Eng. Gas Turbines Power* 139 (7) (2017) 071502–071502–10, doi:10.1115/1.4035592.
[26] Y. Méry, *Combust. Flame* 192 (2018) 410–425, doi:10.1016/j.combustflame.2018.02.007.

Combustion and Flame 223 (2021) 525–540

Contents lists available at ScienceDirect

Combustion and Flame

journal homepage: www.elsevier.com/locate/combustflame

On the spurious entropy generation encountered in hybrid linear thermoacoustic models

Max Meindl*, Camilo F. Silva, Wolfgang Polifke

Technical University of Munich, Garching 85747, Germany

ARTICLE INFO

Article history:
Received 10 June 2020
Revised 16 September 2020
Accepted 16 September 2020

Keywords:
Thermoacoustic combustion instability
Flow-flame interaction
Entropy waves
Flame transfer function
Linearized Navier–Stokes
Linearized reactive flow

ABSTRACT

This work demonstrates that a hybrid approach for linear thermoacoustic stability analysis that combines the Linearized Navier–Stokes Equations (LNSE) with a global Flame Transfer Function (FTF), generates spurious entropy waves when used to model acoustically forced premixed flames. The inability of the global FTF to account for the effects of flame movement is identified as the root cause of this unphysical behavior. Utilization of a local FTF, which resolves unsteady heat release on scales comparable to the reaction zone of the flame, suppresses the spurious entropy perturbations. This affirms that fine-grained resolution of the spatio-temporal distribution of heat release rate fluctuations in the combustion zone is required to model the movement of the flame front, even for acoustically and convectively compact flames. As an alternative to hybrid models, a Linearized Reactive Flow (LRF) approach is employed, which extends the LNSE by the linearized species transport equations as well as the reaction mechanism. Such a monolithic approach inherently accounts for the locally resolved flame dynamics, including the movement of the flame front, and does not require an external model for the flame-flow interaction. Thus the LRF eliminates the need for the cumbersome identification of a local FTF. Two configurations of lean premixed methane-air flames, i.e. a freely propagating 1D flame and a 2D flame anchored in a duct, are considered for validation. All results obtained with linearized modeling approaches and conclusions deduced thereof are validated against high resolution CFD results with excellent quantitative accuracy.

1. Introduction

Gas turbines play an important role not only for propulsion in aero-engines, but also in the energy sector, where they provide flexible generation of electricity to complement highly fluctuating renewable sources of energy. During the past decades, increasing restrictions on pollutant emissions have been enforced, which have promoted the development of lean premixed combustion technology, featuring aerodynamically stabilized, velocity sensitive flames. The downside of this technology is its susceptibility to thermoacoustic instabilities, a phenomenon that results from feedback interactions between unsteady combustion and acoustic velocity perturbations impinging on the flame [1]. The consequences of such instabilities range from increased emissions up to the deterioration and eventual destruction of the engine. Studying the physics, identifying the most influential parameters and predicting the resonant frequencies, stability limits and margins, is thus vital for the design of reliable, flexible and efficient modern gas turbines.

Due to the high costs and restricted diagnostic access on experimental test rigs, numerical simulations are employed to complement or replace experiments during the design process. A plethora of model strategies is available, ranging from linear, quasi-1D network models [2–4] to Computational Fluid Dynamics (CFD) for laminar flames [5–7], or highly resolved and thus very costly Large Eddy Simulation (LES) for turbulent flames [8–10]. Opposed to the monolithic approach of CFD, which naturally incorporates the dynamics of combustion processes, one commonality of most low-order models is their hybrid nature: the acoustics and the flame dynamics are described by dedicated sub-models, which are coupled to each other to construct a complete thermoacoustic model. The propagation of acoustic waves is modeled, e.g., by quasi 1D network models or 2D/3D models based on the Helmholtz Equations, Linearized Euler Equations (LEE) or more recently the Linearized Navier-Stokes Equations (LNSE) [11–18]. In the given order, the complexity and computational cost, but also the capabilities of these formulations increase. For example, LNSE can incorporate so-called convective waves, i.e. the convective transport of perturbations of fuel concentration, entropy or vorticity by the mean flow, which may be important elements of the

* Corresponding author.
E-mail addresses: meindl@tum.de, meindl@tfd.mw.tum.de (M. Meindl).

https://doi.org/10.1016/j.combustflame.2020.09.018
0010-2180/

thermoacoustic feedback loop. Furthermore, LNSE can take into account interactions between acoustics and mean flow as well as other damping mechanisms that result in loss of acoustic energy in a combustor. These capabilities account for the interest in hybrid thermoacoustic models based on the LNSE, see e.g. [15–18].

The sub-model for the flow-flame interaction can in general be chosen independent of the acoustic governing equations. For linear stability analysis, the so-called Flame Transfer Function (FTF), stemming from measurements, numerical simulations or analytical expressions, is often employed. It relates upstream velocity perturbations to fluctuations of the global heat release rate.

Recently, a Linearized Reactive Flow (LRF) model was introduced [19,20]. The formulation is based on an analytical linearization of the governing equations, unlike the numerical linearization approach pursued in [21,22]. The LRF differs from the other linear models mentioned above inasmuch as it is not hybrid[1] in nature. Instead, not only the Navier-Stokes, but also the species transport equations alongside with the reaction kinetics are linearized. This leads to an inherent incorporation of the locally resolved flame dynamics, without the need for a flow-flame sub-model, such as the FTF. In terms of complexity and cost, the LRF is found at the top end of the linear model spectrum. It features the most detailed description of the physics behind thermoacoustic instabilities and consequently, one may expect that it is the most accurate predictive tool – within the limits of a linearized analysis. Much like low-order models, the LRF ansatz can be used to carry out thermoacoustic stability analysis by computing the frequencies and growth rates of eigenmodes [20]. Furthermore, flow-flame interaction can be computed with an LRF formulation e.g. in the form of an FTF, as shown in [19,20,22].

Quantitative differences in the predictions of thermoacoustic oscillations obtained with network, LNSE and LRF models, respectively, were discussed in [20,23]. In these studies, direct sources of acoustic perturbations, i.e. the unsteady heat release rate by the flame itself, were accounted for. The main focus of the present study lies, conversely, on the generation of entropy waves by acoustic-flow-flame interactions, which may represent an important source of indirect sound. Indeed, it is understood that the acceleration of entropy perturbations at the turbine inlet, say, may generate indirect sound with significant impact on thermoacoustic stability and combustion noise, see e.g. [24–40]. It is therefore imperative that a comprehensive thermoacoustic model correctly represents not only the effect of the perturbed heat release rate on the acoustics, but also on the generation of entropy waves. Several studies investigated the dispersion of entropy waves while being convected towards the combustor outlet [37,38,41–43] as well as the conversion of entropy perturbations to acoustic waves due to acceleration of the flow [24,29,30,33,35,39,40,44,45]. There are also several studies concerned with the generation of entropy waves by temperature inhomogeneities in non-reacting flows [46–48] or in acoustically compact reaction zones, which are treated as a discontinuity in the acoustic model [49–52]. To date, the ability of linearized thermoacoustic models to correctly predict the generation of entropy perturbations in a spatially extended combustion zone has been studied only by Steinbacher et al. [43].

The present paper demonstrates that modeling a lean premixed flame by means of the LNSE combined with a global FTF, which represents the perturbed heat release rate in a lumped fashion, leads to unphysical behavior: spurious entropy waves are generated when the flame is forced acoustically, in violation of fundamental conservation laws and contradicting the recent literature [51,52]. Given that the entropy waves encountered in this case are of unphysical nature, the indirectly generated sound in an accelerated flow downstream would thus falsely influence the thermoacoustic oscillations and have a detrimental effect on the correctness of stability predictions. The main objective of the present study is the analysis of the spurious entropy generated by the LNSE paired with a global FTF, and the assessment of two approaches that do not generate spurious entropy, i.e. LNSE combined with a highly resolved *local* FTF, or LRF.

We supply evidence that the global FTF, which outputs a lumped value for the global fluctuation of the heat release rate, cannot properly represent the effect of flame movement, which in turn leads to the spurious entropy waves. Specifically, because the local values of the fluctuating heat release rate are unknown, an assumption about their spatial distribution has to be made. One possibility is to assume that the fluctuations follow in shape the mean heat release rate. This assumption, although intuitive, will be shown to be inadequate when investigating the generation of entropy waves. Indeed, it is a crucial modeling mistake that leads to significant errors in the prediction of entropy production and perturbation fields in the flame region and downstream of the flame. The origin of these errors – as will be shown below – is the inability of the LNSE to properly account for the fact that a premixed flame front is not a heat source at rest, but a heat source in kinematic balance with the approach flow [51,53,54]. The use of a local FTF, which resolves unsteady heat release on length scales comparable to the reaction zone of the flame, is shown to remedy the situation to a large extent. Likewise, the monolithic LRF does not exhibit spurious generation of entropy waves, as it inherently accounts for the local flame dynamics. It represents thus a promising alternative to hybrid models. Note that all results obtained with linearized tools and conclusions deduced thereof are validated against high resolution CFD results with excellent quantitative accuracy.

The paper is structured as follows: the governing equations for CFD, LNSE and LRF are presented in Section 2. Section 3 is dedicated to modeling approaches for the perturbed heat release rate in hybrid models via an FTF. A 1D freely propagating flame is investigated in Section 4 as a bare-bones example for the excess entropy perturbations stemming from the hybrid LNSE approach coupled to a global FTF. A locally resolved FTF is introduced in order to include the effects of flame movement and thereby correctly predict the flow perturbations. This topic is expanded in Section 5 by the analysis of an anchored, 2D, laminar, premixed flame. The paper concludes with a summary and an outlook on the ramifications of the findings. A derivation of the various physical contributions to entropy perturbations by linearization of the entropy transport equation for a reactive flow is provided as Supplementary Material.

2. Governing equations

This section presents the set of governing equations for compressible reactive flow, which represents the basis of all variants of numerical analysis of flame dynamics carried out in the present study, i.e. CFD, LRF and LNSE. Linearization of the governing equations yields the linearized reactive flow (LRF) model. By omitting the species transport equations as well as the reaction rates from the system of equations, the linearized Navier-Stokes equations (LNSE) are obtained.

[1] Note that the LRF, like all low-order models, requires information about the mean flow in the combustor, e.g. the spatial distribution of speed of sound, temperature or mean flow velocity, and could thus be classified as “hybrid” instead of “monolithic”. However, such classification would not make sense in the context of the present study. Instead, throughout this paper, we will regard a model as ”hybrid”, if it consists of dedicated sub-models for acoustics and flow-flame interaction, respectively, and ”monolithic” otherwise.

2.1. Compressible reactive flow

Compressible reactive flow is modeled by the fully compressible Navier-Stokes equations combined with transport equations for the species that comprise the chemical kinetics mechanism:

$$\frac{\partial \rho}{\partial t} + \frac{\partial \rho u_j}{\partial x_j} = 0, \tag{1}$$

$$\frac{\partial \rho u_i}{\partial t} + \frac{\partial \rho u_i u_j}{\partial x_j} = -\frac{\partial p}{\partial x_i} + \frac{\partial \tau_{ij}}{\partial x_j}, \tag{2}$$

$$\frac{\partial}{\partial t}(\rho h - p) + \frac{\partial \rho u_j h}{\partial x_j} = \frac{\partial}{\partial x_j}\left(\alpha \frac{\partial h_s}{\partial x_j}\right) + \dot{\Omega}_T, \tag{3}$$

$$\frac{\partial \rho Y_k}{\partial t} + \frac{\partial \rho u_j Y_k}{\partial x_j} = \frac{\partial}{\partial x_j}\left(D_k \frac{\partial Y_k}{\partial x_j}\right) + \dot{\Omega}_k. \tag{4}$$

Here, ρ is the density, p is the pressure, u_i is the velocity in the Cartesian coordinate direction x_i, h is the total non-chemical enthalpy, h_s is the sensible non-chemical enthalpy, τ_{ij} is the viscous stress tensor, Y_k is the mass fraction of species k, α and D_k are the thermal and species diffusivity, respectively. $\dot{\Omega}_T$ is the volumetric heat release rate due to combustion and $\dot{\Omega}_k$ is the source of species k. The fluid is assumed to behave like an ideal gas,

$$p = \rho R T. \tag{5}$$

Stokes' Hypothesis

$$\tau_{ij} = \mu\left(\frac{\partial u_i}{\partial x_j} + \frac{\partial u_j}{\partial x_i} - \frac{2}{3}\frac{\partial u_k}{\partial x_k}\delta_{ij}\right), \tag{6}$$

is combined with Sutherland's Law

$$\mu = A_S \frac{T^{1/2}}{\left(1 + \frac{T_S}{T}\right)}, \tag{7}$$

for the viscous stress tensor, where μ is the dynamic viscosity, δ_{ij} is the Kronecker-Delta, $A_S = 1.67212 \cdot 10^{-6}\,\mathrm{kg/(msK^{1/2})}$ and $T_S = 170.672\,\mathrm{K}$. The total non chemical enthalpy

$$h = h_s + \frac{1}{2}u_k u_k \tag{8}$$

is defined as the sum of sensible enthalpies of the species,

$$h_s = \sum_k h_{s,k} Y_k, \quad h_{s,k}(T) = \int_{T_{\mathrm{ref}}}^{T} c_{p,k}(\tilde{T})\,\mathrm{d}\tilde{T}, \tag{9}$$

and specific kinetic energy. The Prandtl number $\mathrm{Pr} = \mu/\alpha$ and Schmidt number $\mathrm{Sc}_k = \mu/D_k$ for all species are fixed at 0.71, which is reasonable for a methane-air mixture [55]. Due to the low Mach number of the flows under consideration in this work, viscous heating is neglected. The global two-step chemical kinetics mechanism used in the present study to evaluate the source terms $\dot{\Omega}_T$, $\dot{\Omega}_k$ in Eqs. (3) and (4) is described in Appendix A. The compressible reacting solver `rhoReactingFoam` from the OpenFOAM toolbox [56], which was used to generate the CFD results presented in this study, is based on the above set of equations.

2.2. Linearized governing equations

The unknown variables $\Phi(\mathbf{x}, t)$ of the reactive flow equations can be split into a steady-state mean flow $\bar{\Phi}(\mathbf{x})$ and unsteady perturbations $\Phi'(\mathbf{x}, t)$ by means of a perturbation ansatz,

$$\Phi(\mathbf{x}, t) = \bar{\Phi}(\mathbf{x}) + \Phi'(\mathbf{x}, t). \tag{10}$$

Inserting this ansatz into Eqs. (1)–(4) and assuming that the perturbations are small compared to suitable reference quantities in the mean flow, higher order perturbation terms can be neglected and the linearized reactive flow (LRF) equations are retrieved,

$$\frac{\partial \rho'}{\partial t} + \frac{\partial}{\partial x_j}\left(\bar{\rho}u_j' + \rho'\bar{u}_j\right) = 0, \tag{11}$$

$$\frac{\partial}{\partial t}\left(\bar{\rho}u_i' + \rho'\bar{u}_i\right) + \frac{\partial}{\partial x_j}\left(\bar{\rho}\bar{u}_i u_j' + \bar{\rho}u_i'\bar{u}_j + \rho'\bar{u}_i\bar{u}_j\right) = -\frac{\partial p'}{\partial x_i} + \frac{\partial \tau_{ij}'}{\partial x_j}, \tag{12}$$

$$\begin{aligned}\tfrac{\partial}{\partial t}\left(\bar{\rho}h' + \rho'\bar{h} - p'\right) + \tfrac{\partial}{\partial x_j}\left(\bar{\rho}\bar{u}_j h' + \bar{\rho}u_j'\bar{h} + \rho'\bar{u}_j\bar{h}\right) \\ = \tfrac{\partial}{\partial x_j}\left(\bar{\alpha}\tfrac{\partial h_s'}{\partial x_j} + \alpha'\tfrac{\partial \bar{h}_s}{\partial x_j}\right) + \dot{\Omega}_T',\end{aligned} \tag{13}$$

$$\begin{aligned}\tfrac{\partial}{\partial t}\left(\bar{\rho}Y_k' + \rho'\bar{Y}_k\right) + \tfrac{\partial}{\partial x_j}\left(\bar{\rho}\bar{u}_j Y_k' + \bar{\rho}u_j'\bar{Y}_k + \rho'\bar{u}_j\bar{Y}_k\right) \\ = \tfrac{\partial}{\partial x_j}\left(\bar{D}_k\tfrac{\partial Y_k'}{\partial x_j} + D_k'\tfrac{\partial \bar{Y}_k}{\partial x_j}\right) + \dot{\Omega}_k'.\end{aligned} \tag{14}$$

The linearization of the chemical kinetics mechanism that is required to determine the linearized source terms $\dot{\Omega}_T'$, $\dot{\Omega}_k'$ in Eqs. (11)–(14) is described in Appendix B. For further details, the reader is referred to the work of Avdonin et al. [20].

Full closure of this system of equations is achieved by introducing appropriately linearized expressions for the ideal gas law,

$$\frac{T'}{\bar{T}} = \frac{p'}{\bar{p}} - \frac{\rho'}{\bar{\rho}}, \tag{15}$$

the sensible enthalpy,

$$h_s' = \bar{c}_p T' + \sum_k \bar{h}_{s,k} Y_k', \quad \bar{c}_p = \sum_k \bar{c}_{p,k}\bar{Y}_k, \tag{16}$$

the total enthalpy,

$$h' = h_s' + \bar{u}_k u_k', \tag{17}$$

the viscous stress tensor

$$\tau_{ij}' = \bar{\mu}\left(\frac{\partial u_i'}{\partial x_j} + \frac{\partial u_j'}{\partial x_i} - \frac{2}{3}\frac{\partial u_k'}{\partial x_k}\delta_{ij}\right) + \mu'\left(\frac{\partial \bar{u}_i}{\partial x_j} + \frac{\partial \bar{u}_j}{\partial x_i} - \frac{2}{3}\frac{\partial \bar{u}_k}{\partial x_k}\delta_{ij}\right), \tag{18}$$

and the Sutherland law for the temperature dependence of viscosity, thermal and species diffusivity,

$$\mu' = \bar{\mu}\frac{\bar{T} + 3T_S}{2\left(\bar{T} + T_S\right)}\frac{T'}{\bar{T}}, \quad \alpha' = \mathrm{Pr}\mu', \quad D_k' = \mathrm{Sc}_k\mu'. \tag{19}$$

Including perturbations of the material properties is essential to achieve consistency between the non-linear and the linearized equations [20]. The entropy perturbations, neglecting species mixing, are given by

$$s' = \bar{c}_p\frac{T'}{\bar{T}} - R\frac{p'}{\bar{p}}. \tag{20}$$

In the Supplementary Material, the full entropy perturbations for a reactive flow are derived. In general, entropy perturbations due to species mixing should be accounted for, as they can as well lead to the generation of acoustic waves, see Magri et al. [57]. Although present, this effect is expected to be negligible for the perfectly premixed flames without secondary air flows and unity Lewis number investigated in this paper.

The LNSE are obtained as a sub-set of the LRF Eqs. (11)–(14) by omitting the species transport equations, Eq. (14), and setting $Y_k' = 0$ in Eq. (16). For thermo-acoustic stability analysis, the source term $\dot{\Omega}_T'$ in the linearized energy equation, Eq. (13), is then provided by an FTF instead of the linearized chemical kinetic mechanism. This is described in more detail in Section 3.

2.3. Transformation to frequency domain

The governing equations of the LRF and LNSE can be transformed to the frequency domain by assuming purely harmonic oscillations in all perturbed quantities,

$$\Phi'(\mathbf{x}, t) = \hat{\Phi}(\mathbf{x}) e^{i\omega t}, \tag{21}$$

where $\hat{\Phi}$ is the complex amplitude and ω the frequency of the oscillation. Subjected to appropriate inhomogeneous boundary conditions, the response of a system governed by the LRF or LNSE in the frequency domain to (acoustic) forcing can thus be evaluated at discrete frequencies ω.

Throughout this study, the linearized models will only be evaluated in the frequency domain, as this constitutes a computationally efficient and accurate way to deduce the system response to harmonic forcing, or compute eigenvectors and -values. It is, however, entirely possible to run simulations also in the time-domain.

3. The flame transfer function in hybrid models

The prevailing approach to linear thermoacoustic stability analysis is the use of hybrid models, which combine an acoustic sub-model with a reduced order model for flow-flame interactions. The former ranges, in order of increasing complexity and accuracy, from 1D network models, solvers for the 2D/3D Helmholtz equation to approaches employing the LEE or LNSE. Note that the combustion process is always excluded from these models, e.g. no species transport equations or reaction rates are computed. To account for the main driving mechanism in thermoacoustic systems, i.e. unsteady heat release, a reduced order model for flow-flame interactions is deduced from experiments, CFD or first principles, and combined with the acoustic sub-model. For velocity sensitive flames, such a reduced order model is usually formulated in terms of a complex-valued Flame Transfer Function (FTF), which relates perturbations in heat release rate to velocity fluctuations upstream of the flame.

If the flame is acoustically compact, i.e. if acoustic wavelengths at the frequencies of interest are much larger than the length of the flame, it is usually argued that the exact spatial distribution of the perturbed heat release rate $\hat{\Omega}_T(\mathbf{x})$ has no significant impact on the acoustic waves generated by the flame, and thus on thermoacoustic stability predictions. In that case a *global* flame transfer function $\mathcal{F}_G$ is considered adequate to describe the relation between velocity fluctuations $\hat{u}_{\text{ref}}$ at a reference position upstream of the flame and perturbations of the *spatially integrated* heat release rate,

$$\frac{\int_\Omega \hat{\Omega}_T(\mathbf{x})\,\mathrm{d}\mathbf{x}}{\int_\Omega \bar{\Omega}_T(\mathbf{x})\,\mathrm{d}\mathbf{x}} = \mathcal{F}_G(\omega)\frac{\hat{u}_{\text{ref}}}{\bar{u}_{\text{ref}}}. \tag{22}$$

Note that here fluctuating values of heat release and velocity are normalized with corresponding mean values $\int_\Omega \bar{\Omega}_T(\mathbf{x})\,\mathrm{d}\mathbf{x}$ and $\bar{u}_{\text{ref}}$.

If a flame is not acoustically compact – e.g. at higher frequencies – it is understood that not only the overall fluctuations of heat release rate, but details of the spatial distribution $\hat{\Omega}_T(\mathbf{x})$ may influence thermoacoustic stability. In such cases a *local* flame transfer function $\mathcal{F}_L(\mathbf{x})$ should be used, where gain and phase depend on position $\mathbf{x}$,

$$\frac{\hat{\Omega}_T(\mathbf{x})}{\int_\Omega \bar{\Omega}_T(\mathbf{x})\,\mathrm{d}\mathbf{x}} = \mathcal{F}_L(\mathbf{x}, \omega)\frac{\hat{u}_{\text{ref}}}{\bar{u}_{\text{ref}}}. \tag{23}$$

The local FTF $\mathcal{F}_L$ relates the spatially resolved field $\hat{\Omega}_T(\mathbf{x})$ to the velocity perturbations at the reference position $\hat{u}_{\text{ref}}$. Speaking in the context of an acoustically forced CFD simulation, a scalar transfer function for the perturbed heat release rate *in every cell* of the flame area has to be identified. $\mathcal{F}_L(\mathbf{x}, \omega)$ denotes the union of these transfer functions. Compared to $\mathcal{F}_G$, the amount of data that has to be stored and processed is thus orders of magnitudes larger.

Due to the considerable difficulty and cost of determining a local FTF, studies that include a local FTF for thermoacoustic stability analysis are the exception, not the rule. Martin et al. [58] deduced a fully three-dimensional, local FTF in terms of an $n-\tau$ model with interaction index $n(\mathbf{x})$ and time lag $\tau(\mathbf{x})$ depending on position from Large Eddy Simulation (LES). Subsequent use of this local FTF in a Helmholtz solver showed good agreement of the resulting pressure field and oscillation frequency with LES results. Other studies have determined quasi-1D local FTFs from experiment or CFD with spatial resolution of heat release rate in the axial direction x and explored the impact on thermoacoustic stability [59–67].

The data to identify $\mathcal{F}_G$ and $\mathcal{F}_L$ may originate from the same source, e.g. an acoustically forced CFD simulation of the flame. Effects of non-trivial local phenomena of acoustic-flow-flame interaction – such as flame wrinkling or the transport of convective disturbances along and through the flame – on the heat release rate are thus embodied in both variants of the FTF. Nevertheless, the different post-processing of the raw data distinguishes the two formulations in important aspects. For the global FTF $\mathcal{F}_G$, the perturbed heat release rate is integrated over the whole domain, and $\mathcal{F}_G(\omega)$ is then sought as the transfer function that relates the *scalar* quantities $\int_\Omega \hat{\Omega}_T(\mathbf{x})\,\mathrm{d}\mathbf{x}$ and $\hat{u}_{\text{ref}}$. Due to the spatial integration, information on the local distribution of the perturbed heat release rate is lost. It will be shown in the next sections that this information is relevant to describe important effects of flame movement.

For thermoacoustic network models, usually an infinitely thin "flame sheet" is assumed and therefore the spatial extent of the combustion zone can be neglected altogether. Jump conditions derived from first principles under various simplifications [26,50,51,53,54,68] are employed to directly yield the coupling conditions for acoustic velocity and pressure stemming from unsteady combustion. In this kind of modeling approach, the source terms do not appear explicitly in the acoustic model. Thus, modeling the perturbed heat release rate in a lumped fashion with a global FTF is natural in network models. However, for acoustic models based on the discretization of the wave equation, LEE or LNSE on a continuous domain, the perturbed volumetric heat release rate $\dot{\Omega}'_T(\mathbf{x}, t)$ appears as a source term in the governing equations (compare Eq. (13)) and requires a spatially resolved region. In most studies the spatial distribution of the *perturbed* heat release rate is unknown, because it requires significantly more computational effort and data storage, or more sophisticated techniques to identify from CFD, and is difficult to measure in experiment. Due to lack of this knowledge, a global FTF is often used and the perturbed heat release rate is either assumed to be homogeneous within a simplified combustion zone or to follow the distribution of the *mean* heat release rate. While the first approach is obviously an oversimplification, studies have also shown that the perturbed heat release rate does not follow the distribution of the mean heat release rate for turbulent [58,60–64,69] and even laminar premixed flames [20,22] (compare also Fig. B.14 in this study). While the spatial distribution of the perturbed heat release rate is often considered of minor importance for the generated acoustic waves due to acoustic compactness, the analysis of acoustically compact laminar flames in Sections 4 and 5 will show that it has a major influence on the entropy balance in the combustion zone, which in turn may influence thermoacoustic stability through indirect sources of sound.

4. Freely propagating 1D flame

The response of a freely propagating, 1D, lean premixed, methane-air flame to acoustic forcing is analyzed in this section

to exemplify that use of a global FTF for the spatially integrated heat release rate results in spurious generation of entropy fluctuations. The peculiarity of this seemingly simplistic 1D configuration is that in order to avoid such inconsistencies, it is vital to account precisely for local perturbations of heat release rate in the immediate vicinity of the flame, even though the overall heat release rate fluctuations are negligibly small.

Note that this archetypal setup of a *passive flame* (no fluctuations of overall heat release rate) has proven most useful in the resolution of a well-known classical thermoacoustic paradox [50,70]. In particular, coupling relations for acoustic quantities across a heat source at rest produced results that seemed to be at odds with fundamental conservation laws for mass and energy. Strobio-Chen et al. [51] showed that the paradox can be resolved if jump conditions across the flame are employed that account for flame movement. Likewise, the analysis in this chapter shows that resolution of the local unsteady heat release rate, as provided by the LRF or a local FTF, can represent the flame movement for a spatially resolved combustion zone in an adequate manner and thereby avoid the unphysical behavior from which spurious entropy waves result.

This 1D case is well suited to elucidate the fundamental driving mechanisms for spurious entropy generation, because 2D/3D phenomena like vortex formation and dissipation as well as heat transfer normal to the flow direction (e.g. due to cooled walls) are excluded. The case is computed with CFD, LRF and LNSE, respectively, with both global (LNSE+$\mathcal{F}_G$) as well as local (LNSE+$\mathcal{F}_L$) FTFs for the hybrid LNSE model. Note that the LEE would neglect essential mechanisms like heat transfer in the pre-heating zone of the flame, thus the LNSE are chosen as a basis for the hybrid models.

4.1. CFD simulations

The setup for the CFD consists of a 1D computational domain Ω of length 10 mm, discretized with 10000 uniform cells. The compressible reacting solver `rhoReactingFoam` from the OpenFOAM toolbox [56] is used. The inlet velocity is matched closely to the laminar flame speed s_L such that after ignition, the flame stays in the same location of the computational domain with very minor drift. The aforementioned 2S-CM2 reduced chemical reaction mechanism is used to model the combustion. Boundary conditions are presented in Table 1, the resulting steady-state fields in the combustion zone are shown in Fig. 1. Note that $x = 0$ corresponds to the position of maximum mean heat release rate.

Once the steady-state is reached (apart from the very minor drift mentioned before), a broadband forcing of the inlet velocity with a relative amplitude of 1 % (compared to the mean flow) is added. This low forcing amplitude is chosen to guarantee a linear regime of the flow perturbations. The forcing signal contains frequencies up to 1350 Hz, the simulated time is 1 s. During run time, the perturbations of integrated heat release rate, $\int_\Omega \dot{\Omega}'_T(\mathbf{x}, t)\,\mathrm{d}\mathbf{x}$, as well as the entropy fluctuations $s'_{\text{outlet}}(t)$ (reconstructed from the variables that are solved for via Eq. (20)) at the outlet are tracked. By means of system identification (see [71] for details), $\mathcal{F}_G$, Eq. (22), as well as an entropy transfer function $\mathcal{E}$ (ETF, Eq. (24)) are identified.

$$\frac{\hat{s}_{\text{outlet}}}{\bar{c}_p} = \mathcal{E}(\omega)\frac{\hat{u}_{\text{ref}}}{\bar{u}_{\text{ref}}} \tag{24}$$

Table 1
Boundary conditions of the freely propagating 1D flame.

Boundary	Flow BC	Thermal BC	Species BC
inlet	$u = 0.2452575$ m/s	$T = 293$ K	$\Phi = \left(\frac{Y_{CH4}}{Y_{O2}}\right)/\left(\frac{Y_{CH4}}{Y_{O2}}\right)_{st} = 0.8$
outlet	$p = 1 \cdot 10^5$ Pa	$\frac{\partial T}{\partial x_j} n_j = 0$	$\frac{\partial Y_k}{\partial x_j} n_j = 0$

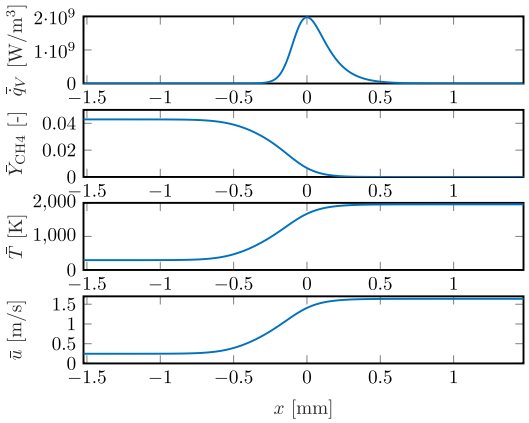

Fig. 1. Most important mean flow fields of the 1D flame case in the combustion zone.

For all transfer functions presented in this work, the inlet of the computational domain is chosen as the reference position. For $\mathcal{E}$, the entropy perturbations are measured at the outlet. Note that the domain is very short, therefore the difference of measuring the entropy perturbations for the ETF at the outlet or directly downstream of the flame is negligible in the frequency band up to 500 Hz investigated in this study. Due to the uniform flow downstream, no mechanisms are present to convert these entropy perturbations to acoustic waves. The ETF nevertheless quantifies the potential to give rise to spurious indirect sources of sound and thereby distort stability predictions, if a similar flame were part of a more complex setup with a choked exit. We chose to neglect entropy perturbations due to species mixing, see Eq. (20), to compute $\mathcal{E}$, such that results from CFD, LRF and LNSE+FTF may be compared against each other in a straightforward manner.

The expected outcome for $\mathcal{F}_G$ is a negligible low gain. The reason is as follows: When forced acoustically with low frequencies, i.e. the flame is compact with respect to the acoustic wavelength, the length of the flame does not change. No deformation of the flame occurs because at every position within the flame, the velocity perturbations are in phase and have the same amplitude (compactness). The flame moves downstream when $u' > 0$ and upstream vice versa as there is no anchoring mechanism to hold the flame in place. The movement results from the kinematic imbalance between flow velocity $\bar{u} + u'$ and laminar flame speed s_L. Because the fuel/air ratio stays constant for both the steady and the forced simulation, s_L is constant and the relative velocity between flame and flow is fixed. As the consumed mass flow of fresh gases is directly proportional to s_L and the integrated heat release rate, no perturbation in the overall heat release rate occurs. The flame movement is a consequence of the constant laminar flame speed and is thus always equal to u'. The cases discussed in this study have low Mach numbers and are set at ambient pressure, thus pressure fluctuations are expected to play a negligible role for the combustion dynamics. Additionally, $p' \approx 0$ in the whole computational domain due to acoustic compactness of the investigated cases in combination with the $p' = 0$ outlet boundary condition. We can therefore observe that the *location* of the heat release rate changes, but the *amount* of spatially integrated heat release rate in the domain remains constant in time.

Furthermore, a premixed laminar flame subject to acoustic forcing does not produce significant perturbations in downstream entropy at low Mach numbers, assuming negligible heat loss and

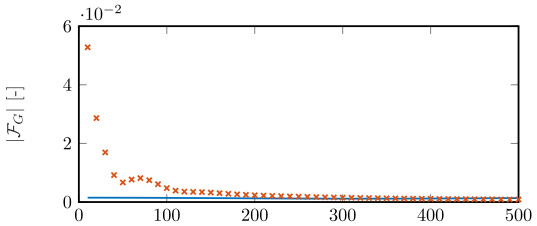

Fig. 2. Gain of the global FTF computed from CFD ___ (system identification) and LRF × (discrete frequency sampling).

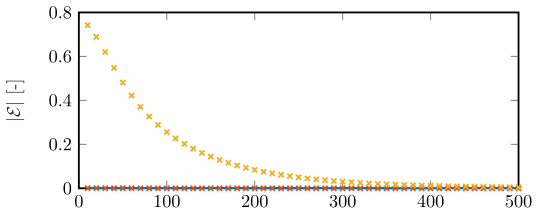

Fig. 3. Gain of the ETF computed from CFD ___ (system identification), LRF × and LNSE+$\mathcal{F}_G$ × (both with discrete frequency sampling).

complete combustion [43,51,52]. Due to the constant fuel/air ratio, the heat released per unit mass by the flame is fixed. Together with the constant mass flow consumption, this yields a fixed ratio of upstream and downstream temperature. Therefore, it is also expected that $\mathcal{E}$ has negligible gain.

Figures 2 and 3 show the gain of $\mathcal{F}_G$ and $\mathcal{E}$, respectively, computed with system identification based on the broadband CFD time series ___. The phase is not shown as it is not meaningful for transfer functions with almost zero gain. As expected, the gain for both transfer functions stemming from CFD data is so low that the effect of heat release rate and entropy perturbations is negligible for this case.

4.2. Linearized simulations

The numerical methodologies for the LRF as well as the LNSE+FTF approaches are identical, i.e. a Discontinuous Galerkin Finite Element Method (DG-FEM) that employs the local Lax-Friedrichs scheme for the inter-element flux and fourth order basis functions is employed. This method has been validated in previous studies and demonstrated impressive agreement with analytical results [20,23]. Using the exact same numerical method for LRF and LNSE should eliminate any discrepancies that could possibly result from numerical inadequacies.

For this 1D flame case, the domain as well as the mesh are identical for the LRF, LNSE and also the CFD cases. The boundary conditions for the LRF and LNSE simulations are given in Table 2. They are consistent with the CFD boundary conditions used for the mean flow and impose an acoustic forcing at the inlet.

Table 2
Boundary conditions of the 1D flame for LRF and LNSE.

Boundary	Flow BC	Thermal BC	Species BC (only LRF)
inlet	$\hat{u} = 0.02452575$ m/s	$\hat{T} = 0$	$\hat{Y}_k = 0$
outlet	$\hat{p} = 0$	$\frac{\partial \hat{T}}{\partial x_j} n_j = 0$	$\frac{\partial \hat{Y}_k}{\partial x_j} n_j = 0$

As mentioned above, elimination of the species transport equations as well as the linearized reaction mechanism reduces the LRF to the LNSE model. In order to incorporate the effects of unsteady heat release rate, global or local FTFs deduced from the CFD time series data are connected to the LNSE model to build the hybrid LNSE+$\mathcal{F}_G$ or LNSE+$\mathcal{F}_L$ models, respectively. Note that for the case of a passive flame investigated in this section with negligible gain of $\mathcal{F}_G$, the results without a flame model for the LNSE+$\mathcal{F}_G$ approach would be essentially identical.

Figures 2 and 3 compare the transfer functions $\mathcal{F}_G$ and $\mathcal{E}$ computed with LRF to the CFD counterparts. Additionally, Fig. 3 shows the entropy transfer function $\mathcal{E}$ for the LNSE+$\mathcal{F}_G$ model. The linearized computations have been conducted in the frequency domain for frequencies from 10 Hz to 500 Hz in 10 Hz steps. Note that $\mathcal{F}_G$ (and $\mathcal{F}_L$) can be computed from the LRF, opposed to the LNSE model, for which the FTF must be provided. $\mathcal{F}_G$ from LRF and CFD show a discrepancy in the low frequency band below 100 Hz. The overall gain however is very low (< 0.06), such that this deviation does not lead to a significant difference in the flow perturbations between both simulations (shown later in Fig. 6). This discrepancy is likely to stem from the slight unsteadiness of the mean flow, which is a snapshot of the last time step of the unforced CFD simulation: On large time scales, 100 ms and more, say, a slight drift of the flame in the CFD exists, caused by a mismatch between the inlet velocity and the laminar flame speed. This minor unsteadiness violates the assumption of steady-state mean flow implied in the perturbation ansatz and thus gives rise to erroneous heat release in the LRF. The effect is minor and indeed only noticeable in the low frequency band, which is associated with larger time scales.

The gain of the entropy transfer function $\mathcal{E}$ for both CFD and LRF stays below 0.001. In strong contrast, the LNSE+$\mathcal{F}_G$ model features excessive amounts of entropy perturbations downstream of the flame, with a maximum gain of almost 0.8 at low frequencies. This is evidence of a significant shortcoming of $\mathcal{F}_G$ to replicate the linearized combustion dynamics of this fundamental case. In the low frequency limit, the spurious entropy generation can be calculated from the jump conditions derived by Strobio-Chen et al. [51]. Simplifying Eq. (34) from [51], assuming perfect premixing and $p_1' = 0$ yields

$$\frac{s_2'}{\bar{c}_{p,2}} = \left(1 - \frac{\bar{T}_1}{\bar{T}_2}\right)\left((\mathcal{F}_G - 1)\frac{u_1'}{\bar{u}_1} + \frac{u_s'}{\bar{u}_1}\right). \tag{25}$$

Here, u_s' is the rate of displacement of the flame and indices 1 and 2 denote quantities up- and downstream of the flame, respectively. Inserting the temperature ratio $\bar{T}_2/\bar{T}_1 = 6.674$, $\mathcal{F}_G = 0$ and assuming no flame movement by setting $u_s' = 0$, we retrieve -0.85 for $\mathcal{E}$ in the low frequency limit, in which the jump conditions represent an exact solution of the governing equations. This spurious outcome, which results from the lack of flame movement, agrees reasonably well with the numerical results of the LNSE+$\mathcal{F}_G$ model, compare Fig. 3.

In order to put the impact of the spurious entropy waves into perspective, the magnitude of indirect acoustic waves, generated by the acceleration of the entropy waves in a fictive nozzle downstream of the flame, is assessed. As an example, we assume a compact supercritical nozzle, for which the generated acoustic wave can be calculated via

$$u_{\mathrm{sec}}' = \bar{c}_2 \frac{M_2}{2 + (\gamma_2 - 1)M_2} \frac{s_2'}{\bar{c}_{p,2}}, \tag{26}$$

as derived by Marble and Candel [24]. Here, the index 2 again denotes quantities downstream of the flame, but upstream of the fictive nozzle. $M_2 = 0.0019$ is the Mach number of the mean flow measured at the outlet of the computational CFD domain. For the 1D case investigated here, the strength of spuriously generated

Table 3
Comparison of ETF gain for the various models in the 1D flame case.

Frequency	$\lvert\mathcal{E}\rvert$			
	CFD	LRF	LNSE+$\mathcal{F}_G$	LNSE+$\mathcal{F}_L$
50 Hz	$9.137 \cdot 10^{-6}$	$4.143 \cdot 10^{-4}$	0.4810	$4.148 \cdot 10^{-2}$
100 Hz	$1.741 \cdot 10^{-5}$	$8.717 \cdot 10^{-5}$	0.2557	$9.630 \cdot 10^{-3}$

compared to the physical primary velocity perturbations downstream of the flame, is 284 % in the low frequency limit. The impact of the spurious acoustics is so dominant for this case because there are no direct acoustic waves from the flame ($\mathcal{F}_G \approx 0$) and effects like the dispersion of entropy waves or losses are not taken into account.

Compared to the LNSE+$\mathcal{F}_G$ model, the LRF features not only the correct spatial resolution of the heat release rate perturbations, but also the linearized species transport equations. Thus, the mere comparison of these two models does not proof in an unambiguous manner that the spurious entropy waves is this case can be attributed to the lack of flame movement alone. However, the results of the LNSE+$\mathcal{F}_L$ model shown later will demonstrate that the fine-grained local resolution of the perturbations in heat release rate mitigate the spurious behavior for the most part, even without accounting for the fluctuations in species transport and sources, see Table 3.

4.3. Importance of flame movement

In analogy to Strobio-Chen et al. [51], we argue that the lack of flame movement is the cause for the spurious entropy production by the LNSE+$\mathcal{F}_G$ model. However, in contrast to the framework of a moving flame described by jump conditions [51,53,54,68], including a flame velocity is not straightforward for the LNSE. While this might be feasible for low frequencies in the 1D case, where the equations derived from jump conditions can be applied approximately due to compactness, finding an analytically closed-form expression for the movement of a 2D/3D flame over the whole frequency band represents a very significant difficulty, because in this case mechanisms like diffusion and convection of entropy and species normal to the flow play an essential role. Instead, we aim to resolve the paradox by accounting for the local perturbations in heat release rate by means of a local FTF $\mathcal{F}_L$, which can be estimated from CFD.

Figure 4 exemplifies that a downstream displacement of the mean heat release by 0.2 mm, say, results in, and can thus be modeled by, local perturbations in heat release rate. These are calculated as the difference of displaced and mean heat release rate, $\dot{\Omega}'_T = \tilde{\dot{\Omega}}_{T,\mathrm{dis}} - \bar{\dot{\Omega}}_T$. By construction, $\int_\Omega \dot{\Omega}'_T \mathrm{d}x = 0$, i.e. no global heat release rate perturbations are generated by a pure displacement of the flame, $\mathcal{F}_G = 0$. This simple example showcases that spatially distributed heat release rate perturbations, i.e. a local FTF $\mathcal{F}_L$, can

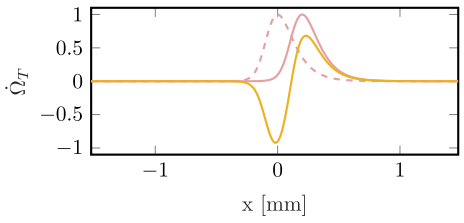

Fig. 4. Sketch of the flame displacement. Normalized mean $\bar{\dot{\Omega}}_T$ - - -, displaced $\tilde{\dot{\Omega}}_{T,\mathrm{dis}}$ ——— and perturbed $\dot{\Omega}'_T$ ——— heat release rate.

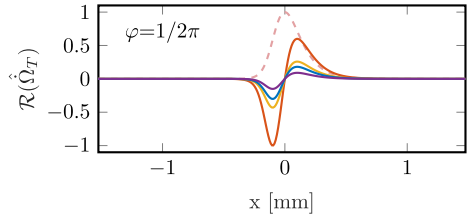

Fig. 5. Real part of the heat release perturbations computed with LRF at the maximum downstream displacement, $\varphi = 1/2\pi$ (forcing velocity purely imaginary). $\omega = 30\,\mathrm{Hz}$ ———, $\omega = 70\,\mathrm{Hz}$ ———, $\omega = 100\,\mathrm{Hz}$ ———, $\omega = 200\,\mathrm{Hz}$ ———. Mean heat release rate $\bar{\dot{\Omega}}_T$ - - - for reference. All values of $\hat{\dot{\Omega}}_T$ are normalized with the maximum amplitude of $\omega = 30\,\mathrm{Hz}$.

represent *flame movement*. However, because the integrated heat release rate perturbations of this movement are zero, $\mathcal{F}_G$ cannot account for this mechanism and its consequences.

Hence, the paradox of a passive flame at rest arises in the LNSE+$\mathcal{F}_G$ model, leading to unphysical flow fields and an excess in entropy perturbations downstream of the flame. In the CFD, the flame can move and thus the paradox is resolved without entropy production. The LRF models the spatially resolved perturbed heat release rate in a similar shape to $\dot{\Omega}'_T$ in Fig. 4, thus also accounting for flame movement.

In order to substantiate the claim that the LRF does indeed capture the effects of flame movement, it is helpful to compare the local perturbation fields to the CFD results. We start with some preceding thoughts about the comparability: The displacement of the flame in the CFD computation depends on the forcing amplitude and frequency, i.e. higher amplitudes induce non-linear behavior and eventually lead to blow out or flash back of the flame, in particular at low frequencies, $\omega \to 0$. The perturbation fields of the LRF, however, are directly proportional to the forcing amplitude by construction (linearity). Blow out or flash back can not happen, as the mean fields, which dominantly impact the linearized heat release rate perturbations, are frozen in place. Instead of a finite displacement amplitude, the LRF results rather show the *tendency* or *onset* of the flame movement resulting from infinitesimal forcing amplitude. A low forcing amplitude in the CFD computations is therefore necessary to retain the linearity and allow one-to-one comparison with the LRF. The CFD and LRF model share the same dependence of the displacement amplitude on the frequency, i.e. the lower the frequency, the larger the displacement, see Fig. 5. This is reasonable, as the displacement is the temporal integral of the velocity perturbations and at lower frequencies, the time to displace the flame within one half period is greater than at higher frequencies.

The data for the CFD was computed by harmonic velocity forcing with a relative amplitude of 1 % at the inlet boundary. 20 oscillation periods were simulated with subsequent Fourier transform of the last period. This guarantees a harmonically oscillating state, similar to the frequency domain simulations of the linearized models. The perturbations were retrieved by subtracting the steady state from the instantaneous fields.

A comparison of the perturbation fields for heat release rate, entropy and velocity between LRF and CFD is presented in Fig. 6. The plots show snapshots for the real part of the perturbed quantities over the first half of an oscillation period at $\omega = 100\,\mathrm{Hz}$, i.e. with phase angle φ ranging from 0 to $7/8\pi$. Note that the second half of the period is equal to the first half with opposite sign for the amplitudes and would therefore provide no additional information. Excellent agreement between LRF and CFD can be observed. The physical mechanisms for the CFD/LRF solutions are as follows:

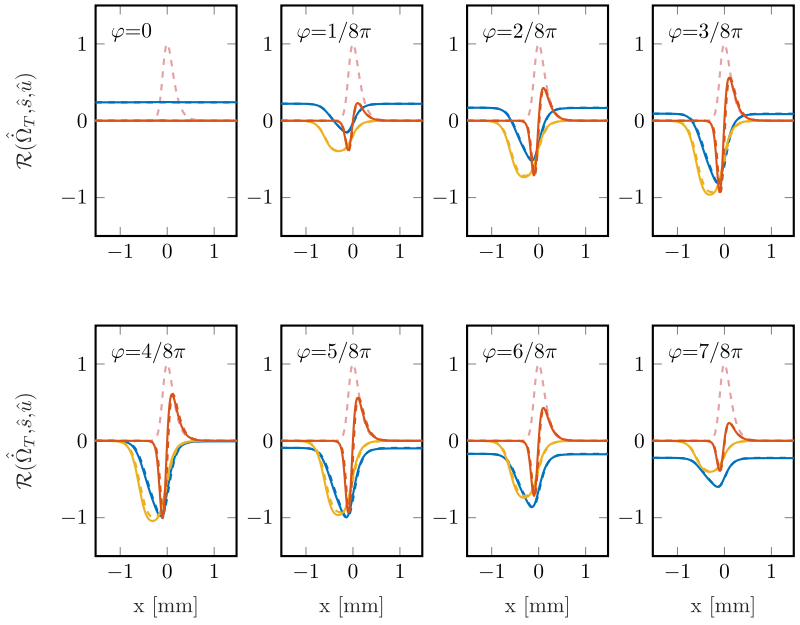

Fig. 6. Real part of heat release rate $\mathcal{R}(\hat{\Omega}_T)$ ——, entropy $\mathcal{R}(\hat{s})$ —— and velocity $\mathcal{R}(\hat{u})$ —— perturbations of the LRF model in the combustion zone, normalized with the respective maximum value of the CFD simulation in this period. Normalized mean heat release rate $\hat{\bar{\Omega}}_T$ - - - for reference with maximum at $x = 0$. Dashed lines show the corresponding quantities from harmonically forced CFD. Plots show oscillation with $\omega = 100\,\text{Hz}$ at various phase angles φ. $\varphi = 0$ corresponds to purely real valued forcing velocity at the inlet.

- $\varphi = 0$: The forcing velocity is at its maximum, thus displacement is zero. Indeed, neither entropy nor heat release rate are perturbed, which confirms that the flame is at the steady-state position.
- $\varphi = 1/8\pi \ldots 3/8\pi$: The downstream displacement of the flame begins. This is indicated by heat release rate perturbations, which are negative in the upstream and positive in the downstream part of the combustion zone. The mean velocity increases across the flame, thus the displacement in the downstream direction results in negative velocity perturbations in the combustion zone. Likewise, negative entropy perturbations result from the flame movement.
- $\varphi = 1/2\pi$: The forcing velocity is zero, the flame displacement towards the downstream end is at its maximum. This is reasonable because the displacement is the temporal integral of the velocity, i.e. phase shifted by $1/2\pi$.
- $\varphi = 5/8\pi \ldots 7/8\pi$: The flame returns back to its steady-state position. At $\varphi = \pi$, the same situation as for $\varphi = 0$ is observed (zero flame displacement), but with negative amplitude of the forcing velocity.
- $\varphi = \pi \ldots 2\pi$: In the second half of the oscillation period, the flame is displaced towards the upstream end of the domain, the explanations given for the first half of the cycle still apply, but with opposite sign.

Note that during the whole oscillation period, any entropy perturbations generated in the combustion zone are also "consumed" by the reaction, such that no entropy waves propagate downstream of the flame. This agrees well with the flame physics of the process, and is represented in the very low gain of the ETF predicted by LRF and CFD.

Figure 7 shows the corresponding comparison between the fluctuating fields of LNSE+$\mathcal{F}_G$ and CFD. The reader is reminded here that $\mathcal{F}_G$ has negligible gain for this case and could thus also be omitted without noticeable impact on the results. In fact, a global FTF is an ill-conceived notion in this setting, where the flame movement is the prominent mechanism and modulation of the overall heat release rate due to changes in the flame shape, speed or structure is absent. It is apparent that the LNSE+$\mathcal{F}_G$ solution strongly differs from CFD results. In contrast to CFD and LRF, the entropy perturbations after the flame are not zero for the LNSE+$\mathcal{F}_G$ solution, indicating spurious entropy production. Quite simply, entropy perturbations s' downstream of the flame are negative, because in the LNSE+$\mathcal{F}_G$ model, the rate of heat addition per unit mass decreases as the mass flow rate across the flame increases. Beyond this, spurious acoustic waves are generated by the LNSE+$\mathcal{F}_G$ model, as can be seen in the velocity perturbations downstream of the flame. This effect is interwoven with the spurious entropy generation and can additionally lead to incorrect prediction of thermoacoustic stability.

This case of a passive flame at rest represents an instance of a classical paradox of thermoacoustics, which has been discussed by Dowling et al. [70] and Bauerheim et al. [50]: when deriving jump conditions for acoustic waves propagating across a compact heat source, the paradox suggests that volume conservation must be used for perturbations at zero Mach number, while mass conservation must be used at non-zero Mach numbers. Strobio-Chen et al. [51] have shown that the paradox is resolved when it is taken into account that a premixed flame front in kinematic balance with the approach flow will change not only its heat release rate, but also its position in response to velocity perturbations. A subsequent study demonstrate, that spurious generation of entropy results from the neglect of flame movement in the description of thermoacoustic interactions [52].

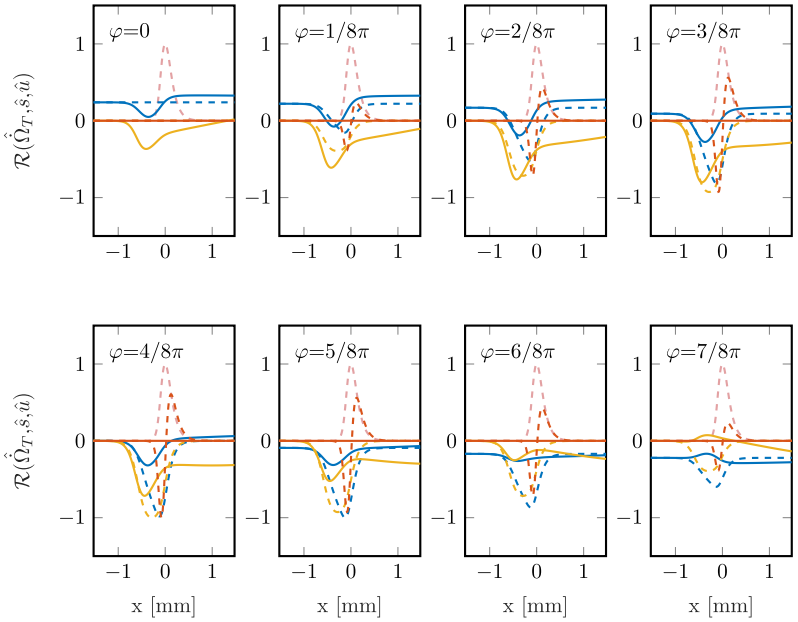

Fig. 7. Same as Fig. 6, but solid lines represent results from LNSE+$\mathcal{F}_G$

For the LNSE+$\mathcal{F}_G$ model, the non-zero Mach number case applies, which allows for the propagation of convective waves. The flame is passive, because the perturbations in integrated heat release rate are essentially zero, and it represents a heat source at rest, because the LNSE+$\mathcal{F}_G$ model with the steady state mean flow excludes flame movement. As shown in [51,52] via jump conditions, in this case an increase in mass flow rate across the flame sheet due to acoustic forcing leads to a reduced hot gas temperature, equivalent to a spurious negative entropy wave.

For a flame with finite thickness, as in the LNSE+$\mathcal{F}_G$ model, jump conditions only yield exact results for the acoustic coupling and the spuriously generated entropy wave, when applied at 0 Hz. For models that do not involve convective (e.g. entropy) waves, jump conditions may be regarded as a valid approximation also for non-zero frequencies, as long as acoustic compactness is satisfied. It would be intuitive to infer that for cases where convective waves are present, convective rather than acoustic compactness should be required to ensure validity of the jump conditions for entropy, Eq. (25).

With a flame thickness of $L_F \approx 1\,\text{mm}$ and a spatially averaged mean flow velocity across the flame of $<\bar{u}_F> \approx 1\,\text{m/s}$, compare Fig. 1, we find that at $\omega = 10\,\text{Hz}$, the ratio of convective wavelength $\delta_C = <\bar{u}_F>/\omega$ to flame thickness, $\delta_C/L_F \approx 100$, i.e. the flame can be regarded convectively compact for frequencies up to 10 Hz. For frequencies up to 100 Hz, and thus $\delta_C/L_F \lessapprox 10$, the same order of magnitude for the spurious entropy perturbations from the LNSE+$\mathcal{F}_G$ model and the jump conditions is obtained.

4.4. Mechanism and low-pass characteristic of spurious generation of entropy

This paragraph aims at shedding light onto the physical mechanisms involved in the spurious generation of entropy by the LNSE+$\mathcal{F}_G$ model. Although diffusive effects strongly impact the quantitative realization of the ETF, the qualitative low-pass nature can be sufficiently described by only accounting for the convective transport. Karimi et al. [46,47] and Yoon [48] showed numerically and analytically that the ETF of a flow described by the Euler equations with steady input of heat from a source at rest exhibits a low-pass character. In order to explain the low-pass behavior of the ETF for the LNSE+$\mathcal{F}_G$ model, we must account for the convection of temperature perturbations through the spatially resolved combustion zone. First, we assume convective compactness, i.e. the acoustic forcing period should be much longer than the convection time through the combustion zone, to show consistency of this explanation with the model derived from jump conditions, Eq. (25). This means that during one convective flow-through of the flame, the acoustic state does not change. When the passive flame at rest is forced acoustically with $u' > 0$, the flow is convected through the heat release zone faster than in steady state. Thus, there is less time during which the flow can be heated, resulting in reduced heat input per unit mass and consequently $T' < 0$ after the flame. This leads to a phase of $-\pi$ for $\mathcal{E}$ in the low frequency limit.

When convective compactness is lost at higher frequencies, the acoustic state, and thus u', changes during one flow-through time of the combustion zone. Recall that for the studies in this paper, the forcing is chosen to be purely real-valued and thus exhibits the maximum positive value at $\varphi = 0$, as represented by a cosine in time domain. A fluid particle first experiences increased convective velocity, leading to $T' < 0$. During the transport through the combustion zone, u' becomes negative ($\varphi > 1/2\pi$), thus the particle is slower than in steady state and is heated more strongly. The increased heating per unit mass during $1/2\pi < \varphi < 3/2\pi$ of the acoustic period cancels the reduced heat input during $3/2\pi < \varphi < 1/2\pi$. This compensation effect, which appears only at frequencies for which the flame is not convectively compact, leads to a reduced amplitude of T', and thus s', after the flame. The mutual cancellation of entropy perturbations in the combustion zone becomes more pronounced for higher frequencies, asymptotically leading to zero gain in $\mathcal{E}$.

The movement of the flame in the CFD/LRF counteracts this spurious mechanism of entropy generation. As already explained earlier, the flame in this 1D case moves with the forcing velocity u'. Thus, the relative velocity between the convected fluid and the flame remains $\bar{u}$, as in the steady state. The convection time through the flame zone is not altered by the acoustic forcing and consequently the amount of heat addition per unit mass to a fluid particle remains constant, resulting in no temperature or entropy waves downstream of the flame.

4.5. Locally resolved FTF

The effect of flame movement on heat addition can be taken into account in a hybrid LNSE model by the usage of a local FTF (LNSE+$\mathcal{F}_L$). $\mathcal{F}_L$ is derived from harmonically forced CFD through Fourier analysis and provides the complex spatially distributed rate of perturbed heat release, referenced to the velocity fluctuations at the inlet. Due to the comparatively high computational effort of the harmonically forced CFD, only two frequencies, 50 Hz and 100 Hz, are investigated. The perturbation fields for the LNSE+$\mathcal{F}_L$ model, Fig. 1 in the Supplementary Material, are identical to the ones of CFD and LRF, which highlights that accounting for the locally resolved heat release rate perturbations with $\mathcal{F}_L$ is sufficient to get outstanding agreement even for local quantities. The results for the ETF in Table 3 demonstrate that the spurious generation of entropy waves in the LNSE+$\mathcal{F}_G$ model is indeed connected to the lack of flame movement, and that the use of $\mathcal{F}_L$ together with the LNSE remedies to a large extent the generation of excess entropy. The remaining discrepancy between the entropy production of the LRF and the LNSE+$\mathcal{F}_L$ model can be attributed to the lack of species transport equations in the LNSE. Although the two main contributions for entropy production stemming from the species transport equations, which are due to species diffusion and generation, cancel out in big parts (see Figs. 2 and 4 of the Supplementary Material), the remainder contributes to the overall balance.

To conclude: the LNSE+$\mathcal{F}_G$ model does not capture the flame movement, which leads to the spurious generation of entropic and acoustic waves, possibly resulting in incorrect predictions of thermoacoustic stability. To mitigate the spurious behavior, it is required to resolve the perturbed heat release rate locally, i.e. on scales that are convectively and acoustically compact. This can be achieved by a highly resolved *local* FTF, which properly represents the heat release rate perturbations that result from flame movement, or by use of the LRF, which indeed resolves the flame movement directly.

5. 2D anchored flame

Further evidence that the spurious entropy perturbations of the LNSE+$\mathcal{F}_G$ hybrid model are connected to the lack of flame movement is presented for the case of an anchored, 2D laminar flame, see Fig. 8. The important difference to the 1D case is that $\mathcal{F}_G$ has significant gain because flame shape and surface area change in response to acoustic forcing. On the other hand, there are no fluctuations in the mixture ratio, therefore we expect negligibly small entropy waves downstream of the flame. In spite of the anchoring at the base of the flame, movement still plays an important role to avoid spurious entropy generation in this case.

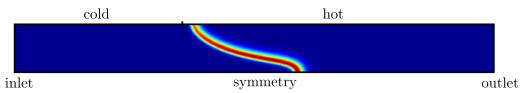

Fig. 8. Slit flame mean heat release rate $\bar{\tilde{\Omega}}_T$ and boundaries.

Table 4
Boundary conditions for CFD of the anchored flame.

Boundary	Flow BC	Thermal BC	Species BC
inlet	$\mathbf{u} = (0.6\text{m/s}, 0)$	$T = 293$ K	$\Phi = \left(\frac{Y_{GAS}}{Y_{O2}}\right) / \left(\frac{Y_{GAS}}{Y_{O2}}\right)_{st} = 0.8$
outlet	$p = 1 \cdot 10^5$ Pa	$\frac{\partial T}{\partial x_j} n_j = 0$	$\frac{\partial Y_k}{\partial x_j} n_j = 0$
cold wall	$\mathbf{u} = (0, 0)$	$T = 300$ K	$\frac{\partial Y_k}{\partial x_j} n_j = 0$
hot wall	$\mathbf{u} = (0, 0)$	$\frac{\partial T}{\partial x_j} n_j = 0$	$\frac{\partial Y_k}{\partial x_j} n_j = 0$
symmetry	$u_j n_j = 0$	$\frac{\partial T}{\partial x_j} n_j = 0$	$\frac{\partial Y_k}{\partial x_j} n_j = 0$

The computational domain is 20 mm long and 2 mm wide, the thermal boundary condition on the upper wall changes from isothermal (cold) to adiabatic (hot) at an axial position of 7 mm. This facilitates the anchoring of the flame directly downstream of this position. In contrast to the 1D case, the 2D flame is anchored at the flame base, while the tip can move freely. This kinematic imbalance leads to a change in the surface area of the flame when forced acoustically. The global heat release rate changes according to the perturbations in flame surface area.

5.1. CFD simulations

A uniform mesh of quadratic cells with edge length 40 µm is used to discretize the computational domain, which results in a total of 25000 cells. This mesh guarantees proper resolution of the combustion with around 10 cells across the flame front. First, an unforced case with constant inlet velocity is computed with the boundary conditions as given in Table 4.

Due to the short domain with fully reflective boundary conditions, the acoustic cavity modes of the system are at very high frequencies at which the flame response is not significant. The intrinsic thermoacoustic eigenmodes, typically found in the low frequency range where flame dynamics is important, are suppressed by the fully reflective boundary conditions of the short domain. Therefore, no self excited instabilities occur. The numerical approach as well as the procedure to obtaining $\mathcal{F}_G$, $\mathcal{F}_L$ and $\mathcal{E}$ from both CFD and linearized simulations is identical to the 1D case.

5.2. Linearized simulations

The reactive flow of the flame is linearized around the steady state of the CFD, boundary conditions are chosen as the respective linearized expressions of the CFD with purely real valued velocity forcing at the inlet, see Table 5. The computations of the LRF and LNSE models are carried out with quadratic discontinuous basis functions on a uniformly resolved mesh consisting of 7668 tetrahedral elements with an average cell size of 120 µm. This amounts to $\approx$ 350k degrees of freedom for LNSE and $\approx$ 788k for LRF. The computation of the flame response at one frequency takes 75 s and 8 GB of RAM for the hybrid LNSE+FTF methods and 180 seconds and 21 GB of RAM for the LRF on a desktop computer (Intel i7-4790 quad core @ 3.60 GHz).

Table 5
Boundary conditions of the anchored flame for LRF and LNSE.

Boundary	Flow BC	Thermal BC	Species BC (only LRF)
inlet	$\hat{\mathbf{u}} = (0.006\text{ m/s}, 0)$	$\hat{T} = 0$	$\hat{Y}_k = 0$
outlet	$\hat{p} = 0$	$\frac{\partial \hat{T}}{\partial x_j} n_j = 0$	$\frac{\partial \hat{Y}_k}{\partial x_j} n_j = 0$
cold wall	$\hat{\mathbf{u}} = (0, 0)$	$\hat{T} = 0$	$\frac{\partial \hat{Y}_k}{\partial x_j} n_j = 0$
hot wall	$\hat{\mathbf{u}} = (0, 0)$	$\frac{\partial \hat{T}}{\partial x_j} n_j = 0$	$\frac{\partial \hat{Y}_k}{\partial x_j} n_j = 0$
symmetry	$\hat{u}_j n_j = 0$	$\frac{\partial \hat{T}}{\partial x_j} n_j = 0$	$\frac{\partial \hat{Y}_k}{\partial x_j} n_j = 0$

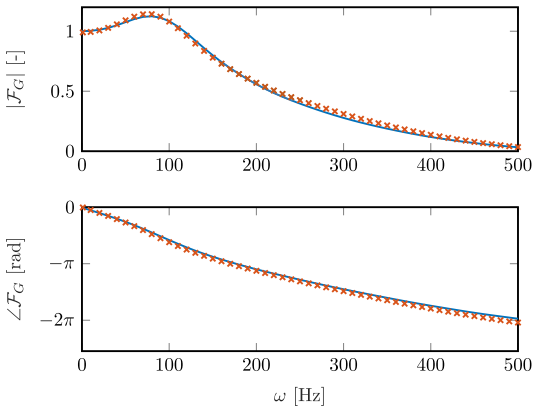

Fig. 9. Global FTF from CFD ——— (system identification) and LRF × (discrete frequency sampling).

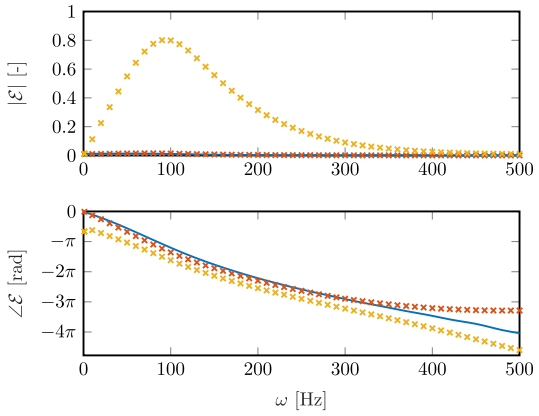

Fig. 11. Entropy transfer function from CFD ——— (system identification), LRF × and LNSE+$\mathcal{F}_G$ × (both discrete frequency sampling).

Figure 9 shows $\mathcal{F}_G$ computed via system identification from CFD as well as from discrete frequency sampling with LRF. Excellent agreement between both methods is observed, only minor deviations in magnitude and phase occur at frequencies beyond the maximum gain. Therefore, we conclude that the LRF can very well represent the combustion dynamics of the anchored flame subject to acoustic forcing. A closer investigation of the frequency response fields of perturbed heat release rate and entropy for CFD and LRF at 100 Hz, Fig. 10, demonstrates good agreement not only in global, but also local quantities.

In analogy to the 1D case, and following established practice [20,23,72], the perturbed heat release rate $\hat{\Omega}_T(\mathbf{x})$ for the 2D LNSE model in conjunction with $\mathcal{F}_G$ is chosen to be directly proportional to the mean heat release rate $\bar{\Omega}_T(\mathbf{x})$. Gain and phase of $\mathcal{F}_G$ are known from the CFD. Subsequently, the frequency domain simulations of the LNSE+$\mathcal{F}_G$ model are performed to obtain $\mathcal{E}$.

The ETFs for CFD, LRF and LNSE+$\mathcal{F}_G$ are depicted in Figs. 11 and 12. As expected for a premixed flame with constant equivalence ratio, the LRF and CFD show negligible entropy perturbations downstream of the flame. Considering the different numerical methods employed (Finite Volume Method with constant cell values and quadratic DG-FEM), the small deviation between LRF and CFD is reasonable and will not noticeably distort any thermoacoustic stability analysis conducted with the LRF. In contrast to this, the LNSE+$\mathcal{F}_G$ ETF deviates strongly from the CFD ETF, it is off by a factor of ~ 30 around 100 Hz. The major difference of these results compared to the 1D case is that the gain in the low frequency range around 0 Hz is close to zero, i.e. the spatial integral of entropy perturbations at the outlet vanishes. In the low frequency limit, the movement of the flame is mainly connected to an increase in flame surface area, leading to an increased heat release rate. The jump conditions, Eq. (25), suggest that with a gain of unity of $\mathcal{F}_G$, as present in this case at 0 Hz, no flame movement ($u'_s = 0$) is required to mitigate spurious entropy production [51]. At closer inspection, however, local spurious entropy generation of the LNSE+$\mathcal{F}_G$ model in the combustion zone can be observed even in the low frequency limit, see Fig. 13.

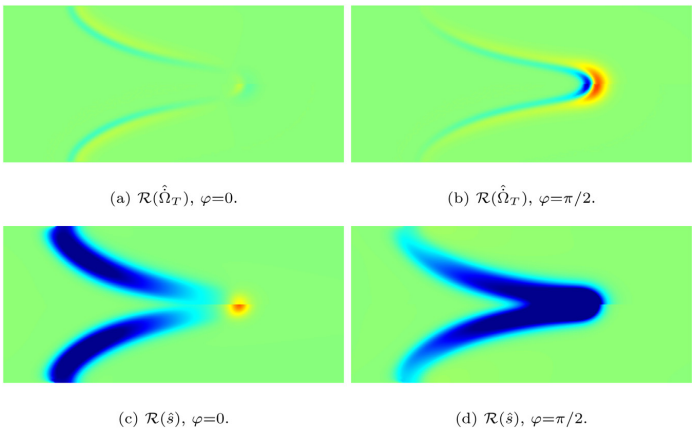

(a) $\mathcal{R}(\hat{\Omega}_T)$, φ=0. (b) $\mathcal{R}(\hat{\Omega}_T)$, φ=π/2.

(c) $\mathcal{R}(\hat{s})$, φ=0. (d) $\mathcal{R}(\hat{s})$, φ=π/2.

Fig. 10. Real part of heat release rate $\mathcal{R}(\hat{\Omega}_T)$ (top row) and entropy $\mathcal{R}(\hat{s})$ (bottom row) perturbations for CFD (top half of each snapshot) and LRF (bottom half of each snapshot) on a symmetric color scale. The scale for heat release rate perturbations is normalized with the maximum value in the period of $\omega = 100$ Hz and is identical for CFD and LRF. The scale for entropy perturbations is over-saturated. Red indicates positive, blue negative and green zero perturbation.

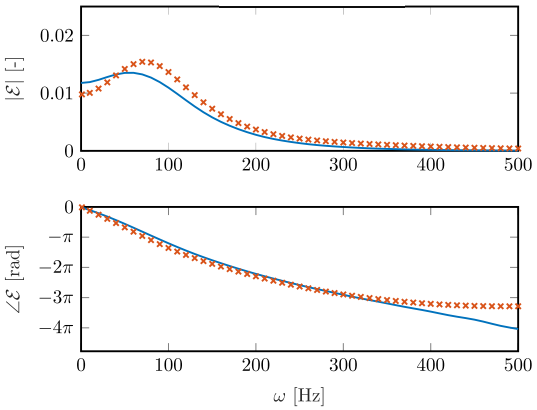

Fig. 12. Zoomed in plot of the entropy transfer function from CFD —— (system identification) and LRF × (discrete frequency sampling).

Table 6
Comparison of ETF gain for the various models in the 2D flame case.

Frequency	$\lvert\mathcal{E}\rvert$			
	CFD	LRF	LNSE+$\mathcal{F}_G$	LNSE+$\mathcal{F}_L$
50 Hz	0.0135	0.0139	0.5494	0.0197
100 Hz	0.0110	0.0137	0.7992	0.0063

At phase $\varphi = 0$, as shown in Fig. 13, the LNSE+$\mathcal{F}_G$ model generates positive entropy perturbations over large parts of the flame surface starting from the base, and negative perturbations at the tip. The flame dynamics can be seen in the LRF model: the flame stretches and is displaced in the downstream direction in phase along its whole length, apparent from the perturbed heat release rate. The strongest magnitude of the heat release rate perturbations are present at the tip. $\mathcal{F}_G$, in contrast, uses $\bar{\dot{\Omega}}_T$ as the reference, which is evenly distributed along the flame. Thus, compared to the LRF fields, there is too much perturbed heat release rate along the sides of the flame and too little at the tip in the LNSE+$\mathcal{F}_G$ model. As a result, the entropy perturbations generated at the sides are over-compensated by the corresponding heat release rate perturbations of $\mathcal{F}_G$, while at the tip, not enough heat release rate perturbations are present to compensate the entropy perturbations. Downstream of the flame, the entropy waves cancel partially due to diffusive effects and can ultimately not be perceived in $\mathcal{E}$ due to the integration procedure for measurement at the outlet. Even though the correct global balance leads to zero entropy perturbations averaged over the outlet (as seen in the jump conditions), locally the flow field is unphysical and stability predictions might be adversely impacted thereby.

The maximum gain of the LNSE+$\mathcal{F}_G$ ETF can be seen around 100 Hz. This behavior can again be ascribed to the lack of flame movement by comparing the perturbed heat release rate at $\omega =$ 1 Hz and $\omega = 100$ Hz, see Fig. 14. Opposed to the in-phase behavior of the perturbed heat release rate at 1 Hz, the flame movement at 100 Hz is more convective in nature and therefore the heat release rate perturbations are not in phase along the flame front: the displacement propagates from the base to the tip. $\mathcal{F}_G$ can only represent a uniform in-phase displacement (or stretch) accompanied by an increase in flame surface area, but not a convective propagation of the displacement. With increasing frequency up to 100 Hz, the lack of convective propagation in the LNSE+$\mathcal{F}_G$ model becomes more and more dominant, which shows in the excess gain of the ETF. The gain of $\mathcal{F}_G$ for the 2D anchored flame, Fig. 9, is further proof for this phenomenon of convective flame movement: the excess of gain around 80 Hz results from an acoustic forcing that constructively interferes with the convective displacement mechanism. For frequencies past 100 Hz, the perturbed heat release rate becomes less important (gain of $\mathcal{F}_G$ drops) and the low-pass filtering quality of entropy generation [46–48] dominates the LNSE+$\mathcal{F}_G$ ETF. The comparison of the perturbation fields of CFD and LNSE+$\mathcal{F}_G$ at 100 Hz, Fig. 15, provides insight into the spurious entropy generation similar to the 1D flame case. The dipole character of the perturbed heat release rate, and thus the flame movement, which is present in both CFD and LRF, is not represented by $\mathcal{F}_G$. As a result, the entropy sources and sinks are not balanced and an entropy wave passes the flame surface and is convected downstream, leading to the high spurious gain of $\mathcal{E}$.

Quantifying the impact of the indirect acoustic waves generated through the acceleration of the spurious entropy waves in a fictive compact supercritical nozzle, Eq. (26) with $M_2 = 0.0047$, yields a ratio of 45.5 % between spurious and physical acoustic velocity perturbations downstream of the flame for $\omega = 100$ Hz. Compared to the 1D flame case, the directly generated acoustics by the 2D flame lessen the relative importance of the spurious indirect acoustics. Nevertheless, we reckon that the detrimental influence of the unphysical indirect acoustic waves would still be significant even in the 2D case.

Opposed to the 1D case, the velocity coupling across the 2D anchored flame does not show significant discrepancy between CFD and LNSE+$\mathcal{F}_G$ (not shown). This is due to the strong influence of the heat release rate perturbations of the flame, which dominantly affect the velocity.

Pursuing the approach of coupling $\mathcal{F}_L$ to the LNSE to include the flame movement, as described for the 1D flame case, again remedies this situation. Figure 5 of the Supplementary Material shows that the entropy perturbations agree very well with CFD data, Table 6 confirms that the spurious excess gain in $\mathcal{E}$ is eliminated by $\mathcal{F}_L$.

However, considerable additional effort is required to compute $\mathcal{F}_L$, rather than $\mathcal{F}_G$, in order to avoid spurious entropy generation by the hybrid model. Thus, even though the time to solve for the

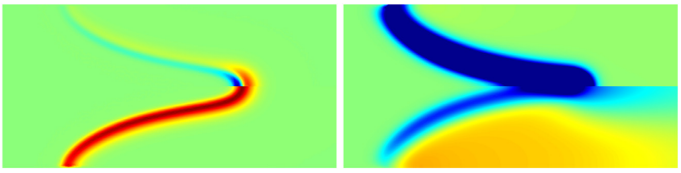

Fig. 13. Real part of heat release rate $\mathcal{R}(\hat{\dot{\Omega}}_T)$ (left) and entropy perturbations $\mathcal{R}(\hat{s})$ (right) for LRF (top half of each snapshot) and LNSE+$\mathcal{F}_G$ (bottom half of each snapshot) on a symmetric color scale at $\varphi = 0$, $\omega = 1$ Hz. The heat release rate scale for the LRF is one order of magnitude higher than for LNSE+$\mathcal{F}_G$, the entropy scale is identical for both models. Red indicates positive, blue negative and green zero perturbation.

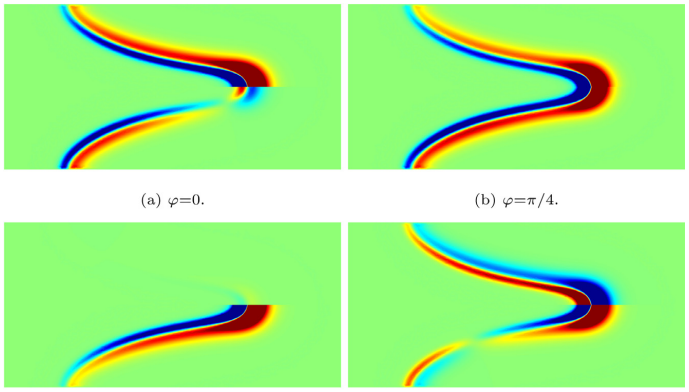

(a) φ=0. (b) φ=$\pi/4$.

(c) φ=$\pi/2$. (d) φ=$3\pi/4$.

Fig. 14. Real part of heat release rate $\mathcal{R}(\hat{\dot{\Omega}}_T)$ computed with LRF at $\omega = 1$ Hz (top half of each snapshot) and $\omega = 100$ Hz (bottom half) for four phase angles. The color scale is over-saturated to highlight the convective features of the flame displacement at $\omega = 100$ Hz. Red indicates positive, blue negative and green zero perturbation.

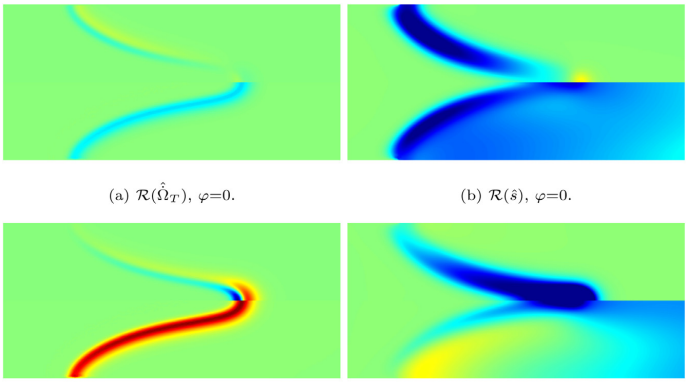

(a) $\mathcal{R}(\hat{\dot{\Omega}}_T)$, φ=0. (b) $\mathcal{R}(\hat{s})$, φ=0.

(c) $\mathcal{R}(\hat{\dot{\Omega}}_T)$, φ=$\pi/2$. (d) $\mathcal{R}(\hat{s})$, φ=$\pi/2$.

Fig. 15. Real part of heat release rate $\mathcal{R}(\hat{\dot{\Omega}}_T)$ (left) and entropy $\mathcal{R}(\hat{s})$ (right) perturbations for CFD (top half of each snapshot) and LNSE+$\mathcal{F}_G$ (bottom half of each snapshot) on a symmetric color scale. The scale for heat release rate perturbations is normalized with the maximum value in the period of $\omega = 100$ Hz. CFD and LNSE have individual scales for the heat release perturbations, the scale of the LNSE is about one order of magnitude smaller. They share the same over-saturated scale for entropy perturbations. Red indicates positive, blue negative and green zero perturbation.

frequency response of the LRF model is larger than that of the hybrid LNSE+$\mathcal{F}_L$ model, when accounting for the computational effort to derive $\mathcal{F}_L$ from harmonically forced CFD, the overall effort of the LRF approach can be significantly lower.

6. Conclusions and outlook

The core finding of the present study is that even for acoustically and convectively compact flames, a fine-grained local resolution of the perturbed heat release rate, which accounts for the effects of flame movement, is required to correctly predict the generation of entropy waves by a premixed flame. In particular, it is demonstrated that spurious generation of entropy waves results when the Linearized Navier-Stokes Equations (LNSE) are combined with a global Flame Transfer Function (FTF), which does not provide the spatial distribution of the perturbed heat release rate. The inadequate representation of flame movement that results from the scalar nature of the global FTF is identified as the root cause of this deficiency. The spurious entropy source term exhibits a low-pass characteristic, which is explained in terms of the perturbed convection time through the combustion zone.

A fine-grained representation of the flame dynamics by means of a highly resolved local FTF eliminates the unphysical behavior. However, it is computationally very demanding to identify a local FTF that resolves the flame dynamics on scales as small as the premix flame reaction zone. Thus the Linearized Reactive Flow (LRF) model is suggested as a viable alternative. Other than the hybrid LNSE+FTF approach, the LRF includes explicitly linearized species transport and combustion kinetics and thereby eliminates the need for an external model like the FTF to account for flow-flame interactions. Results confirm that such a monolithic representation of linearized thermoacoustic interactions and flame dynamics accounts for the effects of flame movement and does not produce spurious entropy waves.

Because self-excited thermoacoustic instabilities in a combustor are a highly complex phenomenon with a large number of influence factors, we have strived in the present paper to demonstrate the spurious entropy generation on premix flame configurations that are as simple as possible. The two seemingly undemanding cases of premixed methane-air combustion investigated, i.e. a freely propagating 1D flame and a 2D flame anchored in a duct of constant cross-sectional area, make the analysis clearer and more stringent than more complex configurations would allow. Nevertheless, one should expect that the range of applications of the LRF can be expanded to acoustically non-compact flames, as present in thermoacoustic high-frequency instabilities. Furthermore, technically premixed flames subject to mixture inhomogeneities in the approach flow can be studied without the need for a flow-flame model explicitly dedicated to the flame response to the mixture perturbations.

Declaration of Competing Interest

The authors declare that they have no known competing financial interests or personal relationships that could have appeared to influence the work reported in this paper.

Appendix A. Chemical kinetic mechanism

The lean premixed combustion of methane and air is modeled by the reduced two-step chemical kinetic mechanism 2S-CM2 as investigated in [73]:

$$CH_4{}^a + 1.5O_2{}^b \rightarrow CO + 2H_2O, \tag{A.1}$$

$$CO + 0.5O_2{}^c \leftrightharpoons CO_2, \tag{A.2}$$

with $a = 0.9$, $b = 1.1$ and $c = 0.5$. One of the novelties of the work presented in this paper is the analytical linearization of this reaction mechanism. Opposed to the work of Avdonin et al. [20], where an irreversible one step chemistry was used, the 2S-CM2 mechanism features reversible oxidation of CO. This leads to better agreement with kinetics of complex chemistry [73], but comes at the cost of including more species transport equations as well as a more laborious analytical linearization procedure (see Section Appendix B).

As the linearization of the kinetic mechanism is at the core of the LRF, a detailed description of the governing equations follows. The source terms for energy and species are modeled as:

$$\dot{\Omega}_k = \sum_{n=1}^{2} W_k \nu_{kn} \mathcal{Q}_n, \tag{A.3}$$

$$\dot{\Omega}_T = -\sum_{n=1}^{2} \Delta h_n^0 \mathcal{Q}_n, \tag{A.4}$$

with ν_{kn} being the stoichiometric coefficient of species k in reaction n and Δh_n^0 the standard enthalpy of reaction n. The progress rate for the first, irreversible reaction is given by

$$\mathcal{Q}_1 = K_{f1} \rho^{(a+b)} \left(\frac{Y_{CH_4}}{W_{CH_4}} \right)^a \left(\frac{Y_{O_2}}{W_{O_2}} \right)^b, \tag{A.5}$$

while the progress rate for the second, reversible reaction results as the difference between the forward and reverse contribution,

$$\mathcal{Q}_2 = K_{f2} \rho^{(1+c)} \frac{Y_{CO}}{W_{CO}} \left(\frac{Y_{O_2}}{W_{O_2}} \right)^c - K_{r2} \rho \frac{Y_{CO_2}}{W_{CO_2}}. \tag{A.6}$$

Here, K_{fn} and K_{rn} are the forward and reverse rates of reaction n, respectively. The forward rates of each reaction are given by the Arrhenius law,

$$K_{fn} = A_{fn} \exp\left(-\frac{T_{an}}{T} \right), \tag{A.7}$$

with the rate constants given in Table A.7.

Table A.7
Rate constants of the C2-SM2 mechanism [73].

Name	Value
A_1	$2 \cdot 10^{1}$5cgs units
T_{a1}	17611.7 K
A_2	$2 \cdot 10^{9}$ cgs units
T_{a2}	6038.29 K

The reverse rate K_{r2} of the second reaction is computed from the forward rate and an equilibrium constant K_{c2} based on molar concentrations,

$$K_{r2} = \frac{K_{f2}}{K_{c2}}. \tag{A.8}$$

K_{c2} is determined via equilibrium thermodynamics from the equilibrium constant K_{p2} based on partial pressures:

$$K_{c2} = \left(\frac{p_a}{R_{\text{univ}} T} \right)^{\sum_{k=1}^{N} \nu_{k2}} K_{p2}, \tag{A.9}$$

$$K_{p2} = \exp\left(\frac{\Delta G_2^0}{R_{\text{univ}} T} \right). \tag{A.10}$$

Here, R_{univ} is the universal gas constant and ΔG_2^0 is the molar-based standard-state Gibbs function change for the second reaction, expressed via

$$\Delta G_2^0 = -\sum_{k=1}^{N} \nu_{k2} (H_k - T S_k), \tag{A.11}$$

with the molar-based enthalpy H_k and entropy S_k of species k and

$$\sum_{k=1}^{N} \nu_{k2} = \nu''_{CO_2,2} - \nu'_{CO,2} - \nu'_{O_2,2} = 0.5. \tag{A.12}$$

Appendix B. Linearized chemical kinetics

Section Appendix A showed that the analytical linearization of the reduced combustion mechanism results in a plethora of terms, especially because all the thermodynamic quantities that are needed to compute the equilibrium constant K_{c2} depend on temperature and are thus perturbed when oscillations in temperature occur. We follow the systematic approach of a first order Taylor expansion to derive the perturbed heat release rate $\dot{\Omega}'_T$ in Eq. (13) and the perturbed species source terms $\dot{\Omega}'_k$ in Eq. (14). The perturbations stem from the perturbed progress rates of the reactions,

$$\dot{\Omega}'_k = \sum_{n=1}^{2} W_k \nu_{kn} \mathcal{Q}'_n, \tag{B.1}$$

$$\dot{\Omega}'_T = -\sum_{n=1}^{2} \Delta h_n^0 \mathcal{Q}'_n. \tag{B.2}$$

The perturbed rates of progress can be written as functions of perturbations in temperature, density and species mass fractions:

$$\mathcal{Q}'_n = \frac{\partial \bar{\mathcal{Q}}_n}{\partial \bar{T}} T' + \frac{\partial \bar{\mathcal{Q}}_n}{\partial \bar{\rho}} \rho' + \sum_k \frac{\partial \bar{\mathcal{Q}}_n}{\partial \bar{Y}_k} Y'_k. \tag{B.3}$$

The derivatives of the mean rates of progress with respect to mean temperature, density and species mass fractions can be seen as

sensitivities of the rates of progress to changes in these quantities and are derived analytically from Eqs. (A.5)–(A.11):

$$\frac{\partial K_{fn}}{\partial T} = K_{fn}\frac{T_{an}}{T^2} \tag{B.4}$$

$$\frac{\partial K_{pn}}{\partial T} = -\frac{K_{pn}}{R_{\text{univ}}T^2}\sum_{k=1}^{N}\nu_{kn}H_k \tag{B.5}$$

$$\frac{\partial K_{cn}}{\partial T} = \left(\frac{\partial K_{pn}}{\partial T} - \frac{K_{pn}}{T}\sum_{k=1}^{N}\nu_{kn}\right)\left(\frac{p_a}{R_{\text{univ}}T}\right)^{\sum_{k=1}^{N}\nu_{kn}} \tag{B.6}$$

$$\frac{\partial K_{rn}}{\partial T} = \frac{1}{K_{cn}^2}\left(\frac{\partial K_{fn}}{\partial T}K_{cn} - \frac{\partial K_{cn}}{\partial T}K_{fn}\right) \tag{B.7}$$

$$\frac{\partial \mathcal{Q}_1}{\partial T} = \frac{\partial K_{f1}}{\partial T}\rho^{(a+b)}\left(\frac{Y_{\text{CH}_4}}{W_{\text{CH}_4}}\right)^a\left(\frac{Y_{\text{O}_2}}{W_{\text{O}_2}}\right)^b \tag{B.8}$$

$$\frac{\partial \mathcal{Q}_1}{\partial \rho} = \frac{a+b}{\rho}\mathcal{Q}_1 \tag{B.9}$$

$$\frac{\partial \mathcal{Q}_1}{\partial Y_{\text{CH}_4}} = K_{f1}\rho^{(a+b)}\frac{aY_{\text{CH}_4}^{(a-1)}}{W_{\text{CH}_4}^a}\left(\frac{Y_{\text{O}_2}}{W_{\text{O}_2}}\right)^b \tag{B.10}$$

$$\frac{\partial \mathcal{Q}_1}{\partial Y_{\text{O}_2}} = K_{f1}\rho^{(a+b)}\left(\frac{Y_{\text{CH}_4}}{W_{\text{CH}_4}}\right)^a\frac{bY_{\text{O}_2}^{(b-1)}}{W_{\text{O}_2}^b} \tag{B.11}$$

$$\frac{\partial \mathcal{Q}_2}{\partial T} = \frac{\partial K_{f2}}{\partial T}\rho^{(1+c)}\frac{Y_{\text{CO}}}{W_{\text{CO}}}\left(\frac{Y_{\text{O}_2}}{W_{\text{O}_2}}\right)^c - \frac{\partial K_{r2}}{\partial T}\rho\frac{Y_{\text{CO}_2}}{W_{\text{CO}_2}} \tag{B.12}$$

$$\frac{\partial \mathcal{Q}_2}{\partial Y_{\text{CO}}} = K_{f2}\rho^{(1+c)}\frac{1}{W_{\text{CO}}}\left(\frac{Y_{\text{O}_2}}{W_{\text{O}_2}}\right)^c \tag{B.13}$$

$$\frac{\partial \mathcal{Q}_2}{\partial Y_{\text{O}_2}} = K_{f2}\rho^{(1+c)}\frac{Y_{\text{CO}}}{W_{\text{CO}}}\frac{cY_{\text{O}_2}^{(c-1)}}{W_{\text{O}_2}^c} \tag{B.14}$$

$$\frac{\partial \mathcal{Q}_2}{\partial Y_{\text{CO}_2}} = -K_{r2}\rho\frac{1}{W_{\text{CO}_2}} \tag{B.15}$$

Eq. (B.10) features the term $Y_{\text{CH}_4}^{(a-1)}$, where $a = 0.9$. In regions where the mean mass fraction of CH4 is (close to) zero, i.e. downstream of the flame, this term tends to infinity. In the final formula for the perturbed heat release, the sensitivity $\frac{\partial \bar{\mathcal{Q}}_1}{\partial \tilde{Y}_{\text{CH}_4}}$ is multiplied by the fluctuations of CH4 mass fraction, Y'_{CH4}, which tends towards zero after the flame for all solutions investigated. To avoid numerical problems that come with a multiplication of infinity and zero, a threshold is introduced for division by $\tilde{Y}_{\text{CH}_4}$ which is equal to $1 \cdot 10^{-4}$ times the maximum value of $\tilde{Y}_{\text{CH}_4}$ in the whole field, $\max\left(\tilde{Y}_{\text{CH}_4}\right) = 0.0429$.

Supplementary material

Supplementary material associated with this article can be found, in the online version, at doi:10.1016/j.combustflame.2020.09.018

References

[1] T.C. Lieuwen, Unsteady Combustor Physics, Cambridge University Press, New York, N.Y., USA, 2012.

[2] B.B.H. Schuermans, W. Polifke, C.O. Paschereit, J.H. van der Linden, Prediction of acoustic pressure spectra in combustion systems using swirl stabilized gas turbine burners, Volume 2: Coal, Biomass and Alternative Fuels; Combustion and Fuels; Oil and Gas Applications; Cycle Innovations, 2000-GT-0105, American Society of Mechanical Engineers, Munich, Germany, 2000, doi:10.1115/2000-GT-0105. V002T02A025

[3] T. Emmert, State Space Modeling of Thermoacoustic Systems with Application to Intrinsic Feedback, TU München, München, Germany, 2016 Ph.D. Thesis.

[4] T. Emmert, M. Meindl, S. Jaensch, W. Polifke, Linear state space interconnect modeling of acoustic systems, Acta Acust. United Acust. 102 (5) (2016) 824–833, doi:10.3813/AAA.918997.

[5] V.N. Kornilov, R. Rook, J.H.M. ten Thije Boonkkamp, L.P.H. de Goey, Experimental and numerical investigation of the acoustic response of multi-slit bunsen burners, Combust. Flame 156 (10) (2009) 1957–1970, doi:10.1016/j.combustflame.2009.07.017.

[6] C.F. Silva, T. Emmert, S. Jaensch, W. Polifke, Numerical study on intrinsic thermoacoustic instability of a laminar premixed flame, Combust. Flame 162 (9) (2015) 3370–3378, doi:10.1016/j.combustflame.2015.06.003.

[7] S. Jaensch, M. Merk, E. Gopalakrishnan, S. Bomberg, T. Emmert, R. Sujith, W. Polifke, Hybrid CFD/low-order modeling of nonlinear thermoacoustic oscillations, Proc. Combust. Inst. 36 (3) (2017) 3827–3834, doi:10.1016/j.proci.2016.08.006.

[8] P. Wolf, R. Balakrishnan, G. Staffelbach, L. Gicquel, T. Poinsot, Using LES to study reacting flows and instabilities in annular combustion chambers, Flow Turbul. Combust. 88 (2012) 191–206, doi:10.1007/s10494-011-9367-7.

[9] P. Wolf, G. Staffelbach, L.Y.M. Gicquel, J.-D. Müller, T. Poinsot, Acoustic and Large Eddy Simulation studies of azimuthal modes in annular combustion chambers, Combust. Flame 159 (11) (2012) 3398–3413, doi:10.1016/j.combustflame.2012.06.016.

[10] M. Merk, R. Gaudron, M. Gatti, C. Mirat, T. Schuller, W. Polifke, Measurement and simulation of combustion noise and dynamics of a confined swirl flame, AIAA J. 56 (5) (2018) 1930–1942, doi:10.2514/1.J056502.

[11] A. Kierkegaard, S. Boij, G. Efraimsson, A frequency domain linearized Navier–Stokes equations approach to acoustic propagation in flow ducts with sharp edges, J. Acoust. Soc. Am. 127 (2010) 710–719, doi:10.1121/1.3273899.

[12] A. Kierkegaard, S. Allam, G. Efraimsson, M. Åbom, Simulations of whistling and the whistling potentiality of an in-duct orifice with linear aeroacoustics, J. Sound Vib. 331 (5) (2012) 1084–1096, doi:10.1016/j.jsv.2011.10.028.

[13] J. Gikadi, T. Sattelmayer, A. Peschiulli, Effects of the mean flow field on the thermo-acoustic stability of aero-engine combustion chambers, ASME Turbo Expo 2012: Turbine Technical Conference and Exposition, American Society of Mechanical Engineers, Copenhagen, Denmark (2012), pp. 1203–1211, doi:10.1115/GT2012-69612.

[14] J. Gikadi, Prediction of Acoustic Modes in Combustors Using Linearized Navier–Stokes Equations in Frequency Space, TU München, München, Germany, 2013 PhD Thesis.

[15] M. Schulze, T. Sattelmayer, A comparison of time and frequency domain descriptions of high frequency acoustics in rocket engines with focus on dome coupling, Aerosp. Sci. Technol. 45 (2015) 165–173, doi:10.1016/j.ast.2015.05.007.

[16] M. Zahn, M. Schulze, C. Hirsch, M. Betz, T. Sattelmayer, Frequency Domain Predictions of Acoustic Wave Propagation and Losses in a Swirl Burner With Linearized Navier-Stokes equations, ASME Turbo Expo 2015: Turbine Technical Conference and Exposition, GT2015-42723, ASME, Montreal, Quebec, Canada (2015), doi:10.1115/GT2015-42723. V04AT04A055

[17] W.C. Ullrich, T. Sattelmayer, Transfer functions of acoustic, entropy and vorticity waves in an annular model combustor and nozzle for the prediction of the ratio between indirect and direct combustion noise, 21st AIAA/CEAS Aeroacoustics Conference, AIAA 2015–2972, American Institute of Aeronautics and Astronautics, Dallas, TX (2015), doi:10.2514/6.2015-2972.

[18] M. Schulze, Linear Stability Assessment of Cryogenic Rocket Engines, TU München, München, Germany, 2016 PhD Thesis.

[19] A. Albayrak, D.A. Bezgin, W. Polifke, Response of a swirl flame to inertial waves, Int. J. Spray Combust. Dyn. 10 (4) (2018) 277–286, doi:10.1177/1756827717747201.

[20] A. Avdonin, M. Meindl, W. Polifke, Thermoacoustic analysis of a laminar premixed flame using a linearized reacting flow solver, Proceedings of the Combustion Institute, 37 (2019), pp. 5307–5314, doi:10.1016/j.proci.2018.06.142.

[21] M. Fosas de Pando, D. Sipp, P.J. Schmid, Efficient evaluation of the direct and adjoint linearized dynamics from compressible flow solvers, J. Comput. Phys. 231 (23) (2012) 7739–7755, doi:10.1016/j.jcp.2012.06.038.

[22] M. Blanchard, T. Schuller, D. Sipp, P.J. Schmid, Response analysis of a laminar premixed M-flame to flow perturbations using a linearized compressible Navier–Stokes solver, Phys. Fluids 27 (4) (2015) 043602, doi:10.1063/1.4918672.

[23] M. Meindl, A. Albayrak, W. Polifke, A state-space formulation of a discontinuous Galerkin method for thermoacoustic stability analysis, J. Sound Vib. 481 (2020) 115431, doi:10.1016/j.jsv.2020.115431.

[24] F.E. Marble, S.M. Candel, Acoustic disturbance from gas non-uniformities convected through a nozzle, J. Sound Vib. 55 (2) (1977) 225–243, doi:10.1016/0022-460X(77)90596-X.

[25] M.S. Bohn, Response of a subsonic nozzle to acoustic and entropy disturbances, J. Sound Vib. 52 (2) (1977) 283–297, doi:10.1016/0022-460X(77)90647-2.

[26] J.J. Keller, W. Egli, J. Hellat, Thermally induced low-frequency oscillations, Z. Angew. Math. Phys. 36 (2) (1985) 250–274, doi:10.1007/BF00945460.

[27] W. Polifke, C.O. Paschereit, K. Döbbeling, Constructive and destructive interference of acoustic and entropy waves in a premixed combustor with a choked exit, Int. J. Acoust. Vib. 6 (3) (2001) 135–146, doi:10.20855/ijav.2001.6.382.

[28] S. Stow, A. Dowling, T. Hynes, Reflection of circumferential modes in a choked nozzle, J. Fluid Mech. 467 (2002) 215–239, doi:10.1017/S0022112002001428.

[29] F. Bake, N. Kings, A. Fischer, I. Roehle, Indirect combustion noise: investigations of noise generated by the acceleration of flow inhomogeneities, Acta Acust. United Acust. 95 (3) (2009) 461–469, doi:10.3813/AAA.918170.
[30] I. Duran, S. Moreau, Solution of the quasi-one-dimensional linearized Euler equations using flow invariants and the Magnus expansion, J. Fluid Mech. 723 (2013) 190–231, doi:10.1017/jfm.2013.118.
[31] C.S. Goh, A.S. Morgans, The influence of entropy waves on the thermoacoustic stability of a model combustor, Combust.Sci. Technol. 185 (2) (2013) 249–268, doi:10.1080/00102202.2012.715828.
[32] A.S. Morgans, I. Duran, Entropy noise: a review of theory, progress and challenges, Int. J. Spray Combust.Dyn. 8 (4) (2016) 285–298, doi:10.1177/1756827716651791.
[33] E. Motheau, L. Selle, F. Nicoud, Accounting for convective effects in zero-Mach-number thermoacoustic models, J. Sound Vib. 333 (1) (2014) 246–262, doi:10.1016/j.jsv.2013.08.046.
[34] M. Leyko, F. Nicoud, T. Poinsot, Comparison of direct and indirect combustion noise mechanisms in a model combustor, AIAA J. 47 (11) (2009) 2709–2716, doi:10.2514/1.43729.
[35] P. Hield, M. Brear, Comparison of open and choked premixed combustor exits during thermoacoustic limit cycle, AIAA J. 46 (2) (2008) 517.
[36] E. Motheau, F. Nicoud, T. Poinsot, Mixed acoustic–entropy combustion instabilities in gas turbines, J. Fluid Mech. 749 (2014) 542–576, doi:10.1017/jfm.2014.245.
[37] Y. Mahmoudi, A. Giusti, E. Mastorakos, A.P. Dowling, Low-order modeling of combustion noise in an aero-engine: the effect of entropy dispersion, J. Eng. Gas Turb. Power 140 (2017), doi:10.1115/1.4037321.
[38] B. Singaravelu, S. Mariappan, A. Saha, Theoretical formulation for the investigation of acoustic and entropy-driven combustion instabilities in gas turbine engines, in: A.K. Agarwal, S. De, A. Pandey, A.P. Singh (Eds.), Combustion for Power Generation and Transportation, Springer Singapore (2017), pp. 169–196, doi:10.1007/978-981-10-3785-6_9.
[39] M.A. Macquisten, A.P. Dowling, Low-frequency combustion oscillations in a model afterburner, Combust. Flame 94 (3) (1993) 253–264, doi:10.1016/0010-2180(93)90072-B.
[40] M. Muthukrishnan, W.C. Strahle, D.H. Neale, Separation of hydrodynamic, entropy, and combustion noise in a gas turbine combustor, AIAA J. 16 (4) (1978) 320–327, doi:10.2514/3.60895.
[41] T. Sattelmayer, Influence of the combustor aerodynamics on combustion instabilities from equivalence ratio fluctuations, J. Eng. Gas Turb. Power 125 (1) (2003) 11–19, doi:10.1115/1.1365159.
[42] A.S. Morgans, C.S. Goh, J.A. Dahan, The dissipation and shear dispersion of entropy waves in combustor thermoacoustics, J. Fluid Mech. 733 (2013), doi:10.1017/jfm.2013.448.
[43] T. Steinbacher, M. Meindl, W. Polifke, Modeling the generation of temperature inhomogeneities by a premixed flame, Int. J. Spray Combust.Dyn. 10 (2) (2018) 111–130, doi:10.1177/1756827717738139.
[44] C.L. Morfey, Amplification of aerodynamic noise by convected flow inhomogeneities, J. Sound Vib. 31 (4) (1973) 391–397, doi:10.1016/S0022-460X(73)80255-X.
[45] F. Bake, N. Kings, A. Fischer, I. Röhle, Experimental investigation of the entropy noise mechanism in aero-engines, Int. J. Aeroacoust. 8 (1) (2009) 125–141, doi:10.1260/147547209786234966.
[46] N. Karimi, M.J. Brear, W.H. Moase, Acoustic and disturbance energy analysis of a flow with heat communication, J. Fluid Mech. 597 (2008) 67–89, doi:10.1017/S0022112007009573.
[47] N. Karimi, M.J. Brear, W.H. Moase, On the interaction of sound with steady heat communicating flows, J. Sound Vib. 329 (22) (2010) 4705–4718, doi:10.1016/j.jsv.2010.05.009.
[48] M. Yoon, The entropy wave generation in a heated one-dimensional duct, J. Fluid Mech. 883 (2020) A44, doi:10.1017/jfm.2019.901.
[49] A.P. Dowling, The calculation of thermoacoustic oscillation, J. Sound Vib. 180 (4) (1995) 557–581, doi:10.1006/jsvi.1995.0100.
[50] M. Bauerheim, F. Nicoud, T. Poinsot, Theoretical analysis of the mass balance equation through a flame at zero and non-zero mach numbers, Combust. Flame 162 (2014) 60–67, doi:10.1016/j.combustflame.2014.06.017.
[51] L. Strobio Chen, S. Bomberg, W. Polifke, Propagation and generation of acoustic and entropy waves across a moving flame front, Combust. Flame 166 (2016) 170–180, doi:10.1016/j.combustflame.2016.01.015.
[52] L. Strobio Chen, T. Steinbacher, C. Silva, W. Polifke, On generation of entropy waves across a premixed flame, Proceedings of ASME 2016 Turbo Expo: Turbomachinery Technical Conference & Exposition, GT2016-57026 (2016), doi:10.1115/GT2016-57026. Seoul, Korea
[53] B.-T. Chu, On the generation of pressure waves at a plane flame front, Symp. (Int.) Combust. 4 (1) (1953) 603–612, doi:10.1016/S0082-0784(53)80081-0.
[54] B.B.H. Schuermans, W. Polifke, C.O. Paschereit, Modeling transfer matrices of premixed flames and comparison with experimental results, Volume 2: Coal, Biomass and Alternative Fuels; Combustion and Fuels; Oil and Gas Applications; Cycle Innovations, ASME 99-GT-132, American Society of Mechanical Engineers, Indianapolis, Indiana, USA, 1999, doi:10.1115/99-GT-132. V002T02A024
[55] J. Sato, Effects of lewis number on extinction behavior of premixed flames in a stagnation flow, Symp. (Int.) Combust. 19 (1) (1982) 1541–1548, doi:10.1016/S0082-0784(82)80331-7.
[56] H. Weller, G. Tabor, H. Jasak, C. Fureby, A tensorial approach to computational continuum mechanics using object-oriented techniques, Comput. Phys. 12 (1998) 620–631, doi:10.1063/1.168744.
[57] L. Magri, J. O'Brien, M. Ihme, Compositional inhomogeneities as a source of indirect combustion noise, J. Fluid Mech. 799 (2016), doi:10.1017/jfm.2016.397.
[58] C.E. Martin, L. Benoit, Y. Sommerer, F. Nicoud, T. Poinsot, Large-eddy simulation and acoustic analysis of a swirled staged turbulent combustor, AIAA J. 44 (4) (2006) 741–750, doi:10.2514/1.14689.
[59] M. Zhu, A.P. Dowling, K.N.C. Bray, Flame transfer function calculations for combustion oscillations, Volume 2: Coal, Biomass and Alternative Fuels; Combustion and Fuels; Oil and Gas Applications; Cycle Innovations, American Society of Mechanical Engineers, New Orleans, Louisiana, USA, 2001, doi:10.1115/2001-GT-0374. V002T02A055
[60] K. Truffin, B. Varoquié, T. Poinsot, Measurements of transfer functions in reacting flows using Large Eddy Simulations, 10th International Congress on Sound and Vibration,Stockholm, Sweden (2003), pp. 785–793.
[61] C.A. Armitage, A.J. Riley, R.S. Cant, A.P. Dowling, S.R. Stow, Flame transfer function for swirled LPP combustion from experiments and CFD, ASME Turbo Expo 2004: Power for Land, Sea, and Air, GT2004-53820, ASME, Vienna, Austria (2004), pp. 527–537, doi:10.1115/GT2004-53820.
[62] S. Kato, T. Fujimori, A.P. Dowling, H. Kobayashi, Effect of heat release distribution on combustion oscillation, Proc. Combust. Inst. 30 (2) (2005) 1799–1806, doi:10.1016/j.proci.2004.08.154.
[63] D. Kang, F. Culick, A. Ratner, Combustion dynamics of a low-swirl combustor, Combust. Flame 151 (3) (2007) 412–425, doi:10.1016/j.combustflame.2007.07.017.
[64] K.T. Kim, J.G. Lee, B.D. Quay, D.A. Santavicca, Spatially distributed flame transfer functions for predicting combustion dynamics in lean premixed gas turbine combustors, Combust. Flame 157 (9) (2010) 1718–1730, doi:10.1016/j.combustflame.2010.04.016.
[65] R. Leandro, W. Polifke, Low-order modelling of distributed heat release, 19th Int. Congress on Sound and Vibration, Int'l Inst. of Acoustics and Vibration, Vilnius, Lithuania, 2012.
[66] M. Schulze, T. Sattelmayer, Eigenvalue analysis for the prediction of initial growth rates of thermoacoustic instability in rocket motors, 53rd AIAA Aerospace Sciences Meeting, American Institute of Aeronautics and Astronautics, Kissimmee, Florida, USA, 2015, doi:10.2514/6.2015-1606.
[67] J. Li, Y. Xia, A.S. Morgans, X. Han, Numerical prediction of combustion instability limit cycle oscillations for a combustor with a long flame, Combust. Flame 185 (2017) 28–43, doi:10.1016/j.combustflame.2017.06.018.
[68] B. Schuermans, Modeling and Control of Thermoacoustic Instabilities, École Polytechnique Fédérale de Lausanne, Lausanne, Switzerland, 2003 PhD Thesis.
[69] B. Varoquié, J.P. Légier, F. Lacas, D. Veynante, T. Poinsot, Experimental analysis and large eddy simulation to determine the response of non-premixed flames submitted to acoustic forcing, Proc. Combust. Inst. 29 (2) (2002) 1965–1970, doi:10.1016/S1540-7489(02)80239-5.
[70] A.P. Dowling, S.R. Stow, Acoustic analysis of gas turbine combustors, J. Propuls. Power 19 (5) (2003) 751–764, doi:10.2514/2.6192.
[71] W. Polifke, Black-box system identification for reduced order model construction, Ann. Nucl. Energy 67C (2014) 109–128, doi:10.1016/j.anucene.2013.10.037.
[72] C.F. Silva, F. Nicoud, T. Schuller, D. Durox, S. Candel, Combining a Helmholtz solver with the flame describing function to assess combustion instability in a premixed swirled combustor, Combust. Flame 160 (9) (2013) 1743–1754, doi:10.1016/j.combustflame.2013.03.020.
[73] J. Bibrzycki, T. Poinsot, A. Zajdel, Investigation of laminar flame speed of $CH_4/N_2/O_2$ and $CH_4/CO_2/O_2$ mixtures using reduced chemical kinetic mechanisms, Arch. Combust. 30 (4) (2010) 287–296.